UNIVERSITEIT VAN PRETORIA
UNIVERSITY OF PRETORIA
YUNIBESITHI YA PRETORIA

OPTICAL, THERMAL AND ECONOMIC OPTIMISATION OF A LINEAR FRESNEL COLLECTOR

by

Mohammad Moghimi Ardekani

Submitted in partial fulfilment of the requirements for the degree
Philosophiae Doctor (Mechanical Engineering)

in the

Department of Mechanical and Aeronautical Engineering
Faculty of Engineering, Built Environment and Information Technology

UNIVERSITY OF PRETORIA

2017

SUMMARY

OPTICAL, THERMAL AND ECONOMIC OPTIMISATION OF A LINEAR FRESNEL COLLECTOR

by

Mohammad Moghimi Ardekani

Supervisor: Prof K.J. Craig

Co-supervisor: Prof J.P. Meyer

Department: Mechanical and Aeronautical Engineering

University: University of Pretoria

Degree: Philosophiae Doctor (Mechanical Engineering)

Keywords: solar, optimisation, optical, thermal, economic, computational fluid dynamics (CFD), ray tracing, ANSYS DX, ANSYS Fluent, SolTrace.

Solar energy is one of a very few low-carbon energy technologies with the enormous potential to grow to a large scale. Currently, solar power is generated via the photovoltaic (PV) and concentrating solar power (CSP) technologies. The ability of CSPs to scale up renewable energy at the utility level, as well as to store energy for electrical power generation even under circumstances when the sun is not available (after sunset or on a cloudy day), makes this technology an attractive option for sustainable clean energy. The levelised electricity cost (LEC) of CSP with thermal storage was about 0.16-0.196 Euro/kWh in 2013 (Kost et al., 2013). However, lowering LEC and harvesting more solar energy from CSPs in future motivate researchers to work harder towards the optimisation of such plants. The situation tempts people and governments to invest more in this ultimate clean source of energy while shifting the energy consumption statistics of their societies from fossil fuels to solar energy.

Usually, researchers just concentrate on the optimisation of technical aspects of CSP plants (thermal and/or optical optimisation). However, the technical optimisation of a plant while disregarding economic goals cannot produce a fruitful design and in some cases may lead

to an increase in the expenses of the plant, which could result in an increase in the generated electrical power price.

The study focused on a comprehensive optimisation of one of the main CSP technology types, the linear Fresnel collector (LFC). In the study, the entire LFC solar domain was considered in an optimisation process to maximise the harvested solar heat flux throughout an imaginary summer day (optical goal), and to minimise cavity receiver heat losses (thermal goal) as well as minimising the manufacturing cost of the plant (economic goal). To illustrate the optimisation process, an LFC was considered with 12 design parameters influencing three objectives, and a unique combination of the parameters was found, which optimised the performance. In this regard, different engineering tools and approaches were introduced in the study, e.g., for the calculation of thermal goals, Computational Fluid Dynamics (CFD) and view area approaches were suggested, and for tackling optical goals, CFD and Monte-Carlo based ray-tracing approaches were introduced. The applicability of the introduced methods for the optimisation process was discussed through case study simulations. The study showed that for the intensive optimisation process of an LFC plant, using the Monte Carlo-based ray-tracing as high fidelity approach for the optical optimisation objective, and view area as a low fidelity approach for the thermal optimisation objective, made more sense due to the saving in computational cost without sacrificing accuracy, in comparison with other combinations of the suggested approaches.

The study approaches can be developed for the optimisation of other CSP technologies after some modification and manipulation. The techniques provide alternative options for future researchers to choose the best approach in tackling the optimisation of a CSP plant regarding the nature of optimisation, computational cost and accuracy of the process.

ACKNOWLEDGEMENTS

After thanking God for His infinite mercies in reaching this milestone, I would like to acknowledge the following people:

- my utmost gratitude to my supervisor, Professor Ken J. Craig, for his eye for detail, excellent feedback, technical guidance and good supervisor-student relationship. The extra hours he invested in checking this work even in his personal time are deeply appreciated;

- my deepest thanks go to my co-supervisor, Professor Josua P. Meyer, for offering his technical and financial support in the attainment of this degree;

- my sincere appreciation to my family members, for their endless love, concern, encouragement, prayer and words of advice;

- special thanks to Miss Sharifeh Vatannia, for her continuous moral support in the successful completion of my PhD degree;

- thanks to all the academic and non-academic staff members of the Department of Mechanical Engineering, University of Pretoria, for making me feel comfortable throughout the course of my PhD programme.

PUBLICATIONS AND AWARD

Parts of the study were presented in the Green Talent 2015 competition, which attracted over 550 researchers from more than 90 countries. The Green Talent is a prestigious German competition, which is hosted annually by the German Federal Ministry of Education and Research (BMBF) and judged by a high-ranking jury of German experts (Available at: http://www.greentalents.de/index.php [Last accessed: 22.07.2016]).

Also, parts of the study were presented in the following list of papers while the study was in progress. Therefore, some parts of this thesis have the same content as many of the articles and conference papers.

Published articles in international journals

1. **Moghimi, M.A.**, Craig, K.J. & Meyer, J.P. (2015). Optimization of a Trapezoidal Cavity Absorber for the Linear Fresnel Reflector. *Solar Energy*, **119**:343-361. **(IF=3.541)**
2. **Moghimi, M.A.**, Craig, K.J. & Meyer, J.P. (2015). A Novel Computational Approach to Combine the Optical and Thermal Modelling of Linear Fresnel Collectors using the Finite Volume Method. *Solar Energy*, **116**:407-427. **(IF=3.541)**
3. Craig, K.J., **Moghimi, M.A.**, Rungasamy, A.E., Marsberg, J. & Meyer, J.P. (2016). Finite-Volume Ray Tracing Using Computational Fluid Dynamics in Linear Focus CSP applications. *Applied Energy*,183: 241-256. **(IF=5.613)**

Manuscripts under review in international journals

4. **Moghimi, M.A.**, Craig, K.J. & Meyer, J.P. Simulation-Based Optimisation of a Linear Fresnel Collector Mirror Field and Receiver for Optical, Thermal and Economic Performance. *Solar Energy*, Submitted. **(IF=3.541)**

Conference Papers

5. **Moghimi, M.A.**, Craig, K.J. & Meyer, J.P. (2014). Response Surface Method Optimization of Cavity Absorber of a Linear Fresnel Reflector. In: Presented at the 2nd Southern African Solar Energy Conference (SASEC 2014), Port Elizabeth, South Africa.

6. Craig, K.J., **Moghimi**, **M.A. &** Marsberg, J. (2014). Optimisation of Solar Cavity Receivers Using ANSYS. In: Presented at 2014 ANSYS Convergence Conference, Pretoria, South Africa.
7. **Moghimi**, **M.A.,** Rungasamy, A., Craig, K.J. & Meyer, J.P. (2015). Introducing CFD in the Optical Simulation of Linear Fresnel Collectors. In: Presented at the 21th SolarPACES International Symposium, Cape Town, South Africa.
8. **Moghimi, M.A.**, Craig, K.J. & Meyer, J.P. (2015). A Novel Computational Approach to Combine the Optical and Thermal Modeling of a Linear Fresnel Collector Receiver. In: Presented at the 3rd Southern African Solar Energy Conference (SASEC 2015), Kruger Park, South Africa.
9. **Moghimi, M.A.**, Craig, K.J. & Meyer, J.P. (2016). Combined Thermal, Optical and Economic Optimization of a Linear Fresnel Collector. In: To be presented at the 22th SolarPACES International Symposium, Abu Dhabi, United Arab Emirates.
10. **Moghimi, M.A.**, Craig, K.J. & Meyer, J.P. (2016). Optimization of Insulation of a Linear Fresnel Collector. In: To be presented at the 22th SolarPACES International Symposium, Abu Dhabi, United Arab Emirates.
11. **Moghimi, M.A.**, Craig, K.J. & Meyer, J.P. (2016). Optimization of Fixed Focal Length for Linear Fresnel Collector. In: To be presented at the 4th Southern African Solar Energy Conference (SASEC 2016), Stellenbosch, South Africa.

WEBINAR

12. Craig, K.J., **Moghimi, M.A.** & Marsberg, J. (2014). Optimization of Solar Cavity Receivers Using ANSYS Software, WEBINAR of Innovation in Metallurgy and Solar Power via CFD, *ANSYS WEBINAR*. Available at: http://resource.ansys.com/Resource+Library/Webinars/Innovation+in+Metallurgy+and+Solar+Power+via+CFD+-+Webinar [Last accessed: 22.07.2016].

Award

13. The author was one of the 27 awardees of the Green Talents 2015 Competition.

TABLE OF CONTENTS

LIST OF FIGURES

LIST OF TABLES

NOMENCLATURE

SYMBOLS

a	Side insulation thickness [m]
A	Area [m^2]
b	Side insulation thickness [m]
c	Cavity top side width [m]
C_d	Mirror distance cost [€/m]
C_e	Elevation cost [€/m]
C_l	Land cost [€/m^2]
C_m	Mirror cost [€/m]
C_r	Receiver cost [€/m]
C^d_c	Direct specific cost of a collector [€/m^2]
c_p	Heat capacity at constant pressure [J/kg-K]
d	Tube bundle offset from cavity top wall [m]
f	Distance in a 2-D plane from the mirror centre to the tube bundle centre [m]
g	Gravitational constant [m/s^2]
g	Tube gap [m]
G	Gap between mirrors [m]
h	Cavity depth [m]
H	Receiver mounting height [m]
i	Interest rate
ID	Tube inner diameter [m]
k	Thermal conductivity [W/m-K]
m	Tube pitch [m]
M_w	Molecular weight of the gas
n	Economic lifetime of a plant in years
N	Number
OD	Tube outer diameter [m]

p	Distance of the outermost tube centre from the cavity aperture edge [m]
P	Mirror pitch [m]
P	Pressure [N/m^2]
q	Horizontal distance of tube centre from the cavity's bottom corner [m]
Q	Heat transfer [W]
r	Tube radius [m]
R	Universal gas constant [J/kg-K]
R	Correlation matrix
t	Top insulation thickness [m]
t_p	Tube thickness [m]
T	Temperature [K]
T_p	Average of all the pipes' outside-wall temperatures at their lowest points facing the incoming irradiation [K]
u	Velocity component along x-axis [m/s]
U_L	Heat loss coefficient [W/m^2-K]
v	Velocity component along y-axis [m/s]
w	Weighting factor
W	Mirror width [m]
W_F	Solar field width [m]
x	Axis direction
$\tilde{x}$	Set of design variable parameters
X	Horizontal distance from the mirror centre to the collector symmetry line [m]
y	Axis direction
Z	Perpendicular tube bundle distance from the mirror field [m]
GREEK SYMBOLS	
α	Central confining angle for each tube [°]
β	Volumetric thermal expansion coefficient [1/K]

β	Angle of the tangential line with the tube bundle line [°]
δ	Top insulation angle [°]
ε	Emissivity
θ	Cavity angle [°]
θ	Polar angle
σ	Stefan-Boltzmann constant [W/m^2-K^4]
σ^2	Variance
κ	Cost modification factor
ζ	Sun position in a transversal plane [°]
μ	Dynamic viscosity [Ns/m^2]
γ	Investment
ρ	Density, kg/m^3
ϕ	Azimuthal angle
ω	Circumferential angle [°]

SUBSCRIPTS

0	Reference, regarding cost, refers to the Solarmundo project
a	Annual
a	Ambient
abs	Absorber
e	Project efforts
Heat loss	Heat loss
m	Mirror
i	Insurance
i	Counter
I	Infrastructure
j	Counter
k	Counter
Mirror field	Mirror field
O&M	Operation and maintenance

operation	Operating
p	Pipe
P	Piping
Plant Cost Factor	Plant cost factor
PU	Power plant unit
S	Surface absorber
t	Tube
T	Tube
Tube bundle	Tube bundle
U	Uncertainties
view area	View area
θ	Angular discretisation in DO setting
ϕ	Angular discretisation in DO setting

SUPERSCRIPTS

Left	Left side
Right	Right side

LIST OF ABBREVIATIONS

Btu	British thermal units
CCD	central composite design
CFD	computational fluid dynamics
CLFR	compact linear Fresnel reflector
COP	Conference of the Parties
CSP	concentrating solar power
DLR	German Aerospace Centre
DO	discrete ordinates
DOE	Design of Experiments
DM	Design Modeler
DX	DesignXplorer
FV	finite volume
HTF	heat transfer fluid

LEC	levelised electricity cost
LFC	linear Fresnel collector
MCRT	Monte Carlo ray tracing
MOGA	multi-objective genetic algorithm
NREL	National Renewable Energy Laboratory, US
NSGA-II	non-dominated sorting genetic algorithm-II
PTC	parabolic trough collector
PV	photovoltaic
RSM	response surface method
RTE	radiative transfer equation
UNFCCC	United Nations Framework Convention on Climate Change
UDF	User-Defined Function
UDM	User-Defined Memory
UDS	User-Defined Scalar
VBA	Visual Basic for Applications
WB	WorkBench

1 INTRODUCTION

1.1 BACKGROUND

One of the critical global crises of this era is global warming. This crisis has drawn global attention since the 1990s because of the increase in the global average of air and ocean temperatures, the increase in the global average sea level, widespread glacier melting and other pieces of evidence (Effects of global warming, 2017). The Copenhagen Accord in 2009 set a limit at the United Nations Framework Convention on Climate Change (UNFCCC) to keep the threshold for “dangerous” human interference with the climate system. This limit was set at a 2 degrees Celsius rise from pre-industrial times (UNFCCC, 2009).

The most influential factor in global warming is greenhouse gas emissions (e.g. carbon dioxide - CO_2) due to the burning of fossil fuels. For example, in 2013, about 81.4% of the world’s primary energy was supplied from fossil fuels (oil, gas and coal); resulting in about 32 190 million tons of CO_2 (IEA, 2015a).

To achieve the 2 °C Copenhagen Accord goal, stabilising greenhouse gas emissions and limiting fossil fuel consumption are inevitable (IEA, 2015b). However, due to human energy dependence on fossil fuels and global energy demand growth, the reduction of fossil fuel consumption without a source of energy substitution leads to the energy crisis and economy instability especially. According to the International Energy Outlook 2016 (EIA, 2016), the world primary energy demand has increased by 48% from 2012 to 2040; from 549 quadrillion British thermal units (Btu) in 2012 to 815 quadrillion Btu in 2040.

In this regard, renewable energy sources can play a vital role. Solar power generation holds endless opportunities for people worldwide. Trieb et al. (2009) investigated the global potential of concentrating solar power (CSP) technologies. They found that the global technical CSP potential was almost 3 000 000 TWh/a, which hugely exceeded the world electricity consumption at that stage, which was 18 000 TWh/a. Figure 1.1 shows the

world map of the long-term average direct normal irradiance of the sun (GeoModel Solar, 2016), indicating the widespread availability of solar energy.

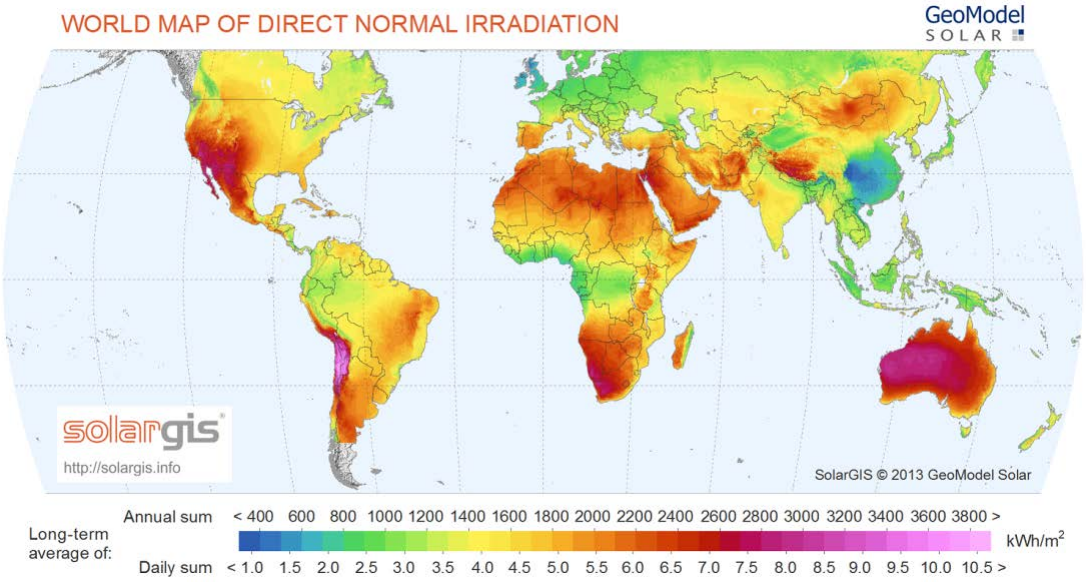

Figure 1.1. World map of long-term average of direct normal solar irradiance (GeoModel Solar, 2016)

From an environmental perspective, CSP electricity generation can reduce CO_2 emissions by 200 to 300 kg per year per installed square metre of concentrator surface (Richter et al., 2009). However, CSP electricity generation technologies usually generate electricity at levelised electricity cost (LEC) of 10 to 20 cents€/kWh in Europe while it has to compete with an LEC of 3 to 4 cents€/kWh for conventional technologies (Pitz-Paal et al., 2005). This comparison shows the enormous potential of techno-economic optimisation of CSP technologies to reduce the solar-generated electricity cost as well as harvesting more solar energy in these technologies.

1.2 MOTIVATION

The sun's energy is currently used as a power source via the photovoltaic (PV) effect or via thermal systems (solar thermal/concentrating solar power). The study focuses on the second conversion because of the ability of CSPs in storing energy and scaling up renewable energy at the utility level. Indeed, in CSP, the energy of the sun is transferred to a working fluid, also called heat transfer fluid (HTF), in what is known as a receiver,

collector or sometimes absorber, depending on the type and implementation. The main types of CSP plants that exist or are in various phases of development and research are as follows: dish, tower receiver, parabolic trough collector (PTC) and linear Fresnel collector (LFC). The surveyed case study in this research is LFC. However, it is noteworthy that the methodology of this study can be implemented for other CSP plants after modification.

Recently, LFC has been considered in solar receiver studies due to significant advantages, especially in comparison with PTC:

1. Easy maintenance, no-tracking absorber and no high-pressure joints, and low height of mirrors.
2. Cheaper due to near-ground mounting reflectors, simple tracking system, planar or slightly curved mirrors, no high-pressure flexible joints, minimal manufacturing, operation and maintenance cost.
3. Effective use of ground area, the location of primary reflectors can be side by side to each other; on the other hand, the shaded area underneath the collector can be considered as parking lots or other essential needs.

In general, an LFC CSP plant is based on an array of linear mirrors that concentrate solar rays on a downward-facing fixed receiver, which is covered with glass and contains pipe absorber/s. The pipes contain a specific HTF, which are heated by absorbing solar energy. The absorbed energy is applied to power generation (see Figure 1.2).

The aim of the research is answering the question of how much more solar energy in a cheaper way can be harvested from such a technology. The situation is tempting people and governments to invest in this source of energy and shift energy consumption statistics of their societies from fossil fuels to solar energy.

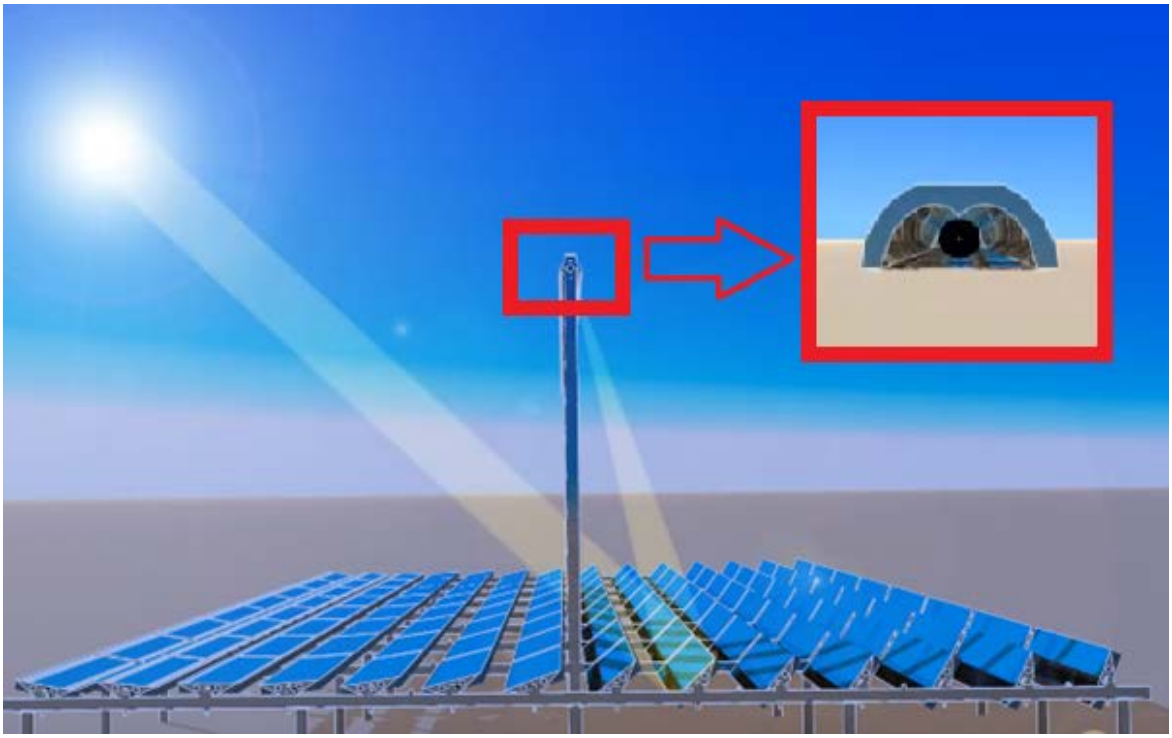

Figure 1.2. Layout of LFC technology with the inserted image of cavity receiver (SUNCNIM, 2017).

1.3 PROBLEM STATEMENT

The aim of CSP plant collectors and receivers is transferring solar energy to a working fluid. This process is accompanied by losses, both optical and thermal. The losses of the entire system could lead to a direct effect on the thermal efficiency of the thermodynamic cycle or the amount of energy harvested from the sun. On top of these technical aspects (thermal and optical), the economic aspect also plays a role in determining the use of solar energy in the future. In other words, by lowering the final cost of the produced solar energy in a plant, the CSP's generated energy price may be more competitive with other sources. However, minimising the costs needs a minimisation of the number of mirrors (cost of mirror field), mirror width (mirror width cost), mirror distances (land cost), cavity height (elevation cost), cavity size (cavity cost), and so on. These minimisations have direct effects on the amount of energy that is harvested from optical and thermal viewpoints (optical and thermal aspects of plants are affected). Therefore, optical and thermal

optimisation of a linear Fresnel collector has to be simulated with economic optimisation goals in an optimisation study to improve the ability of this technology and make it more attractive in the future.

1.4 OBJECTIVE

Thermal, optical and economic optimisation of a plant requires a complete mastery of the available engineering tools and approaches. A researcher has to be wise enough to know how to combine these tools to achieve a reasonable accuracy and computational cost for an optimisation study. Therefore, in the conceptual design phase of the study as the pre-requisite step, thorough investigations of the available and conventional engineering tools and simulation approaches are conducted. As part of this phase, the author also introduces and develops numerical and computational approaches to the thermal and optical simulation of a CSP plant as alternative options. These approaches are compared with conventional methods for finding the best reasonable approach to the optimisation of an LFC plant with reasonable accuracy and computational effort. Finally, based on these studies, an optimisation process is conducted in the entire solar domain to maximise the impinging solar heat flux on the cavity and minimise cavity heat loss while considering economic goals such as minimising the initial cost of the solar plant. Such an optimisation study will lead to a more efficient LFC plant with lower costs of generated solar electricity.

The objectives of the study are summarised as follows:

- Firstly, the conventional approach of optical simulation is to be investigated. In addition, a new approach for optical simulation is formulated and used in conjunction with the conventional method. A sample test case is used to determine the most efficient approach for the optimisation study of an LFC plant.
- The accuracy of the available CFD models of an LFC plant (as a conventional approach to the thermal study of solar plants) is doubtful and has to be improved by using more applicable assumptions and methods to capture physical phenomena accurately. To meet this objective, a thorough study is conducted on CFD modelling to come up with more realistic assumptions and methods followed by validation using a sample test case.

- A new approach to the thermal modelling of a plant that saves computational cost is to be developed. The proposed method is validated with the help of a sample test case simulation. The applicability of the proposed approach is compared with the conventional method to find the most appropriate approach for thermal simulation in the optimisation study to follow.
- The final objective is to conduct an optical, thermal and economic optimisation of the entire LFC collector using tools developed in achieving the previous objectives.

1.5 LAYOUT OF THE THESIS

A literature study regarding the CSP, LFC and its history, LFC mirror field, LFC cavity receiver and LFC optimisation is given in Chapter 2. The emphasis of this chapter is on the importance of the combined thermal, optical and economic optimisation of an LFC plant in one overall optimisation study. In Chapters 3 and 4, the conventional and suggested approaches to optical and thermal simulations of a plant are discussed and implemented in sample LFC test cases. These approaches are compared to find a suitable method for overall optimisation with reasonable accuracy and computational cost. The overall optimisation of an LFC plant with thermal, optical and economic goals is presented in Chapter 5; whereafter the thesis is finalised with concluding remarks in Chapter 6. Several addenda contain supporting information with further details to complement the body of the thesis.

2 LITERATURE STUDY

2.1 INTRODUCTION

Linear Fresnel collector technology is one of the main types of concentrating solar power technologies which have been developed since the 1960s. LFC has received more attention recently due to its advantages in comparison with other types of CSP plants such as lower capital cost, easy and low maintenance and high-ground utilisation. The late development of LFC technologies left plenty of room for its optimisation and made it an interesting topic among researchers. The objective of this chapter is to conduct a literature study to identify the different investigations on the receiver, collector and optimisation as well as the modelling techniques and approaches which have been used in this regard. The layout of the chapter begins with a brief discussion of CSP and LFC, which is followed by a literature survey of receiver and mirror field designs. Lastly, the optimisation considerations and modelling approaches in literature are discussed in a separate section because of the emphasis of the study on the optimisation of an LFC plant.

2.2 CONCENTRATING SOLAR POWER

The study focuses on solar thermal applications because of the ability of CSP plants in storing energy and scaling up renewable energy at the utility level. In CSP, the energy of the sun is transferred to a working fluid in what is called a receiver, collector or sometimes absorber, depending on the type and implementation. This characteristic of CSP can be paired in a hybrid configuration with another plant that either generates or consumes large quantities of heat (Miller et al., 2015). Also, the characteristic of CSP that allows thermal energy storage to be incorporated into the design of CSP plants, means that a solar thermal plant can run around the clock even after the sun sets.

The development of CSP technologies has a strong tie with global energy crises. The first period of CSP development started with the oil and energy crisis from 1973 to 1979 (Ross, 2013). This global crisis led to grants for scientific work to find a reliable alternative

source of energy. Due to the funded scientific works in this period all around the world, successful constructions of CSP plants were begun in the 1980s (listed in Table 2.1).

However, this period of crisis helped CSP technologies to prove themselves to be reliable and eco-friendly sources of solar energy. The period ended with the lifting of the crisis and the dropping of oil prices around the world. The second golden period of investment into CSP technologies was initiated by global warming in the ’90s and the Kyoto Protocol in 1997 (United Nations, 2016a) and was affected by the worldwide economic crisis. For instance, the Spanish government placed a moratorium on the construction of new renewable energy technologies that had not yet been approved (Government of Spain, 2012). This moratorium stopped the development of the LFC, which signified the end of the second period of CSP development. The third period of CSP development started with the role of the US in loan guarantees of different companies manufacturing CSP plants. This period mainly began because of energy dependence issues of the US government (Abbas et al., 2013). The achievements of the 21st Conference of the Parties (COP 21) to the United Nations Framework Convention on Climate Change (UNFCCC), which took place in Paris, France, in 2015 (United Nations, 2016b), increased the expectation of the commitments and motivations of other countries to subsidise and move towards renewable energy. Now countries focus more on renewable energy and CSPs to reduce their carbon footprint, which, in turn, opens new doors for the advancement of CSP technologies.

The development periods introduced four main CSP technologies, which are as follows:

Dish: This technology is a type of point-focusing CSP technology. It includes a parabolic dish-shaped reflector with a two-axis tracking system, which concentrates the incoming solar radiation throughout a day onto the dish’s focal point to generate electricity (Figure 2.1). The concentration ratio of this technology is usually above 2 000 (SolarPACES, 2011a) with 50 to 150 m^2 of the reflector area (Pitz-Paal, 2011). The operating temperature of the HTF in this technology is about 750 °C (Richter et al., 2009). The electrical output of the current dish technology with a Stirling engine or a Brayton cycle is about 25kWe and 30kWe respectively

(SolarPACES, 2011a). The German Aerospace Centre (DLR, 2007) rates the technology maturity as moderate with high reliability.

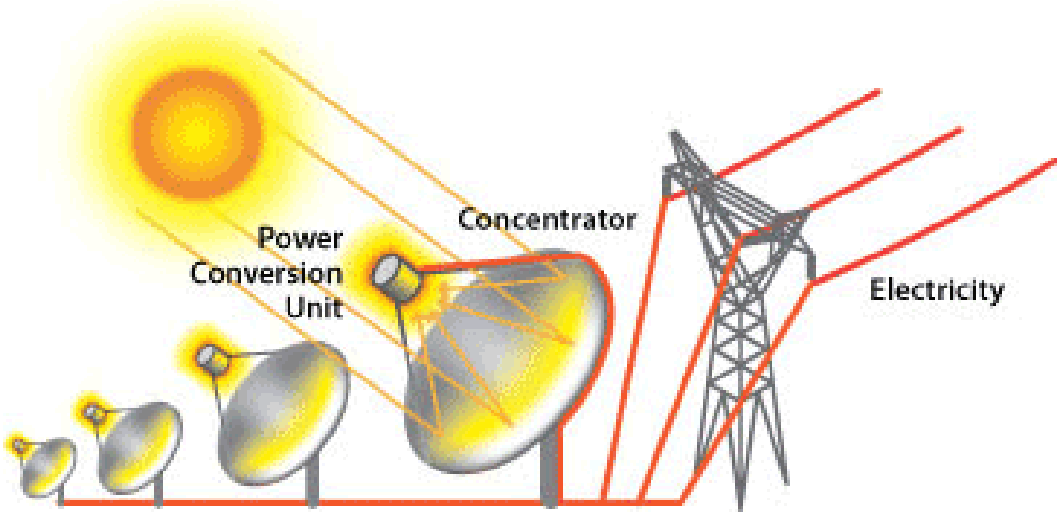

Figure 2.1. Solar dish technology (Image extracted from NASA, 2016).

Tower Receiver: This technology is a type of point-focusing technology. It consists of a circular array of sun-tracking mirrors (heliostats) to concentrate the solar radiation at the top of a tower. This concentrated energy is used to generate electricity in conventional power cycles (Figure 2.2). Concentration ratios of this technology are usually in the range of 500 to 1 500 (lower than the dish technology) (Pitz-Paal, 2011) with 50 to 150 m^2 of reflector area per heliostat (SolarPACES, 2000). The operating temperature of current tower technologies is limited to about 1 000 °C (European Commission, 2002). The electrical output of current tower technologies is about 30 to 400 MWe. In addition, the capacity factor of this technology is about 25% and 65% for without and with storage capability cases respectively (SolarPACES, 2011b). The German Aerospace Centre rates both technology maturity and reliability as moderate (DLR, 2007).

Table 2.1 Early CSP plants (Aringhoff & Brakmann, 2003; Spiewak, 1996).

Name	Location	Size (MW)	Type, HTF	Operation Date	Sponsor
Aurelios	Adrano, Sicily	1	Tower, Water-Steam	1981	EC
SSPS/CRS	Almeria, Spain	0.5	Tower, Sodium	1981	US and 8 European Countries
SSPS/DCS	Almeria, Spain	0.5	Trough, Oil	1981	US and 8 European Countries
Sunshine	Nio, Japan	1	Tower, Water-Steam	1981	Japan
Solar One	California, US	10	Tower, Water-Steam	1982	USDOE, Utilities
Themis	Targasonne, France	2.5	Tower, Molten Salt	1982	France
CESA-1	Almeria, Spain	1	Tower, Water-Steam	1983	Spain
MSEE	Albuquerque, US	0.75	Tower, Molten Salt	1984	USDOE, Utilities
SEGS I- IX	California- US	9 plants 354 MW in combined	Trough, Oil	1984 to 1989	Luz (Private Company)
Vanguard 1	US	0.025	Dish, Hydrogen	1984	Advanco Corp.
MDA	US	0.025	Dish, Hydrogen	1984	McDonnell-Douglas
C3C-5	Crimea, Russia	5	Tower, Water-Steam	1985	Soviet Union

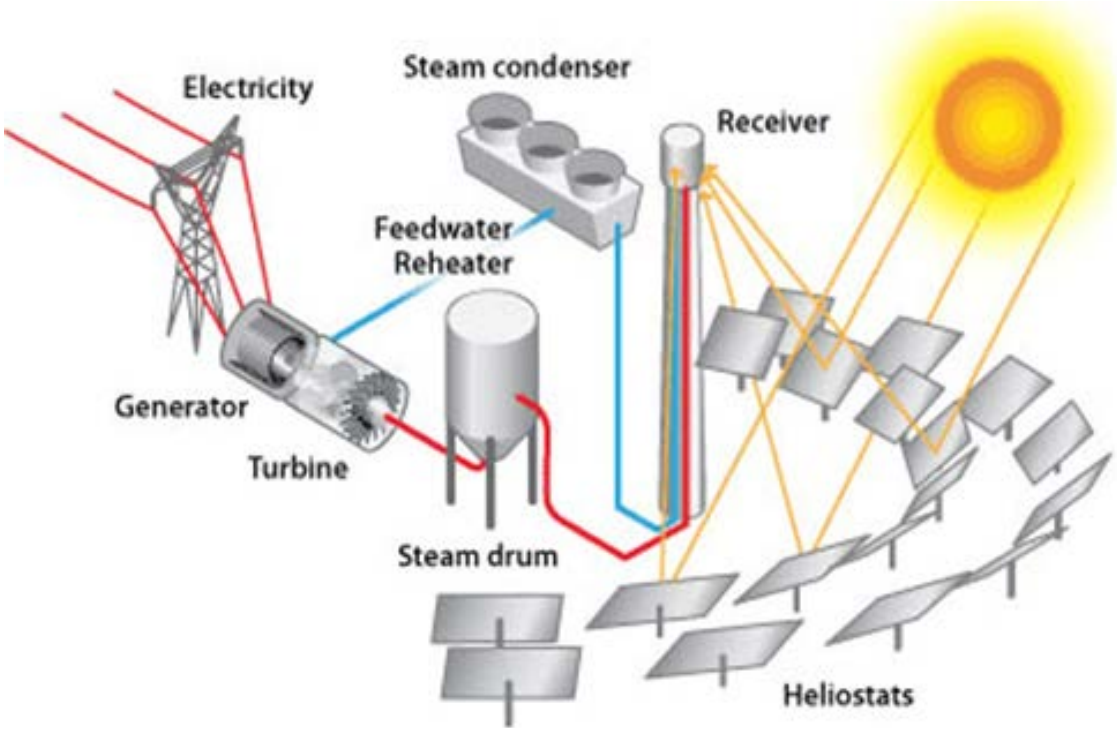

Figure 2.2. Tower receiver technology (Image extracted from Solarflame, 2016).

Parabolic Trough Collector: This technology is categorised as a line-focusing technology. The parabolic shaped solar reflector with a single-axis tracking system concentrates the incoming solar radiation throughout a day onto an evacuated tube placed in the trough's focal line. The evacuated tube is filled with HTF, usually thermal synthetic oil, which absorbs the solar energy and converts it to electricity in conventional power cycles (Figure 2.3). Concentration ratios between 30 and 100 are captured by this technology (Bennett, 2007; Geyer et al., 2002; SolarPACES, 2011c). The maximum operating temperature of this technology is about 400 °C, which is limited by the synthetic oil properties. The first commercial PTC power plant was built in 1984 and continues to operate to the present day. A survey conducted by the German Aerospace Centre describes PTC as the most mature and reliable technology which is commercially available (DLR, 2007; Richter et al., 2009).

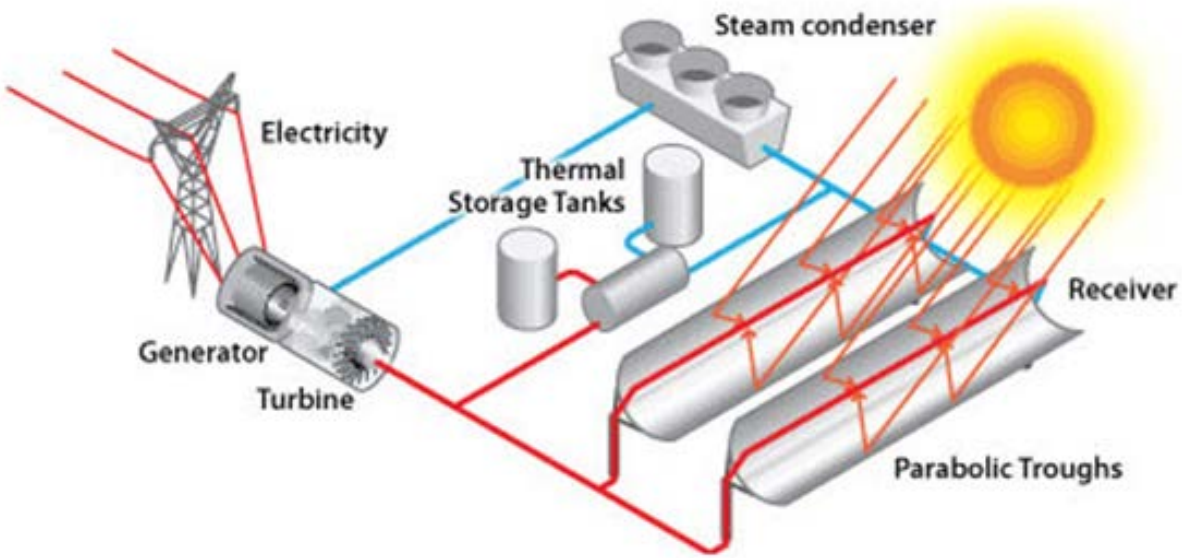

Figure 2.3. Parabolic trough collector (Image extracted from Solarflame, 2016).

Linear Fresnel Collector: LFC technologies consist of an array of nearly flat mirrors that concentrate the incoming solar radiation onto an inverted linear receiver. The face-down cavity, which surrounds the tube receiver, compensates for inaccurate solar tracking and increases the effective absorber area. The cavity aperture is covered with glass to reduce the convective heat loss of the absorber. The flowing HTF within the absorber tube converts solar energy to electrical in a conventional power cycle (Figure 2.4). For this technology, mean concentration ratios between 10 and 30 are reported by researchers (Choudhury & Sehgal, 1986; Goswami et al., 1990; Mathur et al., 1991a,1991b; Mazumder et al., 1987; Negi et al., 1989). The maximum operating temperature of the technology is below 300 °C, according to these studies. However, Abbas (2015) states that with high quality mirrors, this technology could reach 500 °C with superheated water and 550 °C with molten salt. The German Aerospace Centre study rates this technology as low maturity with unknown reliability, which is still in a pre-commercial phase (DLR, 2007). This statement shows the potential room for research and development of the technology, which could be due to the LFC late development in the respective CSP development periods. For example, by the end of the 1980s, while significant investment had been made into other CSP technologies, scientific research in LFC

developments had only just begun and was halted at the end of the oil crisis and falling oil price (late in the first period). As another example, in the second period, despite the fact that the first LFC plant in Spain was commissioned and displayed its competitiveness with PTC, the Spanish moratorium stopped the development of LFC because this technology was still new and had not been proved.

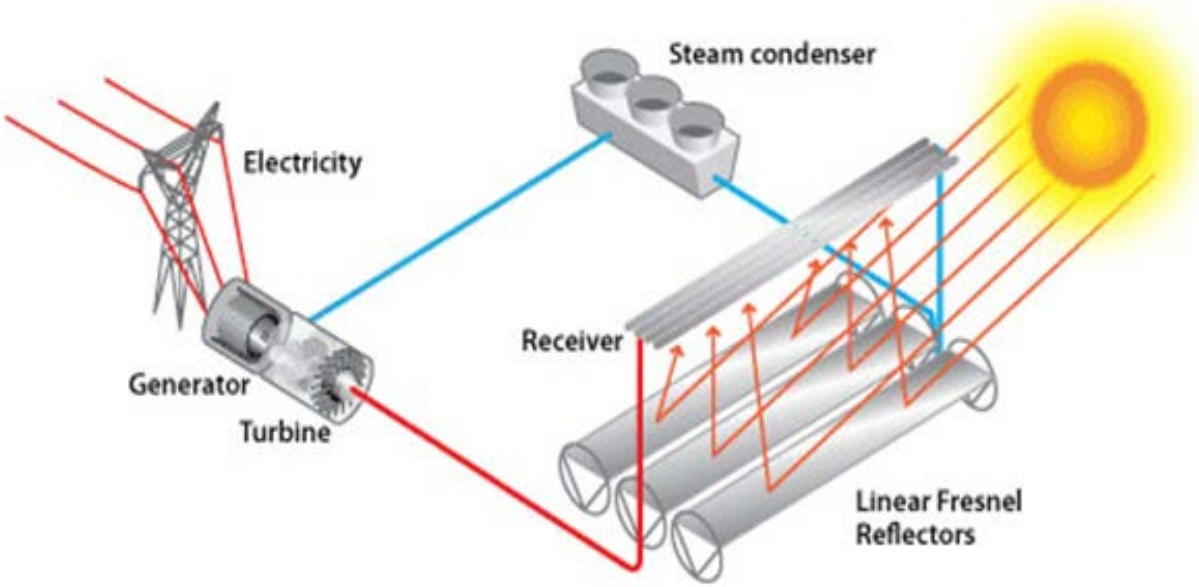

Figure 2.4. Linear Fresnel collector (Image extracted from Solarflame, 2016).

2.3 LINEAR FRESNEL COLLECTOR HISTORY

The technology is named after the French scientist Augustin-Jean Fresnel, who invented the Fresnel lens in the 18th century for lighthouses (Figure 2.5a - Augustin-Jean Fresnel, 2016). His idea was the grinding of a conventional convex lens to a multi-section lens to have a cheaper and lighter lens, which properly collimates light (Figure 2.5 b-c - Fresnel lens, 2016). The main idea of the LFC was inspired from the Fresnel lens to divide a parabolic mirror into a series of reflecting mirrors to concentrate collimated rays onto a focal point or line (Figure 2.5d), depending on whether the reflectors are circular or linear.

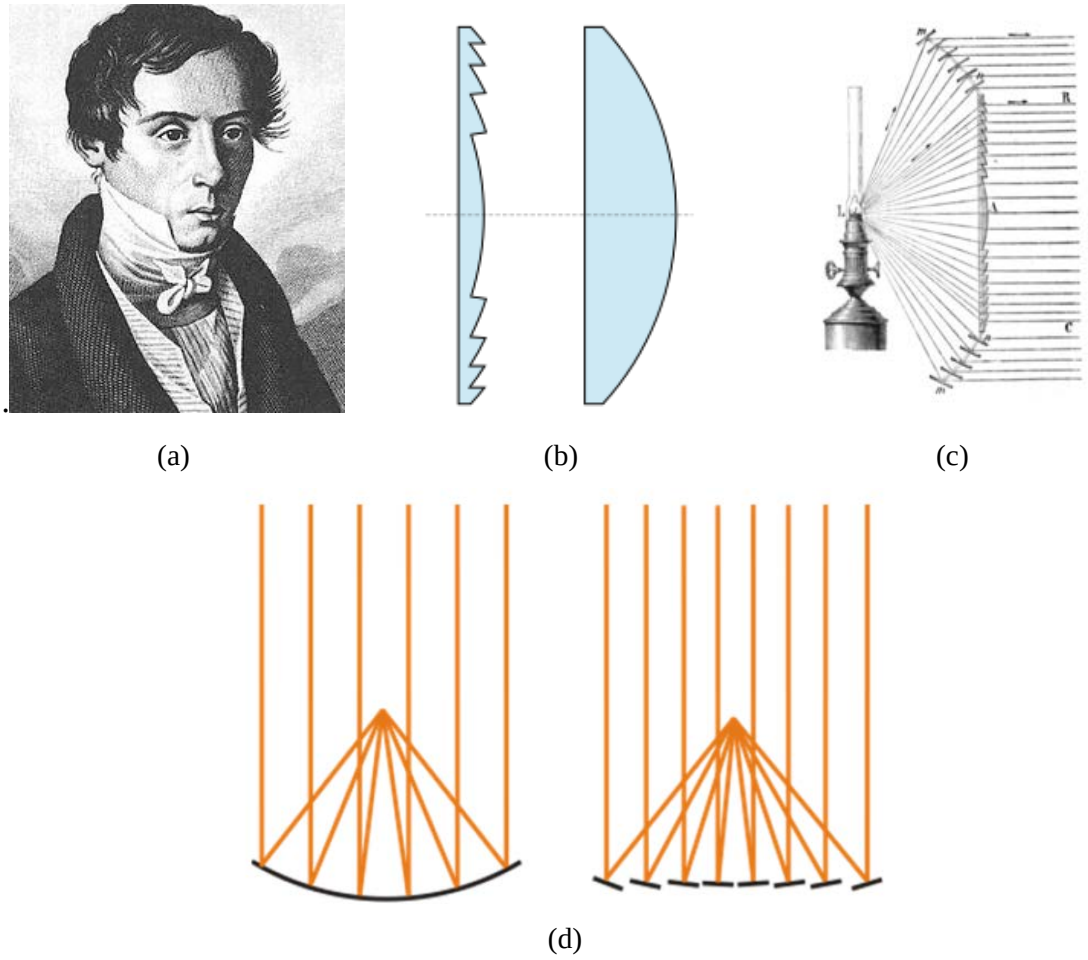

(a) (b) (c)

(d)

Figure 2.5. The Fresnel principle.

(a) Augustin-Jean Fresnel (Image extracted from Augustin-Jean Fresnel, 2016). (b) Fresnel lens (left) and conventional lens (right) (Image extracted from Fresnel lens, 2016). (c) Schematic sketch of collimating rays by a Fresnel lens (Image extracted from Fresnel lens, 2016). (d) Schematic sketch of optical characteristics of Fresnel mirrors vs. parabolic mirror (Image extracted from Günther, 2016).

The history of the first LFC prototype dates back to 1962 before Giovanni Francia filed a patent for the technology in 1963 in Italy. The first LFC prototype was built in Genoa and a year later was tested at the Lacédémone-Marseilles solar station, France by Francia and his colleagues (Figure 2.6). However, the history of the first large-scale LFC study dates back to the late ’60s when Francia and his colleagues worked on the “Solar City Project-Hypothesis for an Urban Structure” project. This project had been targeted at using solar

energy for electricity generation as well as space cooling and heating for an urban area with about 100 000 population (Figure 2.7).

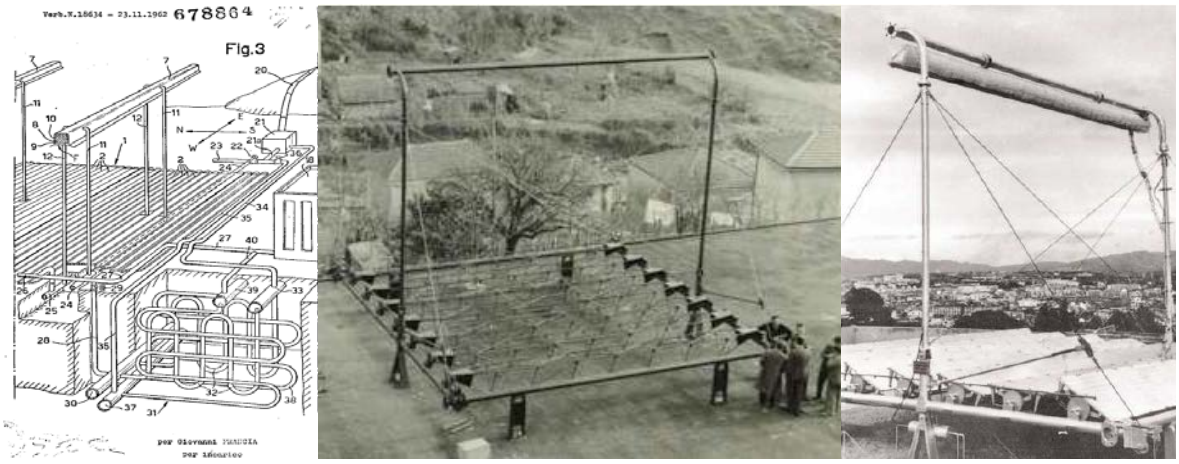

(a) (b) (c)

Figure 2.6. Francia's first LFC prototype (Images extracted from Silvi, 2009).

(a) Drawing of LFC patent, Patent No. 18634. (b) LFC building in Italy. (C) LFC testing in France.

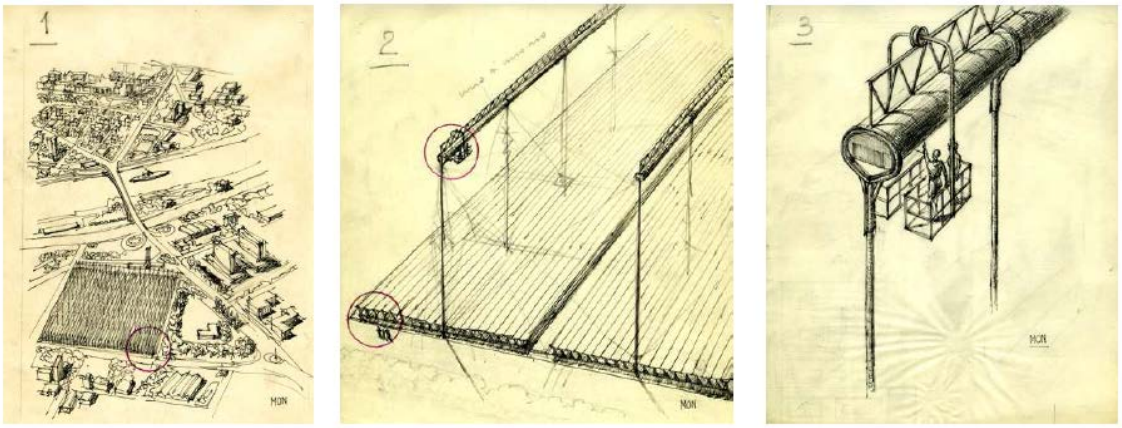

Figure 2.7. Francia's drawings for the first large-scale LFC study (Images extracted from Silvi, 2009).

The potential and advantages of the Fresnel technology were not revealed until the beginning of the new millennium when the results of the Solarmundo prototype (Häberle et al., 2002) were presented. The advantages drew the attention of academy and industry, which led to the construction of more LFC plants around the world. A few of these plants are listed in Table 2.2.

Table 2.2 LFC concentrating solar power plants around the world

Project Name	Country	Purpose	Power (MW)	HTF	Output temperature (°C)	Receiver	Storage (hours)	Operating	Reference
Alba Nova 1	France	Commercial	12	Water	300	Mono-tube & Secondary reflector	1	2015	Alba Nova 1, 2016a; 2016b.
Augustin Fresnel 1	France	Demonstration	0.25	Water	300	Mono-tube & Secondary reflector	0.25	2012	Augustin Fresnel 1, 2016a; 2016b.
Dhursar	India	Commercial	250	-----	-----	Multi-tube	0	2014	Dhursar, 2016; AREVA India projects, 2016.
eCare	Morocco	Demonstration	1	Water	280	Mono-tube & Secondary reflector	2	2014	eCare solar thermal project, 2016; CNIM eCare Solar Thermal Project, 2016.
Kimberlina STPP	US	Commercial	5	Water	300	Multi-tube	0	2008	Kimberlina Solar Thermal Power Plant, 2016; Kimberlina STTP, 2016.

Table 2.2 Continued

Project Name	Country	Purpose	Power (MW)	HTF	Output temperature (°C)	Receiver	Storage (hours)	Operating	Reference
Liddell Power Station	Australia	Commercial	6	Water /Steam	270	Multi-tube	0	2012	Liddell Power Station, 2016; Liddell Solar Thermal Station, 2016.
Llo	France	Commercial	9	Water	285	Mono-tube & Secondary reflector	1	2015	Llo solar thermal project, 2016; Centrale Solaire Thermodynamique Llo, 2016.
Puerto Errado 1	Spain	Commercial	1.4	Water	270	Mono-tube & Secondary reflector	0.5	2009	PE1, 2016; Puerto Errado 1, 2016.
Puerto Errado 2	Spain	Commercial	30	Water	270	Mono-tube & Secondary reflector	0.5	2012	PE2, 2016; Puerto Errado 2, 2016.
Solarmundo	Belgium	Prototype	-----	Water /Steam	----	Mono-tube & Secondary reflector	0	2001	Lovegrove and Stein, 2012.

The advantages of LFC technologies, in comparison with other CSP technologies, are:

1. Stationary receiver (not requiring tracking of the sun's position): hence no requirement for high-pressure joints, allowing very long absorber tube, i.e. PE1 and PE2 reaching to 806 and 940 m respectively (PE1, 2016; PE2, 2016), which reduces pressure losses due to less flow directional changes; suitable for direct steam generation since most rays hit the absorber from below; easy maintenance; and separated receiver and reflector parts.
2. Cheaper: due to its inexpensive planar or slightly curved mirrors in both manufacturing and maintenance processes in comparison with parabolic ones (Dersch et al., 2009; Novatec-Solar, 2016); a simple tracking system which can be shared by reflectors because all mirrors rotate with the same speed (Zhu et al., 2014); its smaller footprint and height (low structural support expenses by near-ground mounted mirrors); lack of high-pressure flexible joints; no heat exchanger necessary due to direct steam generation in some cases; using conventional glass on the bottom side of the cavity receiver (Moghimi et al., 2015c); and minimal manufacturing, operation and maintenance costs because it is compatible with automatic washing and maintenance mechanisms (Zhu et al., 2014). These factors make this technology a cost-effective CSP solar technology, i.e. Häberle et al. (2002) claim that the total cost reduction of a linear Fresnel solar field is about 50% of a comparable parabolic trough technology. In addition, Morin et al. (2009) report a 55% potential in capital cost reduction of LFCs in comparison with PTCs, which can be achieved by 20% less material usage due to newer technology (Morin et al., 2012). The break-even point of the LFC technology cost is estimated from 28-30% (Morin et al., 2012) to 54% (Hoyer et al., 2009) of the PTC technology.
3. High-ground utilisation: this technology is much more space efficient in comparison with PTC. According to Cau and Cocco (2014) and Lovegrove and Stein (2012), an LFC required space is up to three times less than for a PTC because the location of the primary reflectors could be next to each other, with the added benefit that the shaded area underneath the collector could be considered as either a parking lot or a greenhouse for growth of shadow plants even in arid areas. Häberle et al. (2002) state that by using the diffused light and the light reflected on the back of the mirrors (about 300W/m^2), a controlled greenhouse can be implemented in this space.

In the following sections, the literature is reviewed to investigate the researchers' concerns in designing and improving the efficiencies of this technology.

2.4 LFC MIRROR FIELD DESIGN

In the designing of an LFC mirror field, the effects of different factors have to be taken into account in improving the number of solar rays impinging on a cavity receiver (the LFC optical efficiency), namely solar field orientation, the mirror locations in the transversal plane, the mirror widths, the mirror curvatures, the receiver assembly and the receiver design. The first four factors in literature are reviewed in this section while the last two ones will be discussed in the next section.

With regard to solar field orientation, researchers discuss the advantages and disadvantages of north-south vs. east-west direction. The most comprehensive comparison of these orientations is presented by Zahler et al. (2009), who claim that the north-south orientation harvests higher annual solar energy while the east-west orientation results in less variable monthly generation. This proves why the north-south direction is more popular among researchers, and even the current solar fields (e.g. Fresdemo and Puerto Errado I and II) are oriented as such (Bernhard et al., 2008a, 2008b; Morin et al., 2006).

With regard to mirror locations in the transversal planes, the effect of this factor has been considered for the improvement of the optical efficiency of a plant since the 1980s. Mirror placement in the transversal plane, regarding the abscissa and the ordinate, is usually dealt with in researchers' investigations of the mirror distances and mirror mounting heights across the field respectively. For example, the following researchers conducted investigations on the mirror distances across the field: Choudhury and Sehgal (1986) suggested the installation of similar mirror widths at different mirror distances across the field. Indeed, this suggestion was presented to reduce the blocking effect without going through the optimisation of the mirror field set of design variables. Later researchers (Mathur et al., 1990, 1991b; Negi et al., 1990; Singh et al., 1999, 2010a; Velázquez et al., 2010) targeted no blocking effects for the case of the sun at the zenith by optimising the mirror distances across the field. These studies were conducted by considering constant

mirror width across the field with different receiver shapes (tubular, triangular, horizontally flat or vertically flat), which will be discussed later. Recently, researchers such as He et al. (2012) and Nixon and Davies (2012) focused on shading and tried to design a plant with no shading effects by appropriately setting the mirror distances for a given sun elevation with a constant mirror width across the field. The above researchers advocated the influence of mirror locations from the centre line on the shading and blocking alleviation of a plant and focused on optical efficiency improvement by setting different mirror distances across a field. In contrast, other researchers such as Bernhard et al. (2008a, 2008b), Lin et al. (2013) and Morin et al. (2006) focused on the simplicity and practicality of the collector design. Therefore, they implemented the idea of a constant mirror distance across the field in their works, which was also used in the construction of solar plants such as Fresdemo and Puerto Errado. With regard to the ordinate mirror locations in the transversal plane, researchers suggested mounting mirrors at different heights across the field to match mirror layout with specific patterns. For example, Chaves and Collares-Pereira (2009) suggested the etendue-matched mirror field, paired with a compact linear Fresnel design, to increase the optical efficiency of the plant. This idea can be found in the work of later researchers such as Chaves and Collares-Pereira (2010), Canavarro et al. (2011), Moghimi et al. (2015a) and Rungasamy et al. (2015). However, to the best of the author's knowledge, due to the complexity of the mirror field, researches on the ordinate mirror locations in the transversal plane are in the conceptual design phase and neither commercial nor prototype plant based on this idea has yet been constructed.

With regard to the width and the curvature of mirrors, Singh et al. (1980) was among the early researchers who raised the mirror width of the field along with mirror distances and mirror angles as the crucial factors in designing an LFC solar field. Researchers of the early 1990s, such as Goswami et al. (1990), Mathur et al. (1990, 1991a), Negi et al. (1990) and Sootha and Negi (1994), who investigated the optimum mirror locations in the transversal plane, also conducted studies on mirror widths of solar fields. Those researchers achieved a nearly constant low concentration, which was due to the usage of flat mirrors in their solar fields, according to Abbas (2015). As Abbas (2015) explains, using flat mirrors limits the upper bound of the mirror width to the receiver aperture width

as well as leading to astigmatism or the off-axis aberration phenomenon in the solar field, which reduces the solar concentration of the field. Some researchers suggested slightly curved mirrors for achieving better performances in LFCs (e.g. Abbas et al., 2013; Feuermann & Gordon, 1991; Morin et al., 2006). Using curved mirrors in LFC designs is not limited to academic research but in both prototypes and commercial plants, this idea was used. For example, in the installed prototype by Lin et al. (2013), a 3 m mirror curvature radius was considered for the LFC plant where its receiver was mounted 1.5 m above the mirror plane; or in the FRESDEMO project, which was constructed in Plataforma Solar de Almería (PSA) in Spain, 25 slightly curved mirrors were used (Bernhard et al., 2008a).

The other parameters which are widely discussed in the literature are the receiver's factors and their effects on the efficiency of an LFC plant. A literature study of these parameters is presented in the next section.

2.5 LFC RECEIVER DESIGN

After discussing the mirror field design factors in the previous section, a literature study of the effect of LFC receiver technology is presented here. In this regard, the concept of an LFC receiver was extensively analysed by researchers. Some of the proposed receiver technologies are in the prototyping and engineering phase while others are either in theoretical exploration or conceptual evaluation phase. Two main receiver parameters, which affect the LFC collector technology and its optical efficiency, are the receiver assembly and the receiver design. These two factors are discussed in the following section.
With regard to the receiver assembly, numerous LFC concepts are suggested either in conceptual designs or practice. Of these, the following suggestions are presented in the literature: either assembling one single receiver tower or two separate receiver towers for a single mirror field (known as compact linear Fresnel reflector - CLFR) or, assembling the receiver in horizontal, vertical or triangular configurations (see Figure 2.8). However, the popular concept, which is broadly used in scientific works, as well as prototype and commercial plants, is an independent array of mirrors with an individual horizontally downward receiver in the middle of the array. This configuration is the focus of the thesis.

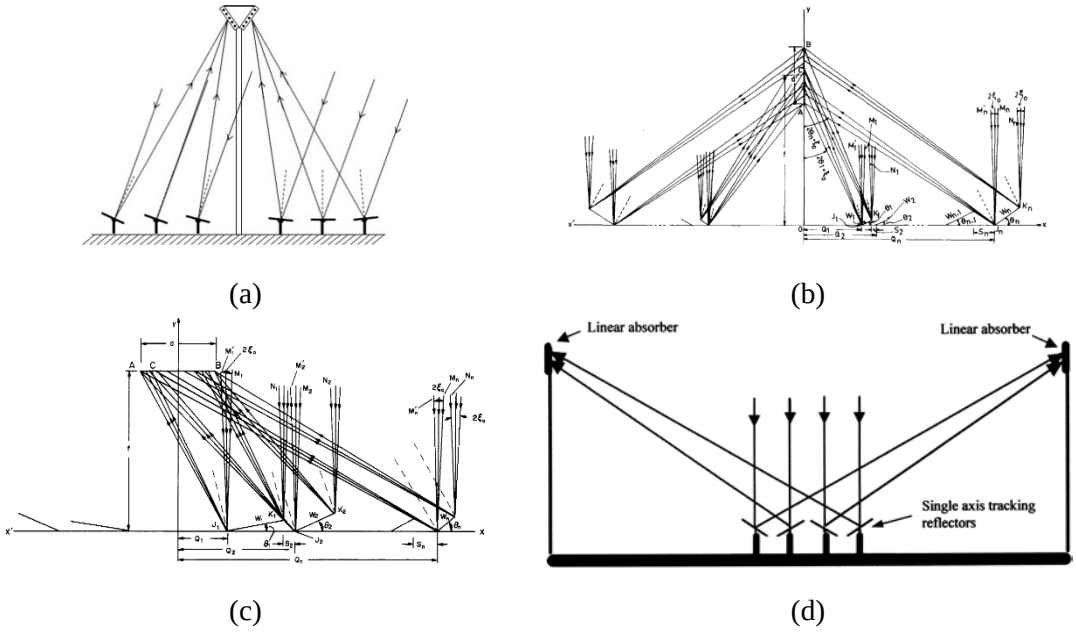

Figure 2.8. Receiver assembly configurations.

(a) Triangular receiver tower (Image extracted from Abbas et al., 2012). (b) Vertical receiver tower (Image extracted from Negi et al., 1990). (c) Horizontal receiver tower (Image extracted from Mathur et al., 1991a). (d) CLFR (Image extracted from Mills & Morrison, 2000).

With regard to the horizontally downward receiver design, interesting designs and investigations have been done in the research and development of LFC receivers to improve the optical performance of the plant (see Figure 2.9). While a significant amount of effort has gone into receiver designs, two commercialised designs have received more attention by researchers. They are the LFC with a multi-tube cavity receiver (Abbas et al., 2013; Dey, 2004; Hongn et al., 2015; Moghimi et al., 2014; Pye, 2008; Reynolds et al., 2004; Sahoo et al., 2012; Singh et al., 1999, 2010b) (see Figure 2.10b) and the mono-tube cavity receiver with a compound parabolic shape secondary reflector (Häberle et al., 2002; Heimsath et al., 2014; Moghimi et al., 2015a; Qiu et al., 2015; Rabl, 1976, 1985; Sharma et al., 2015; Winston & Hinterberger, 1975;) (see Figure 2.10a). The first technology was commercialised by Areva Solar (Areva Solar, 2016) and the second by Novatec Solar (Novatec-solar, 2016) and Solarmundo (Zhu et al., 2014). The next section reviews the literature on the optimisation investigations conducted to improve the thermal and optical efficiencies of these two commercialised concepts.

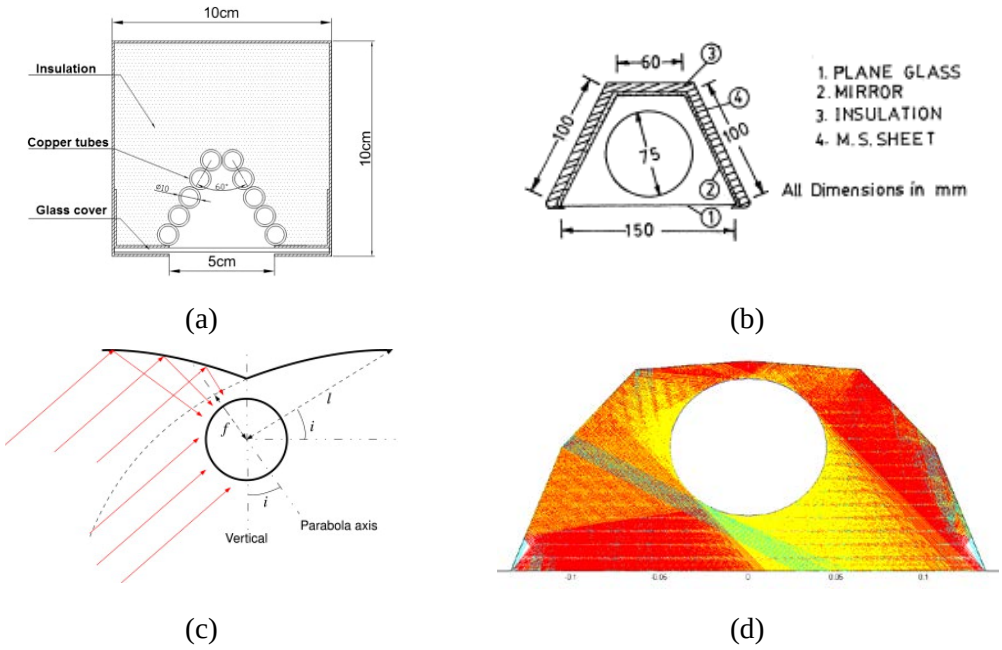

Figure 2.9. Receiver designs.

(a) V-shaped cavity design (Image extracted from Lin et al., 2013). (b) Mono-tube trapezoidal cavity design (Image extracted from Singh et al., 1999). (c) A two-parabolic-shaped wings geometry (Image extracted from Grena & Tarquini, 2011). (d) A heptagon cavity design (Image extracted from Walker, 2013).

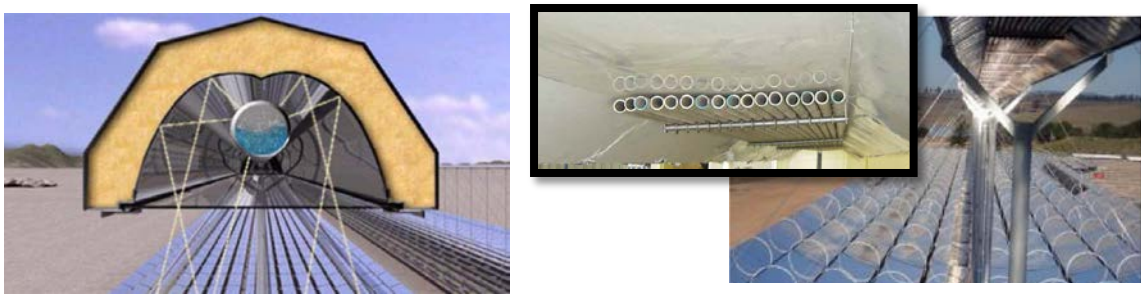

Figure 2.10. Commercial linear Fresnel receiver technology.

(a) Mono-tube secondary reflector cavity receiver used in Nova-1 project (Novatec solar technology - Image extracted from Selig & Mertins, 2010). (b) Multi-tube trapezoidal cavity receiver, installed in Kimberlina solar plant (Areva Solar technology - Image extracted from Conlon, 2011) with inserted picture of multi-tube arrangement in the cavity (Image extracted from Pye, 2008).

2.6 OPTIMISATION

Studies of the performance of LFCs usually focus on the two commercialised concepts of LFC discussed above due to their popularity among researchers. One can easily find a vast amount of effort which has gone into pure thermal or optical studies of these concepts. For example, for the multi-tube trapezoidal cavity receiver concept, Pye (2008), Facão and Oliveira (2011), Sahoo et al. (2012) and Lai et al. (2013) are among researchers who conducted pure thermal case studies on various aspects of this configuration. Their focus was on the reduction of heat losses and the improvement of the thermal efficiency of an LFC. Although these researchers graphically displayed the influence of different parameter variations in individual graphs, the interaction between various geometrical variables on the thermal efficiency was not evident. For example, the effect of cavity depth in isolation on thermal losses was shown by Facão and Oliveira (2011), Lai et al. (2013) and Sahoo et al. (2012) and the effect of the cavity angle on the thermal loss was presented by Pye (2008). The interaction of various parameters on the efficiency of an LFC cannot be determined until such a configuration goes through an optimisation study.

There is defnitely an interest in LFC technology optimisation; however, due to the definition of a variety of optimisation goals, the results of the optimisation studies vary and hence do not provide a fixed utopian design. This issue will be dealt with later when the results of a thermal and optical optimisation study are compared with the results of an economic optimisation study on the same LFC configuration (Chapter 5). Traditionally, researchers conduct the economic optimisation of a CSP plant via the definition of levelised electricity cost (LEC, also known as levelised cost of electricity (LCOE, 2016)) and its minimisation. The results of LEC minimisation may not predict the same utopian design as a pure optical or thermal optimisation. For instance, Bernhard et al. (2008a) reported on the results of an optimisation study of the FRESDEMO project, which concerns an LFC plant with a mono-tube cavity receiver and a secondary reflector. In that study, firstly, the receiver height, the tube diameter, and then the mirror width were determined based on practical restrictions. Then the optimisation was done on the set of independent parameters, consisting of the following: the number of mirrors, the mirror

gaps, the mirror curvature, mirror aiming points and the shape of the secondary reflector. They reported that, for a constant field width, thermal efficiency reached its maximum value with 22 mirror rows, while the LEC optimisation of a similar problem showed that the minimum cost of the field occurred with 30 mirrors (Figure 2.11). Indeed, adding more than 22 mirrors decreased the thermal efficiency because of mirror shading and blocking effects in the constant field width while tracking cost decreased when increasing rows beyond 30.

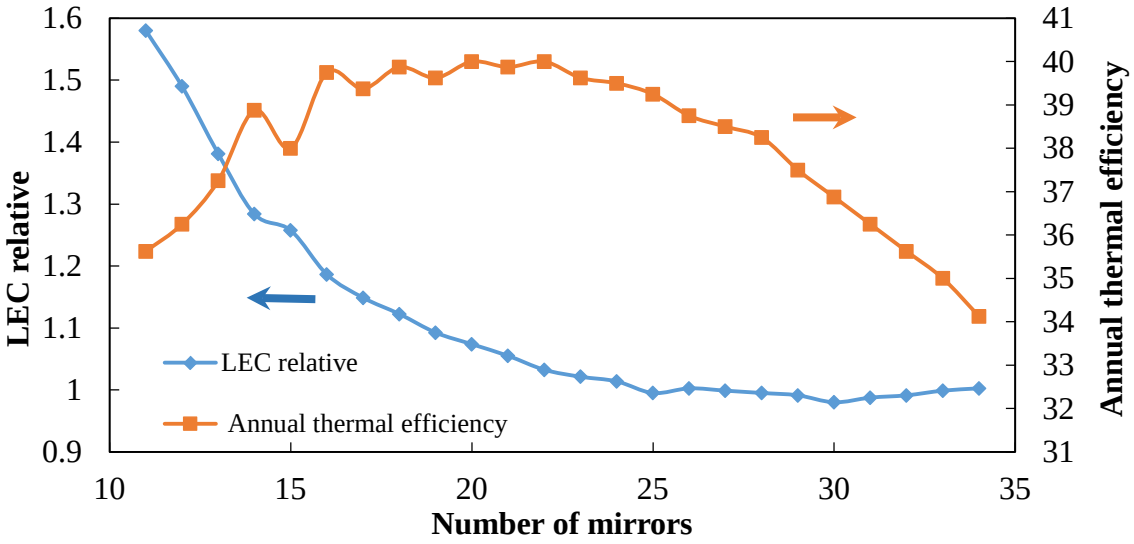

Figure 2.11. Effect of number of mirrors on annual thermal efficiency and relative LEC (Data were taken from Bernhard et al., 2008a).

In another study, Montes et al. (2012) conducted an optimisation study on the optical and geothermal losses of the mirror field of the FRESDEMO plant disregarding economic factors of the plant and thermal and optical losses of the cavity receiver. The focus of their study was on minimisation of shading and blocking, end and lateral losses, and mirror reflection losses of the FRESDEMO plant by changing the receiver height and mirror field total width parameters of the plant. These researchers showed that, for a constant receiver height, by increasing the mirror field width, annual energy efficiency was boosted (Figure 2.12a), but that such a configuration (increasing mirror field width) increased the required material and land cost. Because a wider solar field decreased the shading and blocking annual ratios (Figure 2.12b) and more solar rays impinged on the absorber tube, the annual harvested energy was boosted. However, due to the installation of mirrors on a

structure, a heavier and more expensive structure, as well as a greater land area, was required. Morin et al. (2006) did LEC optimisation on the same configuration and found that there was an optimum mirror gap, and that it was not economical at all to increase mirror gaps and consequently increase mirror field width as much as a designer would like to (Figure 2.12c). The same study can be repeated for an optimum economic mirror width.

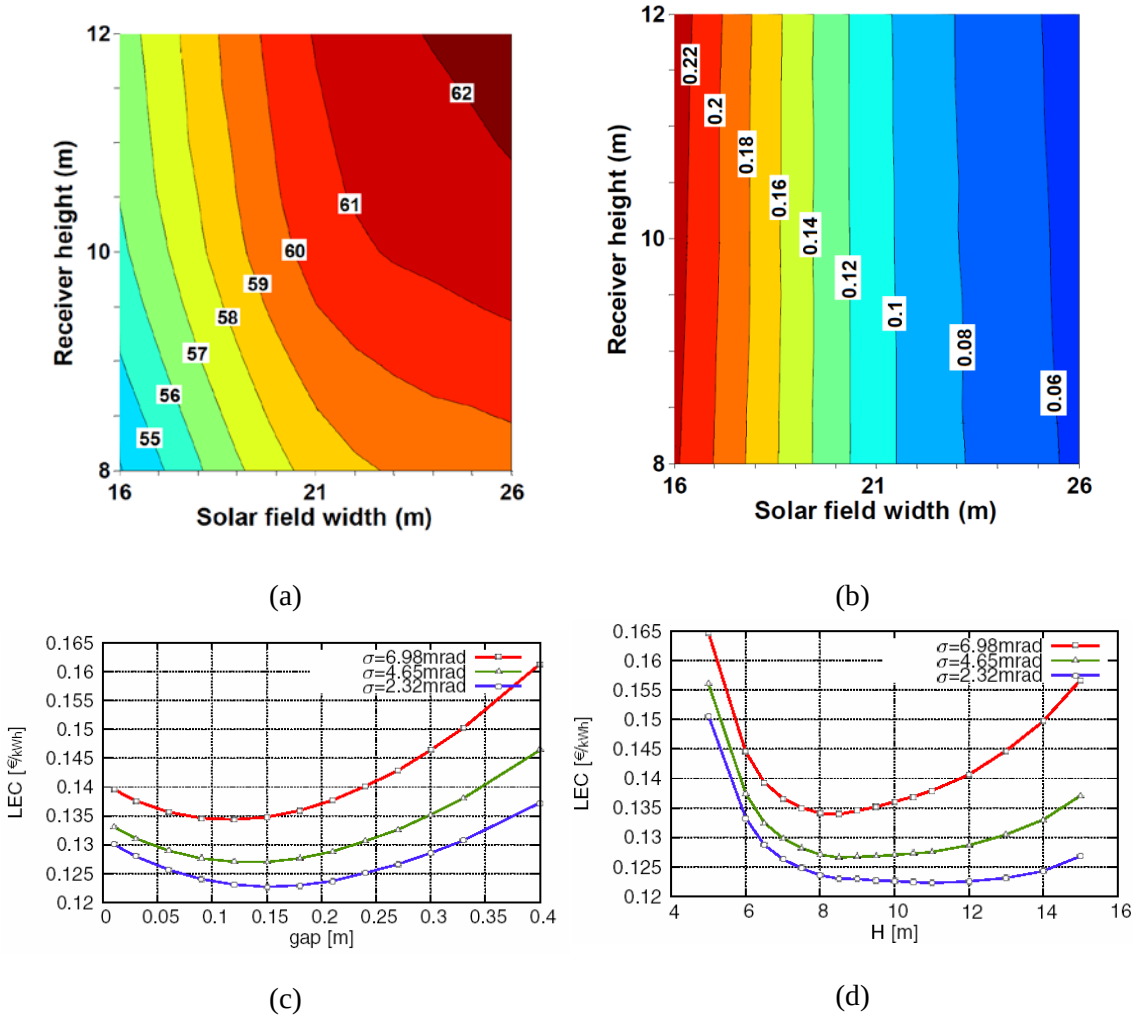

Figure 2.12. Effects of different goals on optimisation outcomes of previous researchers.

(a) Annual energy efficiency of LFC (Image extracted from Montes et al., 2012). (b) Annual shading of LFC (Image extracted from Montes et al., 2012). (c) Effects of mirror gap on LEC (Image extracted from Morin et al., 2006). (d) Effects of receiver height on LEC (Image extracted from Morin et al., 2006).

Regarding receiver elevation, Montes et al. (2012) and Morin et al. (2006) are among the researchers who tried to define an optimum receiver height with or without considering

economic factors. Whether economic factors are included (Figure 2.12d, from Morin et al. 2006) or not (Figure 2.12a, from Montes et al., 2012), the optimum receiver height can lead to contrasting optimum designs. Note that the optimum height of about 8 to 10m is specific to the set-up studied by Morin et al. (2012), and not generally applicable. When the additional cost of the structure required to support a high receiver is excluded, a high receiver makes optical sense (Figure 2.12a), but when the cost is taken into consideration, there is a break-even point above which a higher receiver is penalised regarding cost (Figure 2.12d).

With regard to receiver configuration, Mertins (2009) surveyed the economic optimisation of an LFC with single-tube receiver. For instance, he studied the effect of two separate receiver tube diameters on the LEC, as well as the relative location of the tube receiver.
The interesting and common point among previous studies is that usually, German researchers (Bernhard et al., 2008a; Morin et al., 2006; Mertins, 2009) reported the influence of optimisation design variables on both performance and cost of LFC technology. The reason for this could be the access that these researchers had to some specific tools which were developed by Fraunhofer ISE for the FRESDEMO project. Indeed, Fraunhofer ISE was responsible for the techno-economic optimisation of the system in the conceptual design phase. In this regard, a set of tools in the modelling of optical, thermal, (simplified) electrical and cost simulation of an LFC, as well as an optimising algorithm, was developed by them for that project (Bernhard et al., 2008a). In addition, all of the above-mentioned economic optimisations were conducted on the mono-tube receiver with secondary reflector (Novatec-solar, 2016), while a similar comprehensive optimisation study for the trapezoidal multi-tube receiver (Areva Solar, 2016) has not been conducted, or at least not reported in the open literature. This thesis focuses on the rapezoidal multi-tube receiver configuration and presents a comprehensive study on thermal, optical and economic optimisation of such a plant.

However, successful simulation and economic optimisation of a multi-tube trapezoidal LFC configuration need a thorough discussion of the available economic modelling as well as engineering approaches to accurately tackle the optical and thermal simulations of an

LFC plant with engineering tools. The next sections of this chapter are allocated to reviewing German literature, especially the PhD thesis of Mertins (Mertins, 2009), and adapting its LEC model for this study. In addition, these sections review literature to find the available numerical modelling and engineering tools for the accurate simulation of thermal and optical performance of an LFC domain. The applicability of these tools and models are investigated through test case studies in the following chapters to find a compromise for the best approach to the overall optimisation study presented in Chapter 5.

2.7 ECONOMIC MODELLING IN LITERATURE

Various independent factors and goals, such as plant efficiencies, resource consumption, environmental impacts and CO_2 emissions, can affect the economic optimisation of energy technologies. However, considering most of these factors and trying to quantify their costs and adverse effects on the environment require appropriate weighting factors, as well as evaluation criteria that are mostly difficult to estimate. Moreover, these factors are usually influenced by the political conditions of local communities and cannot easily be determined at global level due to these influences on investment decisions. If an actual cost penalty of an environmental impact (e.g. a clean-up of the technology at the end of the plant's life cycle) or a specific cost-benefit (e.g. a tariff rebate because of a CO_2 emission savings) can be quantified, they can be included in the present analysis and tool set. The current work focuses on a purely monetary and financial evaluation of the technology assuming that these case-specific data are not available.

Economic studies in the literature usually concentrate on the minimisation of the electricity production costs. Indeed, the electricity generation costs, quantified here as LEC, is a technical term for the calculation of average annual cost per kilowatt hour of electricity. This strategy was explained by Mertins (2009) for economic optimisation of a mono-tube cavity receiver with a secondary reflector. Actually, for his realistic economic calculations, Mertins (2009) took detailed costs of the Solarmundo project, which has an LFC mono-tube cavity receiver with secondary reflector, and rationally modified these costs to estimate the cost of design parameters in his study. This thesis focuses on the economic optimisation of an LFC with a *multi-tube trapezoidal* cavity.

Before discussing cost assumptions, it is worth discussing the difference between price and cost. Cost usually quantifies the financial expenses, while the price is the value that is determined by supply and demand in the market. Therefore, as mentioned before, this study focuses on the expenses of plants. Moreover, the real costs of an LFC project can ultimately be determined when a commercial LFC project has been completed and its performance is published in open access sources. As reported on the National Renewable Energy Laboratory website (NREL, 2016) and in Table 2.2, the number of LFC projects around the world is limited and they are mostly of the mono-tube cavity receiver with secondary reflector type. Among the demonstration/pilot and commercial projects, there is limited information about the detailed cost of LFC plants, especially the one with a multi-tube trapezoidal cavity. Therefore, to meet a realistic cost assumption, it seems appropriate to follow the approach of Mertins (Mertins, 2009) and rationally modify those costs in some cases to estimate the cost of the design parameters of a multi-tube cavity receiver.
The following categories were considered by Mertins (2009) to describe the major cost contributors of an LFC plant:

2.7.1 Mirror cost factor (C_m)

The factors that play a role in the specific cost of a mirror per unit length for a plant could be the mirror itself, its mounting and elevation, storage and transportation, the driving motors (stepper motors) and controllers, and its assembly. This cost factor is defined as C_m and reported per unit width of mirror. Mirror cost factor in the Solarmundo project (C_{m0}) was 30.5 €/m for a half metre mirror width (Mertins, 2009). In this study, mirror cost factor (C_m) scaling was assumed to be a linear coefficient of (C_{m0}) as defined in Equation (2.1). The mirror width, W, is indicated in Figure 5.1a.

$$C_m = C_{m0} * \left(\frac{W}{0.5[m]} \right) \quad [€/m] \qquad \textbf{(2.1)}$$

2.7.2 Mirror distance cost factor (C_d)

In order to reduce the shading and blocking effects, adjacent mirrors are installed on a common structure with a gap distance G (see Figure 3.1 and Figure 5.1a) defined as the mirror pitch (P) minus the mirror width (W), i.e. the gap when the mirrors are all facing

vertically upwards. The specific mirror distance cost per unit length is reported as C_d (also known as mirror gap cost factor). This cost factor in the Solarmundo project (C_{d0}) was 11.5 €/m for 0.01 m mirror distance (Mertins, 2009). It is evident that by changing the gap, the material cost of the structure, as well as land occupation, is varied. Therefore, it would be rational to assume that C_d is scaled linearly using C_{d0} as in Equation (2.2).

$$C_d = C_{d0} * \left(\frac{G}{0.01\,[m]} \right) \qquad [€/m] \tag{2.2}$$

2.7.3 Elevation cost factor (C_e)

The receiver is mounted at a distance H over the mirror field (see Figure 3.1 and Figure 5.1a). The specific cost of mounting the receiver at that elevation is C_e. This cost is reported per unit length and unit elevation. The elevation cost adaptation was exponentially related to the elevation cost in the Solarmundo project (C_{e0}=19.8 €/m^2) and tube outer diameter (OD) as introduced by Mertins (2009), in terms of Equation (2.3).

$$C_e = C_{e0} \left(\frac{OD}{0.219[m]} \right)^{n_{ce}} \qquad [€/m^2] \tag{2.3}$$

where the exponent n_{Ce} is calculated via Equation (2.4). The Mertins formulation (Mertins, 2009) is adapted by modifying the exponent n_{Ce} (Equation (2.4)) by the inclusion of an N_t factor, which denotes the number of tubes for a multi-tube cavity case to differentiate from Mertins's single tube. The use of the tube diameter as the cost factor is motivated by the fact that the tube diameter is directly linked to cavity side wall projected area (as the main factor) and the tube-wall thickness (as the subsidiary factor), where the former one increases the structural cost due to the wind load, and the latter one increases the total weight and crane lifting capacity as well as structural cost due to seismic load.

$$n_{Ce} = \frac{\ln\left\{ \sum \frac{C_i \times N_t}{C_{e0}} \left(\frac{OD}{0.219[m]} \right)^{n_{ci}} \right\}}{\ln\left(\frac{OD}{0.219[m]} \right)} \tag{2.4}$$

Table 2.3 contains the values used in Equation (2.4).

Table 2.3 Elements of elevation cost in Equation (2.4). (Mertins, 2009)

	n_{Ci}	C_i **[€/m]**
Construction	1.4	14.2
Transportation and packing	1	0.9
Assembly	1	4.6

2.7.4 Receiver cost factor (C_r)

The main parameters that play a role in receiver cost factor are the absorber tube, coatings, welding and construction, assembly and transportation. The specific cost of receiver per unit length is defined as C_r (see Equation (2.5)). The receiver cost in the Solarmundo project (C_{r0}) was 654 €/m for a mono-tube receiver with tube outer diameter 0.219 m. The Mertins formulation (Mertins, 2009) is again adapted by modifying the exponent n_{Cr} (Equation (2.6)) by the inclusion of an N_t factor, which denotes the number of tubes. The use of the tube diameter in the cost factor is motivated by the fact that the tube diameter was considered as the scaling factor of the receiver size. In other words, the receiver size and consequently, the receiver cost, is scaled based on the absorber tube diameter.

The suggested receiver cost factor is:

$$C_r = C_{r0}\left(\frac{OD}{0.219[m]}\right)^{n_{cr}} \quad [€/m] \qquad \textbf{(2.5)}$$

where the exponent n_{Cr} is calculated via Equation (2.6):

$$n_{Cr} = \frac{\ln\left\{\sum \frac{C_i \times N_t}{C_{r0}}\left(\frac{OD}{0.219[m]}\right)^{n_{ci}}\right\}}{\ln\left(\frac{OD}{0.219[m]}\right)} \qquad \textbf{(2.6)}$$

Table 2.4 contains the values used in Equation (2.6).

Table 2.4 Elements of receiver cost in Equation (2.6). (Mertins, 2009)

	n_{Ci}	C_i [€/m]
Absorber tube	2	161.2
Selective coating	0.9	56.6
Welding	0.7	116.4
Construction	1.4	136.5
Transportation and packing	0.6	26.4
Assembly	0.6	112.6

2.7.5 Direct, indirect and total cost calculations

Combining the above cost factors, the direct specific cost of a collector [€/m^2] is:

$$C_c^d = \frac{C_m \times N_m + C_e(4+H) + C_d\,(N_m - 1) + C_r}{N_m \times W} \qquad \textbf{(2.7)}$$

where N_m and W denote the number of mirrors and the mirror width, respectively. The cost of the land and its preparation is excluded from the direct cost because it is included later under indirect costs. According to Mertins (2009), the reason for considering $C_e(4+H)$ in the collector specific cost formula, is that the mirror fields are mounted 4 m above the ground, and that the receiver, therefore, is effectively mounted at $(H+4)$. In this study, the same mirror field was used due to lack of information for any other field.

In addition to the direct costs of an LFC, the indirect costs of the plant are outlined as follows: the piping, infrastructure, land cost, project effort, uncertainties, power plant unit, operating and maintenance, and insurance.

By considering a fixed power plant unit, almost all of the above parameters would be fixed and independent from the properties of a collector except land cost. Mertins (2009) suggested multiplying $N_m \times W \times \left(1 + \frac{G}{W}\right)$ by a factor to represent the land cost. This factor is denoted C_l. The indirect costs used are reported in Table 2.5.

Therefore, the total investment of an LFC plant is:

$$\gamma_{Total\,investment} = \left[C_c^d \times N_m \times W \times (1+\kappa_e) + C_l \times N_m \times W \times \left(1+\frac{G}{W}\right) + \gamma_I \right] \times (1+\kappa_u) + \gamma_{PU} \quad \textbf{(2.8)}$$

By annual distribution of total investment cost and considering insurance premiums, personnel and spare parts costs, the total annual cost of the plant is:

$$\gamma_a = (\kappa_a + \kappa_i + \kappa_{O\&M}) \times \gamma_{Total\,investment} \quad \textbf{(2.9)}$$

The LEC is defined as total annual cost of the plant over the annual electrical yield of the plant (E_{el}):

$$LEC = \frac{\gamma_a}{E_{el}} \quad \textbf{(2.10)}$$

Assuming a fixed electricity output of the plant (constant power plant unit and infrastructure) , on the one hand, and the existence of constant terms and coefficients in Equations (2.8)-(2.10), on the other hand, one can consider that the terms which play a role in the minimisation of LEC are:

$$\gamma_{Plant\,Cost\,Factor} = C_c^d \times N_m \times W \times (1+\kappa_e) + C_l \times N_m \times W \times \left(1+\frac{G}{W}\right) \quad \textbf{(2.11)}$$

where $\gamma_{Plant\,Cost\,Factor}$ comes from the first two terms on the right-hand side of Equation (2.8).

Table 2.5 Indirect costs of a 50 MW linear Fresnel power plant, according to Mertins (2009).

Name	Cost	units	Other
Land costs (C_l)	3	€/m^2	Including land acquisition and preparation
Piping (γ_P)	4002	t€	Plant total cost including piping, steam traps, etc. “t” refers to “thousands”.
Power plant unit (γ_{PU})	33600	t€	Plant total cost considering turbine, feed water tank, a one-stage preheater,

			condenser, generator, etc.
Infrastructure (γ_I)	640	t€	Including building for staff and spare parts as well as site development
Annuity factors (κ_a)	9.368%		This factor is a percentage of total investment. The annuity factor is calculated as introduced by Göpple (1999): $\kappa_a = \frac{(1+i)^n i}{(1+i)^n - 1}$ where i is the economic lifetime of the plant and n is the interest rate which were respectively considered 25 years and 8% in this study.
Project efforts (κ_e)	22.5%		This factor is a percentage of total investment and includes engineering effort, project management, contractor, licensor rights.
Operation and maintenance ($\kappa_{O\&M}$)	2%		percentage of total investment
Insurance (κ_i)	1%		percentage of total investment
Uncertainties (κ_u)	5%		percentage of total investment

The author does not claim this goal definition to be the best goal definition for economic optimisation of Fresnel collectors, but at least this definition would help future researchers to have a first rough optimisation goal for finding a utopian region in the optimisation process. In addition, defining a realistic LEC goal which meets industry needs would be a complex issue. Such a realistic goal definition would require much information on economic aspects of linear Fresnel projects that, due to lack of data on Fresnel plants in open access sources, would be almost impossible.

Therefore, in future economic optimisation studies which need more accurate and complex economic objectives, for example, industrial projects, it is recommended that researchers keep to the discussed goal as a first estimation in their economic optimisation investigations and then try to define and apply other complex economic goals for the next step of their optimisation process.

2.8 OPTICAL MODELLING IN LITERATURE

From a simulation standpoint, the accuracy of determining the optical and thermal performance of an LFC installation (mirror field and receiver performance) requires a validated prediction model that can evaluate the complex interaction between solar irradiation, including wavelength and temperature dependency, and the HTF. This means that the optical performance of the mirror field must be simulated accurately to determine the influence of the sun angle, sun shape, concentration ratio, blocking and shading, reflectivity and reflector errors on the absorbed radiation on the collector absorber surfaces (tubes in this case). This section presents a literature survey of CFD and Monte Carlo approaches as possible and accurate options of ray tracing for the optical simulation of an LFC plant. In the following subsections, a literature study is conducted of these software approaches, and in the following chapters, the accuracy of these code results is compared for sample case studies. In addition, these chapters discuss the advantages and disadvantages of the engineering tools to see which one is more suitable for numerical optimisation studies.

2.8.1 Monte Carlo ray-tracing (MCRT) approach

MCRT methodology consists of following stochastic paths of a large number of rays as they interact with reflecting, absorbing or transmitting surfaces. Each ray carries the same amount of energy and has a specific direction determined from an appropriate probability density function based on the defined sun shape. The interaction of each ray with surfaces depends on the transmissive, reflective and absorptive behaviour of the surface, which is described by a set of statistical relationships (Xia Shuai & Tan, 2008). Band-selective

reflection, absorption or emission, and complex geometries require special treatment and for these applications, CFD FV (finite volume) is suggested by the author.

Monte Carlo has established its ability in getting accurate optical solutions for any solar plant where, traditionally, researchers used the Monte Carlo ray-tracing approach to tackle the optical efficiency of LFCs (e.g. Facão & Oliveira, 2011; Lin et al., 2013). The MCRT method is so popular among researchers that different commercial and public ray-tracing codes were developed by various research institutes and companies (e.g. SolTrace, 2016; Tonatiuh, 2016; TieSOl, 2016). The advantages and disadvantages of some of those codes were discussed by researchers (e.g. Bode & Gauché, 2012; Garcia et al., 2008; Mutuberria et al., 2011; Roccia et al., 2012; Wendelin et al., 2013).

Bode and Gauché (2012) introduced SolTrace, a free ray-tracing software tool developed by the National Renewable Energy Laboratory (NREL), as suitable for complex optical modelling and the evaluation of CSP plant performance. The main drawbacks of this software are its non-user-friendly graphical interface and domain where elements are introduced. The element definition in the software requires laborious processes especially for LFC (defining the number of mirror elements in comparison with a one-piece mirror in PTC) where for every sun angle, the aiming points of arrays of mirrors have to be correctly set unless automation is set up for that. Fortunately, available scripting and automation are some of the advantages of this software that allow users to define a large number of elements for extensive solar field plants. Another drawback of this code is the lack of open access to online sources for the definition of mirror field element surfaces and their aiming points based on the sun position. This issue is dealt with in Addendum I, where the required mathematical formulations for element surface definition in SolTrace based on the sun position are presented. In the following section, a more detailed SolTrace simulation of an optical modelling for a sample LFC domain is presented as a case study.

2.8.2 **CFD FV ray-tracing approach**

Although MCRT has proved its ability in getting high-accuracy solutions for solar applications, the interaction of each ray and its treatment of band-selective reflection,

absorption or emission, as well as special treatment of radiation in a complex geometry (e.g. specular or diffuse reflection in complex geometries) have led some to suggest CFD as an alternative for ray tracing in solar applications.

Optical modelling of an LFC plant in CFD requires the solution of the radiative transfer equation (RTE). (For more information about the RTE equation and radiative boundary conditions, consult Addenda II and III.) One of the methods for solving the RTE or its general form, the Boltzmann transport equation (photon radiation transport), is the S_N or discrete ordinates (DO) method (Miller & Reed, 1977). The DO method is easy to implement in FV, and easy to solve especially in serial calculations. In addition, the DO method determines the solution of the RTE on the same mesh as the energy, mass and momentum conservation equations, which leads to a close coupling of surface temperature and radiative energy. This ability implies that the DO can be applied to complex geometries for different participating media such as non-grey, anisotropically scattering, non-isothermal, absorbing and emitting media. Nevertheless, the DO method has two major shortcomings due to its FV nature, namely the “ray effect” and “false scattering” (Brunner, 2002; Chai & Patankar, 2006; Moghimi et al., 2015d), which affect result accuracy.

As discussed in Addendum IV, these shortcomings can be overcome in CFD, and ANSYS Fluent will lead to a reasonable solution, if the following suggested options by Moghimi et al. (2015a; 2015b; 2015d) are implemented in a simulation:

1. increasing the control angle count;
2. increasing the spatial mesh count; and
3. using a higher-order spatial discretisation scheme for the DO direction equations.

The question is now whether previous researchers have implemented DO and FV in solar applications. If so, what are the main obstacles for using an FV DO solution of the RTE? The obstacles are as follows: ensuring the accuracy by using an appropriate FV mesh and angular discretisation, and considering the associated computational cost.

Hachicha (2013), in his PhD thesis, simulated the optical modelling of a parabolic trough in CFD. He tried to solve the accuracy question by implementing an RTE solver that separated collimated and diffuse radiation for different spatial and angular discretisations. This method is similar to the modified discrete ordinates method (Ramankutty & Crosbie, 1998), where the intensity is split into a direct and diffuse component. Hachicha (2013) was able to significantly reduce false scattering and the ray effect for the test case discussed in Addendum IV (Figure IV.1), even for a mesh of 25*25 and an $N_\theta \times N_\phi$ of 3*20 using this approach. Unfortunately, this split method is not currently available in ANSYS Fluent. However, as discussed in Addendum IV, this software is able to capture accurate solutions of the RTE with available CFD algorithms without any further code development.

Being aware of the sufficient discretisation level for accuracy can result in considerable computational savings, e.g. Martinek and Weimer (2013) used DO and FV in a high-temperature solar thermal process application and compared the results with those obtained using the Monte Carlo approach. The simulation of their model was done in ANSYS Fluent. Spatial and angular discretisations were chosen for the simulation of a 2-D closed cavity with a single-tube and a five-tube configuration as follows: four unstructured grids ranging from 2 364 to 132 453 elements and control angle increments $(N_\theta \times N_\phi)$ of 5*5, 15*15, and 25*25 with 3*3 pixellation in each case. According to Martinek and Weimer (2013), approximate solution times for the five-tube cavity increased from 11 to 1 000s and 270 to 20 000s for the coarsest and finest mesh respectively when changing from a 5*5 to 25*25 combination for $N_\theta \times N_\phi$. Their corresponding Monte Carlo solution time varied between 11 000 and 30 000s depending on the configuration and boundary conditions. As shown in Figure IV.2 and Figure IV.3 in Addendum IV (for a simple geometry), Figure 3.9 later (for a much more complex case) and Hachicha (2013), when considering a planar 2-D domain, only three angular increments are required for the first dimension. In other words, the 25*25 increments used by Martinek and Weimer (2013) were unnecessary and resulted in a computational cost of 4*25*25 versus 4*3*25, an increase by a factor of more than 8.

However, the studies of both Hachicha (2013) and Martinek and Weimer (2013) are good examples of the applicability of the DO solution using FV for solar applications. Both compared results with a Monte Carlo solution. The remaining question is whether a commercial CFD solver, e.g. ANSYS Fluent, is suitable for modelling solar applications, especially those of reflected solar irradiation in CSP line-focus technologies. In Chapter 3, the applicability of ANSYS Fluent for the optical modelling of an LFC configuration is investigated and the suitability of this approach to an optimisation study will be discussed.

2.9 THERMAL MODELLING IN LITERATURE

The concentration of solar rays onto the absorber tubes causes high local temperatures and re-radiation losses, which are influenced by the geometry of the receiver and the receiver material and optical or surface radiation properties. For a fixed operating condition, for example, a constant flow rate and inlet temperature, these losses can affect the energy availability for conversion and hence the energy output of the thermodynamic cycle is affected. Therefore, the minimisation of these losses would directly influence the total efficiency of the CSP plant or the harvesting of freely available solar energy.

The successful thermal optimisation on an LFC plant depends on the heat loss calculation with reasonable accuracy and computational effort. In this regard, two evaluation approaches were introduced in literature: computational fluid dynamics (CFD) and the so-called view area approach. In the following subsections, a literature study of these approaches is conducted, while the accuracy and practicality of these approaches to optimisation studies are investigated in the next chapters.

2.9.1 CFD for thermal simulation

The most popular approach to the thermal simulation of a solar plant is CFD, which has been widely used by previous researchers. This approach has proved its applicability to the simulation of different engineering problems for years; however, the accuracy and reliablity of its results are highly dependent on the considered assumptions in its simulation. For example, Facão and Oliveira (2011), Häberle et al. (2002), Heimsath et al. (2014), Lai et al. (2013), Manikumar and Valan Arasu (2014a), Pye (2008) and Sahoo et

al. (2012) used CFD to conduct thermal simulations of their LFC plants. In their simulations, the researchers sometimes considered simplified assumptions without verfication, which may cast doubt on the accuracy of their results.

For example, the effect of solar irradiation on the outer surfaces of tube absorbers in an LFC receiver is replaced by a constant temperature on the outer surface of the pipes. This assumption has been widely used by previous researchers for both a mono-tube (Häberle et al., 2002; Heimsath et al., 2014) and a multi-tube (Facão & Oliveira, 2011; Lai et al., 2013; Pye, 2008; Sahoo et al., 2012; 2013a; 2013b) LFC receiver. However, the accuracy of this assumption was not checked in those studies.

As another example, inside the cavity domain, the natural convection mechanism is driven by the temperature differences between the HTF tube walls and cavity walls. To capture this phenomenon inside the cavity, previous researchers analysing LFC cavities mostly used the relatively simple Boussinesq approximation when modelling density in the governing equations of natural convective flow. Pye et al., in different papers (Pye et al., 2003a, 2003b, 2003c), used the Boussinesq approximation for modelling the buoyancy force in fluid flow but Pye later claimed in his PhD thesis (Pye, 2008) that "it should be noted that the Boussinesq approximation was used in this cavity modelling, without verification of its accuracy. A calculation using extreme air temperatures of 610 K and 370 K, and a mean air density of 0.75 kg/m^3 (460 K) gives a density variation ratio $\Delta\rho/\rho = 0.49$. Further modelling should be performed to quantify the variation in the flow patterns arising from the Boussinesq assumption". In addition, other researchers (Facão & Oliveira, 2011; Lai et al., 2013; Sahoo et al., 2012, 2013a) used the same approximation without checking its accuracy, which might cast doubt on the validity of their results. Manikumar et al. (2014b) explicitly mentioned that for modelling natural convection in an LFC cavity receiver, the Boussinesq approximation cannot lead to an accurate solution. Guidelines for the applicability of the Boussinesq approximation are given in the literature, e.g. when the actual change in density is small (ANSYS, 2013a) or when $\beta\Delta T << 1$ (Bejan, 1993), where β is the volumetric thermal expansion coefficient. Because CSP cavities

often experience large temperature differences, the more accurate incompressible or even compressible ideal gas assumption may be more applicable.

In this study, before presenting the CFD thermal simulation of solar cavity receivers, the accuracy of the discussed assumptions is checked for a sample test case in Chapter 4.

In addition, to improve the accuracy of CFD thermal simulation, wavelength-dependent radiation must be simulated in the computational domain. This wavelength-dependent radiation definition is especially important in the current work, because the cavity utilises a glass window at the cavity aperture to limit convection losses as well as some re-radiation losses in the so-called 'greenhouse effect'. This greenhouse effect implies that at least a dual non-grey band must be considered in the computational domain. Almost all of the high-wavelength incident radiation on the glass is absorbed or reflected while for short-wavelength incident radiation, only a portion of the energy is absorbed and reflected so that the rest passes through this material (Moghimi et al., 2015c; 2015d). In addition, a wavelength-dependent radiation model is necessary to capture both specular and diffuse reflection from opaque surfaces in the cavity (Moghimi et al., 2015c). To the best of the author's knowledge, the investigation of the specular behaviour of thermally emitted radiation and considering dual non-grey band radiation are two of the novel aspects of this work.

2.9.2 **View area for thermal simulation**

The second thermal approach which is suggested in this study is view area. This approach is suggested as an alternative method in thermal modelling of a solar plant, particularly for optimisation study. This approach is justified by the fact that radiation is the most dominant heat loss mechanism when the cavity is covered with glass. This was proved both experimentally (Flores Larsen et al., 2012; Jance et al., 2000; Reynolds et al., 2004;) and numerically (Facão & Oliveira, 2011; Moghimi et al., 2014, 2015c, 2015d) by previous researchers in literature. Dey (2004) claims that the radiative loss constitutes about 80% of the total heat loss from the absorber.

In addition, due to the high temperature of tube surfaces in comparison with other cavity walls as well as their high emissivity (high absorptivity based on Kirchhoff's law) of tubes compared with low emissivity (low absorptivity) of other cavity walls, the absorber tube temperature and surface properties are the main drivers of radiation and heat loss in the cavity. Therefore, one can assume that heat losses from a cavity receiver are only influenced by the radiation heat transfer mechanism. This idea was implicitly implemented in previous researchers' work (Facão & Oliveira, Flores Larsen et al., 2012; 2011; Khan et al., 1999; Manikumar & Valan Arasu, 2014a; Natarajan et al., 2012; Negi et al., 1989; Singh et al. 2010a; 2010b), in which they looked for empirical correlations for heat losses from LFC cavity receivers. The power-law correlation was mostly used in this regard to satisfy radiation heat transfer effects because researchers were motivated by the observation that the losses would significantly increase with tube absorber temperature. Moghimi et al. (2016a; 2016c) asked why the thermal optimisation of an LFC plant could not be conducted based only on the optimisation of radiative heat transfer from a cavity if radiation was the most dominant mechanism in the calculation of heat losses from a receiver. Therefore, in their optimisation study, they focused on minimising the absorber tube areas that faced the mirror field (view area of absorber tubes to mirror field) to minimise the radiative heat transfer mechanism from receiver (cavity thermal loss).

This idea is the foundation of the view area approach, which will be discussed in detail in Chapter 4. The fact should be considered that calculating heat loss via a view area approach cannot be as accurate as a CFD approach. However, this method can be a very useful tool in speeding up the expensive process of optimisation and saving huge computational costs and resources, which will be discussed in Chapter 5 (Moghimi et al. 2016a; 2016c).

2.10 CONCLUSION

This chapter reported on the background required to conduct a comprehensive optical, thermal and economic optimisation study on an LFC field with a multi-tube cavity receiver (Areva Solar, 2016) while building on previous research. The work reported here introduced the approaches and engineering techniques for tackling such a problem,

answering the crucial questions faced by designers and researchers when designing an LFC plant with a multi-tube trapezoidal cavity receiver optimally. These questions could include the following: What is the optimum number and width of mirrors, because these combined would define the total mirror area? What is the optimum gap between the mirrors? What is the optimum number of tubes in a tube bundle? What tube diameter should be considered for absorber tubes? What should the arrangement of tubes be? What is the optimum configuration trapezoidal cavity? And finally: What is the optimum mounting height of a cavity receiver?

3 OPTICAL MODELLING

3.1 INTRODUCTION

When conducting a comprehensive optimisation of all solar field plants, researchers should take stock of the available engineering tools, and realise how these can be implemented in the numerical modelling and optimisation process. Due to the importance of conducting thermal and optical simulations accurately and the effects that these simulations have on optimisation results, this and the next chapter are allocated to the investigation of the accuracy of available methods and suggested approaches by the author for these simulations.

This chapter investigates the available tools and numerical modelling which researchers can use in the optical simulation of a solar field, with specific application to LFC. The chapter firstly presents the layout of a sample LFC test case.The optical simulations of the test case are then conducted via modelling techniques and engineering tools presented in literature either from previous researchers (MCRT ray tracing) or suggested by the author (CFD FV ray tracing). After optical simulations of the test case, the accuracy and applicability of these models are compared to survey the effectiveness of the discussed approaches for the optical simulation of an LFC domain. Before further discussion of the advantages and disadvantages of these approaches to find the most suitable method for numerical optimisation in Chapter 5, the same study and comparison are done on a complementary test case (mono-tube LFC cavity receiver with secondary reflector) to prove the generalisation of CFD FV as a novel approach to the optical simulation of solar fields.

3.2 LAYOUT OF MULTI-TUBE LFC TEST CASE

An LFC is a combination of an array of linear primary mirrors, which concentrates solar rays on a cavity receiver mounted at a specific height. Therefore, the optical efficiency of such plants is affected by different field factors such as primary mirror positions, width, and space, while their thermal efficiency is affected by cavity factors such as the position of tube/tubes, insulation thickness and the geometry of the cavity. Therefore, to determine

both the optical and thermal efficiency of such a plant, and to conduct optimisation studies, the cavity receiver and solar field must be defined completely.

The cavity receiver considered in this study is covered by a glass panel and is not evacuated. The glass window has interesting properties. Glass is opaque to high-wavelength radiation and semi-transparent for the rest of the spectrum resulting in the so-called greenhouse effect. The solar irradiation reflected by the LFC mirror field passes through the glass with a small proportion being absorbed depending on the specified absorption coefficient. It then impacts on the absorber tubes that are opaque to radiation and are coated with a specific solar-absorbing coating to absorb more solar energy (in the short-wavelength spectrum) but to re-radiate less energy to their surroundings as their temperature increases (in the high-wavelength spectrum). The portion of the energy not absorbed by the tubes is reflected towards the cavity side walls and back to the glass. The side walls are insulated to limit heat loss. These cavity side walls and tube surfaces are opaque and both diffusely and specularly reflective, i.e. they absorb radiation and reflect it in a way that depends on the incident radiation wavelength, which interacts with the surface roughness height such that reflection is either specular or diffuse.

A solar mirror field (mirror width, mirror gap and number of mirrors) is considered based on what was defined in the FRESDEMO project (Mertins, 2009; Bernhard et al., 2008a). The multi-tube trapezoidal cavity receiver considered here is close to the initial case used by Moghimi et al. (2014; 2015c), as displayed in Figure 3.1.

A parallel four-tube bundle with tubes made of carbon steel (solid grey areas in the zoomed-in region of Figure 3.1) is located in a trapezoidal cavity that is filled with air. The name “tube” is mostly used in this text except when referring to other texts that use “pipe”. They both refer to the same cylindrical geometry. The cavity side and top walls are insulated with insulation of different thickness (dotted area in the zoomed-in region of Figure 3.1). The cavity aperture (lower wall) is covered by a 3.2 mm thick glass (not shown). The collector geometry is parameterised with the values and definitions summarised in Table 3.1.

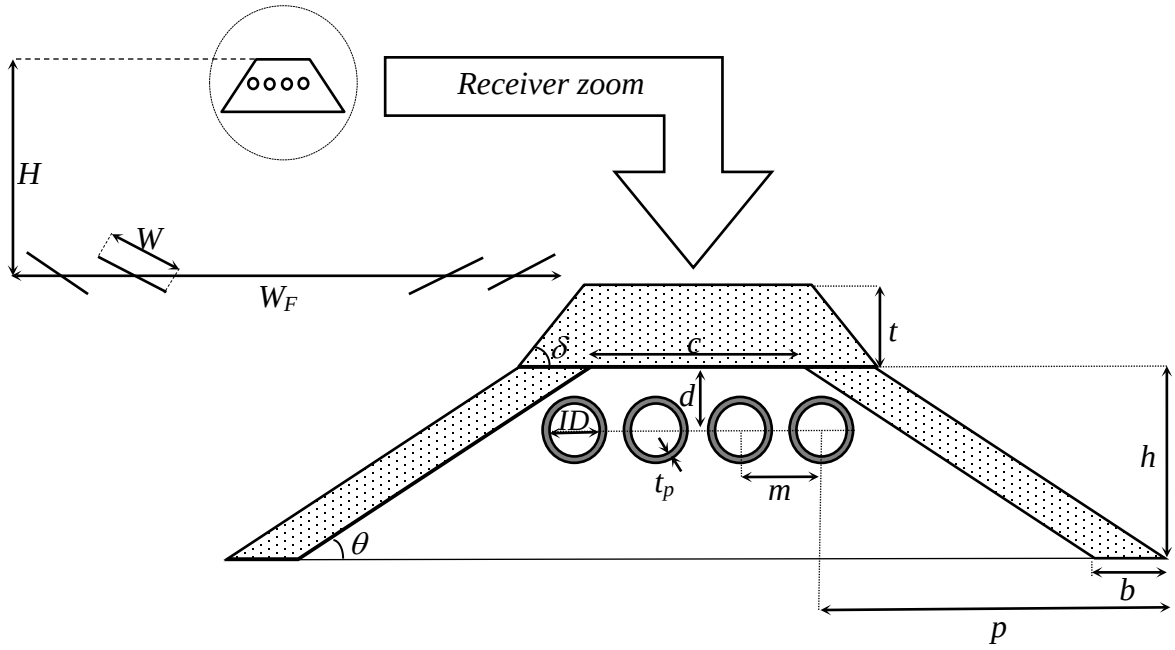

Figure 3.1. Schematic layout of the LFC mirror field and cavity receiver (not to scale).

Table 3.1 Geometrical parameters of LFC with parameter values for parameters indicated in Figure 3.1.

Number of mirrors (N_m)	25	Tube thickness (t_p [mm])	5	Cavity top side width (c [mm])	400
Mirror width (W [m])	0.6	Tube ID (ID [mm])	40	Tube pitch (m [mm])	75
Solar field width (W_F [m])	21	Tube bundle offset from cavity top wall (d [mm])	55	Distance of the outermost tube centre from the cavity aperture edge (p [mm])	503
Receiver mounting height (H [m])	8	Cavity depth (h [mm])	240	Top insulation thickness (t [mm])	85
Side insulation thickness (a [mm])	40	Top insulation angle δ [°]	60	Cavity angle θ [°]	30

3.3 SOLTRACE OPTICAL SIMULATION

A SolTrace model was constructed of the proposed LFC layout, with the optical parameters summarised in Table 3.2. For more information on how to simulate in SolTrace, see Addendum I. Since the focus of this thesis is on the development and validation of approaches for a comprehensive optimisation study, in Table 3.2 ideal assumptions are considered which might not comply with physical or realistic data. Future researchers who are interested in more realistic studies, have to define the parameters more accurately, e.g., consult with Rabl (1985) for sun shape definitions, or consult with manufacturers for primary mirror properties, cavity side walls properties and so on.

Table 3.2 SolTrace parameters for LFC optical modelling.

Sun shape	Gaussian	2.73 mrad	*z*-direction (noon)
Primary mirrors	Reflectivity = 1	Slope error = 0.0001	Specularity error = 0.0001
Tubes	Reflectivity = 0.05		
Glass	Transmissivity = 1	Refraction ratio = 1.5	
Cavity side walls	Reflectivity = 0.95 (Mertins, 2009)	specular	
Direct normal irradiation (DNI)	1 000 W/m^2		

Based on the geometrical definition of the solar field and the SolTrace settings, a sample solution of ray trace is shown in Figure 3.2. Individual rays (vertical yellow lines) trace downwards from the noon position of the sun and reflect off the linear mirror segments (green segments at the bottom of Figure 3.2a) and concentrate upwards onto the tubes enclosed with a trapezoidal cavity wall and glass cover (Figure 3.2b).

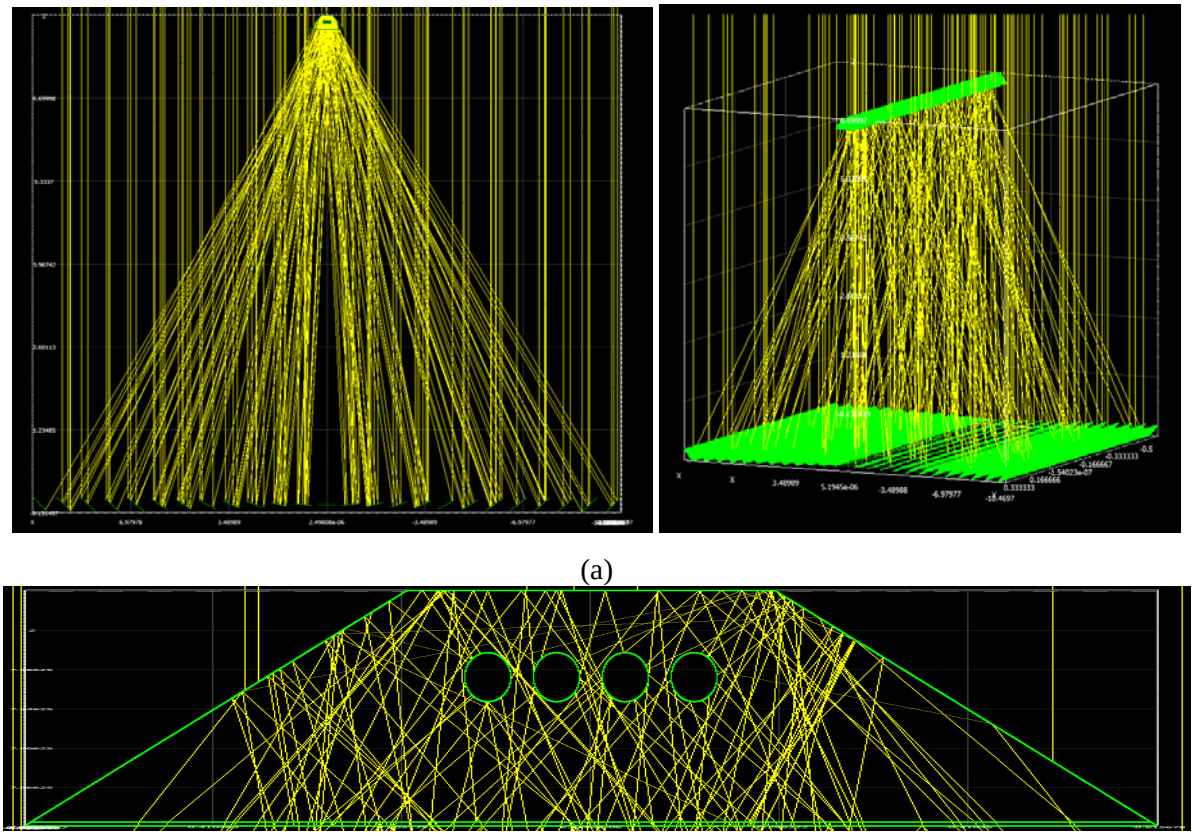

(a)

(b)

Figure 3.2. Ray tracing for the LFC test case in SolTrace.

(a) Entire optical domain (front and isometric view). (b) Zoomed-in view of cavity receiver.

For assurance of SolTrace solution convergence, the “Desired number of ray intersections” parameter in SolTrace was increased until the average heat flux value on each tube stabilised, and its symmetrical counterpart converged to the same value. The average heat flux absorbed by all four tubes was monitored as well. In this study the tubes are numbered from left to right. The convergence results are summarised in Table 3.3 and Figure 3.3.

Due to the symmetry of the geometry, the average value of the absorbed heat flux for the symmetrical tubes (2 & 3 and 1 & 4) has to be the same. Table 3.3 shows that by increasing the “Desired number of ray intersections”, the results of symmetrical tubes converge to numbers that are similar but not exact because of the Monte Carlo process. Even for the minimum “Desired number of ray intersections” value, the average value of the heat flux is well predicted, but not necessarily symmetrically distributed. Based on

Table 3.3 and Figure 3.3, apparently, a ray count of 1 000 000 can be considered as providing a converged solution for the average value.

However, the circumferential distribution of the ray hits is another parameter that must be considered for cavity performance evaluation. SolTrace outputs ray data that can be further post-processed. These data are a set of intersection points and direction cosines. Using a VBA (Visual Basic for Application) code written in Microsoft Excel and Microsoft Access, the number of ray hits on a certain circumferential increment of each tube was calculated and converted using the power per ray value to an equivalent heat flux. The resulting circumferential distribution of the heat flux for the third and fourth tube obtained using SolTrace is depicted in Figure 3.4 for different desired ray intersections ranging from 5 000 to 1 000 000. The origin of the circumferential coordinate is indicated in the insert.

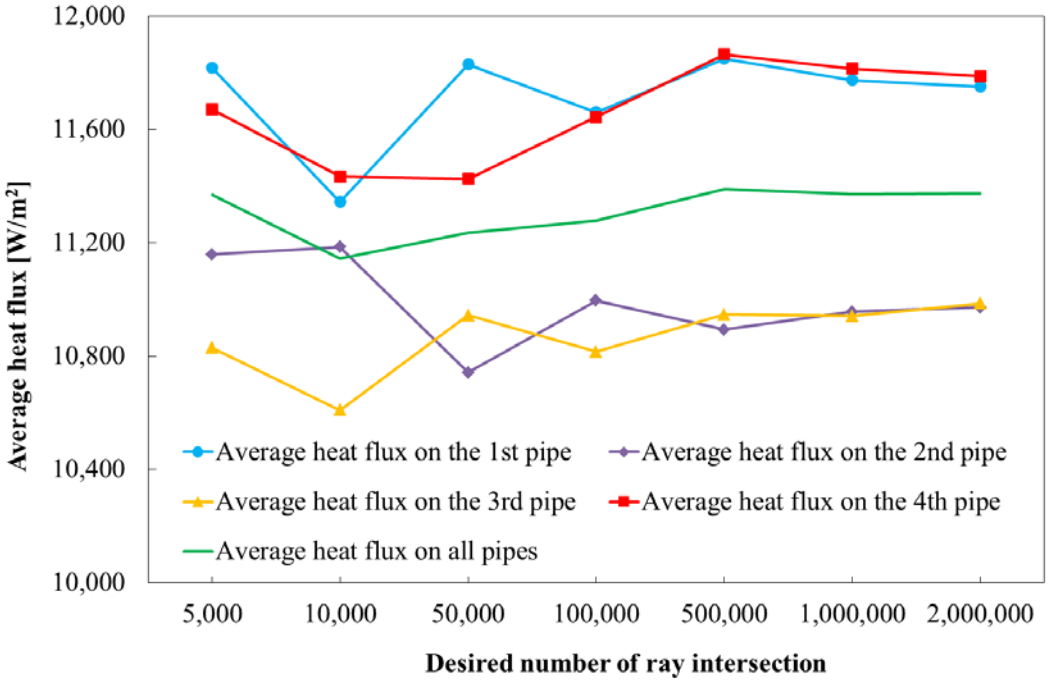

Figure 3.3. Convergence study of average heat flux on absorber tubes in SolTrace.

Table 3.3 Convergence study of SolTrace.

Desired number of ray intersections	**Ray count**	**Power per ray**	**Average of heat flux on the 1st tube from left to right**	**Average of heat flux on the 2nd tube from left to right**	**Average of heat flux on the 3rd tube from left to right**	**Average of heat flux on the 4th tube from left to right**	**Average of all heat fluxes on tubes**
5,000	11,393	3.00273	11,8167	11,159	10,829	11,670	11,369
10,000	23,022	1.48597	11344	11,185	10,609	11,434	11,143
50,000	116,066	0.294747	11,829	10,741	10,944	11,425	11,235
100,000	231,347	0.147874	11,660	10,995	10,815	11,644	11,279
500,000	1,152,422	0.0296854	11,850	10,893	10,946	11,865	11,388
1,000,000	2,307,140	0.0148279	11,773	10,957	10,941	11,814	11,371
2,000,000	4,615,871	0.00741141	11,751	10,972	10,985	11,788	11,374

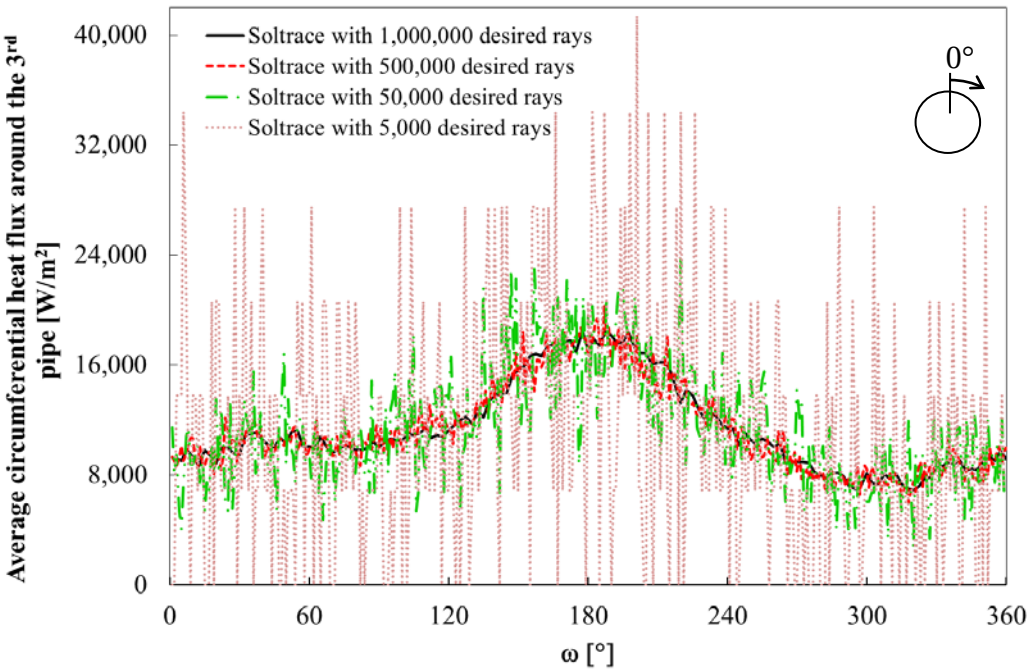

(a)

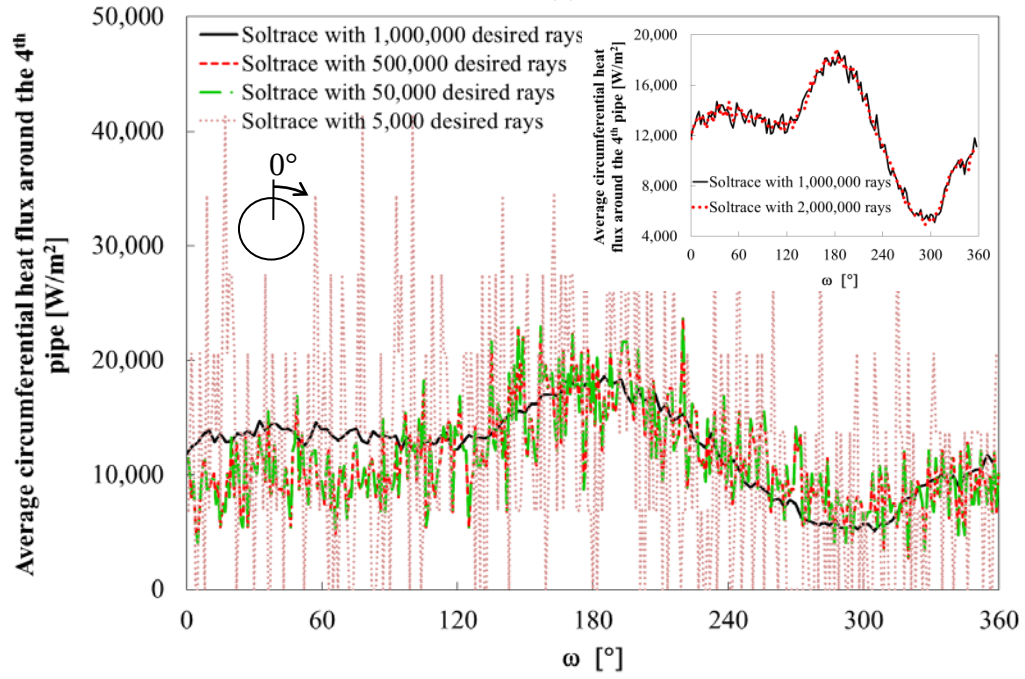

(b)

Figure 3.4. Fluctuation of SolTrace results for different desired rays.

(a) Absorbed circumferential heat flux [W/m^2] around the 3rd tube. (b) Absorbed circumferential heat flux [W/m^2] around the 4th tube.

It can be seen that by increasing the desired number of rays, the fluctuations in the distribution decrease as the stochastic nature of the Monte Carlo process provides a more distributed profile with an increasing ray count. An interesting phenomenon in the range 0 to 100° occurs for the fourth tube (Figure 3.4b). Apparently, due to the presence of the oblique corner of the cavity close to the fourth tube and ray tracing error in simulation under 500 000 rays count, the heat flux trend was underestimated until this number of ray counts. For ray counts more than 1 000 000 (see the inserted picture in Figure 3.4b), the distribution remained unchanged. For both distributions, the heat flux was a maximum at 180° (the bottom of the tubes) as expected, but the mostly reflecting side and top walls resulted in significant heat absorption on the upper parts of the tubes as well.

By increasing the number of desired ray intersections, the symmetrical property of the absorbed heat flux is also ensured. Figure 3.5 illustrates the symmetrical result by flipping the results of the first and second tube and superimposing them on the fourth and third tube respectively. This comparison is made for 1 million desired ray intersections.

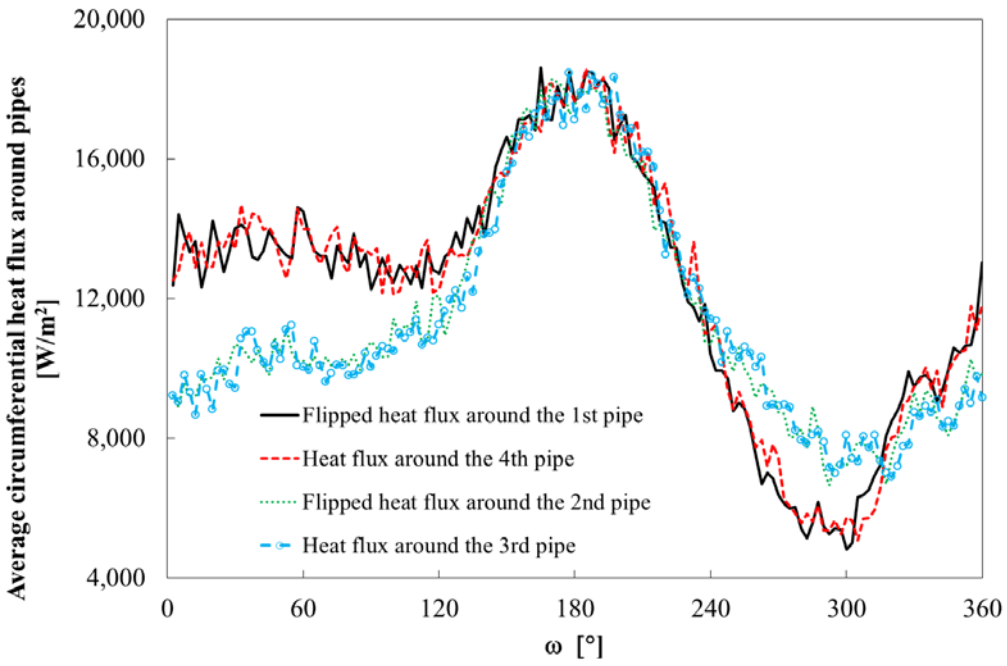

Figure 3.5. Checking the symmetrical nature of the circumferential tube heat flux distributions.

3.4 CFD FV OPTICAL SIMULATION

Apart from Martinek and Weimer (2013), who also used ANSYS Fluent to determine the solar heat flux distribution, other solar cavity researchers mostly used a Monte Carlo ray tracer to capture the non-uniform heat flux of more complex geometries. For example, Cheng et al. (2012), He et al., (2011), Ghadirijafarbeigloo et al. (2014) and Wirz et al. (2014) used SolTrace and another Monte Carlo code to capture the non-uniform solar heat flux on the absorber pipe of a parabolic trough collector. The following section describes the use of ANSYS Fluent as an accurate FV solver in the calculation of the non-uniform heat flux distribution of the LFC cavity receiver and mirror field. Because the work was not considered by previous researchers, it is described in more detail in following subsections.

3.4.1 Optical geometry and meshing

To do the optical modelling of the LFC layout based on the specifications listed in Table 3.1, a symmetrical 2-D model of the entire optical domain was created in ANSYS Workbench (ANSYS, 2013b) and meshed in the ANSYS Meshing tool (ANSYS, 2013b). The 2-D simulation of the plant is justifiable since the position of the sun on a summer day is almost located on the transversal plane for a North-South LFC domain. The geometry and meshes are displayed in Figure 3.6. The top boundary is a semi-transparent wall where the solar irradiation enters the domain. The mirrors form the lower boundary together with the gaps between them. The gap between the mirrors as well as the right edge of the domain, are modelled as black bodies that capture all the radiative energy reaching them. The left edge of the domain is a symmetry edge, providing pure reflection. The cavity is modelled with glass covering its aperture and surrounded by insulation (required for the thermal modelling to follow). The tubes are modelled with only their outer surface to provide a boundary condition where the resulting fluxes can be obtained. Figure 3.6b shows the 86 725 cell mesh (see Table 3.6).

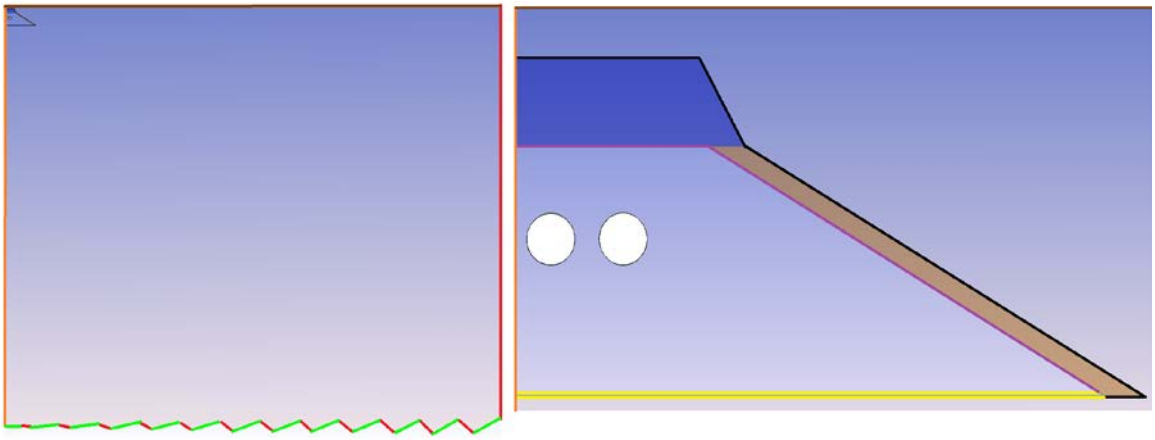

(a)

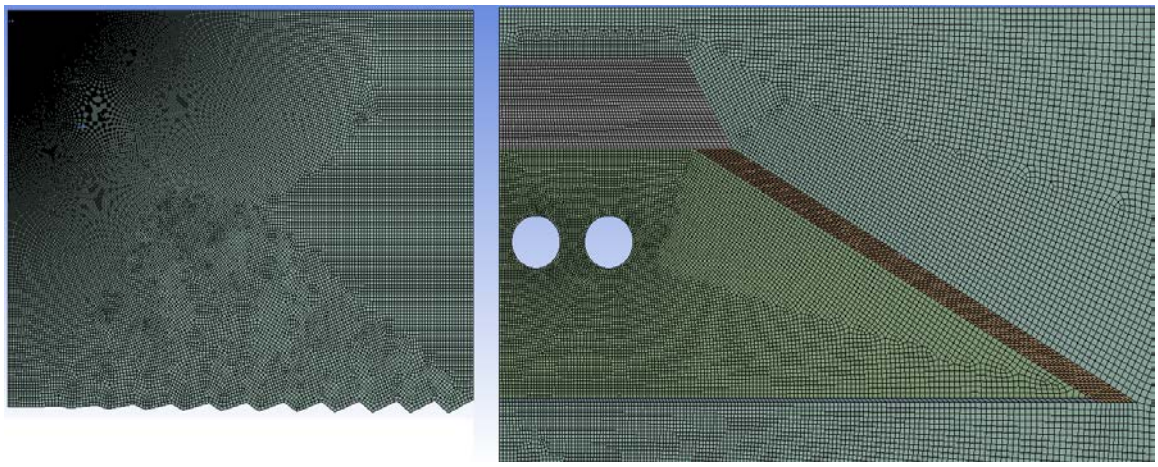

(b)

Figure 3.6. CFD model of the optical geometry of LFC.

(a) Geometry (whole symmetrical domain – left, zoomed-in view of cavity receiver – right). (b) Mesh (whole symmetrical domain – left, zoomed-in view of cavity receiver – right).

3.4.2 Boundary conditions and material properties of optical modelling

The assumption can be made that air is transparent to radiation for the current application and its extent (compared with the atmosphere, for example) and the effect of convective heat transfer is neglected in this section because the only energy in optical modelling that will be captured on the HTF tubes is the solar load. As such, the air between the mirror field and cavity and inside the cavity is modelled as a solid with the thermal properties of air and being transparent to radiation (absorption coefficient of 0). This simulation means

that only the RTE and energy equations need to be solved in the computational domain, which reduces the computational overhead significantly. In addition, to isolate the solar load, all opaque walls in the domain are modelled as cold, having a specified temperature of 1K. This low temperature eliminates any thermal re-radiation.

For the optical modelling, the glass cover needs special treatment. The glass zone is modelled as two semi-transparent walls containing a solid medium which participates in radiation. Firstly, glass provides refraction of which the effect would depend on its thickness. Secondly, this medium is almost opaque to the higher wavelength band of radiation (>~4μm) while it is almost semi-transparent to lower wavelengths, which leads to the greenhouse effect. This phenomenon can be modelled accurately based on the definition of dual-band absorption coefficient (Moghimi et al., 2014; 2015c) in the ANSYS Fluent DO implementation. However, because the current optical model only considers solar irradiation energy that is mostly concentrated in the shorter wavelengths, a single band can be used for this evaluation. The material properties used are summarised in Table 3.4. The insulation properties are given here for completeness and will be used in the thermal evaluation to follow. The boundary conditions for the optical domain are summarised in Table 3.5. As it is shown in this table, the temperature of all the boundaries were set to 1 K to all but eliminate thermal re-radiation from these boundaries, i.e., to just capture the effects of the incoming solar radiation on the absorber tubes.

3.4.3 **Mesh and angular independence**

To determine the correct settings for an accurate simulation of radiative transfer problems in ANSYS Fluent, both a mesh and an angular discretisation independence study must be implemented. These discretisations can alleviate the major shortcomings (false scattering and ray effect) of the numerical solution of radiative transfer problems (please consult Addendum IV for more information). A second-order upwind discretisation was used for the DO calculations of the study. All simulations were run for 2 000 iterations to ensure that the normalised residual for DO was less than 1e-6 and stable monitors on the area-weighted average absorbed the heat flux on each tube. The results are reported in Table 3.6 and Table 3.7 for mesh independence and angular independence respectively. Figure 3.7

provides a graphic form of the tabular data with Figure 3.7a concentrating on the heat flux and Figure 3.7b on the computational cost. The wall clock time values are reported when running on five cores of an Intel core™ i7-3970X CPU with 32 GB RAM. The second to fourth columns of Table 3.6 provide proof that the mesh quality is consistent during the mesh refinement process. For the mesh refinement, the angular discretisation setting was kept constant at 3*30 for $N_\theta \times N_\phi$ and 3*3 pixels. In the definition of angular discretisation for a planar problem, N_ϕ has the main contribution in the accuracy of the numerical solution (e.g., compare the results of 3*30 and 30*3 in Figure 3.9). An accurate (0% deviation) result was based on a 1 040 700 cell case, and the relative cost measure deemed this case 100% expensive.

Table 3.4 Material properties

Material	**Participating in radiation**	**Absorption coefficient [m^{-1}]**	**Refractive index**	**Other**
Solid air in and around cavity	Yes	0	1	Thermal conductivity = 0.0242 [W/m-K], Specific heat = 1 006.43 [J/kg-K], Density = 1.225 [kg/m^3]
Semi-transparent glass	Yes	106	1.5	Thermal conductivity = 1.5 [W/m-K], Specific heat = 786 [J/kg-K], Density = 2 650 [kg/m^3]
Insulation - glass wool (TIASA, 2001)	No	0	1	Thermal conductivity = piecewise-linear [W/m-K], Specific heat = 446 [J/kg-K], Density = 48 [kg/m^3]

Table 3.5 Boundary conditions for optical domain

Surface	BC type	Thermal condition	Temperature [K]	Emissivity	Others
Solar field top side	Semi-transparent	Constant temperature	1	1	Beam width $\theta = 0.53^{\circ}$ & $\phi = 0.53^{\circ}$, Direct irradiation=1 000 [W/m^2] downwards
Solar field right side and gaps between mirrors	Opaque and black body	Constant temperature	1	1	-
Mirrors	Opaque and pure reflective	Constant temperature	1	0	-
Solar field left side	Symmetry	-	-	-	-
External surfaces of insulation	Opaque	Constant temperature	1	1	-
Cavity walls	Opaque and reflective	Constant temperature	1	0.05	-
Glass sides	Semi-transparent	Coupled	-	0	-
Outer surface of pipes	Opaque with selective coating	Constant temperature	1	0.95	-

Table 3.6 Mesh study.

Number of cells	Aspect ratio	Jacobian ratio	Mesh quality	Clock time [s]	Area-weighted average of absorbed heat flux on 3rd tube [W/m^2]	Area-weighted average of absorbed heat flux on 4th tube [W/m^2]	Average of both tubes [W/m^2]	Deviation percentage of result accuracy from levelling-off case % (based on the average of both tubes)	Computational cost ratio percentage in comparison with levelling-off cost (based on CPU time)
459	1.71	1.72	0.71	32.7	2,994	2,511	2,753	-52.9	0.0
1101	1.44	1.41	0.79	40.2	3,079	3,671	3,375	-42.3	0.1
2927	1.21	1.23	0.87	61.7	4,029	4,722	4,375	-25.2	0.2
7896	1.16	1.18	0.90	135.6	4,743	5,501	5,122	-12.4	0.4
86,725	1.08	1.05	0.96	1,286	5,384	6,062	5,723	-2.1	3.5
346,900	By using Fluent mesh adaptation			5,188	5,506	6,108	5,807	-0.7	14.0
1,040,700	By using Fluent mesh adaptation			36,993	5,548	6,145	5,846	0	100

Table 3.7 Angular discretisation study.

DO Discretisation setting $N_\theta \times N_\phi$	**Clock time [S]**	**Area-weighted average of absorbed heat flux on 3rd tube [W/m^2]**	**Area-weighted average of absorbed heat flux on 4th tube [W/m^2]**	**Average of both tubes [W/m^2]**	**Deviation percentage from levelling off % (based on the average of both tubes)**	**Computational cost ratio percentage in comparison with levelling-off cost based on CPU TIME**
3*5	234.4	859	1,144	1,001	-88.9	1.5
3*10	436.9	2,039	2,357	2,198	-75.7	2.7
3*30	1,286	5,384	6,062	5,723	-36.7	8.0
3*50	2108	6,937	7,702	7,320	-19.1	13.2
3*100	3,958	8,263	8,918	8,591	-5.0	24.9
3*200	7,711	8,621	9,294	8,958	-0.95	48.5
3*400	15,915	8,711	9,377	9,044	0.00	100.0

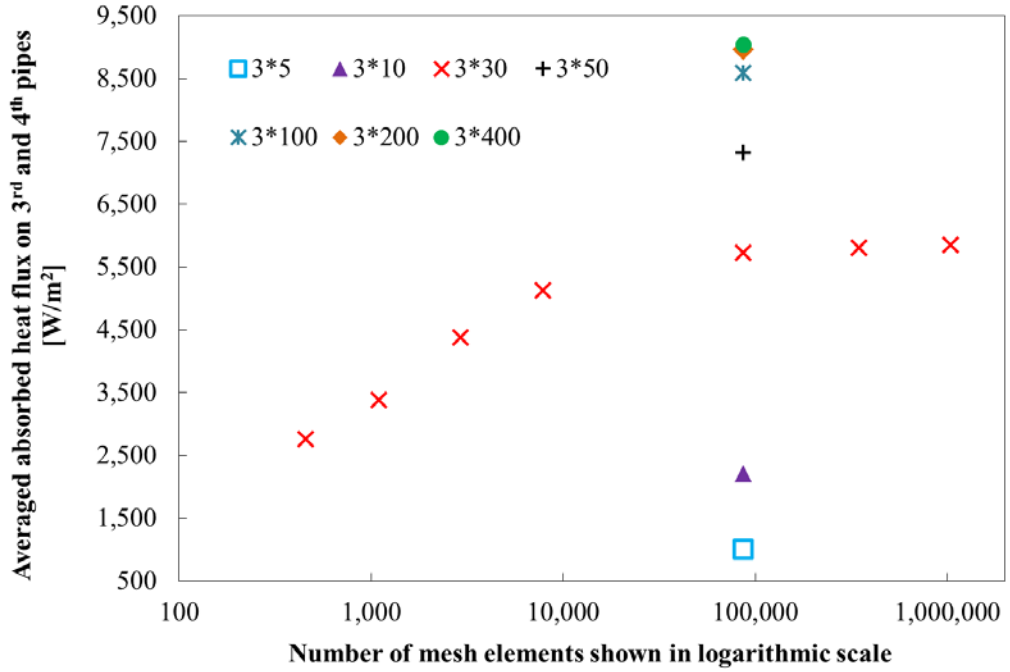

(a)

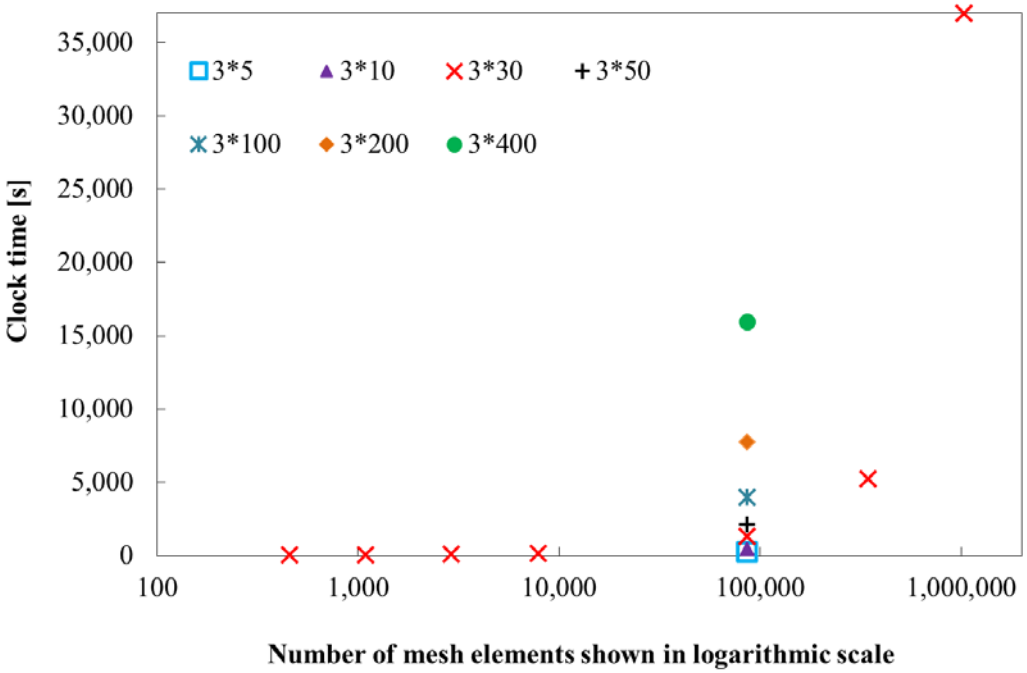

(b)

Figure 3.7. Mesh and angular independence study.

(a) Average absorbed heat flux [W/m^2] versus mesh count for various angular discretisation settings. (b) Computational cost in clock time versus mesh count for various angular discretisation settings.

The effect of varying the angular discretisation settings was investigated for a constant mesh count of 86 725 cells with a constant pixellation of the discrete ordinates of 3*3 (Table 3.7). An $N_\theta \times N_\phi$ of 3*400 was considered to be the most accurate case (0% deviation) and the most expensive (100%).

If a 1% accuracy level is deemed accurate enough, then a 3*200 angular discretisation setting for a mesh count of 346 900 or more can be considered to be in the region of convergence. The graphic portrayal of the tabular data in Figure 3.7 confirms this conclusion and allows for the following observations to be made:

1. In Figure 3.7a, the variation in results when refining the control angle extension for a specific mesh count is much wider (almost three times) than the variation in results obtained by mesh refinement. In other words, when using second-order upwind discretisation for DO, refining the control angles has a much larger effect than refining the mesh. The reason for this effect is discussed in Addendum IV, i.e. the ray effect error is reduced by increasing the angular discretisation, while refining the mesh only removes the false scattering error, which is already reduced by the second-order discretisation of the DO equations.
2. When the mesh number is increased beyond a certain count, there is a dramatic increase in computational cost because of the $4 \times N_\theta \times N_\phi$ equations that are being solved on the mesh (Figure 3.7b). As can be seen from the angular discretisation variation at a mesh count of 86 725, the same dramatic increase occurs for larger N_ϕ values. The asymptotic behaviour of the heat flux value above a count of 100 000 cells (Figure 3.7a) confirms that this mesh gives an independent result.

Based on the above, the suggested method of conducting a mesh and angular discretisation study is to first conduct a mesh independence study of the coarsest control angle. After determining a suitable and converged mesh, then conduct an angular discretisation study and try to refine the control angles as much as is feasible.

3.5 COMPARING ANSYS FLUENT RESULTS WITH SOLTRACE

To compare the results of ANSYS Fluent and SolTrace, the glass absorption (as defined in Table 3.4) was neglected in the ANSYS Fluent simulation by setting the absorption coefficient of the glass material to zero to allow for a direct comparison with SolTrace. This neglect means that the absorbed flux on the tubes is higher than the values listed in Table 3.7. Table 3.8 lists the average circumferential heat flux of the third and fourth tubes as well as the total average flux. It can be seen that there is an excellent agreement between ANSYS Fluent and SolTrace, although enhanced by a fine mesh (346 900 cells) and a high DO setting (3*200). One million desired rays were used for SolTrace. The heat flux distributions are compared in the radar plots of Figure 3.8, again for the same settings. It can be seen that the distributions are also in excellent agreement, providing confidence that the FV method can accurately predict non-uniform heat flux distributions, albeit at a higher cost. As before, the maximum heat flux occurs on the lower part of the tubes facing the mirrors with the lowest flux on the top side of the tube. The slight asymmetry in the top left quadrant of the third tube (Figure 3.8a) is caused by blocking and shading of the adjacent tube. The fourth tube again displays an interesting phenomenon around 0° to 60°. There is an asymmetry in the distribution caused by the proximity of the inclined cavity wall and its junction with the top wall of the cavity. Interestingly, this is the only region where the ANSYS Fluent and SolTrace results do not fall on top of each other. Remember that this was also the region in Figure 3.4b where the result only stabilised after the ray count was increased to 1 million and above.

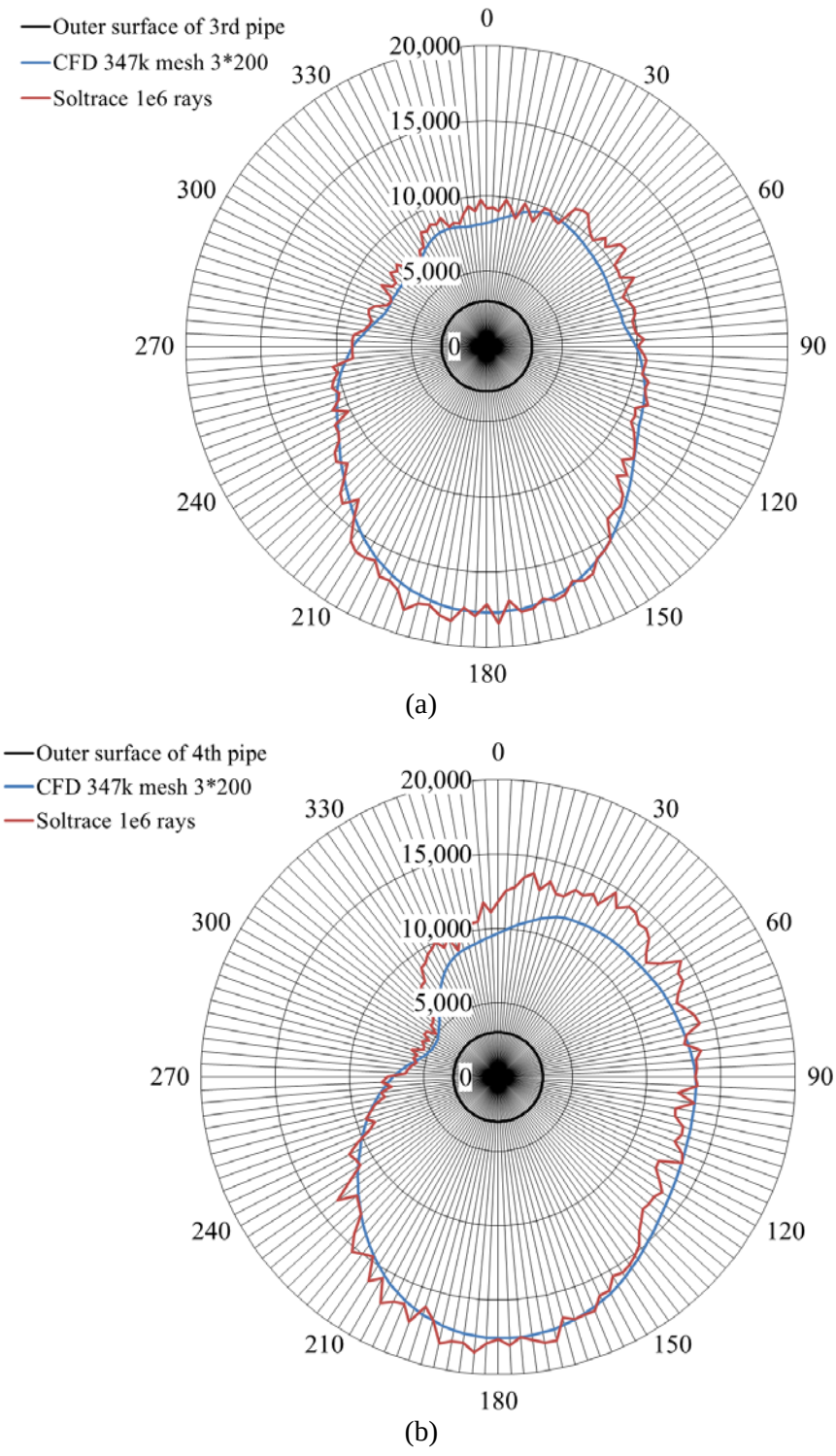

Figure 3.8. Radar plots of heat flux distribution [W/m^2] around absorber tubes between CFD (mesh 346 900 cells, 3*200 DO) and SolTrace (1 million rays).

(a) 3rd tube distribution. (b) 4th tube distribution.

Table 3.8 Comparison of ANSYS Fluent and SolTrace heat flux.

Method	**Area-weighted average of absorbed heat flux on the 0.0375 distance from centre (average of Tubes 2 & 3) [W/m^2]**	**Area-weighted average of absorbed heat flux on the 0.1125 distance from centre (average of Tubes 1 & 4) [W/m^2]**	**Average of all tubes [W/m^2]**	**Deviation percentage of ANSYS FLUENT result for all tubes from SolTrace result (%)**
FV without glass absorption (347k mesh, 3*200 DO)	11,021	11,671	11,346	-0.22
Ray tracing (1e6 rays)	10,949	11,794	11,371	0

Figure 3.9 confirms that it is unnecessary to use the same discretisation on both control angles (N_θ=N_φ). This is true not only for the simple case presented in Addendum IV, but also here for a complex and realistic 2-D planar geometry (LFC domain - Figure 3.2). Only the N_φ control angle plays an important role in the results, with a wise choice leading to less computational effort. As representative, Figure 3.9 contains results for 3*3, 30*3, 3*30 and 30*30 angular discretisations on the same spatial discretisation (86 725 mesh). As shown, the results of 30*3 (30 discretisation over θ control angle with 3 discretisation over φ), which is in great agreement with the 30*30 discretisation, are obviously far from what 3*30 and or 3*3 estimate.

In addition, to illustrate how the ray effect and false scattering are reduced for this more realistic application than that described in Addendum IV (with a more complex geometry

and a subtended sunbeam angle instead of collimated light), Figure 3.9 displays the results for various mesh and DO settings as compared with those of SolTrace. For the coarsest main control angle (φ) 3 and 10 (which respectively are displayed as (30*3) and (3*10)), the flux value is much lower than it should be, although the distributions have the correct shape. This offset can be attributed to both a ray effect and a false scattering (diffusion) error. The effect of refining the control angle (3*30, 3*100 and 3*200) is to reduce the ray effect but not necessarily the false scattering. Figure 3.9 shows that the shape of the absorbed radiation profile remains constant when the control angle settings of the 86 725 mesh case are changed from 3*100 to 3*200. The false scattering effect is only removed when the mesh is further refined to 346 900 cells. Note that the false scattering effect has contributions from the whole computational domain, including the region of the reflecting mirrors. Therefore, the complexity of the modelled geometry makes it difficult to isolate individual error contributions.

It is, of course, important to capture the shape and correct value of the heat flux distribution, especially when an accurate thermal evaluation of the cavity is required. The severity of the non-uniformity of the heat flux distribution is also important to capture as it would lead to non-uniformity in the pipe temperature distribution, which could result in undesirable thermal expansion and thermal stresses.

And last but not least, the incident radiation contours for the 346 900 mesh and 3*200 angular discretisation are shown in Figure 3.10. The maximum contour display value in this figure is set to 25 000 (W/m^2) instead of the global maximum calculated value of 45 907 (W/m^2) to highlight the optical effects of blocking and shading of adjacent mirrors as well as the concentration effect at the receiver.

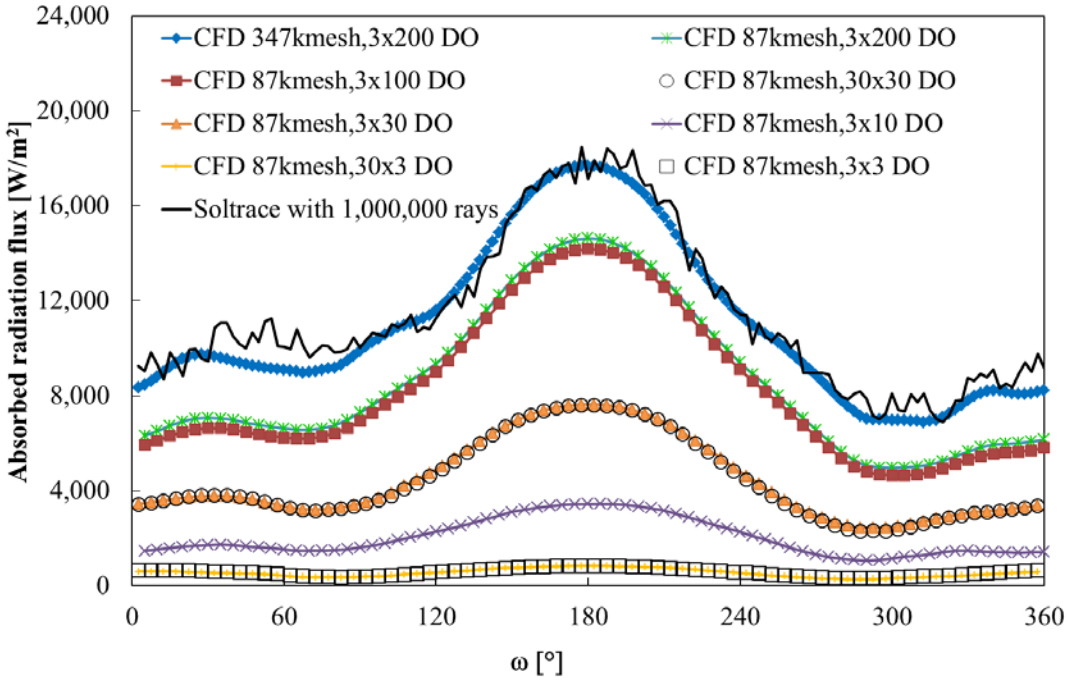

(a)

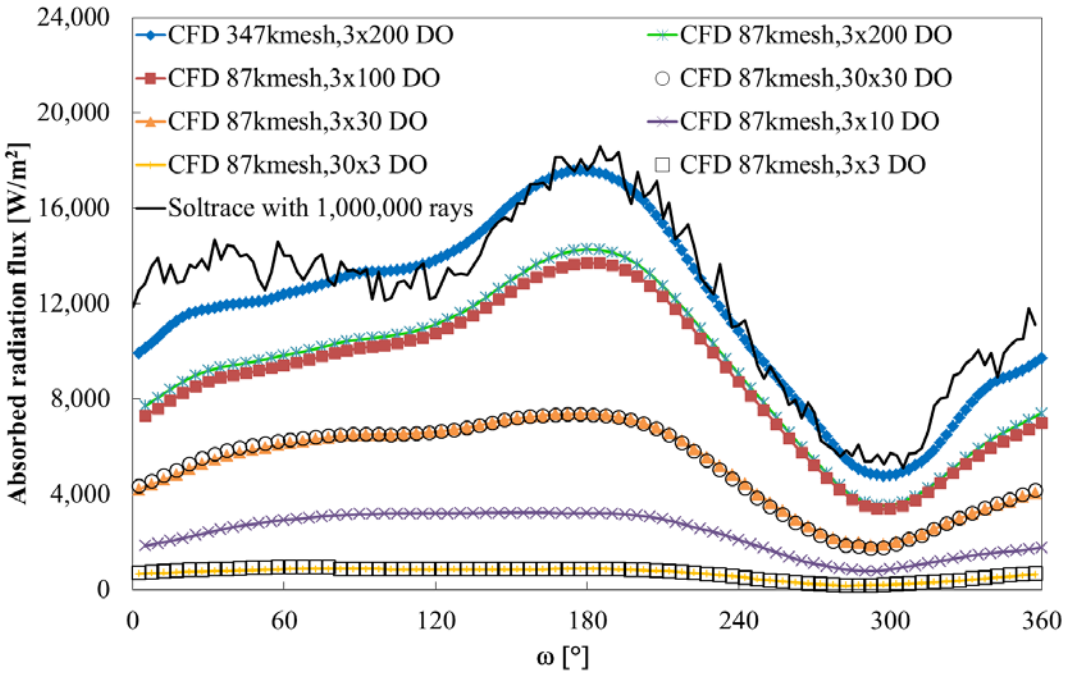

(b)

Figure 3.9. Comparison of heat flux distribution [W/m^2] around absorber tubes for different CFD settings and SolTrace (1 million rays).

(a) 3rd tube. (b) 4th tube.

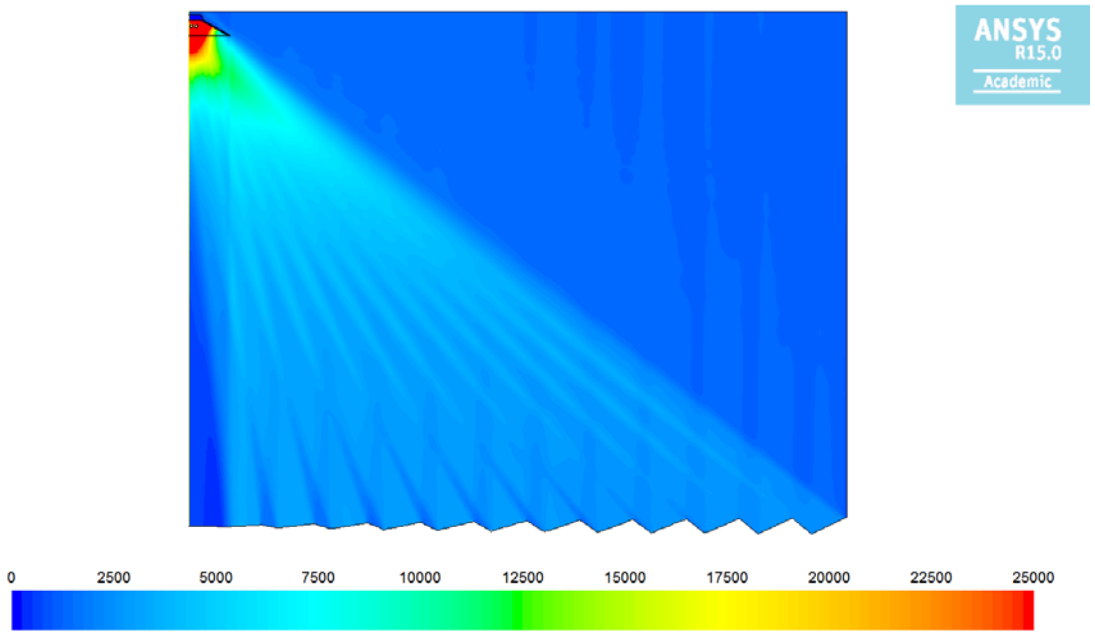

Figure 3.10. Contours of incident radiation [W/m^2] in the LFC domain for 346 900 mesh and 3x200 angular discretisations at noon.

3.6 COMPLEMENTARY CASE STUDY: MCRT AND CFD FV OPTICAL SIMULATION OF AN LFC WITH MONO-TUBE SECONDARY REFLECTOR CAVITY RECEIVER

As a complementary test case study, a cavity very similar to the FRESDEMO project (Bernard et al., 2008a), a mono-tube LFC with a secondary reflector cavity, was used. The curves of the secondary reflector were approximated by creating a curve fit through extracted points from the Novatec Solar cavity design (Selig & Mertins, 2010). A glass window was situated at the aperture of the cavity to limit thermal re-radiation and the effects of forced and natural convection. For comparison with SolTrace, no absorption was modelled for the glass solid material as in the previous case study (Section 3.2), i.e. only refraction through the glass was considered. This case used the same mirror field as the first test case (Section 3.2, see Table 3.1 for properties), while the single-tube outer diameter was changed to 70 mm. The computational domain with an insert showing the mesh in cavity receiver is shown in Figure 3.11. The semi-transparent boundary was slanted compared with before, with the realisation that only the region influenced by the reflected radiation from the mirror field needed to be considered.

The material properties and boundary conditions are detailed in Table 3.4 and Table 3.5 respectively. The mesh and DO independence study yielded a 477 454 cell mesh and a 3x200 DO discretisation, while the ray count sensitivity study in SolTrace required a minimum of a million ray intersections as before.

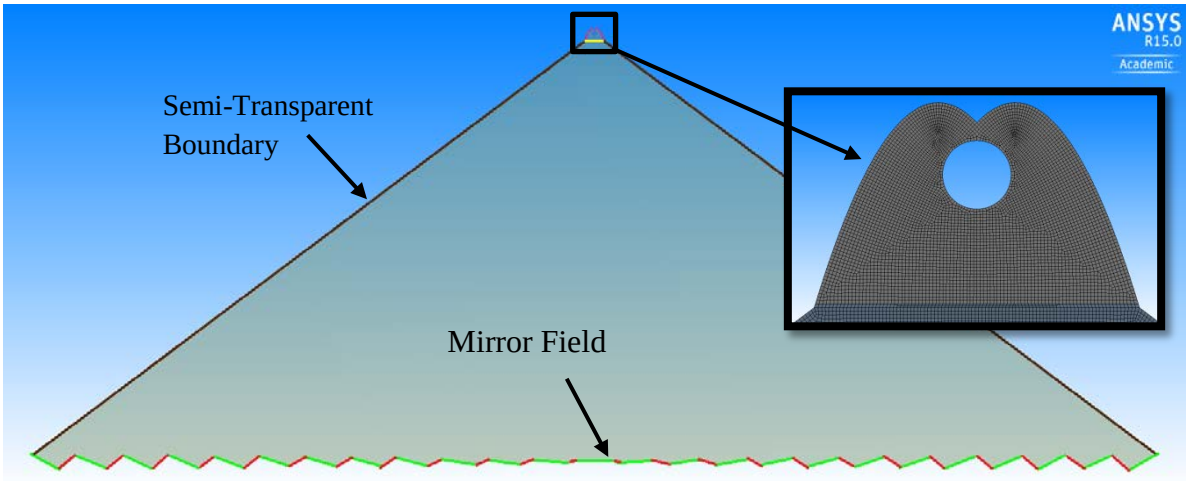

Figure 3.11. Computational domain of LFC with an insert showing mesh in cavity receiver.

The incident radiation contours and the SolTrace results of the solar field and the cavity close-up of the LFC for the converged case at noon are shown in Figure 3.12 and Figure 3.13 respectively. To compare the results of ANSYS Fluent and SolTrace, the detailed absorbed radiation profiles and integrated amount of absorbed radiation are compared in Figure 3.14 and Table 3.9 for 2 million ray intersections. The CFD solution yielded reasonably accurate results when compared with SolTrace for the mono-tube with a secondary reflector cavity. The higher percentage error of the CFD model's integrated absorbed radiation value than that obtained in Table 3.8 for the trapezoidal cavity is likely due to the secondary's additional concentrating effect, which creates a higher accuracy requirement of the radiation model due to the directional complexity of the incoming radiation.

Anyway, as shown in this document, CFD could accurately capture the optical simulation of any complex geometry if and only if the angular and spatial discretisation were set properly.

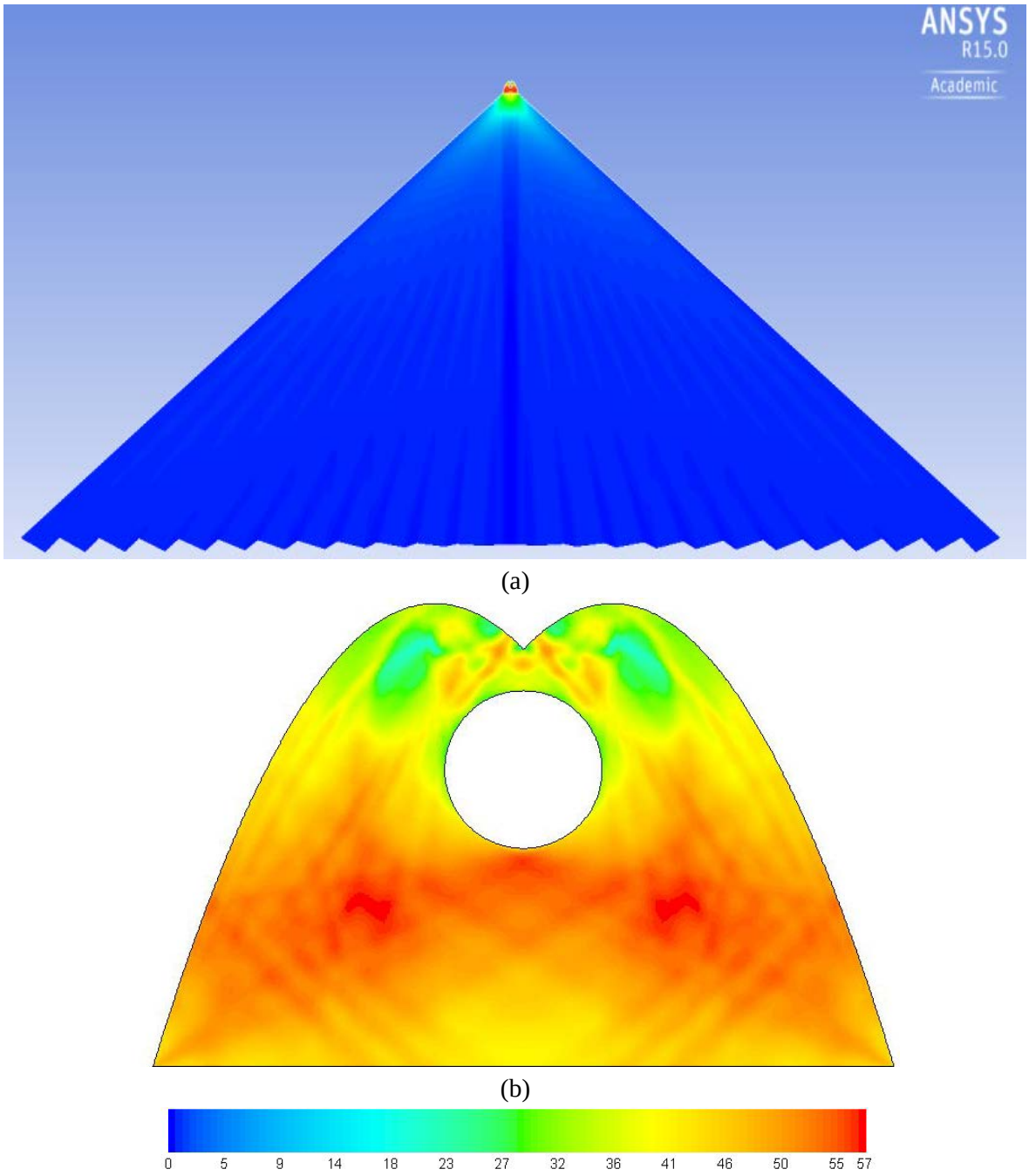

Figure 3.12. Incident radiation contours [suns] of the converged case (477k mesh cells and 3*200 angular discretisation) at noon. 1 sun = 1000W/m^2.

(a) The entire collector. (b) Close-up of the receiver.

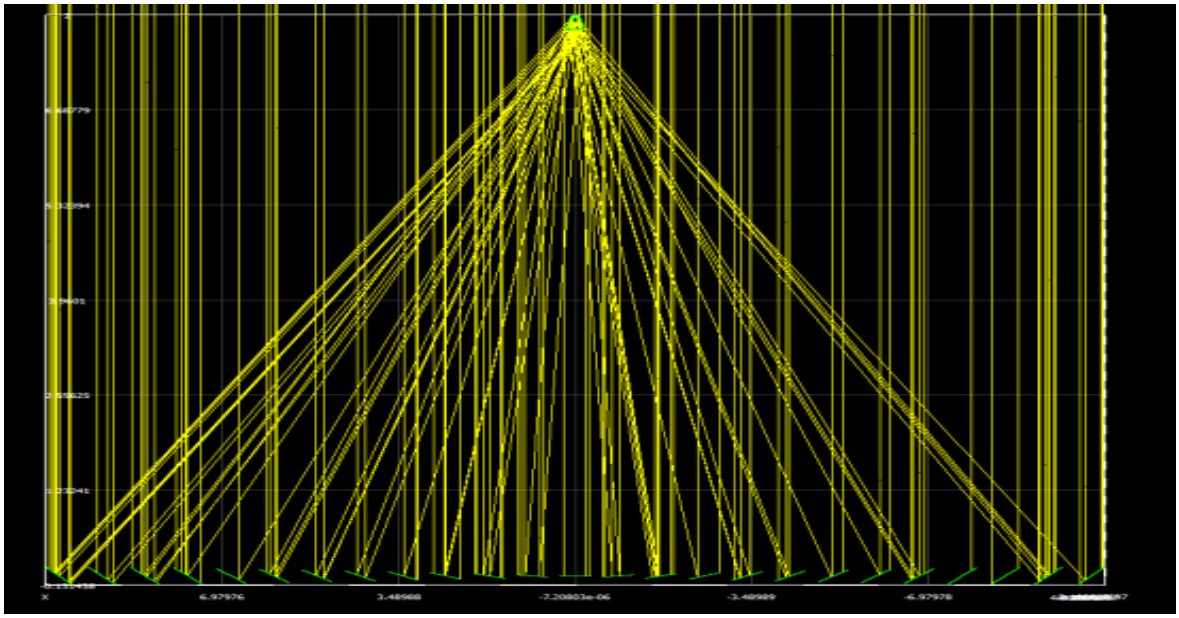

(a)

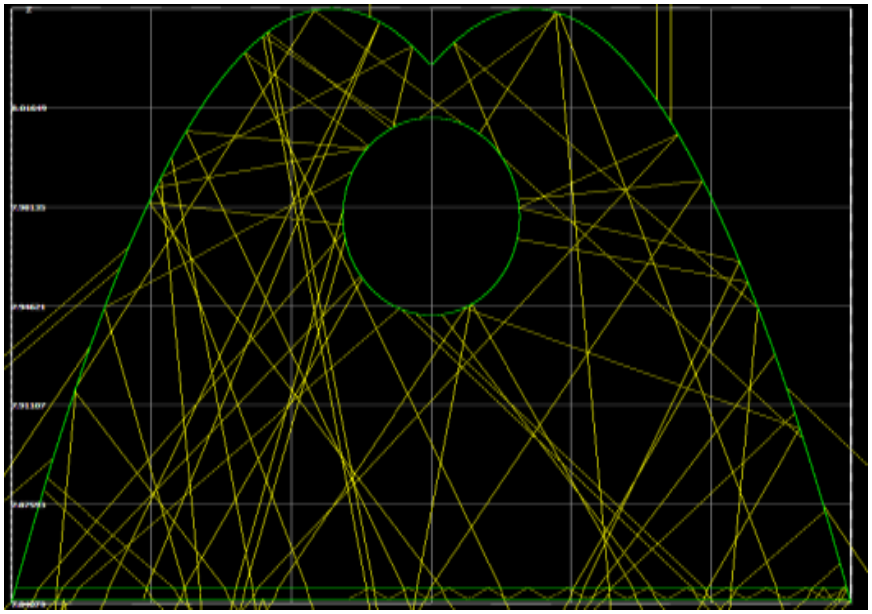

(b)

Figure 3.13. SolTrace results of converged case (1e6 rays) at noon.

(a) Solar field. (b) Cavity close-up.

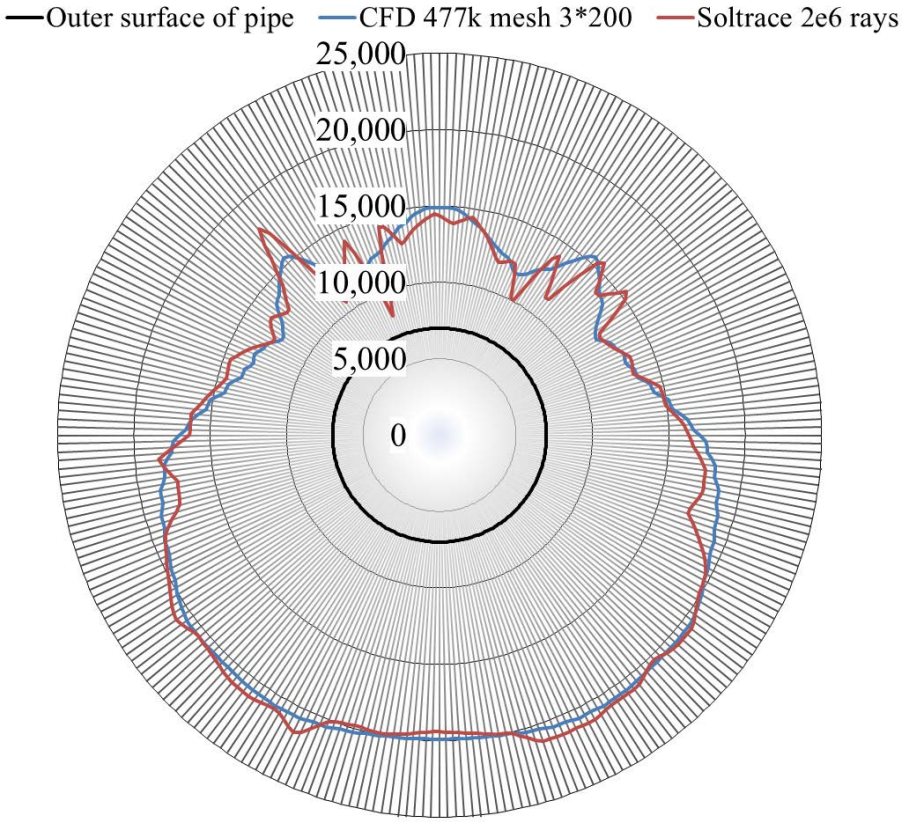

Figure 3.14. Radar plot comparison of heat flux distribution [W/m^2] around the absorber tube obtained by CFD and SolTrace.

Table 3.9 Comparison of ANSYS FLUENT CFD and SolTrace heat flux.

Method	**Area-weighted average of absorbed heat flux on tube [W/m^2]**	**Deviation percentage of CFD result from SolTrace result (%)**
CFD (477k mesh, DO 3×200)	16,772	-3.6
Ray tracing	17,397	0

At last but not least, as a complementary study, effects of the different sunshape options in SolTrace (Gaussian and Pillbox) and ray counts beyond 1 000 000 rays on the circumferential heat flux distribution around the absorber tube are displayed in Figure 3.15. As shown in this figure, the sun shape options do not have a large impact on the result

distributions. In addition, as mentioned before, for ray counts beyond 1 000 000 the distribution remained unchanged.

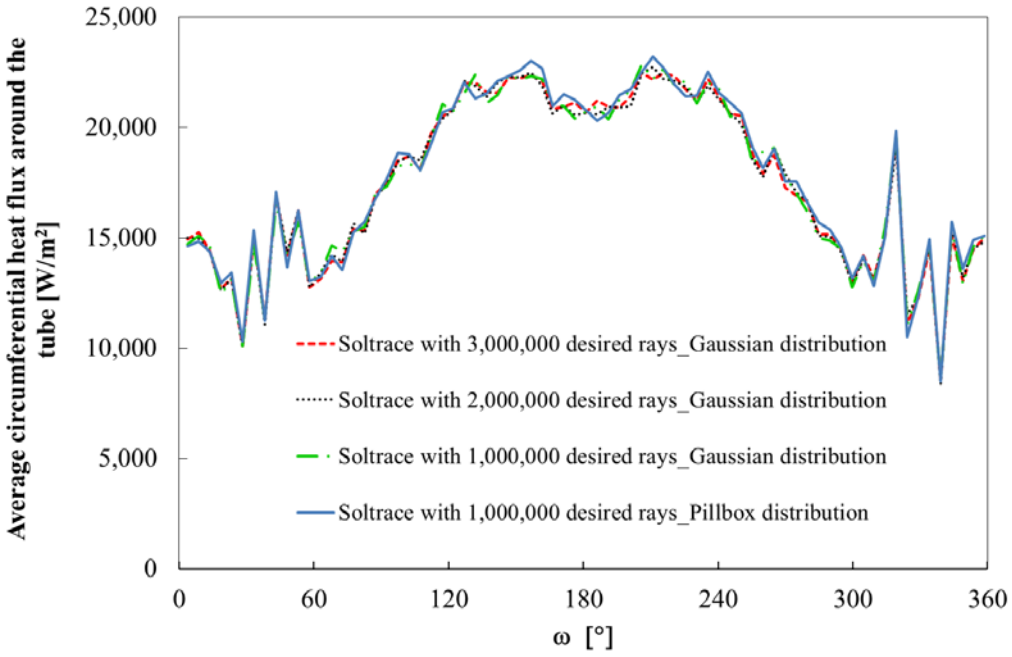

Figure 3.15. Effects of sunshape distributions and raycounts beyond 1 000 000 on the circumferential tube heat flux distributions.

3.7 FURTHER DISCUSSION OF ADVANTAGES AND DISADVANTAGES OF RAY TRACING USING CFD VERSUS MONTE CARLO FOR OPTIMISATION STUDY

1. Traditionally, MCRT is used for calculation of optical performance and then with the help of additional scripting and processing, the MCRT data are extracted and patched in thermal simulation domain. When using a single environment, this processing step is eliminated. The simulation of optical performances in the ANSYS Fluent is integrated into the same software environment as the conjugate heat transfer simulation. This integration helps to patch the non-uniform solar heat flux load onto the conjugated heat transfer thermal model and determine the heat transfer to the HTF as well as cavity thermal losses without extra coding and cumbersome

MCRT data processing for patching (see Addendum V for a patching sample test case).

2. The simulation of the optical performance in ANSYS Fluent provides a single simulation-optimisation environment where the parameterised model can be fully integrated. This integration helps in the calculation of the optical and thermal performances as they are conducted in one engineering tool. This property facilitates the simulation-based optimisation process and could be useful for a single-objective optimisation or optimisation processes with a small number of independent parameters.

3. The post-processing of ray tracing in CFD aids in the development of improved receiver designs and could be useful in topology optimisation of the receiver. Two of the informative post-processing CFD results could be: the solution of incident radiation contours and iso-surfaces of incident radiation contours. The solution of incident radiation contours provides useful information in the improvement of the receiver designs. As an example, an interpretation of Figure 3.12b shows that the absorber tube is located too high as the maximum incident radiation contour is situated below it. The plotting of iso-surfaces of incident radiation contours provides a visual representation of concentration ratio that could, for example, aid in the optimal design of an absorber geometry that would have a uniform radiation distribution. As an example, consider Figure 3.16 where contours of iso-values of incident radiation for the complementary LFC test case study (Section 3.6) are plotted. The dashed rectangle is located in a region of fairly constant and high concentration. Its size is chosen to have the same surface area as the circular tube.

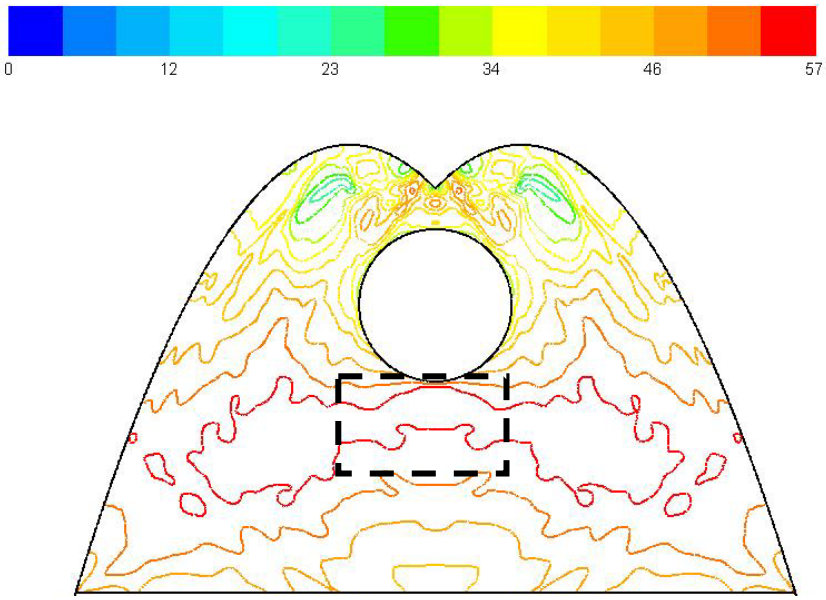

Figure 3.16. Iso-values of incident radiation [suns] - the second LFC test case. 1 sun = 1000W/m^2.

4. Another advantage of ray tracing in CFD is the accurate capturing of the complex treatment in media. For example, the treatment of scattering semi-transparent media (like falling particle receivers) can easily be implemented using CFD. In addition, band-selective coatings and surface radiative properties can easily be incorporated into the DO method using a multiple band or wavelength approach. As shown later, this approach can also incorporate the wavelength-dependent absorption of a glass cover to simulate the greenhouse effect afforded by covering a CSP receiver with a glass window. Therefore, if the optimisation study focuses on one of the complicated media treatments (e.g. band-selective coating optimisation), the author suggests optimisation being conducted with the help of ray tracing in CFD FV.

5. The main disadvantage of ray tracing in CFD is its cost compared with the MCRT method. This cost not only includes having a considerable memory budget but also requires long solution times when compared with MCRT. Associated with this cost is the cost of conducting a mesh refinement and DO discretisation refinement study to determine the combination of these two factors in limiting the ray effect and false scattering errors for a specified accuracy.

3.8 CONCLUSION

The following conclusions can be made based on the work presented in this chapter:

- Within the realm of thermoflow simulations, the accuracy of the CFD solution is determined exclusively by whether the mesh is fine enough, whereas for radiation modelling, both the mesh and DO settings' refinement affect the solution. The model requirements can be determined through the mesh and DO independence studies.

- Modelling radiation accurately either for simple or complex geometry in a CFD environment can be achieved by reducing the numerical errors associated with finite volume solvers. The errors associated with ray effects can be reduced by increasing the control angle count of the model in the phi direction (N_ϕ), while the errors associated with false scattering can be reduced by increasing the spatial mesh count or using a higher-order DO model. It should be noted that these error reduction strategies should be used in conjunction for the most accurate results.

- The user has to choose either CFD or Monte Carlo as the engineering ray-tracing approach to the optimisation process depending on the optimisation study goals, namely the ability of CFD and Monte Carlo in capturing these goals, the advantage of using one single simulation-optimisation environment, the required computational efforts for optical simulation in each of these tools (solution time, memory budget and the convergence study cost) and finally, the expensiveness of the optimisation itself (having an extensive list of objective and independent parameters for optimisation which its effects will be discussed later).

- The future readers have to consider that the focus of this chapter was on the methodology and possible approaches for the optical simulations. The results of this chapter are based on ideal assumptions as listed in Table 3.2. The presented circumferential heat flux distributions and values would be impacted by

consideration of the physical or realistic assumptions for the mirror field, e.g., primary mirror propertes, sun shape, DNI value, etc.

4 THERMAL MODELLING

4.1 INTRODUCTION

In general, an LFC plant is based on an array of linear mirrors that concentrate solar rays on a fixed receiver which contains tube absorber/s. The tubes contain a specific working heat transfer fluid (HTF), which is heated by absorbing solar energy. In the current implementation, a glass cover is situated at the aperture to act both as a barrier to heat losses due to external wind conditions, while enhancing the greenhouse effect to trap heat in the cavity. The energy that is absorbed by the HTF is applied to power generation. Any transfer of energy to an HTF is associated with losses, with thermal losses being the focus of this section.

The successful optimisation study of a plant directly depends on accurate calculation of these heat losses (thermal simulation of a plant) with fairly reasonable computational effort. In this regard, two evaluation approaches are discussed in this chapter: CFD and the view area approach. The first one has been widely used by previous researchers; however, to improve its accuracy, the author suggests some new assumptions and methods that have not been implemented before, to the best of the author's knowledge. In addition, the second approach is an alternative method suggested by the author to conduct thermal simulation with reasonable accuracy and computational effort.

In this chapter, a sample test case is simulated by both of these approaches to validate the assumptions of the methods. In addition, the accuracy and effectiveness of these methods for implementation in an optimisation study are discussed to provide a better perspective of the advantages and disadvantages of each approach to the thermal simulation of a plant. The considered test case in this chapter is the proposed multi-tube cavity receiver of Section 3.2 (see the cavity in Figure 3.1).

Before further discussion of the heat loss calculation approach, reading Addendum VII will provide a profound insight into the available heat transfer mechanism in a cavity and will help to understand these current treatments.

4.2 CFD APPROACH

To thermally optimise an LFC cavity receiver based on CFD simulations, one has to simulate the thermal model accurately in CFD as well as conjugating the CFD code with optimisation tools.

With regard to conjugating CFD codes with an optimisation tool, ANSYS created a platform which allows researchers and designers to use its commercial CFD codes in conjunction with response surface-based optimisation tools (DesignXplorer (DX)) within their WorkBench (WB) environment. Parameters for the geometry are defined in the Design Modeler module of WorkBench. This study uses the ANSYS platform for both CFD modelling and optimisation. However, thermal optimisation without accurate CFD simulation of the LFC plant is impossible. In the following sections, the CFD method and the approaches in accurately capturing the results of an LFC test case (discussed in Section 3.2) are explained in more detail. This study first presents the CFD assumptions and mathematical formulation of the test case. This is followed by the mesh generation, material and boundary conditions, and the settings used for ANSYS Fluent. Finally, the validation section evaluates the CFD results and proposed assumptions of the discussed problem.

4.2.1 CFD assumptions

The cavity is defined as a symmetrical quadrilateral shape containing four HTF tubes (see Figure 3.1). Based on an overall heat balance in a steady-state condition, the heat absorbed in the cavity equals the heat released in the cavity. Like previous researchers (Facão & Oliveira, 2011; Häberle et al., 2002; Heimsath et al., 2014; Lai et al., 2013; Pye, 2008; Sahoo et al., 2012; 2013a; 2013b) who considered a constant temperature on the outer walls of the HTF pipes, the effect of solar irradiation on the tube outer surfaces is modelled by a constant temperature on the outer surface of the pipes. However, the accuracy of this

assumption was not checked in those studies, but it will be in the validation section of this chapter.

Inside the cavity domain, the natural convection mechanism is driven by the temperature differences between HTF tube walls and cavity walls. To capture this phenomenon inside the cavity, previous researchers (Facão & Oliveira, 2011; Lai et al., 2013; Pye et al., 2003a, 2003b; 2003c; 2008; Sahoo et al., 2012; 2013a) used the relatively simple Boussinesq approximation. As discussed in the literature review chapter, this assumption cannot be accurate for the LFC domain because CSP cavities often experience large temperature differences. Therefore, the incompressible ideal gas assumption is suggested as a more applicable assumption, as will be shown.

To properly capture the greenhouse effect, inside cavity dual bands are defined based on typical glass absorption band definitions as 0-4.25 μm and beyond 4.25 μm (Dhall et al., 2009). This definition will be explained in detail in Section 4.2.4. The Dhall et al. (2009) study is based on quartz glass which may be too costly for the current application, hence it may be more recommendable to use low-iron soda-lime glass, which has similar optical properties to quartz glass. The dual non-grey band definition also captures specular and diffuse reflections of cavity surfaces (for more information see Addendum III), which are novel aspects of this work. In the study, all opaque surfaces inside the cavity receiver are considered to reflect diffusely in the short-wavelength band and specularly in the long-wavelength band. The glass surface is considered to be highly polished with a negligible surface roughness (RMS ~0) (Mellott et al., 2001) and hence specular reflection is prescribed on the glass walls for the whole wavelength domain.

The resulting thermal re-radiation and natural convection (collectively called conjugate heat transfer), as well as other transport phenomena (discussed in Addendum VII) are, however, calculated with the help of the discussed CFD model in the following sections.

4.2.2 **Conservation equations**

The LFC cavity was simulated in ANSYS Fluent 15 by considering the following assumptions. The two-dimensional model of the cavity is in a steady-state condition and the tube outer surfaces are considered to be at a constant temperature. The two-dimensional model also implies that secondary flows along the length of the plant are ignored in this study. Moreover, the cavity is filled with air of which the viscosity, heat capacity and thermal conductivity are temperature dependent as defined based on Lienhards' table (Lienhard IV & Lienhard V, 2003). The fluid is considered to be Newtonian and laminar. The laminar assumption is justified based on the results presented in Chapter 4 and 5 (Figure 4.5 and Figure 5.14) where an estimate of the Reynolds number for the maximum velocity cases are in the order of a few hundreds. The no-slip boundary condition for the momentum equation is considered at walls adjacent to the fluid domain. To capture natural convection inside the cavity, the density of air is modelled as an incompressible ideal gas where pressure variation is assumed to be insignificant compared with temperature variation. Due to definitions of the heat transfer mechanisms (Addendum VII), almost all energy boundary conditions are considered as coupled. Therefore, by considering the above-mentioned assumptions, the transport equations for the fluid flow that are solved on each computational cell or control volume in the mesh are as follows:

$$\frac{\partial(\rho u)}{\partial x}+\frac{\partial(\rho v)}{\partial y}=0 \tag{4.1}$$

$$\frac{\partial\left(\rho u^{2}\right)}{\partial x}+\frac{\partial(\rho uv)}{\partial y}=-\frac{\partial(P)}{\partial x}+\frac{\partial}{\partial x}\left(\mu\frac{\partial u}{\partial x}\right)+\frac{\partial}{\partial y}\left(\mu\frac{\partial u}{\partial y}\right) \tag{4.2}$$

$$\frac{\partial(\rho uv)}{\partial x}+\frac{\partial\left(\rho v^{2}\right)}{\partial y}=-\frac{\partial(P)}{\partial y}+\frac{\partial}{\partial x}\left(\mu\frac{\partial v}{\partial x}\right)+\frac{\partial}{\partial y}\left(\mu\frac{\partial v}{\partial y}\right)-g\left(\rho-\rho_{0}\right) \tag{4.3}$$

$$u\frac{\partial\left(\rho c_{p}T\right)}{\partial x}+v\frac{\partial\left(\rho c_{p}T\right)}{\partial y}=\frac{\partial}{\partial x}\left(k\frac{\partial T}{\partial x}\right)+\frac{\partial}{\partial y}\left(k\frac{\partial T}{\partial y}\right)+Q_{radiation} \tag{4.4}$$

where the last term in Equation (4.3) is the body-force term, while the last term in Equation (4.4) is the volumetric heat source, which is generated by radiation. x and y are the two-dimensional axis directions, ρ the density, P the pressure, u and v the velocity

components, μ the dynamic viscosity, c_p the heat capacity at constant pressure, g the gravitational constant, T the temperature and k the thermal conductivity. ρ_0 is a reference density. ANSYS Fluent defines ρ for the incompressible ideal gas assumption as the following function of temperature:

$$\rho = \frac{P_{operation}}{\frac{R}{M_w}} \times \frac{1}{T} \tag{4.5}$$

where $P_{operation}$ is the operating pressure, R is the universal gas constant and M_w the molecular weight of the gas. When using the incompressible ideal gas assumption for natural convection, one should check after the fact that the pressure variation inside the domain is insignificant in comparison with temperature variation. This check is described in later sections.

For solving the transport phenomena equations (Equations (4.1)-(4.4)), the term $Q_{radiation}$ must be determined with the help of the radiative transfer equation (RTE), where the definition of the dual non-grey bands has been implemented in the RTE. For more information on the mathematical formulation of RTE and the radiative boundary condition, check Addendum II and Addendum III.

4.2.3 **Mesh generation**

The test case geometry dimensions were determined based on the selected data of the previous multi-tube test case as summarised in Table 3.1. Note that the test case geometry in this study was modelled in its entirety, i.e. symmetry is not used.

The meshing package of ANSYS WB 15 was used to generate the mesh. A triangular mesh with different face sizing elements in each zone was selected for the geometry. The insulation zones, internal cavity domain and glass zone were paved with 0.012, 0.007 and 0.005m triangular element sizes respectively. To provide more freedom for automatic mesh generation during the optimisation process, the behaviour of these face size elements was set to “Soft”. CFD, Fluent and 100 were selected as “Physics Preferences”, “Solver Preference” and “Relevance” in the meshing tools. To ensure a smoother mesh with cells

concentrated around the tubes and near the cavity walls (due to the high gradients expected in those areas), the “Relevance Centre” and “Smoothing” settings were selected as fine, and the “Curvature Normal Angle” and “Growth Rate” were set at 7° and 1.05 respectively. Figure 4.1 depicts the mesh generated for the computational domain. The zoomed-in plot in Figure 4.1b illustrates the mesh concentration around the tubes.

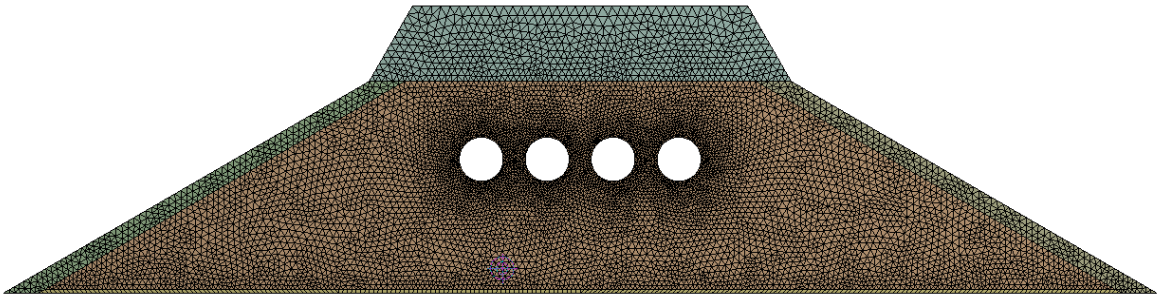

(a)

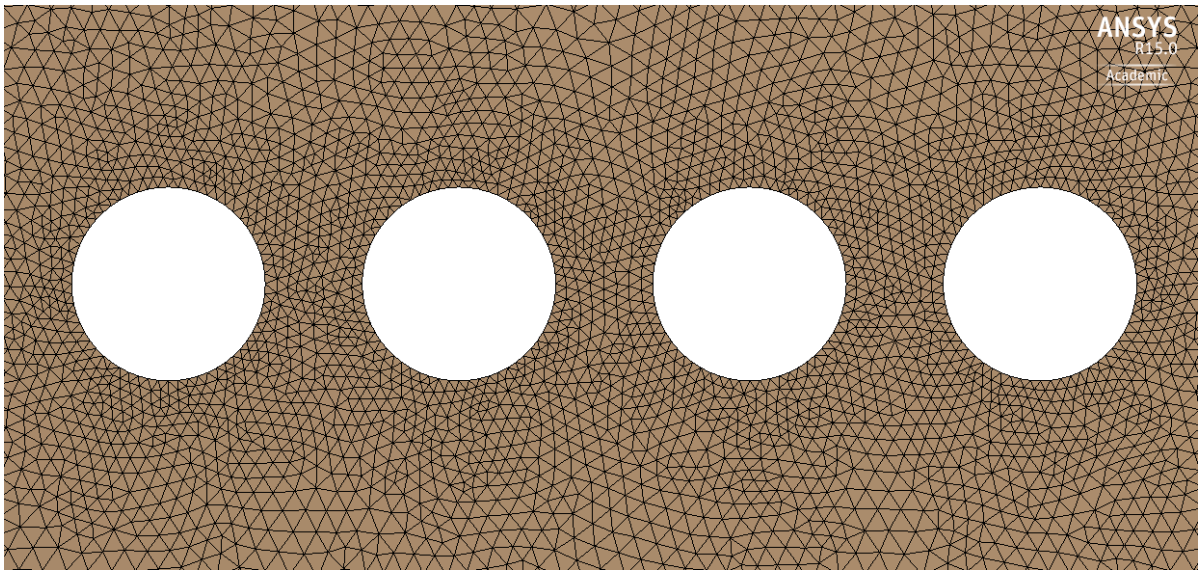

(b)

Figure 4.1. Generated mesh in the test case.

(a) Entire zone mesh. (b) Zoomed-in mesh around tubes in the cavity.

A total of 16 359 elements were generated in the computational domain. Since poor mesh quality might produce problems in convergence and influence the accuracy of the results, the skewness and aspect ratio of the mesh were checked inside the computational domain.

According to Bakker (2013), the skewness should not exceed 0.85 and the local variations in cell size should be minimised, and adjacent cells should not have size ratio greater than 1.2 for a high triangular mesh quality. For the proposed problem, the maximum skewness and minimum skewness of elements in the whole domain were 0.5698 and 1.3 e-6 respectively, with an average value of 5.7 e-2. The maximum and minimum aspect ratios of elements in the entire domain were 1.0008 and 2.5203 respectively, with the average value of 1.1895. In general, the average element quality in the entire domain was 0.9588, which provided an excellent mesh quality for the computational domain.

4.2.4 Material properties and boundary conditions

The material properties are defined in Table 4.1. As mentioned before, glass is modelled to be opaque in the high-wavelength band. According to Dhall et al. (2009), when using the Beer-Lambert law for a 3.25mm glass thickness, the glass absorption coefficient values should be converted to 29% and 99% absorption of wavelengths below and above $4.25\,\mu m$.

For the outer surfaces of the cavity, both convective and radiative thermal boundary conditions were applied. Due to the assumption of external forced convection provided by an approaching wind, a constant convective surface heat transfer coefficient was chosen. The top and side walls were assumed to radiate to sky temperature while the lower cavity surface was assumed to radiate to the LFC mirror temperature, assumed to be 5K higher than ambient (Pye, 2008).

The boundary conditions are summarised in Table 4.2. The reader may wonder why such radiative properties were chosen for the tube surfaces. The selective solar coating which is usually implemented on absorber tubes has a low emissivity in the higher wavelength band and a high absorptivity at lower wavelengths. For further information please consult Norton (1992) and Kennedy (2002).

Table 4.1 Material properties.

Material	**Density [kg/m^3]**	**Specific heat [J/kg-K]**	**Thermal conductivity [W/m-K]**	**Other**
Air in cavity (Lienhard IV & Lienhard V, 2003)	Incompressible ideal gas	Piecewise linear function of temperature	Piecewise linear function of temperature	Viscosity [Pa.s]: Piecewise linear function of temperature
Tube - carbon steel (Incropera et al., 2006)	7818	670	54	-
Semi-transparent glass (Bansal & Doremus, 1986)	2650	786	1.5	Refractive index = 1.5, absorption coefficient [m^{-1}] = 106; 2300 for wavelength below and above 4.25μm (Dhall et al., 2009)
Insulation - glass wool (TIASA, 2001)	48	446	Piecewise linear function of temperature	-

Table 4.2 Boundary conditions.

Surface	Velocity components [m/s]	Temperature [K]	Heat transfer coefficient [W/m^2-K]	Emissivity
Tube outer side	0, 0	500	-	0.95 in lower wavelength band and 0.1 in higher wavelength band. The cut-off wavelength is 4.25μm.
Top, side walls	0, 0	-	-	0.05
Glass inner side	0, 0	-	-	0.9 (Pye, 2008)
Glass outer side	-	300 (conv), 305 (rad)	5	0.75
Insulation outer side	-	300 (conv), T_{sky}=0.0522* 300$^{1.5}$ (rad) (Guo et al., 2014)	5	0.75

4.2.5 **CFD model settings**

A 2-D model was simulated in ANSYS WB 15 (ANSYS, 2013b). Radiation was modelled using the discrete ordinates method. All emitted (re-)radiation was assumed to be diffuse. Each polar (θ) and azimuthal (ϕ) angle was divided into 3 and 10 divisions as control angles with three subdivisions (pixels) for each angular discretisation respectively. These settings were chosen after an angular discretisation independence study, which for the sake of brevity, isnot provided here.

The CFD settings strategy included using the SIMPLE algorithm for the first 400 iterations and then switching on the Pressure-Based Coupled Solver with Pseudo-Transient activation for pressure-velocity coupling and solving for 3 000 iterations. Then, after a

boundary adaptation was implemented using a normal distance of 0.2m from all pipe surfaces in the cavity domain, 2 500 iterations were solved. Finally, after another adaptation in the same region, a final 1 500 iterations were run. The spatial discretisation of the equations for pressure, momentum, energy and discrete ordinates was chosen as PRESTO, second-order upwind, second-order upwind, and first-order upwind, respectively. This setting strategy led to convergence of the test case by damping all instability in the solution of this case due to natural convection, radiation and other factors inherent.

4.2.6 **Validation**

Due to the novelty of using the incompressible ideal gas assumption for the solution of the temperature-dependent variation of density, the accuracy of this assumption was tested. The requirement for accuracy when modelling naturally convective flow is that the pressure variation should be insignificant when compared with temperature variation.

The contours of static pressure and temperature in the test case for a tube outer-surface temperature of 500 K with an ambient temperature of 300 K are displayed in Figure 4.2.

It can be seen that the static pressure varies from -0.097 to 0.1 Pascal, while temperature field varies from 290 K to 500 K. This small variation in pressure as a result of the much larger temperature variation, confirms that the incompressible ideal gas assumption is valid.

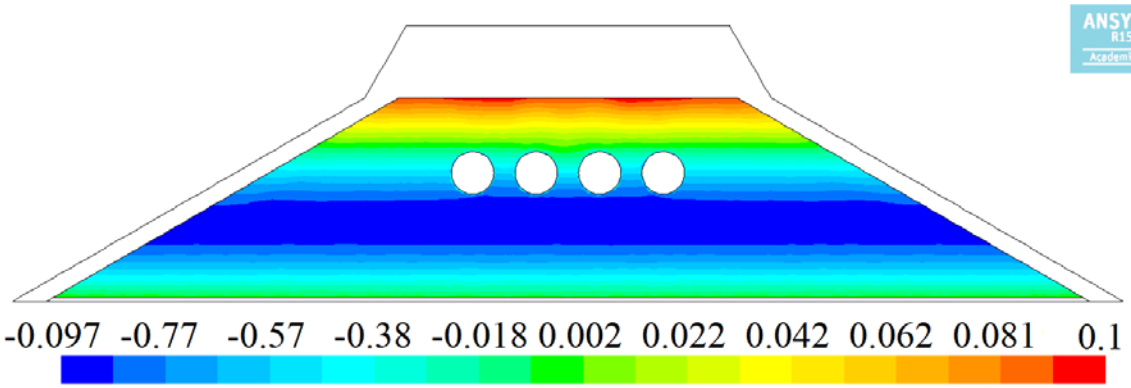

(a)

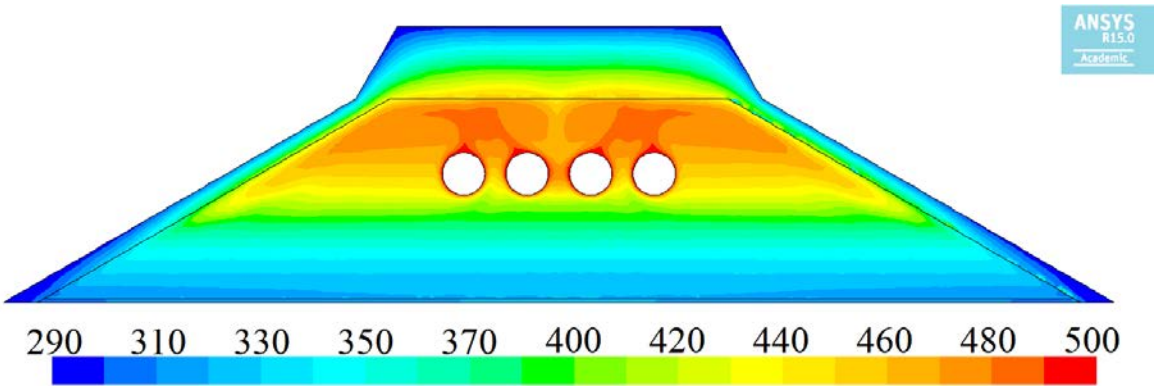

(b)

Figure 4.2. Contours inside the cavity and in insulation for 500 K tube outer-surface temperature and 300K ambient temperature for test case geometry.

(a) Static pressure. (b) Static temperature.

After getting the assurance of the validation of the incompressible ideal gas assumption in the cavity receiver, a code-to-code validation case was done to survey the accuracy of the constant temperature assumption on the outer wall of the tube. The accuracy of this assumption for an LFC cavity receiver, has not been investigated, to the best of the author's knowledge, to determine how far it deviates from a realistic situation (which has a non-uniform solar heat flux load on the outer surface of tubes). Of particular interest is how such an assumption would affect the calculation of heat losses from the external boundaries and how it would influence the fluid pattern in the cavity domain. Therefore, in this section of the study, the accuracy of this assumption is investigated for this case study. However, future researchers must consider that validation of the present case study does not validate this assumption in general. Hence, it is recommended to validate this assumption for their cases, before implementing it in their studies.

For the investigation, the results of a 3-D simulation domain with a non-uniform solar heat flux load on the tubes (taken from SolTrace simulation in Section 3.3) are compared with the results of a 2-D model with an equivalent constant tube bundle temperature (constant heat flux). More detailed information about the precise procedure for mapping non-

uniform heat flux loads on tubes in the 3-D simulation is provided in Addendum V or Moghimi et al. (2015d). The cavity domain in the 3-D model is a 1cm extrusion of the 2-D model in the *z*-direction that now includes the tube thickness as well as the HTF inside the tubes. The HTF inside the tubes is assumed to be turbulent with fully developed inlet profiles as defined by a User-Defined Function (UDF) (see Addendum VI).

Figure 4.3 displays the radar plots of the non-uniform heat flux distributions in SolTrace (calculated in the previous study – Section 3.3) on the two tubes in the right half of the cavity shown in Figure 3.1. The 3-D conjugate heat transfer domain in ANSYS Meshing is shown in Figure 4.4a and the mapped non-uniform solar flux as imposed on the tubes in ANSYS Fluent is shown in Figure 4.4b. The region with a highly dense mesh includes HTF zones, tube and surrounding of tubes in the cavity receiver in Figure 4.4a. The correspondence between the distributions in Figure 4.3 and the contour colours in Figure 4.4b is clear.

A comparison between the temperature and velocity field in the cavity as obtained by the current 2-D test case simulation and the comparative 3-D simulation with a SolTrace distribution is depicted in Figure 4.5.

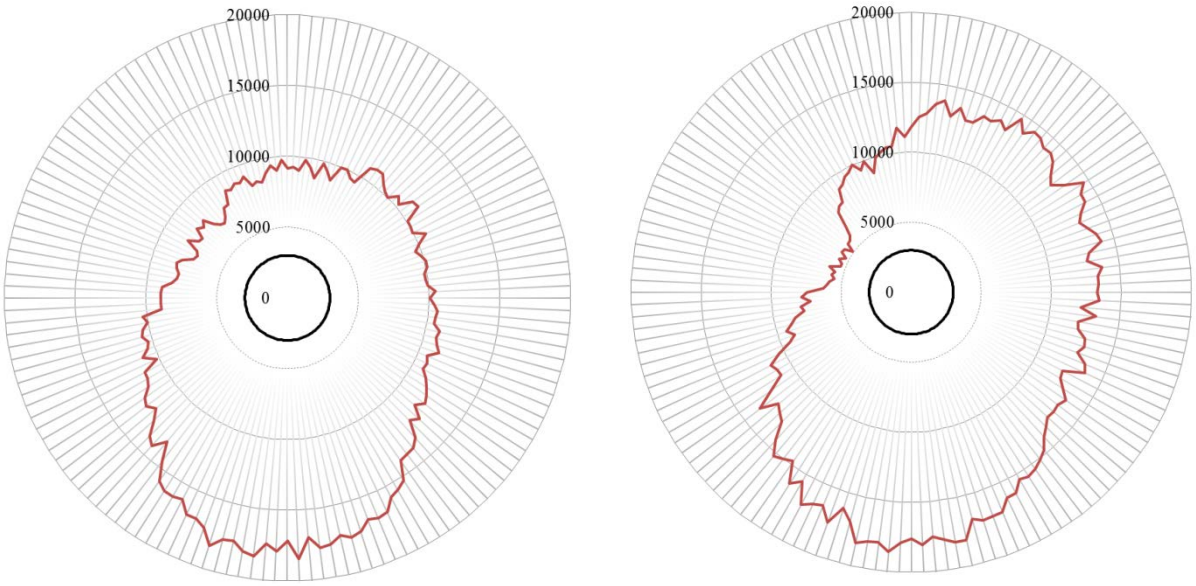

(a) (b)

Figure 4.3. Non-uniform solar heat flux distribution as calculated by SolTrace on tubes in W/m^2. (These results were taken from SolTrace optical study in Section 3.3.)

(a) 3rd tube from the left. (b) 4th tube from the left.

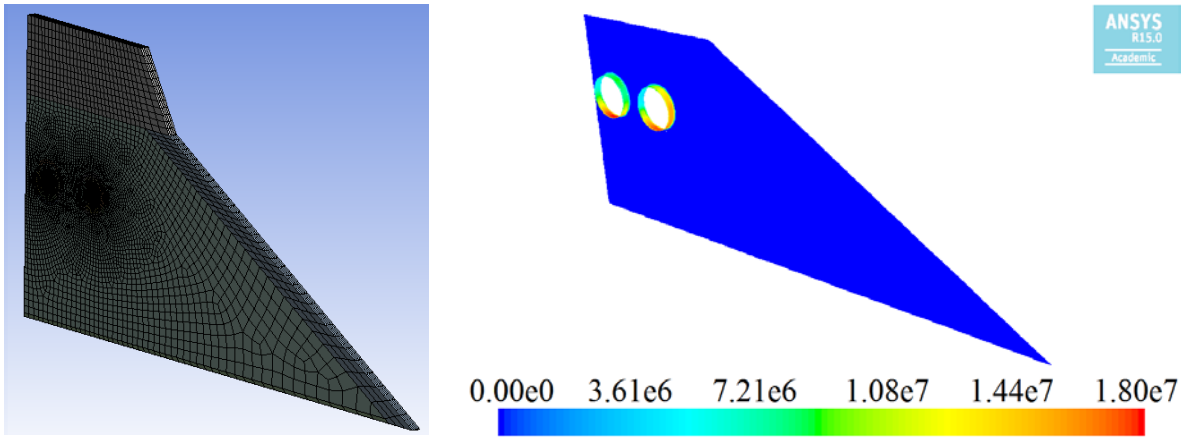

(a) (b)

Figure 4.4. (a) 3-D CFD cavity domain with mesh. (b) Mapped non-uniform solar heat flux [W/m^3] as volumetric heat load on the tubes of cavity receiver in ANSYS Fluent.

Figure 4.5 shows temperature contours overlaid with velocity vectors for the 3-D with HTF model (at the mid-cross-sectional plane) and the current 2-D test case. Good qualitative agreement is evident, especially in the natural convection plume formation. For the test geometry, it can be seen that natural convection plays a significant role because of the convection of hot air from the tube surfaces towards the upper insulation. As indicated in the figure heading, the minimum and maximum velocity magnitude values due to natural convection are very similar between the two simulations, further confirming the good agreement. The tube outside surface temperature obtained in the 3-D model is compared with the uniform temperature specified in the 2-D case in the insert in Figure 4.5a. The effect of the non-uniform heat flux distribution clearly results in a similarly shaped non-uniform temperature distribution with deviations in the order of 2 to 3K. The average outside surface temperature of 500K for the 3-D case (to be comparable with the specified 2-D value of 500K) was achieved by a trial-and-error procedure by varying the bulk inlet HTF temperature with a converged value of 492K. The heat loss values (indicated in Figure 4.5a and Figure 4.5b and also summarised in Table 4.3) confirm that there is an excellent agreement between the two models with the total heat loss differing by less than 1%. This implies that at these temperatures, the uneven distribution of heat flux does not play a significant role in the thermal performance of the cavity for this case study. In other words, the constant temperature assumption on the outer wall of the tube could be a valid assumption for thermal modelling of the LFC cavity receiver of this case study. Note that the 3-D heat loss values are scaled by 200 for a direct comparison (2x because of the half symmetry and 100x to compensate for the 1cm length of the pipes because 2-D results are reported per metre or 100cm).

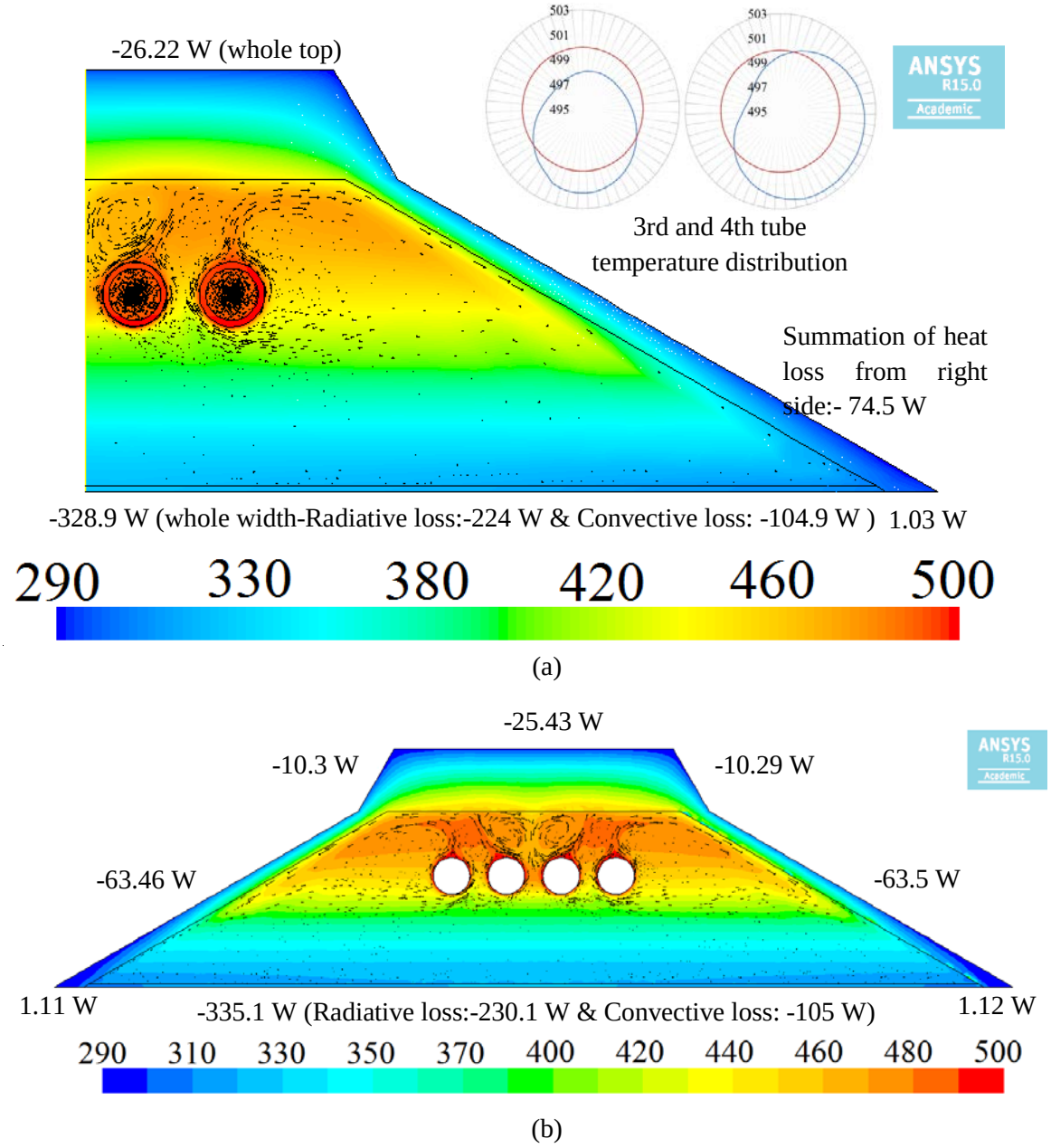

Figure 4.5. Temperature contours [K] overlaid with velocity vectors and heat losses and gains from external boundaries.

(a) On the mid-plane of 3-D case; Maximum velocity (midplane of 3-D domain) = 0.15 m/s, minimum velocity = 3.6e -5 m/s. Insert showing the deviation of the non-uniform (blue) temperature distribution from a uniform (red) distribution around the two tubes shown. (b) 2-D test case; Maximum velocity = 0.15 m/s, minimum velocity = 1.9e -5 m/s.

Table 4.3 Heat loss comparison from external boundaries for 2-D and 3-D cases [W].

Surfaces	**2-D sample case (per metre)**	**3-D case (*200)**
Glass	-335.1	-328.9
Insulation bottom surfaces (right and left sides)	2.232	2.062
Insulation side surfaces (right and left sides)	-147.6	-149.1
Insulation top surface	-25.46	-26.22
Total heat loss	-505.9	-502.2

To conclude the validation section, a comparison is made with the correlation for heat loss provided by previous researchers. In this validation, the published experimental heat loss coefficient power-law correlations were compared with the CFD model results. The heat loss coefficient (U_L) is one of the thermal performance indices of a cavity receiver. According to Flores Larsen et al. (2012), the empirical correlation of U_L for a cavity receiver should follow a power-law relation with respect to the area of all tubes, A_p, and the difference between the average of all the tubes' outside wall temperatures at their lowest points facing the incoming irradiation, T_p, and the ambient temperature, T_a. Therefore, according to Flores Larsen et al. (2012), U_L is defined as:

$$U_L = \frac{Q_{loss}}{A_p (T_p - T_a)} \tag{4.6}$$

and

$$U_L = x(T_p - T_a)^y \tag{4.7}$$

where x and y are constants. Such a power-law concept was widely used by different researchers (Facão & Oliveira, 2011; Flores Larsen et al., 2012; Khan et al., 1999; Manikumar & Valan Arasu, 2014a; Natarajan et al., 2012; Negi et al., 1989; Singh et al. 2010a; 2010b) and is motivated by the observation that the losses would significantly increase with temperature. A summary of power-law correlations found in the literature for

a single glass cover trapezoidal cavity is presented in Table 4.4 and compared with the current test case solved for seven different tube outside temperatures (350, 375, 400, 425, 450, 475 and 500 K). The corresponding heat loss coefficient is plotted in Figure 4.6 against the temperature difference with a power law fitted. A similar result for x and y in Equation (4.7) to the result by other researchers is found (see Table 4.4), but it can be seen from the simulated values that a power-law fit is not necessarily the best fit. Considering, for example, a cubic curve fit, regression coefficient value of 1 is obtained. The last one good performance is interesting because it can have a physical reason. If most of the energy is dissipated through radiation (as confirmed by the relative heat loss values in Figure 4.5), then the heat loss is expected to be a quartic function of the temperatures: $Q_{loss} = f\left(T_p^4 - T_a^4\right)$, and thus based on Equation (4.6), the heat loss coefficient is a cubic function of pipe and ambient temperature $U_L = f\left(T_p^3, T_a^3, combination\ of\ lower\ orders\right)$. A cubic polynomial fit is also shown in Figure 4.6 and should be considered for future comparison.

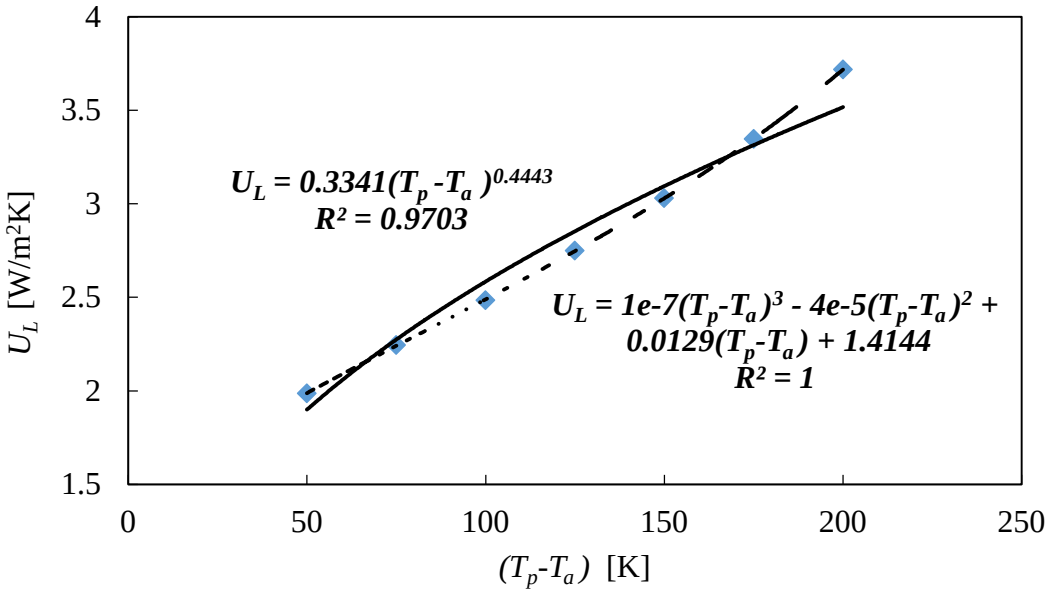

Figure 4.6. Heat loss coefficient variation and power-law and cubic polynomial fits for sample case geometry.

Table 4.4 Power-law relations in this paper and previous researches.

Researchers	Power-law relation	Regression coefficient	Restriction
This study	$U_L = 0.3341(T_p - T_a)^{0.4443}$	0.9703	$350K < T_p < 500K$
Flores Larsen et al. (2012)	$U_L = 0.357(T_p - T_a)^{0.5184}$	0.8862	$110^\circ C < T_p < 285^\circ C$
Manikumar & Valan Arasu (2014a)	$U_L = 0.37(T_s)^{0.58}$	0.99	In Manikumar & Valan Arasu (2014a), T_s is absorber temperature in $^\circ C$, and the valid range is $95^\circ C \le T_s \le 145^\circ C$. This relation is for absorbers with black chrome coating.
	$U_L = 0.37(T_s)^{0.62}$	0.99	This relation is for absorbers without coating.
Singh et al. (2010a)	$U_L = 0.5805(T_{abs})^{0.4903}$	----	In Singh et al. (2010a), T_{abs} is absorber temperature in $^\circ C$, and the valid range is $50^\circ C \le T_{abs} \le 250^\circ C$. This relation is for a round tube absorber covered with ordinary black paint.
	$U_L = 0.5637(T_{abs})^{0.4456}$	----	This relation is for a round tube absorber covered with a selective surface coating.

This study proves that CFD simulation was accurately simulated and can be applied as an engineering tool to a thermal optimisation study.

4.3 VIEW AREA

The second thermal approach which is suggested in this section and which could be useful for the thermal optimisation of a cavity receiver as a low fidelity approach, is view area. The fact should be considered that calculating heat loss via the view area approach is not as accurate as the CFD approach (the discussed method in Section 4.2), due to simplified assumptions which are discussed later. However, this method can be a very useful tool in speeding up the expensive process of optimisation and saving huge computational costs and resources.

To justify this approach, consider the response surface method (RSM) – the optimisation process followed in Chapter 5. To capture an accurate response surface, the optimisation process needs an adequate number of design points, which are generated via numerical algorithms. Then, for each individual design point, the goals have to be modelled and calculated via their corresponding tools. Now assume that for the collector optimisation process, heat loss is calculated via CFD tools. As will be explained later, for collector domain optimisation (see Section 5.4.1), more than 1 800 design points are needed. Assuming one hour as the computational time required for each CFD simulation, the calculation of heat loss goal (thermal goal) alone would take more than two and half months, without considering the computational cost to calculate other objectives (economic and optical goals) and the optimisation process. Therefore, introducing a low fidelity approach to tackle the heat loss calculation with acceptable accuracy is justified in the optimisation process.

The researchers should consider that even if an optimisation process is being conducted based on a low fidelity approach, a complementary study has to be conducted on the optimum case to calculate the realistic values of those objective goals which were predicted by the low fidelity approaches. Hence, in this study after conducting an optimisation process based on view area approach for calculation of heat loss, the final

optimum case has to go through either a CFD simulation (as it was discussed in previous sections) or any high fidelity approaches, to calculate the actual heat losses of the optimum case. This CFD simulation will redress the shortcomings of the view area approach in the prediction of correct heat losses due to its simplified assumptions.

4.3.1 **Mathematical formulation**

The justification for this approach is the assumption that radiation is the most dominant heat loss mechanism as discussed in the literature review chapter. The dominance of radiation mechanism in heat loss from a cavity receiver was explicitly shown in Figure 4.5. Figure 4.5a and b show that in this case study, the amount of radiative losses from the glass, are, respectively 68% and 69% of total dissipated energy from that boundary (glass). In Figure 4.5 the tube surface temperature of 500K is much higher that the average glass surface temperature of 317 K (Figure 4.5a and b).Due to fact that radiation is a quartic function of surface temperature and that the glass temperature is not much higher than the mirror temperature, one can say that most of the cavity heat loss dissipates from the bottom glass as a result of re-radiation from the absorber tubes to the mirror field. Hence it is rational to optimise heat loss by minimising radiative heat loss. Moreover, as a simplified assumption, in this study the radiative absorption of glass was ignored. This simplified assumption means that the dual wavelength-dependent behaviour of the glass toward the incident radiation is ignored in this approach. In other words, this approach assumes that all the radiation inside the cavity can go through the glass and reach to mirror field. In addition, as proved in Section 4.2.6, the thermal simulation of a multi-tube trapezoidal cavity receiver can be conducted with a constant circumferential temperature assumption as the driving thermal source in the cavity. According to Stefan-Boltzmann law the radiation energy from grey bodies is proportional to the fourth power of the absolute temperature of the body and the first power of the emissivity of that body $\left(Q \propto \varepsilon T^4\right)$. Therefore, due to the aforementioned assumptions and the high temperature of tube surfaces in comparison with other cavity walls as well as the high emissivity of tubes compared with low emissivity of other cavity walls, the absorber tubes' temperature and their surface properties are the main drivers of radiation and heat loss in the cavity.

Therefore, as a simplifying assumption, one can assume that minimising the absorber tube areas that face the mirror field (view area of absorber tubes to mirror field) will minimise radiative heat transfer mechanism (cavity thermal loss).

View area is not a novel concept in radiation heat transfer theory. Actually, this concept is taken from view factor, which is a well-known radiative term in heat transfer textbooks. According to Cengel and Ghajar (2010), the view factor is the fraction of radiation leaving surface *i* that strikes surface *j* directly and view area is analogous to this concept. The accuracy of the view area approach can be improved by considering in detail surface to surface radiation exchanges (e.g., between cavity surfaces, insulation surfaces with sky, glass surface with mirror, …) as well considering glass absorption in the analytical calculation. As it will be shown in Figure 4.7**,** this approach is underpredicting the CFD heat loss calculation at 500K by 21% .

The following relationships between parameters have to be defined for the defining view area. See Figure 5.1b by considering an N_t-tube's tube bundle with tube pitch *m*, which is located centrally in the cavity. Then:

$$2p + (N_t - 1) \times m = Aperture\,width \qquad \textbf{(4.8)}$$

where N_t is the number of tubes in the cavity. Therefore:

$$p = 0.5 \times [Aperture\,width - (N_t - 1) \times m] \qquad \textbf{(4.9)}$$

where *p* is the horizontal distance of the first/last tube from the closest cavity's bottom corner. Then the horizontal distance of the i_{th} tube centre from the cavity's left bottom corner ($q^{left}_{i_{th}\,tube}$) is:

$$q^{left}_{i_{th}\,tube} = p + (i-1) \times m \qquad \textbf{(4.10)}$$

where *i* is the tube counter from the left side. Therefore, the distance of the i_{th} tube centre from the cavity's right bottom corner is:

$$q^{right}_{i_{th}\ tube} = Aperture\ width - q^{left}_{i_{th}\ tube} \quad \textbf{(4.11)}$$

In addition, the angle of the tangential line with the tube bundle line is named β. The tangential line is defined as a line that passes through the i_{th} tube centre and coincides with the circumference of the adjacent tube. Since β is a fixed property (due to the fixed tube radius and pitch), its specification is independent of the tube counter:

$$\beta = \sin^{-1}\left(\frac{r}{m}\right) \quad \textbf{(4.12)}$$

For defining the area of a tube that faces the mirror field, one has to consider the constraint factors that confine view area: the proximity to the adjacent tube and the tube centre distance from the left and right corners. Therefore, two central angles for each individual tube are defined ($\alpha^{left}_{i_{th}\ tube}$ and $\alpha^{right}_{i_{th}\ tube}$) to capture the view area. These central angles for the i_{th} tube are:

$$\alpha^{left}_{i_{th}\ tube} = Min\left[\left(\frac{\pi}{2}-\beta\right), \tan^{-1}\left(\frac{q^{left}_{i_{th}\ tube}}{h-d}\right)\right], \text{ except for the left-most tube, which}$$
$$\text{has } \alpha^{left}_{1_{st}\ tube} = \tan^{-1}\left(\frac{q^{left}_{1_{st}\ tube}}{h-d}\right) \text{ where } q^{left}_{1_{st}\ tube} \text{ equals } p \text{ (Equation (4.9))} \quad \textbf{(4.13)}$$

$$\alpha^{right}_{i_{th}\ tube} = Min\left[\left(\frac{\pi}{2}-\beta\right), \tan^{-1}\left(\frac{q^{right}_{i_{th}\ tube}}{h-d}\right)\right], \text{ except for the right-most tube, which}$$
$$\text{has } \alpha^{right}_{N_{t\,th}\ tube} = \tan^{-1}\left(\frac{q^{right}_{N_{t\,th}\ tube}}{h-d}\right) \text{where } q^{right}_{N_{t\,th}\ tube} \text{ equals } p \text{ (Equation (4.9))} \quad \textbf{(4.14)}$$

In Figure 5.1b, the confining angles for the left side of the i_{th} tube are shown in blue and red. These help explain why the minimum function is used in Equations (4.13) and (4.14) to define $\alpha^{left}_{i_{th}\ tube}$ and $\alpha^{right}_{i_{th}\ tube}$.

Therefore, the view area of the i_{th} tube per unit length is:

$$view\,area_{\,i_{th}\,tube} = r \times \left(\alpha^{\,left}_{\,i_{th}\,tube} + \alpha^{\,right}_{\,i_{th}\,tube}\right) \quad \textbf{(4.15)}$$

with r being the tube radius.

Therefore, minimisation of tube bundle radiation loss is possible by minimising the total view area of the tube bundle per unit length:

$$view\,area\,of\,tube\,bundle = \sum_{i=1}^{N_t} view\,area_{\,i_{th}\,tube} \quad \textbf{(4.16)}$$

4.3.2 **Validation**

The accuracy of the suggested view area approach is investigated in this section. In this regard, the studied test case in Section 4.2 is reconsidered for this study. The test case geometry dimensions were summarised in Table 3.1. Based on the introduced geometry, the $Aperture\,width$ and N_t in Equation (4.8) are 1231 mm and 4 respectively. The rest of the parameters for view area calculation were defined in Table 3.1.

The heat loss calculation via the view area approach is computed by means of Equation (4.17). This heat loss calculation is reported per unit length as:

$$Q_{heat\,loss} = \sigma\varepsilon_{Tube\,bundle}\, A_{view\,area}\left(T^4_{Tube\,bundle} - T^4_{Mirror\ field}\right) \quad \textbf{(4.17)}$$

where σ is the Stefan-Boltzmann constant, $\varepsilon_{Tube\,bundle}$ is the emissivity of the tube bundle, $A_{view\ area}$ is the view area of the tube bundle per unit length (calculated from Equation (4.16)), $T_{Tube\,bundle}$ is the tube bundle temperature and $T_{Mirror\ field}$ is the temperature of the mirror field.

Figure 4.7 shows how accurate this approach could be in the heat loss prediction of an LFC plant in comparison with the CFD approach. The CFD study of this test case was run under no wind condition (convective heat transfer coefficient equal to 0 W/m^2-K) for comparison. Because of the dominance of the radiation mechanism, the heat loss approach trend follows a similar trend to the CFD approach, with the view area approach underpredicting the total heat loss at 500 K by about 21%.

Figure 4.7 also gives an indication of how the radiative heat losses increase with receiver tubes temperature as would be the case in an LFC plant. It however does not provide an indication of convection heat losses and how they would change relative to radiation losses. This could be a topic for future work.

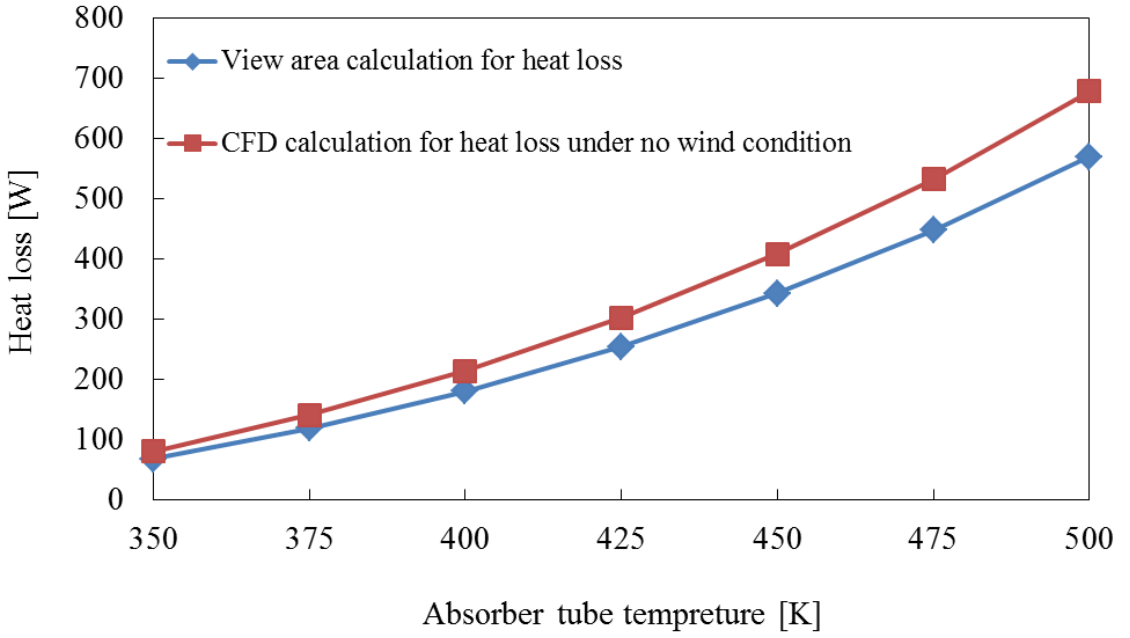

Figure 4.7. Heat loss comparison of CFD and view area approach for no wind condition.

4.4 CONCLUSION

This chapter concludes with the following:

- The assumption of replacing the effect of solar irradiation with a specified outside temperature (and thereby assuming a uniform flux) is shown to be a good one by validating the approach against a more expensive and elaborate method that incorporates a non-uniform solar heat flux distribution on the pipes.

- The traditional approach to thermal modelling of an LFC plant is CFD simulation. Accurate CFD modelling of all the heat transfer mechanisms is required to assess their relative importance in the optimisation process utilising the CFD approach. This includes accounting for natural convection. The traditional use of the

Boussinesq approximation in CFD to relate the density of the air in the cavity to the temperature was questioned because of the large temperature range expected. Therefore it was replaced with the incompressible ideal gas assumption that is not limited to small temperature variations. Proof was provided that the pressure remained fairly constant in the cavity.. The insulation material is included in the model since its shape influences the local conduction, especially in the cavity corner area. The selective absorption of the glass cover is incorporated with a dual-band grey approach into the discrete ordinates method in CFD simulation. This method allows for the capture of the greenhouse effect caused by the glass cover. The radiation properties of the cavity and absorber tube surfaces can be treated with a dual grey-band approach based on their surface roughness. This approach implies that they reflect radiation specularly at high wavelengths but diffusely for the rest of the spectrum. The dual band also enables the modelling of selective coatings through the band-selective specification of surface absorptance and emissivity.

- Heat loss estimation with reasonable accuracy and computational effort speeds up the calculation process of thermal modelling. This low-fidelity approach is one of the essential requirements for a comprehensive optimisation study to run the simulation in a reasonable time frame and assess the relative importance in the optimisation process. The traditional use of the CFD simulation can be replaced with a quicker approach with reasonable accuracy. The approach is called the view area approach, which is based on the fact that the most dominant mechanism in heat loss from an LFC cavity is radiation heat transfer. In this method, the tube bundle temperature is taken as the main driver of the radiative heat loss mechanism, and the portion of its area, which participates in radiation to the mirror field, is determined as the view area. This approach has been proved to have a reasonable accuracy, coupled with a significant reduction in computational effort. However, the accuracy of this approach could be significantly improved if the radiation exchange between surfaces in cavity as well as glass absorption were considered in this approach.

5 OPTICAL, THERMAL AND ECONOMIC OPTIMISATION OF AN LFC

5.1 INTRODUCTION

This chapter focuses on a comprehensive optimisation investigation - an optical, thermal and economic optimisation study - on an LFC field with a multi-tube cavity receiver (Areva Solar Technology). Indeed, this study tries to answer the questions faced by designers and researchers when designing an LFC with a multi-tube trapezoidal cavity receiver (as investigated by Moghimi et al., 2016a; 2016b; 2016c), for example, what is the optimum number of mirrors? What is the optimum gap between mirrors? What optimum width should a mirror have? What is the optimum number of tubes in a tube bundle? What tube diameter should be considered for the absorber tubes? What should the arrangement of tubes be? What is the optimum configuration trapezoidal cavity? What is the optimum mounting height of cavity receiver? And so on.

In this regard, the chapter focuses on harvesting the maximum solar energy throughout a day (maximising plant optical efficiency for 11 different sun positions during a day), while minimising plant thermal heat loss (maximising plant thermal efficiency), as well as plant cost (the economic optimisation of the plant), together resulting in the generation of cheaper solar electricity from an LFC plant with a multi-tube cavity receiver. For the receiver, optimal cavity shape, tube bundle arrangement, tube numbers, cavity mounting height and insulation thickness are considered, while for the mirror field, the number of mirrors, mirror width, mirror gaps and mirror focal length are considered to achieve the optimisation goals. To speed up the optimisation process, a multi-stage optimisation process is followed. Firstly, optical (using SolTrace), thermal (using a view area approach) and economic performance are combined in a multi-objective genetic algorithm as incorporated into ANSYS DX. This definition leads to an optimal LFC with a variable focal length for each mirror. After modifying the design to determine a more practical fixed optimal focal length for all the mirrors, a CFD approach is used to optimise the thermal insulation of the cavity receiver for minimal heat loss and minimal insulation material. The process is automated through the use of ANSYS Workbench and Excel (coding with VBA and LK Scripting in SolTrace). The

view area approach (as discussed in Chapter 4) provides an inexpensive way of calculating radiation heat loss from the receiver, which is shown in the subsequent CFD analysis to be dominating the heat transfer loss mechanisms. The optimised receiver is evaluated at different LFC plant tube temperatures to assess its performance.

The chapter firstly presents the definition of the optimisation problem in the context of the collector layout, followed by a brief discussion of the engineering optimisation tools and modelling, in particular of the optical modelling throughout a day. These are followed by the definition of the optimisation problems and optimisation algorithm settings. Finally, after discussing the optimisation and detailed CFD and ray-tracing results, conclusions are reached.

5.2 COLLECTOR LAYOUT

An LFC is an array of slightly curved or flat mirrors that concentrates solar energy on a collection of absorber tubes surrounded by a downward-facing fixed receiver. In this chapter, a multi-tube trapezoidal cavity is considered as the LFC's receiver with the mirrors all having a slight parabolic curvature. The cavity is filled with air, and the cavity aperture is covered by glass 3.2 mm thick to reduce radiative and convective heat losses from the cavity. Figure 5.1 presents a schematic sketch of the proposed LFC. The aperture width is fixed at 332 mm to approximate the aperture condition of Solarmundo, which was designed with a mono-tube secondary reflector cavity receiver. The aperture size selection essentially defines the system in terms of its ability to capture reflected solar energy. To determine an optimum LFC with these conditions, the other geometric parameters that are outlined later have to form design variable set for the optimisation process. These parameters are as follows: number of mirrors and mirror width (allowed to vary independently but together defining total mirror area), mirror gap, mounting height of the cavity, cavity depth, location of the tube bundle in the cavity, number of tube absorbers, tube pitch, tube outer diameter, cavity angle, side and top insulation thicknesses, and angle of top insulation. In addition to these independent parameters, there are some dependent parameters that play a role in the optimisation process. These are determined by the design variable set mentioned above. The slightly parabolic curvature of the mirrors is one such dependent parameter. The ideal parabola function for an LFC mirror's curvature, in terms of its focal length, f, is:

$$y = \frac{1}{4f} x^2 \qquad \textbf{(5.1)}$$

where f is the distance in a 2-D plane from the mirror centre to the tube bundle centre (focal length).

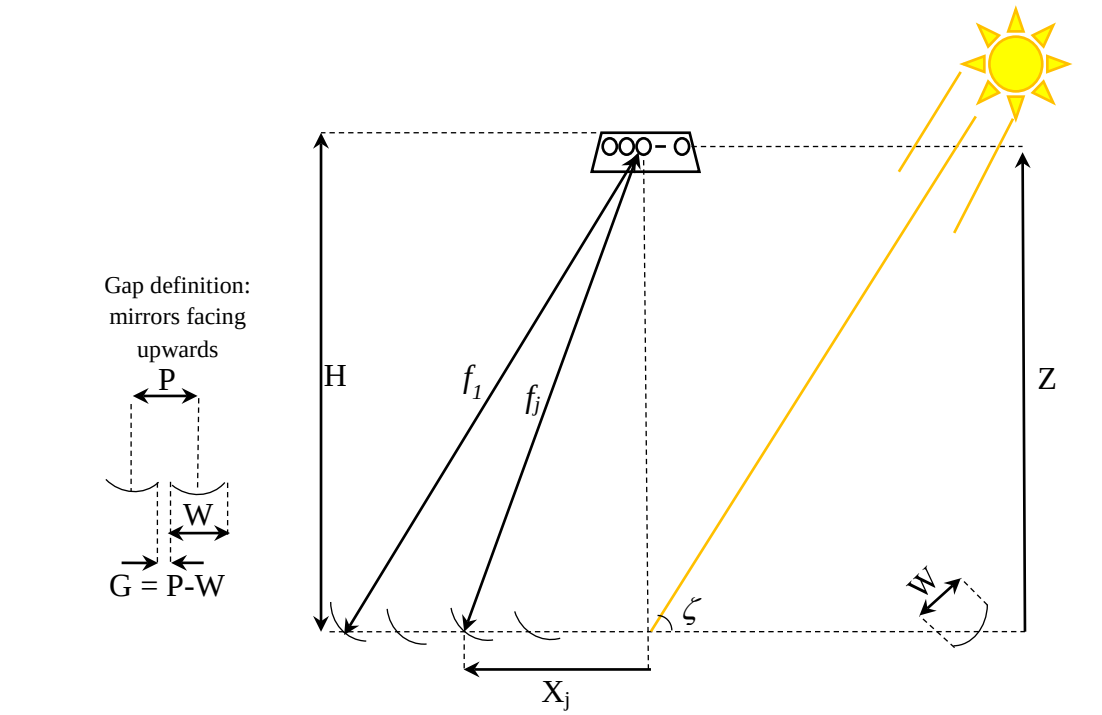

(a)

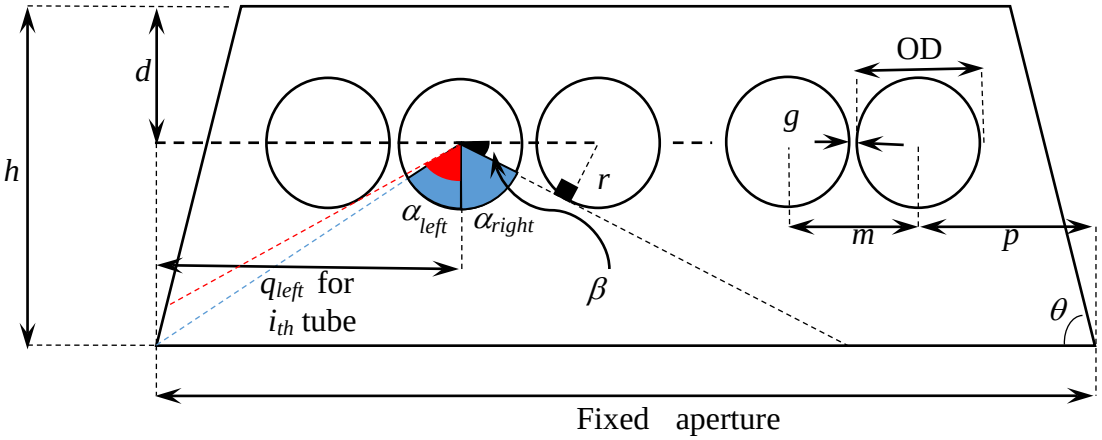

(b)

Figure 5.1. Schematic sketch of an LFC.

(a) Entire collector domain. (b) Cavity receiver.

Therefore, as displayed in Figure 5.1a, the focal length of the j_{th} mirror is calculated as:

$$f_j = \sqrt{X_j^2 + Z^2} \qquad \textbf{(5.2)}$$

where X_j is distance from the j_{th} mirror centre to the collector symmetry line (as influenced by the parameters: *mirror gap*, *mirror width* and *number of mirrors*), and Z is the perpendicular tube bundle distance from the mirror field (determined mainly by the parameter: *mounting height of the cavity*, and to a lesser extent by the parameter: *location of the tube bundle centre in the cavity*).

Before conducting the optimisation process, the applicable engineering tools and methods used in the calculation of the optimisation goals are surveyed.

5.3 REQUIRED TOOLS AND MODELLING FOR OPTIMISATION

To conduct thermal, optical and economic optimisation of an LFC plant, one has to use an optimisation tool. There are various optimisation tools and software available (e.g. LS-OPT, Isight, Excel, Matlab), which are mostly used as third-party software to calculate the optimisation goal in another software (Moghimi et al., 2015c). For the example of thermal optimisation of a plant, the optimisation codes have to interact with commercial CFD codes (e.g. ANSYS Fluent) to optimise a thermoflow domain and its properties.

However, ANSYS (ANSYS, 2013b) created a platform which allows researchers and designers to interact with Excel, commercial CFD codes, engineering tools and an optimisation tool (DX) in one integrated platform: WorkBench (WB). This platform makes the optimisation process more robust, customised, user-friendly and easier since the external interactions of different engineering tools with external third-party codes for the optimisation process have been eliminated. These are the reasons that ANSYS is used as the optimisation platform in the current study.

The optimisation simulation in WB is straightforward with the steps described in the following. For a graphical illustration of flow work of the optimization problem steps in WB please consult Figure 5.3 and Figure 5.5.

Step 1: Geometry design parameters are introduced in Excel, Design Modeller (DM) or other ANSYS modules, and are automatically brought into WB.

Step 2: These design parameters are then linked to optimisation goal parameters, which can be defined in any corresponding modules of ANSYS (Excel, FLUENT, etc.), depending on the goal definitions and approaches for their calculations.

Step3: The relationship between independent parameters (definition of dependent parameters) as well as the definition of any new independent parameters and goals which could not have been defined in the previous steps, are accomplished in the “Parameter Set” block. Then, the defined modules for design parameters and goal calculations are linked to the DX module, which is a response surface-based optimisation tool.

Step 4: The lower and upper limits of each parameter are set in “Design of Experiments”. Then, an adequate number of design points are generated based on the combination of defined parameters. Finally, each individual design point is evaluated in a numerical investigation to determine its corresponding optimisation goal parameters (objectives).

Step 5: Mathematical response surfaces are fitted through the objective results of previous step.

Step 6: A predefined numerical algorithm looks for optimum region(s) on the generated response surfaces.

The following features of ANSYS DesignXplorer (DX) (ANSYS, 2013c) are used for the optimisation study. The response surface method (RSM) is chosen for the mathematical optimisation. The Design of Experiments (DOE) is done using a central composite design (CCD) to determine the different combinations of independent parameters of the optimisation study. The construction of the responses is done using either full second-order polynomial or Kriging. The optimum location on these surfaces is determined using the multi-objective genetic algorithm (MOGA), which is based on the fast and elitist evolutionary algorithm: NSGA-II (non-dominated sorting genetic algorithm II). This method results in a Pareto optimal set giving competing objectives. This set represents the family of optimal designs on the combined objective response surfaces through the variation of the relative weighting of the competing objectives (ANSYS, 2013c). In Addenda IX and X, the salient features of Kriging and MOGA are summarised in different sections.

Based on the nature of the RSM optimisation process, reducing the number of independent parameters will hugely save the computational cost of the optimisation process. Therefore, the author suggests a two-stage optimisation process. The main aim of this suggestion is breaking down the independent parameters to two dependent sets, which can be used separately in two optimisation processes. This separation will speed up the optimisation process, reduce the complexity of simulation as well as lead to more accurate response surfaces.

However, because the main aim of this study is the optical, thermal and economic optimisation of the collector, breaking the whole set of independent parameters into two smaller sets is impossible with the thermal engineering tools (CFD approach) unless, instead of the CFD approach, the view area approach is used. With the help of the view area approach, the thermal objective goal of the collector optimisation is independent from a CFD calculation. This fact leads to the suggestion of a series two-phase optimisation approach in which the independent parameter sets are not dependent. In the first phase, the collector domain goes through a thermal, optical and economic optimisation study, while the second phase uses the results of the first phase to find the thermal and economic optimal insulation around the proposed cavity.

The goal of the first optimisation is to find a optimum collector where the total plant cost factor ($\gamma_{Plant\,Cost\,Factor}$) and view area are minimised, while maximising daily solar power. The total plant cost factor is a mathematical definition which specifies a factor of total plant cost with significant influence on the LEC calculation (see Section 2.7). The view area is defined as the total absorber tube area that faces the mirror field. This mathematical definition is directly proportional to the view factor definition in heat transfer textbooks (see Section 4.3). Daily solar power is defined as the average of solar power incident on all tubes of the receiver throughout a typical summer day. The first two goals of the first stage optimisation (the total plant cost factor and the view area) are calculated via Equations (2.11) and (4.16) respectively, while the calculation of the daily solar power as the last optimisation goal is more complicated (this calclculation is based on 11 optical simulations on an LFC throughout a summer day, the steps are described in Figure 5.2).

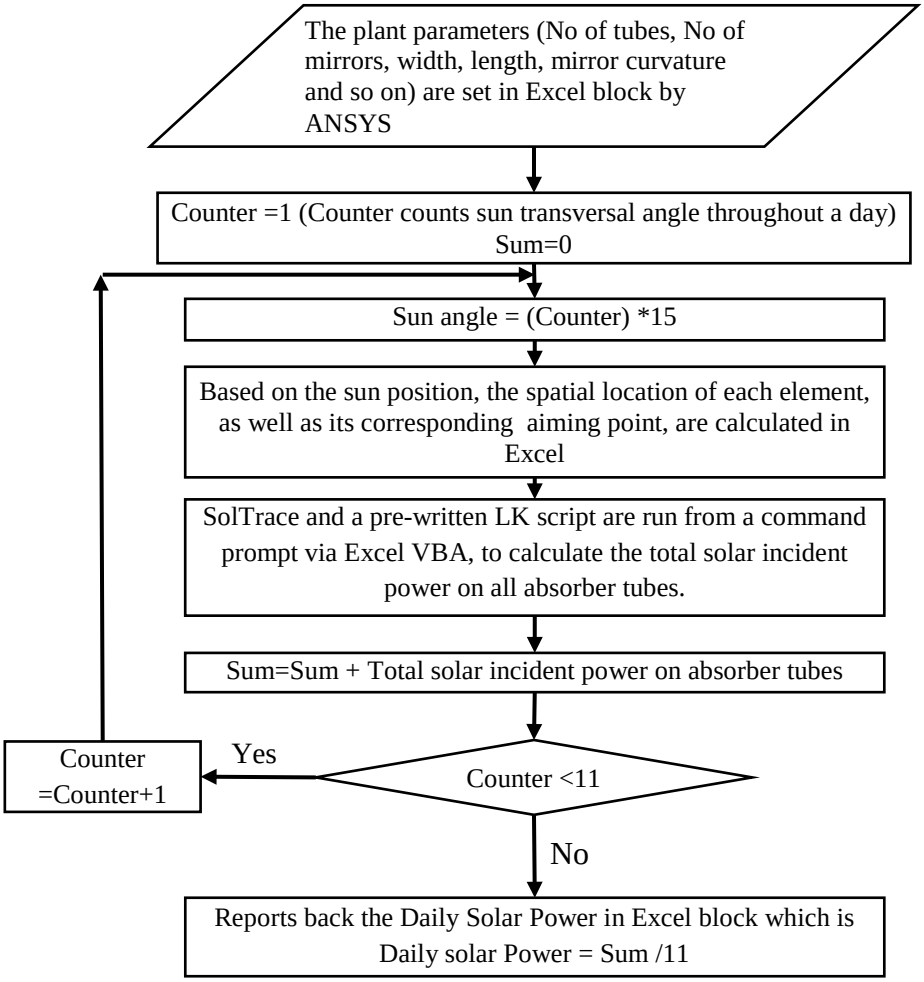

Figure 5.2. The flowchart of Daily Solar Power definition.

Based on the goal definitions, the complexity of the optimisation process and the cost of the computational of an RSM optimisation process, the following tools and approaches are considered as the most rational option for the first phase. In the first optimisation phase, the view area approach (discussed in Section 4.3), the Monte Carlo ray-tracing approach (discussed in Section 3.3), the economic approach (discussed in Section 2.7) and ANSYS DX optimisation modelling (Moghimi et al., 2015c) are used to conduct a thermal, optical and economic optimisation study on collector domain parameters, except the insulation thickness parameters.

The second phase of the current optimisation study is defined to optimally insulate the cavity of the first phase in the optimum collector. The optimisation goals of the second phase are defined as minimising the cavity heat loss and the required insulation area. This definition leads to the thermal and economic optimisation of the insulation. Because the cavity

properties (to name some number of tubes, tube diameter and tube locations) are determined in the first phase of the study, these parameters are fixed in the second phase, which speeds up the optimisation process and saves computational effort. In the second phase, the proposed tool for the calculation of thermal performance is the CFD approach (discussed in Section 4.2), while the insulation area or material is defined as the second optimisation goal.

5.4 OPTIMISATION PROBLEM DEFINITION

5.4.1 First-stage optimisation problem (collector optimisation)

The set of design variable parameters investigated at this stage of the optimisation includes (the notation was defined in Figure 5.1): number of mirrors (N_m), mirror width (W), mirror gaps (G), mounting height of cavity or cavity top wall distance from mirror line (H), tube radius (r), tube gap (g), tube bundle offset from cavity top wall (d), cavity angle (θ) and cavity depth (h). This set of variables combined tries to find a optimum collector where the total plant cost factor ($\gamma_{Plant\,Cost\,Factor}$) and view area are minimised, while maximising daily solar power.

The definition and calculation of design variable parameters and goals are subsequently described.

The variable set is defined in an Excel file. This variable set is then used in calculations of the total plant cost factor and view area based on formulations in previous sections (Sections 2.7 and 4.3). The calculation of daily solar power is done through an exchange of information between Excel and SolTrace, using coding in VBA and the LK scripting language respectively (for the detailed codes, see Addendum VIII). The scripting languages are very useful in setting up parametric runs and optimisations. The calculation procedure uses a “for” loop in VBA for a determined set of variables throughout a day as discussed below (please see Figure 5.2 for graphical illustration) :

Firstly, for a specific sun position, according to the variable set and SolTrace definitions, the VBA calculates the spatial location of each element, as well as its aiming point in Excel spreadsheets (for detailed mathematical formulations, see Addendum I). In addition to this information, the width, length and type of each element that defines the element curvature are automatically determined. A text file containing all these data is exported from Excel via

VBA. Subsequently, SolTrace and a pre-written LK script are run from a command prompt in VBA. The pre-written LK file imports data from the Excel-exported file, and after pre-setting and modelling all the elements in SolTrace, the simulation is run in SolTrace. The script reads the net solar incident power on each absorber tube and reports them back into the Excel file. By adding up the incident power values, the Excel file calculates the total received solar power on the tubes in the cavity for an individual sun position. This procedure is repeated for every 15 degrees of sun angle (11 separate sun positions) throughout a day. Finally, the VBA calculates the average and reports it as daily solar power.

After defining all design parameter variables and optimisation goals in Excel, the Excel file is linked to DX in WB and the optimisation loop is closed and ready for execution. Figure 5.3 shows the optimisation loop in WB.

The optimisation problem of this section is formulated as:

$$\begin{aligned} &Minimise\ \left(w_1\, View\ Area\left(\tilde{x}\right) + w_2\, \gamma_{\,Plant\,Cost\,Factor}\left(\tilde{x}\right)\right), \\ &Maximise\ \left(w_3\, Total\ Daily\ Solar\ Power\left(\tilde{x}\right)\right) \end{aligned} \qquad \textbf{5.3)}$$

subject to bounds $\tilde{x}$, where $\tilde{x}$ is the set of design variable parameters.

The weighting factors w_k are implicitly defined based on the MOGA, and the optimisation process explained in detail in Section 5.4.3. The design variable set, allowable ranges and derived parameters are introduced in Table 5.1. In this and the following table, the allowable ranges of parameters were set based on literature and limitations of design in this study.

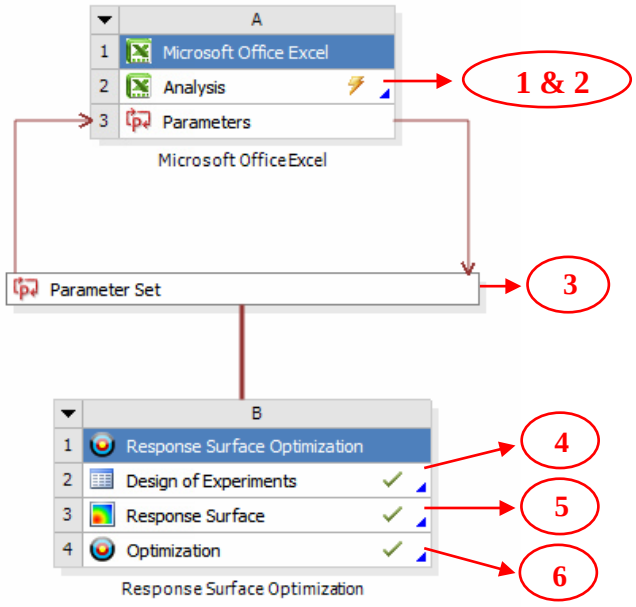

Figure 5.3. Optimisation loop for collector optimisation problem in ANSYS WBwith inserted step numbers.

Table 5.1 Definition of objective and parameter ranges (notations used in the table are based on their definition in Figure 5.1).

Independent parameters	**Lower bound**	**Upper bound**	**Other**
Number of mirrors – N_m	10	50	Discrete value and the variation step is 2.
Mirror width – W [mm]	100	1 000	Continuous variation
Mirror gap – G [mm]	10	1 000	Continuous variation
Mounting height of cavity – H [m]	5	20	Continuous variation
Tube radius – r [mm]	10	30	Continuous variation
Tube gap – g [mm]	1	4	Continuous variation
Tube bundle offset from cavity top wall – d [mm]	25	50	Continuous variation
Cavity angle – θ [degree]	50	90	Continuous variation
Cavity depth – h [mm]	100	150	Continuous variation
Dependent parameters	**Relation**		**Other**
Tube outer diameter – OD	$OD = 2 \times r$		
Tube pitch – m [mm]	$m = OD + Tube\,Gap$		
Number of tube absorber – N_t	$N_t = Round\,down\left\{ \frac{1}{m} \times \left[332 - 2\left(\frac{h-d}{\tan\theta} \right) \right] \right\}$		Derived parameter with integer output constraint
Focal length of j_{th} mirror	$f_j = \sqrt{X_j^2 + Z^2}$		Where X_j is the distance of the j_{th} mirror centre to the collector symmetry line and Z is the perpendicular tube bundle distance from the mirror field. Therefore, for an N_m mirror field, $N_m/2$ focal lengths have to be determined.
aperture [mm]	332		Fixed constraint
Optimisation objective	**Relation**		**Objective**
Heat loss	View area of tube bundle		Minimisation
Plant cost	$\gamma\,Plant\,Cost\,Factor$		Minimisation
Solar power	Daily solar power		Maximisation

5.4.2 Second-stage optimisation (insulation optimisation)

This optimisation stage is defined to optimally insulate the cavity of the previous stage in the optimum collector. The set of design variables of this optimisation study (see Figure 5.4) is side insulation thickness (*b*), top insulation thickness (*t*), and top insulation angle (δ).

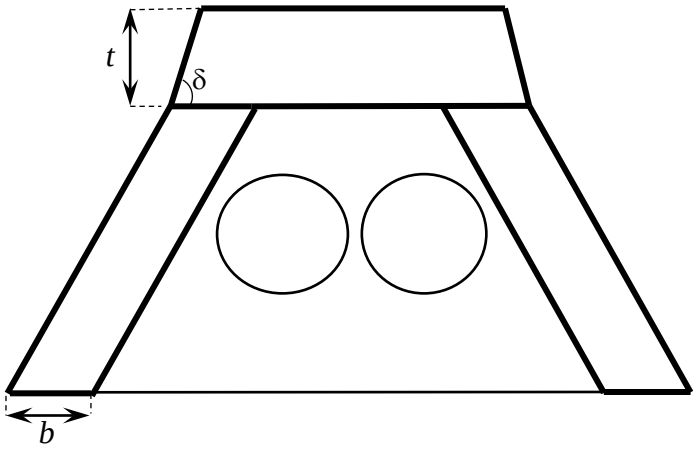

Figure 5.4. Variation definition in insulation optimisation. The cavity parameters are those determined in the previous optimisation study.

In the optimisation study, minimising the cavity heat loss and minimising the insulation area ($Total\ area = 2\times h\times b + 2\times b\times t - \frac{t^2}{\tan\delta} + \left(332 - \frac{2\times h}{\tan\theta}\right)\times t$ where the derivations are provided in addendum XI) are considered as the thermal and economic goals of optimisation. Because the cavity properties (i.e. number of tubes, tube diameter and tube locations) were determined in Section 5.4.1 and have already been fixed at this stage of the optimisation, the view area approach defined in Section 4.3 is not applicable. In this study, the proposed tool for the calculation of the thermal performance is the CFD approach (Section 4.2) in WB, while the calculation of the insulation area as an optimisation goal is done by introducing Equation (XI.4) into DX (see Addendum XI).

Figure 5.5 shows the optimisation loop of the study in WB. The proposed geometry (Figure 5.4), as well as the design variable parameters, was set in the ANSYS CAD module DM. The defined domain was then meshed in the ANSYS meshing tool and linked to the ANSYS CFD tool, FLUENT, where the net heat loss from the cavity boundaries is calculated and linked to DX for the optimisation study.

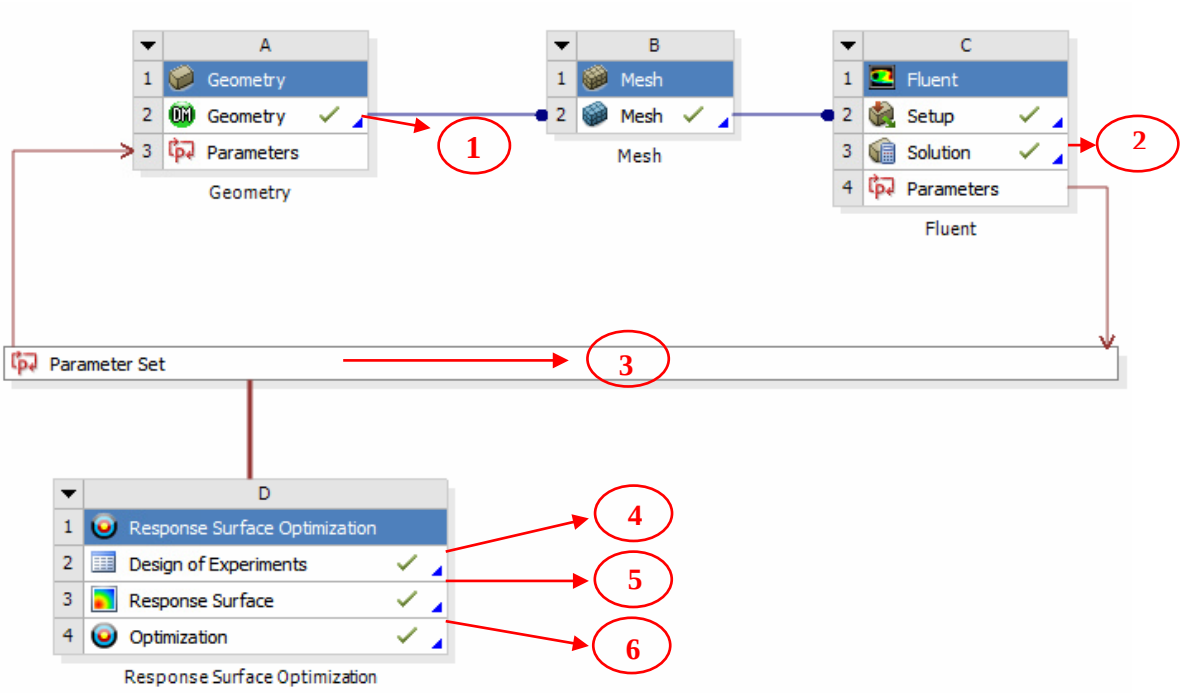

Figure 5.5. Optimisation loop for the insulation optimisation problem in ANSYS WB with inserted step numbers.

The optimisation problem of this section is:

$$\begin{aligned} &\textit{Minimize}\ \left(w_4 f_4(\tilde{x}) + w_5 f_5(\tilde{x})\right) = \\ &\qquad \textit{Minimize}\ \left(w_4\, \textit{heat loss}(\tilde{x}) + w_5\, \textit{Insulation area}(\tilde{x})\right) \\ &\textit{Subject to bounds}\ \tilde{x}\ \textit{with}\ \tilde{x} = (b, \delta, t) \end{aligned} \tag{5.4}$$

The allowable ranges of the design variables are listed in Table 5.2.

Table 5.2 Definition of objective and parameter ranges (notations used in the table are based on their introduction in Figure 5.4 and Figure 5.1)

Independent parameters	**Lower bound**	**Upper bound**	**Other**
Side insulation thickness – d [mm]	25	100	Continuous variation
Top insulation thickness – e [mm]	10	60	Continuous variation
Top insulation angle – δ	40°	90°	Continuous variation
Dependent parameters	**Relation**		
Tube radius – r, tube gap – g, tube bundle offset from cavity top wall – d, cavity angle – θ, cavity depth – h, tube outer diameter –OD, tube pitch – m, number of tube absorber – N_t, aperture	Fixed constraint		The implemented values in the optimisation study are in terms of the proposed optimum case results of Section 5.5.1.
Optimisation objective	**Relation**		**Objective**
Heat loss from boundaries	Summation of heat losses from outer boundaries		Minimisation[1]
Insulation area [mm^2]	$Total\ area = 2\times h\times b + 2\times b\times t - \frac{t^2}{\tan\delta} + \left(332 - \frac{2\times h}{\tan\theta}\right)\times t$		Minimisation[2]

[1] If the losses are reported as an absolute value, then the goal is the minimisation of losses; however, if the losses are defined as a negative value (the way in which it is reported in ANSYS Fluent), then the goal should be maximised.

[2] Where h and θ in the discussed formula are substituted by 144 and 51 respectively (the results of the optimum cavity in Section 5.5.1). The mathematical formulation is discussed in more detail in Addendum XI.

5.4.3 Optimisation algorithm and settings

The following features of ANSYS DX were used for the optimisation. The RSM was chosen for the mathematical optimisation. The DOE was done using Latin hypercube sampling design (ANSYS, 2013c) applied to a specific number of design points. The number of design points was automatically determined according to combinations of the optimisation independent parameters based on the DOE type and sampling algorithm. For each of three optimisation problems, the number of design points and independent parameters is reported in Table 5.3.

Table 5.3 Number of design points and independent parameters for different optimisation problems

Optimisation problem	Design points	Independent variables	DOE type	Sample type
First problem (collector optimisation – Section 5.4.1)	1 881	9	Latin hypercube sampling	CCD
Second problem (insulation optimisation for determined cavity – Section 5.4.2)	15	3	Latin hypercube sampling	CCD

In each of the optimisation problems (Sections 5.4.1 and 5.4.2), the corresponding engineering tools and calculations are run to extract the allocated goals of that problem for each individual design point. Then, the construction of response surfaces is done using a full second-order polynomial for the first optimisation problem (due to discrete nature of one of the design parameters, mirror number) and Kriging for the second problem (due to continuous nature of all design parameters). The determination of the optimum location on these surfaces is done using MOGA. This method results in a Pareto optimal set giving competing objectives. This set represents the family of optimal designs of the combined objective response surfaces through the variation of the relative weighting of the competing objectives. The MOGA settings for each of these optimisation problems are tabulated in Table 5.4.

Table 5.4 MOGA settings for different optimisation problems.

Optimisation problem	Number of initial samples	Number of samples per iteration	Maximum allowable Pareto percentage	Maximum number per iteration
First problem (collector optimisation – Section 5.4.1)	200	200	90%	200
Second problem (insulation optimisation for determined cavity – Section 5.4.2)	50	50	90%	100

5.5 RESULTS AND DISCUSSION

5.5.1 Optimisation results for the first problem (collector optimisation)

The optimisation on the combined response surfaces converged after 2 936 iterations, considering a higher importance for the daily solar power objective and a default importance for the other objectives (view area of tube bundle, γ plant cost factor). In addition, a strict constraint (values greater than 0) was set on the plant cost objective to force optimisation convergence to a physically meaningful value.

To show the effect of independent parameters on optimisation objectives, 12 3-D response surfaces are presented in Figure 5.6 to Figure 5.8. These response surfaces are presented for the introduced independent parameters under the chosen feasible optimum case column in Table 5.5. Due to the impossibility of physically displaying a surface in more than three dimensions, these 12 surfaces are broken up into three groups of four, which are displayed in three consecutive figures (Figure 5.6 to Figure 5.8). In these figures, the independent parameters are held constant at their optimum values when not plotted in a particular sub-figure. In Figure 5.6, Figure 5.7 and Figure 5.8, respectively, the γ plant cost factor, daily solar power and view area of tube bundle objectives are considered fixed, and the effect of each two independent parameters on that objective is shown and discussed.

Figure 5.6a displays the effects of cavity depth and angle on γ plant cost factor. It can be seen that the γ plant cost factor increases by increasing the cavity angle, while the opposite

trend is shown for the cavity depth. These two independent parameters affect the available space in the cavity to house the tube bundle. Increasing the cavity angle transforms the trapezoidal shape of the cavity towards a rectangular shape, which leads to an increase in available space, while for a fixed trapezoidal cavity angle, increasing the cavity depth decreases the available space for the tube bundle (due to the determined location of the tube bundle from the cavity top wall). Hence the effects displayed in Figure 5.6b make sense physically according to the following reasoning: for a constant tube radius case, by reducing the available location for a tube bundle, the number of tubes in the tube bundle

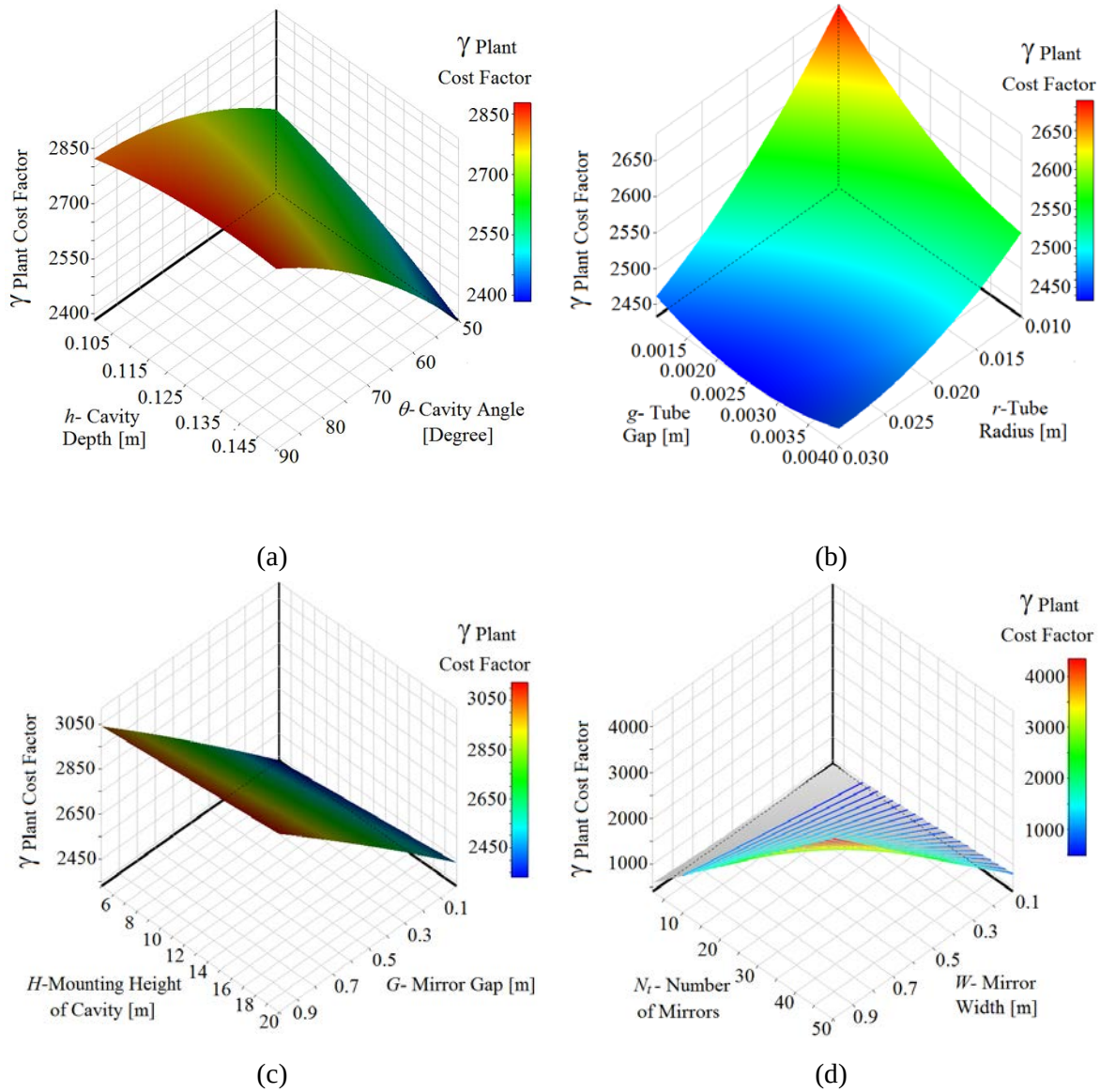

Figure 5.6. Response surfaces of the plant cost factor term vs. independent parameters.

(a) Plant cost factor vs. cavity depth and cavity angle. (b) Plant cost factor vs. tube gap and tube radius. (c) Plant cost factor vs. mounting height of cavity and mirror gap. (d) Plant cost factor vs. number of mirrors and mirror width.

decreases. Reducing tube numbers leads to a cheaper cavity collector due to the cost of the tube, welding tube cost, tube coating cost, etc. Figure 5.6b shows the effect of tube radius and tube gap on the γ plant cost factor. According to the previous discussion, by increasing the tube radius and tube gap, one can expect a decrease in cavity cost, since fewer tubes can fit into a cavity, as shown in Figure 5.6b. Figure 5.6c indicates that, by increasing the gap between mirrors, as well as the cavity mounting height, the plant cost increases mainly because of the increased land use area and higher supporting structure. Although the effect of the cavity mounting height on the γ plant cost factor may not be as obvious as the effect of the mirror gap in Figure 5.6c, it is proved by observing the colour gradient along a fixed mirror gap. These objective dependencies are also justified by mathematical formulations – Equations (2.7) and (2.11) – of the plant cost factor term $\left(\gamma_{Plant\,Cost\,Factor}\right)$ where mirror gap (G) affects both the land cost term and the direct specific cost of a collector term (C_c^d), whereas the mounting height only influences the latter term. Finally, the effects of mirror numbers and mirror width on the plant cost factor term are depicted in Figure 5.6d. Note that as the number of mirrors is a discrete variable, the response surfaces (in Figure **5.6**d and subsequent figures, Figure 5.7d and Figure 5.8d) are a set of slices or lines and thus not continuous. The trend of the response surface in Figure 5.6d makes sense because increasing both the mirror width and the number of mirrors increases the land cost and mirror field cost as discussed.

In the following discussion, the effects of the independent parameters on the objective of the view area of the tube bundle are displayed in Figure 5.7a to Figure 5.7d. This objective is reported per unit length of the plant. Figure 5.7a shows the effects of cavity angle and cavity depth on the view area of the tube bundle. Due to the fixed aperture assumption, a decrease in cavity angle or increase in cavity depth leads to less available space in the cavity for fitting a tube bundle or fewer tubes in the cavity. Therefore, the view area falls. Figure 5.7b depicts the effects of tube radius and tube gap on the view area. As shown in this figure, either increasing the tube radius or the tube gap reduces the view area of the tube bundles, because fewer tubes fit into the cavity. Figure 5.7c and Figure 5.7d show the effects of the cavity mounting height, the gap between the mirrors, as well as the number of mirrors and the mirror width on the view area. As expected, the mirror field parameters (i.e. the number of mirrors, the mirror width, the mirror gap and the mounting height of the cavity) have less influence on the view area objective (see the range on the vertical axis). Actually, this is

expected for these parameters, in terms of the discussion of view area (Section4.3). The physical constraints that limit re-radiation of the tube bundle to the mirror field are the closeness of the tube to the side cavity walls or to adjacent tubes. These constraints are effectively limited by cavity parameters, not by mirror field parameters.

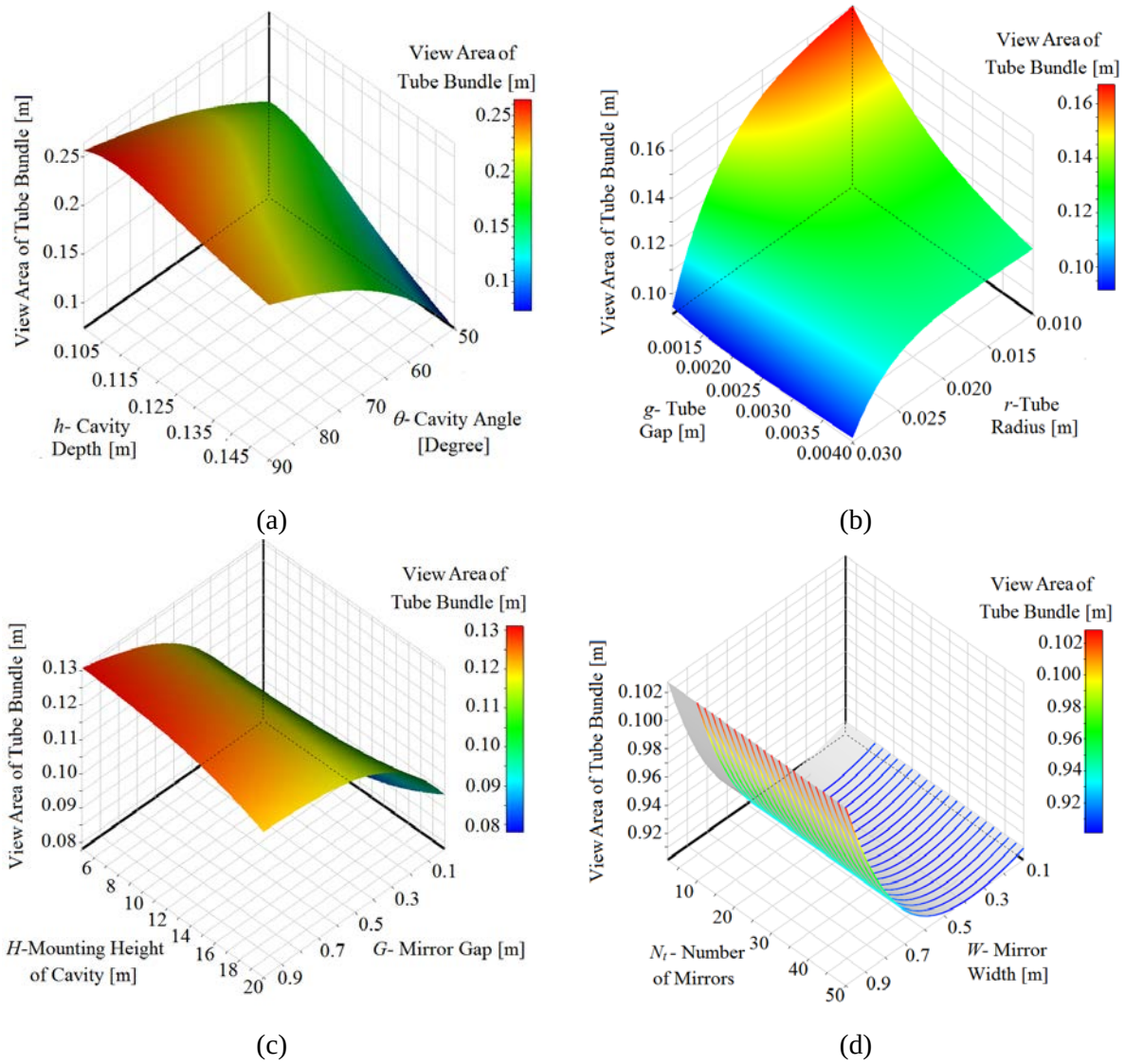

Figure 5.7. Response surfaces of the view area of tube bundle vs. independent parameters.

a) View area of tube bundle vs. cavity depth and cavity angle. b) View area of tube bundle vs. tube gap and tube radius. c) View area of tube bundle vs. mounting height of cavity and mirror gap. d) View area of tube bundle vs. number of mirrors and mirror width.

Finally, Figure 5.8 shows the effect of the optimisation-independent parameters on the daily solar power objective. Figure 5.8a depicts the effect of cavity depth and cavity angle on daily solar power. A decrease in cavity angle or increase in cavity depth leads to fewer tubes fitting into the cavity, which means that fewer reflected rays from the mirror field will hit the absorber tubes or that the absorbed solar power throughout a day will decrease. Figure 5.8b

displays the effects of the tube radius and the tube gap on daily solar power. Increasing the tube gap parameter means that the tubes are situated further from each other in the cavity, which leads to more reflected rays hitting the absorber tubes in the cavity. This increases the absorbed daily solar power, which is shown in this figure. In addition, for a specific tube gap,

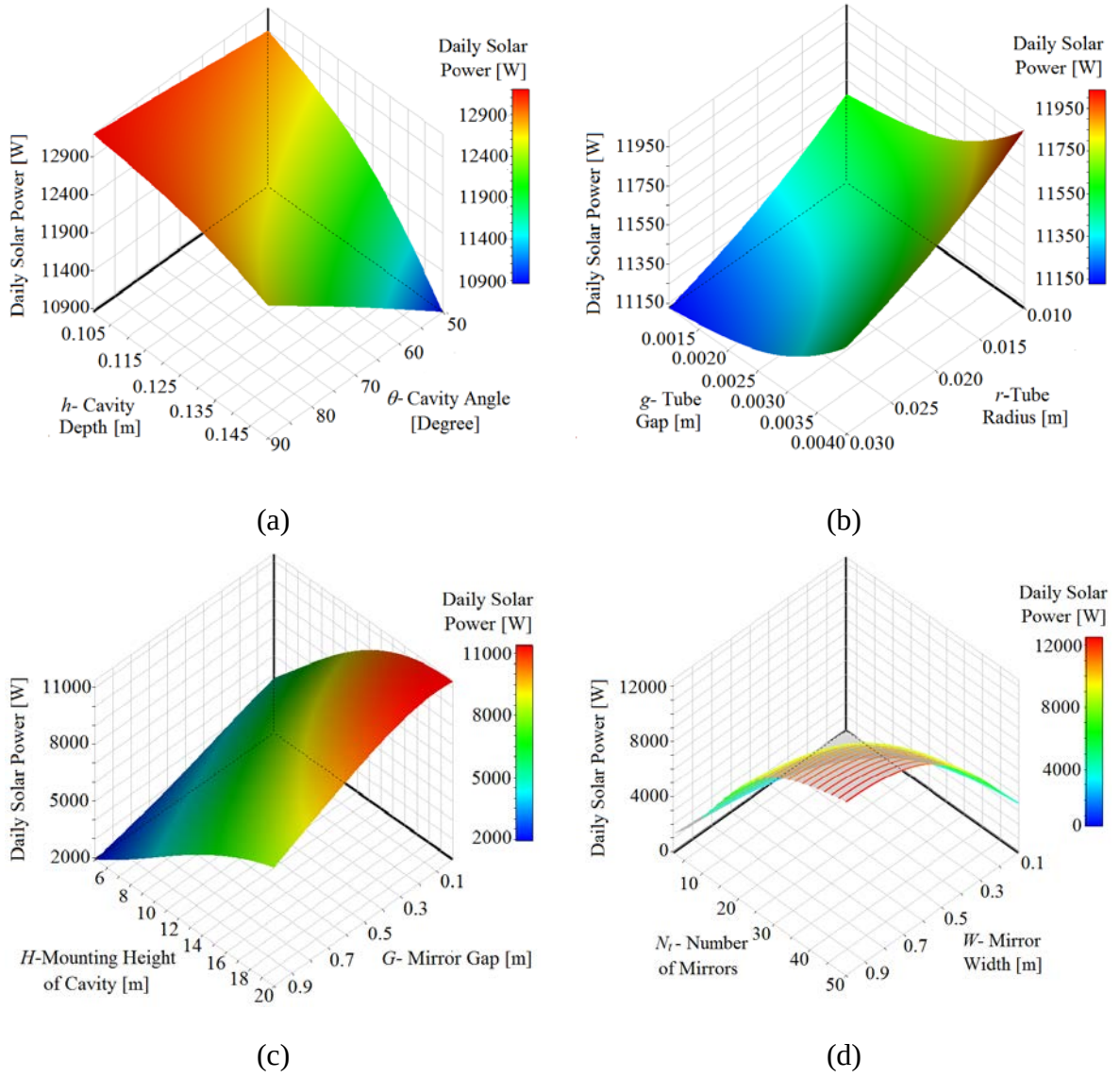

Figure 5.8. Response surfaces of daily solar power vs. independent parameters.

a) Daily solar power vs. cavity depth and cavity angle. b) Daily solar power vs. tube gap and tube radius. c) Daily solar power vs. mounting height of cavity and mirror gap. d) Daily solar power vs. number of mirrors and mirror width.

by increasing tube radius, the absorbed daily solar power drops. Indeed, increasing the tube radius leads to fewer tubes in the tube bundle due to insufficient fitting space in the cavity, and consequently, fewer rays hitting the absorber tubes. Figure 5.8c shows the effects of mirror gap and the mounting height of the cavity on daily solar power. As displayed, by

increasing the mounting height of the cavity, the daily solar power increases. Increasing the mounting height of the cavity leads to less blocking and shading in the mirror field. In addition, for a specific mounting height of the cavity, decreasing the mirror gap leads to the compactness of mirror field. Although the field compactness increases the blocking and shading effects of the mirror field, due to a fixed aperture assumption, this fact also lets more mirrors play a role in solar ray concentration on the tube bundle throughout a day. This leads to increasing the daily solar power by reducing the mirror gap. Figure 5.8d displays the effect of the number of mirrors and the mirror width on the daily solar power. The response surface shows that by adding more mirrors or by increasing the mirror width, the daily solar power increases. This is to be expected, because increasing these independent parameters leads to increasing the mirror field reflected area, which consequently results in more solar rays impinging on the absorber tubes.

Lastly, the values of three optimum designs are presented by ANSYS DX among all the feasible Pareto optimal cases on the pareto front (please see Figure 5.9). The suggested optimum points based on the response surface optimisation are reported in Table 5.5 and shown on pareto front in Figure 5.9. These parameter combinations are re-calculated using Excel and SolTrace to provide the “calculated” values in the table. There is a difference between the predicted and verified calculated values, but the latter should be used as it is based on a simulation and not on a response surface prediction. Choosing a candidate among those three suggested points is left to user. Indeed, the most suitable candidate is chosenbased on the weight of the optimiation goals of the suggested candidates.

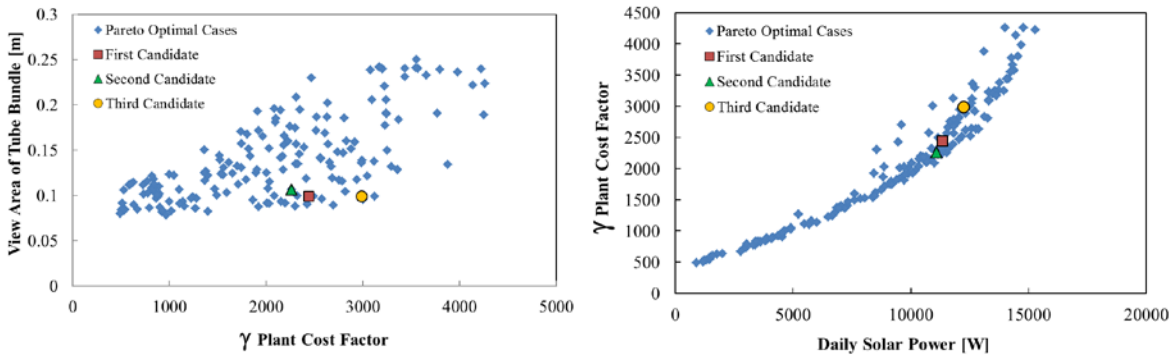

(a) (b)

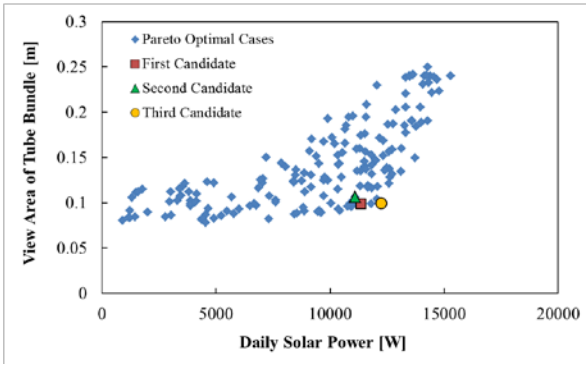

(c)

Figure 5.9. Projection of 3D pareto front feasible cases on three main orthogonal planes.

a) View area of tube bundle vs. Plant cost factor. b) Daily solar power vs. Plant cost factor. c) Daily solar power vs. View area of tube bundle.

Cavity depth and cavity angle parameters in all candidates tend towards maximum and minimum bounds respectively. This driving to extreme bounds tries to move the cavity receiver to its deepest and most acute-angled case. According to what has been discussed, this physically makes sense, because the deepest and most acute-angled case traps the highest amount of solar rays (increasing solar power on the tube bundle), while these two parameters decrease the available cavity room for placing the tube bundles (decreasing the number of tubes), which has a significant effect on reducing the cavity's economic cost and the view area of the tube bundle. These two parameters tend towards their extremes because they could satisfy all optimisation objectives. However, the rest of the parameters are unconstrained at the optimum values.

Due to the prediction of output goals, the first-point candidate is suggested as the final result for further investigation. However, it should be considered that although these inlet parameter values might mathematically lead to optimum results, it would not be practical to fabricate such a collector due to the existence of manufacturing limitations or material availability. For instance, not every mathematical tube's outer diameter that was calculated in the optimisation process is available on the market. According to Table 5.6, the closest available industrial pipe that could be purchased had a 60.33 mm outer diameter. In general, due to manufacturing and procurement limitations (i.e. cutting, bending, welding and manufacturing processes' tolerances, as well as material availability on the market), the values of the first-point candidate parameters had to be adjusted to feasible values. Such data are reported under the chosen feasible optimum case column in Table 5.5.

Table 5.5 Candidate optimum points.

Parameters [unit]	**First candidate**	**Second candidate**	**Third candidate**	**Chosen feasible optimum case**
Number of mirrors – N_m	38	34	48	38
Mirror width – W [mm]	681.4	684.1	684	681
Mirror gap – G [mm]	22.8	13.7	31.4	23
Mounting height of cavity – H [m]	18.605	18.404	18.605	18.605
Tube radius – r (tube outer diameter – OD) [mm]	29.235 (58.47)	29.245 (58.49)	29.235 (58.47)	30.165 (60.33)
Tube gap – g [mm]	3	3.8	3	2
Tube bundle offset from cavity top wall – d [mm]	38.8	38.7	38.8	39
Cavity angle – θ [degree]	51.1	52	51.1	51
Cavity depth – h [mm]	143.6	142.9	144	144
Number of tube absorber – N_t	2	2	2	2
Optimisation objective	**Predicted (calculated)**	**Predicted (calculated)**	**Predicted (calculated)**	
View area of tube bundle [m]	0.099131 (0.11616)	0.10627 (0.11670)	0.099179 (0.11605)	0.11956
γ *Plant Cost Factor*	2 441.7 (2 449.3)	2 263.1 (2 237.1)	2 990.2 (2 999.1)	2 459.9
Daily solar power [W]	11 342 (13 113)	11 090 (12 205)	12 232 (14 644)	13 161

Finally, the determined optimisation objectives are recalculated for the optimum case as reported in Table 5.5. In the process, the output daily solar power curve is determined as shown in Figure 5.12, to be discussed later. The final configuration of the optimum collector case is displayed in Figure 5.10. The variation in focal length is shown in the figure to provide context for the next section.

Table 5.6 Industrial pipes close to 56 mm OD (TPS, 2016; Industrial Business Link, 2016).

Nominal pipe size (NPS)	Nominal diameter (DN)	OD [in (mm)]
1 1/4	32	1.660 (42.16)
1 1/2	40	1.900 (48.26)
2	50	2.375 (60.33)
2 1/2	65	2.875 (73.03)
3	80	3.500 (88.90)

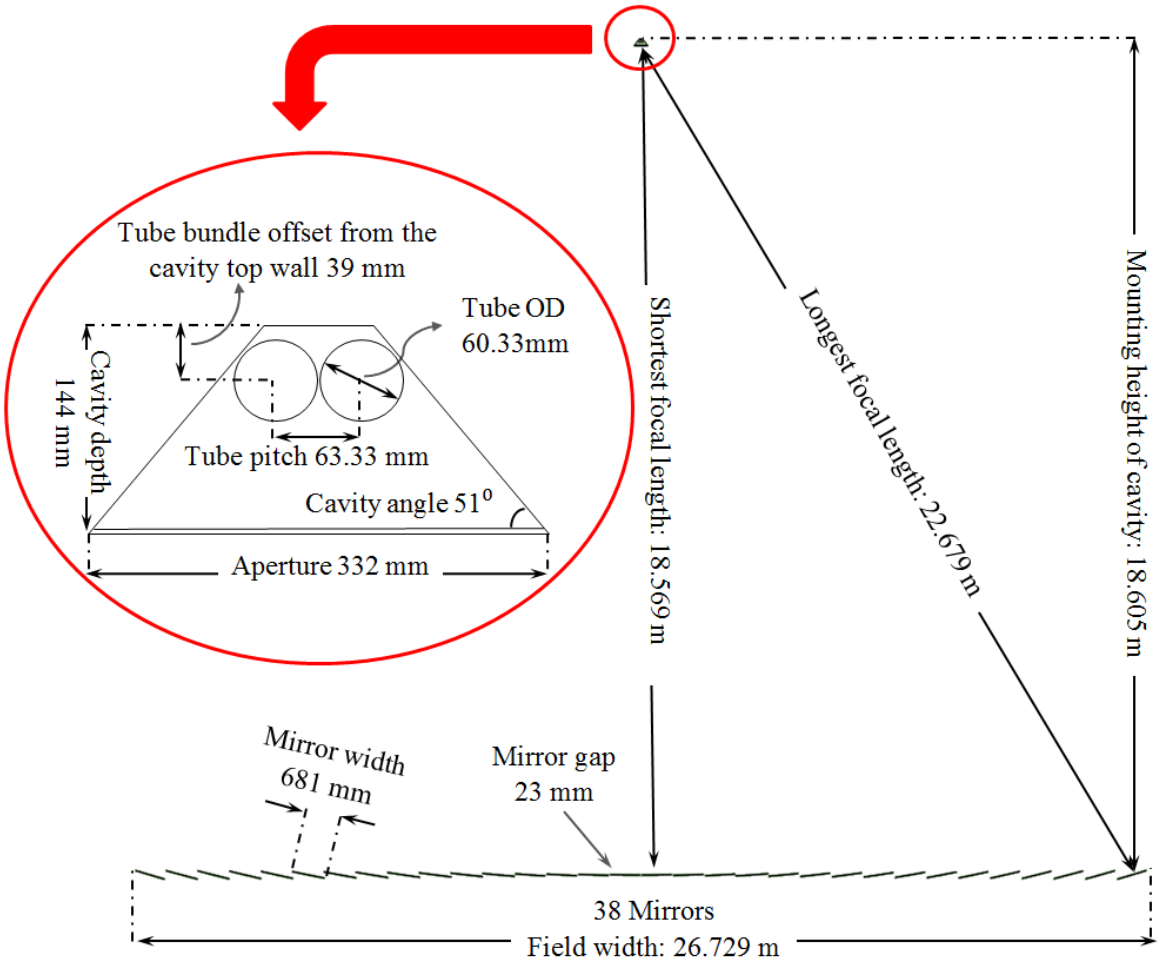

Figure 5.10. The configuration of the optimum LFC collector is displayed at 12 noon.

The optimisation process resulted in an ideal feasible optimum collector, where each individual mirror had a unique focal length. Theoretically, considering individual mirror focal lengths across the mirror field might seem beneficial because they lead to better solar ray

concentrations on the cavity tube bundle (higher solar output). However, in practice, it might be impractical, because the manufacturing process, assembly and maintenance process of the collector get more complicated. For example, the proposed optimum case requires 32 mirror rows, which means that at least 16 mirror manufacturing lines are needed to bend the mirrors properly and provide the required focal lengths, or 16 storage lines have to be considered for mirror spare parts. As a consequence, the process of mirror maintenance and collector assembly is complex. In addition to the complexity, this increases the final cost of the mirror field. Unfortunately, there is no economic model available to check how the complexity of the mirror field affects the economic cost of a field. However, it is possible to check the optical penalty of using a single focal length for the proposed optimum collector domain. Therefore, a supplementary optimisation study is conducted to improve the practicality of the proposed optimum ideal collector. In this study, an optical optimisation investigates the optimum fixed focal length for the entire proposed collector. It should be noted that only a typical summer day is considered in the study. The reader may wonder that why a day near one of the equinoxes (a spring or autumn day) was not chosen for this study as more representative. This study mainly focused on the approaches and methodology and integrating them in one optimisation platform. This study is intended to serve as an introduction of how to tackle an optimization problem of a CSP in general. Therefore, a more representative annual performance is outside the scope of this thesis but can be contained by constructing a total solar power based on a seasonal variation in the solar angle (down to almost 45° in winter) and then finding the fixed focal length that maximises annual performance.

The optimisation process, tools and loop in this case are the same as those described in Section 5.4.1 and Figure 5.3. However, instead of defining a set of design variables in the optimisation of multi-objective goals, only one independent variable (focal length) and one goal (daily solar power) are considered with the other variables held fixed at the values determined above. A focal length range of 10 to 50 m is allowed in the optimisation.

The optimisation converges after 618 iterations on the Kriging one-dimensional response surface when considering the default importance for the daily solar power objective. The result of this optimisation process is shown in Figure 5.11. A single maximum is observed at a focal length of 24 m.

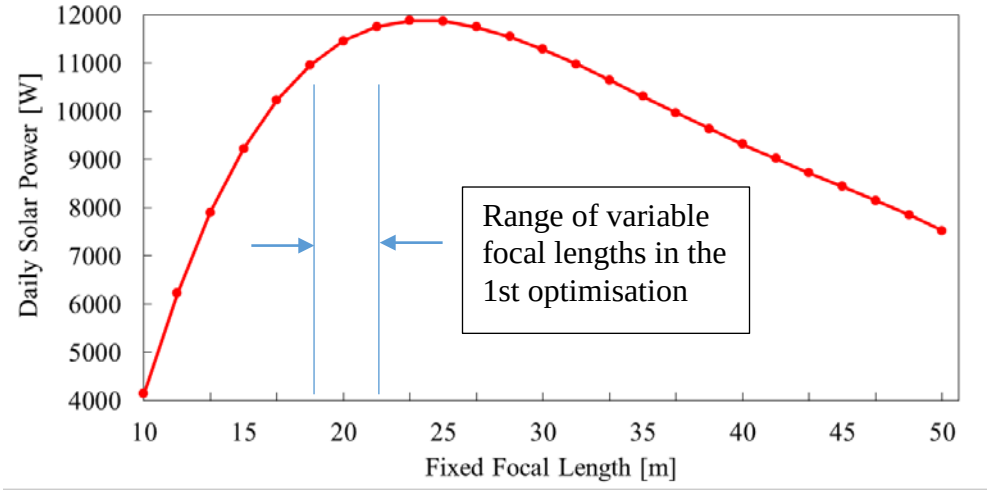

Figure 5.11. Response curve of independent variable vs. daily solar power

According to Figure 5.10, at a focal length of 24 m, all the mirrors across the field concentrate their reflected rays at the optimum point *beyond* the tube bundle. This concentration means that the tube bundle truncates the reflected rays from a mirror before the convergence of rays at a point. In other words, instead of point concentration rays on a point in the cavity, an optimum region of the tube bundle is hit by rays from each mirror (due to the truncation of the ray concentration cone). This phenomenon leads to the optimum harvested solar power on the tube bundle for this study (see Figure 5.11).

Finally, the daily solar power trends of both the fixed optimum focal length case and the case of individual focal lengths are displayed in Figure 5.12, confirming the compromise in total power as a result of the practical single focal length implementation.

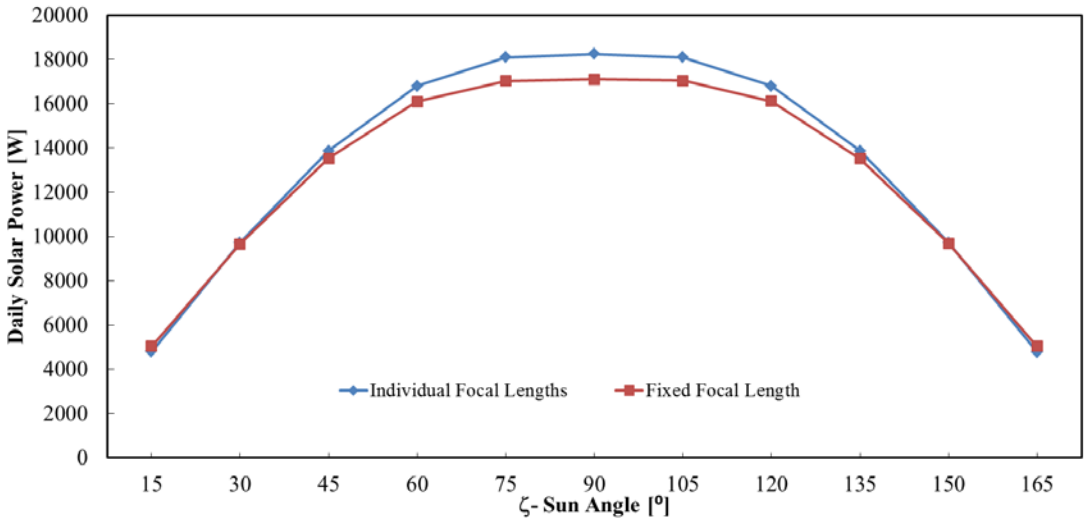

Figure 5.12. Solar power curve for both fixed and individual focal length cases throughout a day.

The interesting fact in Figure 5.12 is the reduction of the magnitude of daily solar power for the optimum collector from 13 161 (W) to 12 713 (W) for the fixed focal length case (3.4%). It is an expected phenomenon, because by using a single focal length for the entire mirror field, the mirrors defocus much more than in the case where each individual mirror focuses perfectly on the cavity receiver. This phenomenon is the penalty imposed on designing a much simpler and more practical LFC, but surprisingly, the penalty is not as severe as the author initially expected.

5.5.2 Optimisation results for the second problem (insulation optimisation for the proposed optimum cavity)

As displayed schematically in Figure 5.4, the cavity arrangement of the optimum collector case is obtained. However, the optimum insulation of this optimum cavity will find a balance between thermal heat losses from the cavity and the cost of the required insulation. Therefore, in this section, the results of the cavity insulation optimisation are presented. The optimisation problem was discussed in Section 5.4.2. The optimisation converges after 138 iterations when considering a higher importance for the heat loss objective and a default importance for the insulation area objective. The effect of independent parameters on optimisation objectives is presented in Figure 5.13. This figure is displayed for the introduced independent parameters in the feasible case column in Table 5.7. In this figure, the independent parameters are held constant at their optimum values when not plotted in a particular sub-figure. The effects of the side and top insulation thicknesses on the insulation area and heat loss objectives are shown in Figure 5.13a and Figure 5.13b respectively. Increasing both the side and top insulation thicknesses increases the insulation area, and consequently, insulation cost, while the heat loss from the cavity is reduced as expected (the response surface moves to less negative values, which means improved insulation). In Figure 5.13c, the effect of the third independent parameter of this optimisation (top insulation angle) on the insulation area and on heat loss is depicted, respectively. By increasing this angle, the insulation area increases. This is the expected effect and can be physically justified due to its definition. Indeed, by increasing this parameter, the top insulation shape transforms from a trapezoidal shape to a rectangular shape. The non-linear behaviour of the top insulation angle trend on heat loss is due to the singularity (sharp point in the physical shape) of the cavity's top corners, which is displayed in Figure 5.13c. A similar behaviour was observed in by Moghimi et al. (2015c). As displayed in this figure, by increasing the angle, the heat loss decreases.

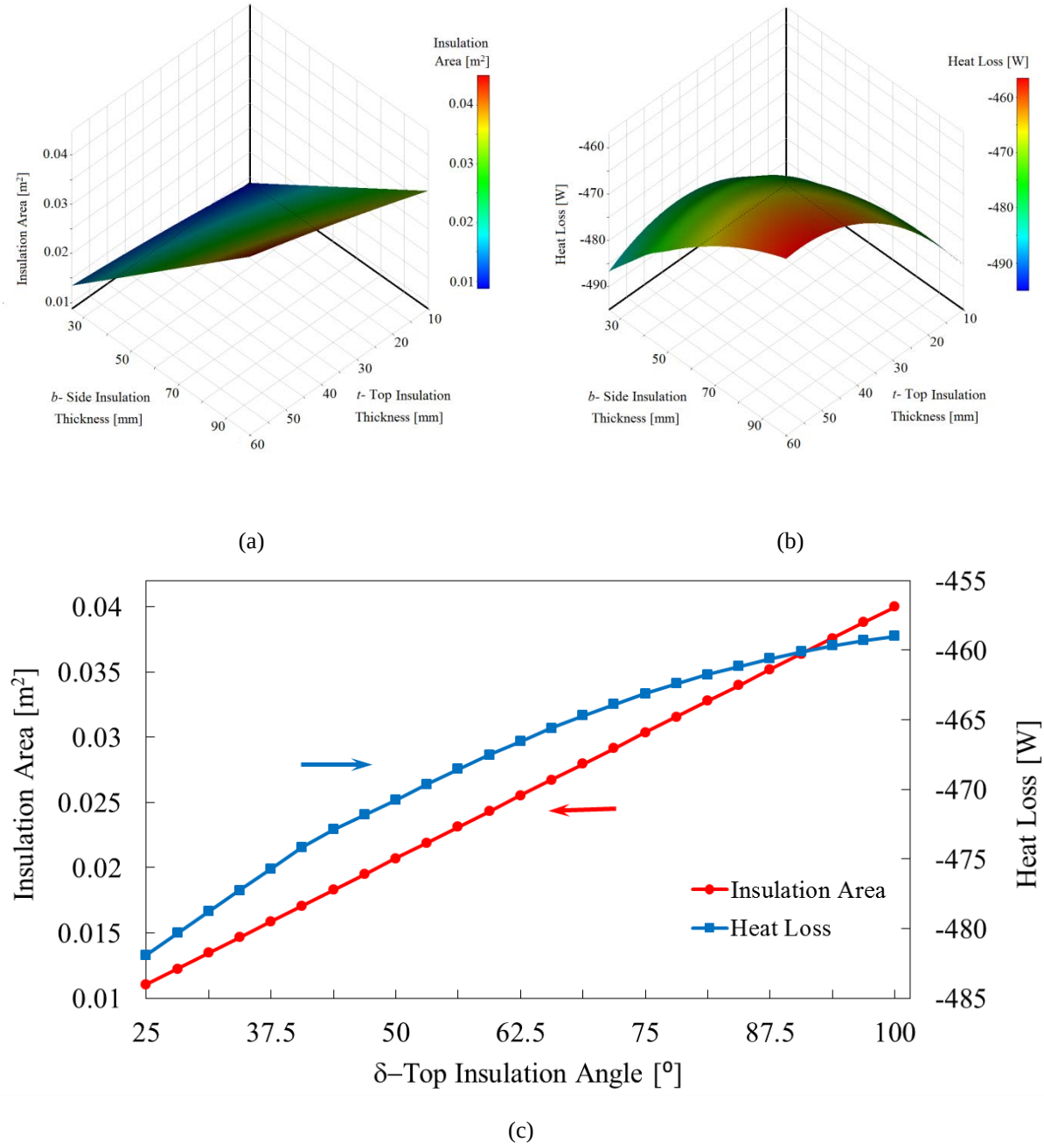

Figure 5.13. Response surfaces of objective goals vs. independent parameters.

a) Insulation area vs. side and top insulation thickness. b) Heat loss vs. side and top insulation thickness. c) Insulation area and heat loss vs. top insulation angle.

Finally, ANSYS DX reported values of three optimum points among all feasible Pareto optimal cases. Before further discussion of these optimum points, it has to be considered that the above observations are based on a temperature of 500 K in the tube bundle in the cavity, while in an LFC plant, the tube bundle temperature increases steadily across the plant length, depending on pipe routing, heat transfer fluid type, etc. Therefore, the optimal insulation layout could be different for different parts of the plant, based on the local tube bundle

temperature. As an attempt to deal with this issue, the optimisation process is replicated for two more tube bundle temperatures of 300 K and 400 K. The optimum points for all suggested temperatures (including 500 K) are tabulated in Table 5.7.

Because of the practicality considerations and reducing the complexity of plant control, it is conceivable to pick one insulation configuration for the whole plant. In addition, due to the fact that 500K is the critical condition among other cases which has significantly higher heat loss values from cavity, the results of optimisation for 500K were considered for further investigation. Moreover, since heat loss and its effects on the plant efficiency plays a role in the operating cost of the plant, this goal outweighs the insulation area as a parameter in the capital cost of the plant, therefore, the third candidate which has the minimum heat lossfor the 500 K case (critical condition) is selected for further study. However, due to manufacturing limitations, the candidate parameters are rounded off to feasible values as reported in the feasible case column in Table 5.7.

Finally, the CFD simulation is repeated for the feasible case and insulation area. The heat loss results are reported in Table 5.7 and Figure 5.14. In addition, Figure 5.14 displays the detailed CFD results of the proposed cavity with optimum insulation, evaluated at a tube temperature of 350 K and 500 K. The figure is depicted in the form of temperature contours overlaid with velocity vectors due to natural convection at different stages of a plant (350 K and 500 K tube temperature) under two different atmospheric conditions. In this figure, the effect of the atmospheric condition is simulated by changing the convective coefficient in the CFD simulations. The heat loss contributions from the different external boundaries are also displayed in Figure 5.14. As shown, by increasing the tube bundle temperature, the heat loss increases significantly due to the dominance of the radiation heat loss mechanism. This fact can also be seen in the contribution of re-radiation from the glass cover in comparison with the other heat loss from other boundaries (please see Figure 4.5). This phenomenon proves the claim of Section 4.3 about the dominance of the radiation mechanism heat loss. In addition, the negative slope stratification of temperature leads to low velocity in the bottom of the cavity and higher velocity close to the tubes, thereby reducing internal convection loss. This behaviour was also observed by Moghimi et al. (2015c). In addition, the velocity of the natural convective fluid flow is influenced more by the tube bundle temperature than by the atmospheric conditions, which is a physically expected phenomenon since the tube bundle temperature difference with environmental temperature is the main driver of the natural

convection phenomenon. Hence a higher tube bundle temperature results in higher velocity magnitudes.

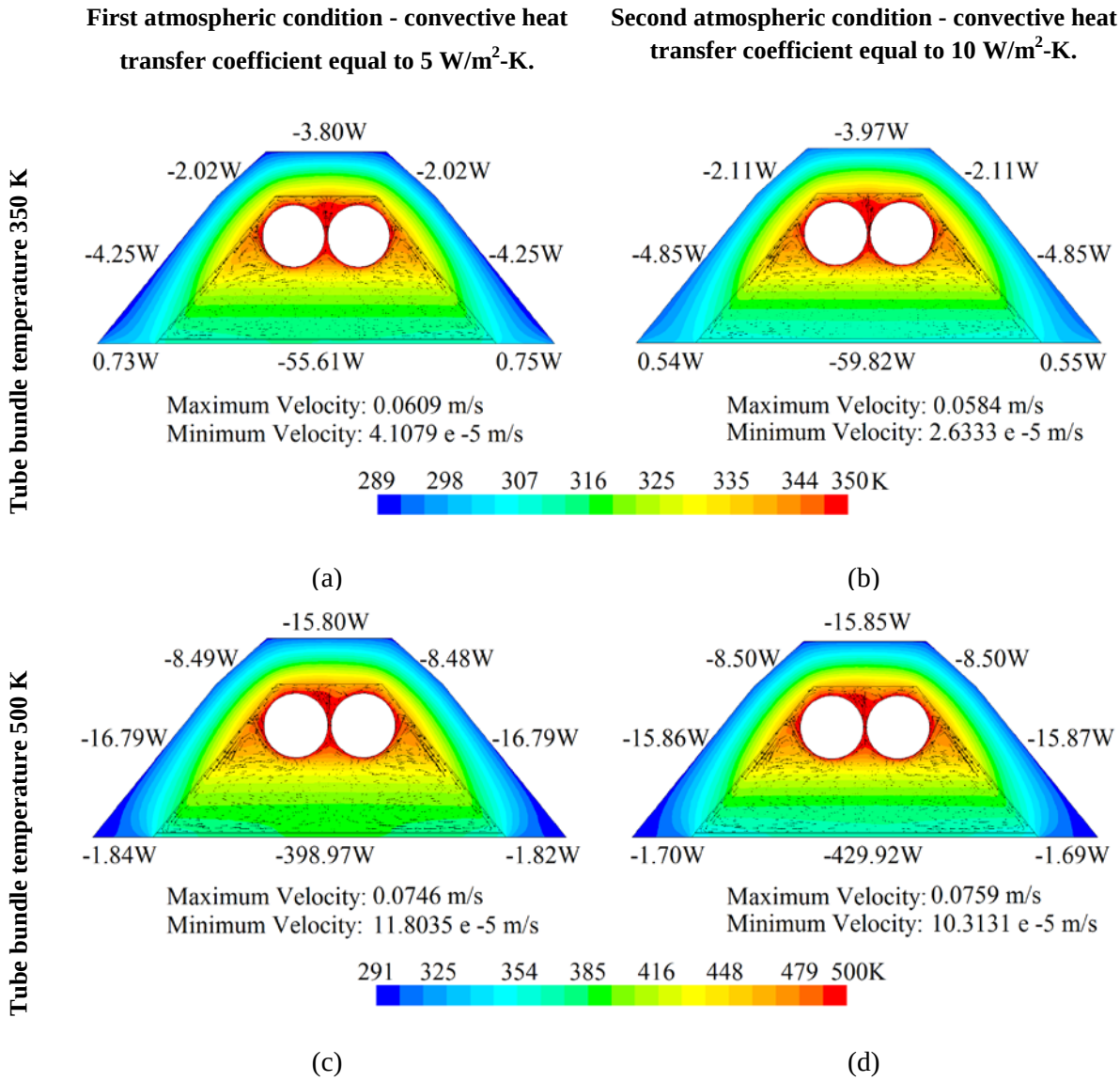

Figure 5.14. CFD temperature contours overlaid with velocity vectors for the cavity optimum case under different convective conditions and different tube bundle temperatures.

a) under first atmospheric condition with tube bundle temperature 350K. b) under second atmospheric condition with tube bundle temperature 350K. c) under first atmospheric condition with tube bundle temperature 500K. d) under second atmospheric condition with tube bundle temperature 500K.

Table 5.7 Candidate optimum points

	Tube temperature at 300 K			**Tube temperature at 400 K**			**Tube temperature at 500 K**			**Feasible case**
Parameters [unit]	**First candidate**	**Second candidate**	**Third candidate**	**First candidate**	**Second candidate**	**Third candidate**	**First candidate**	**Second candidate**	**Third candidate**	
Top insulation angle $-\delta$ [degree]	40.5	42.8	88.7	73.4	43.3	82.6	82.6	88.1	41.8	42
Top insulation thickness – t [mm]	12.3	30.1	57	52.1	46.3	51.9	51.9	48.6	42.5	43
Side insulation thickness – b [mm]	25.7	27	95.8	67.7	56.3	71.1	71.1	66.3	56.6	57
Optimisation objective	**Predicted (Calculated)**	**Predicted (Calculated)**	**Predicted (Calculated)**	**Predicted (Calculated)**	**Predicted (Calculated)**	**Predicted (Calculated)**	**Predicted (Calculated)**	**Predicted (Calculated)**	**Predicted (Calculated)**	**Calculated**
Heat loss from boundaries [W]	-5.139 (-7.042)	-5.080 (-6.502)	-4.604 (-5.020)	-163.6 (-163.5)	-166.6 (-166.9)	-163.0 (-163.0)	-460.2 (-460.5)	-462.3 (-462.6)	-468.5 (-469.4)	See Figure 5.13
Insulation area [m^2]	0.03799 (0.03799)	0.0352 (0.0352)	0.02744 (0.02744)	0.03573 (0.03573)	0.02744 (0.02744)	0.03799 (0.03799)	0.01166 (0.01166)	0.01239 (0.01239)	0.0525 (0.0525)	0.02766

5.6 CONCLUSION

Mathematical optimisation is a powerful tool to help reach engineering optimisation goals. In this study, the optimisation of an LFC with a multi-tube trapezoidal cavity configuration was conducted through a two-phase series optimisation process to find the most appropriate collector with minimum constructional cost and expense, highest solar absorption power throughout a day, as well as minimum heat loss. The first goal led to the economic optimisation of a collector (cheaper solar electricity generation from an LFC plant), while the other goals resulted in a more optically and thermally efficient collector (harvesting more solar energy throughout a day). The multiple objectives were incorporated using a multi-objective genetic algorithm to find multiple Pareto optima. If all competing objectives are not included in a design formulation, one objective might be optimised at the expense of other performance parameters. Some specific conclusions can be made regarding the work:

- The careful selection of geometrical parameters and splitting them into two groups that govern the geometry of collector and insulation allow the design optimisation process the freedom to suggest candidate optimum designs to achieve the objectives in a quick and reasonable approach. In a departure from a previous LFC cavity optimisation that studied a fixed number of tubes (Moghimi et al., 2015c), the current study treated the tube number as a variable. Interestingly, the optimal design led to a cavity with only two tubes, as a trade-off was found between cavity cost, optical performance and heat loss.

- Letting each LFC mirror have a unique focal length that was aimed at the cavity provided the highest optical performance. A more practical alternative was investigated by conducting an optimisation of the ideal fixed focal length of all the mirrors. Interestingly, a focal length *beyond* the tube centers was found, implying that all mirrors are slightly defocused for the optimal capture of solar energy. This configuration only resulted in a 3.4% reduction compared with the more costly individually focused mirrors.

- Heat loss estimation with reasonable accuracy and computational effort speeds up the calculation process of thermal modelling. This low-fidelity approach is one of the essential requirements for such a comprehensive optimisation study to run the simulation in a reasonable time frame and assess the relative importance in the optimisation process. The traditional use of the CFD simulation was replaced with a quicker approach (view area approach) with reasonable accuracy in the optical and thermal economic optimisation phase.

- With the help of the view area approach, the thermal objective goal of the collector optimisation was independent from a CFD calculation. This fact led to the suggestion of a series two-phase optimisation approach. In the first phase, the collector domain went through a thermal, optical and economic optimisation study, while the second phase used the results of the first phase to find the thermal and economic optimal insulation around the proposed cavity. This series approach sped up the process of optimisation by reducing the number of independent parameters in each phase, as well as reducing the complexity of the simulation.

- A limited investigation of varying the specified tube bundle temperature was conducted for the insulation optimisation to mimic the fact that an LFC cavity receiver would be operating at different temperatures, depending on the location along the length of the plant. Here, the radiation mechanism was again proved to be dominant, while natural convection velocities in the cavity were increased with increasing tube bundle temperatures.

6 CONCLUSION AND FUTURE WORK

6.1 CONCLUSION

Mathematical optimisation is a powerful tool to help reach engineering optimisation goals. In this study, the optimisation of an LFC with a multi-tube trapezoidal cavity configuration was conducted through a two-phase series optimisation process to find the most appropriate collector with minimum constructional cost and expense, highest solar absorption power throughout a day, as well as minimum heat loss. The first goal led to the economic optimisation of a collector (cheap solar electricity generation from an LFC plant), while the other goals resulted in a more optically and thermally efficient collector (harvesting more solar energy throughout a day). The multiple objectives were incorporated using a multi-objective genetic algorithm to find multiple Pareto optima. If all competing objectives are not included in a design formulation, one objective might be optimised at the expense of other performance parameters.

Some specific conclusions can be made regarding the work, as follows:

- The careful selection of geometrical parameters and splitting them into two groups that govern the geometry of collector and insulation allow the design optimisation process the freedom to suggest candidate optimum designs to achieve the objectives in a quick and reasonable approach.

- The thesis illustrated a systematic approach to solving the multi-objective optimisation problem. Various engineering tools were evaluated and carefully selected based on their accuracy and solution cost (both time and memory requirements). It was shown that the single optimisation environment as implemented in ANSYS WorkBench held significant advantages in integration and automation of the optimisation process. The latter is particularly significant because of the extensive list of objectives and independent design parameters considered.

- In the optimisation approach, both the Monte Carlo ray-tracing method and a view area approach to quantifying thermal radiation were shown to be cost effective and sufficiently accurate for optimisation purposes. The more costly CFD approach to ray tracing, while having some advantages, was found to be too expensive. However, CFD is used as tool in the optimisation of the insulation of an LFC cavity receiver. Accurate modelling of radiation in a CFD environment is achievable by reducing the numerical errors associated with finite volume solvers. The errors associated with ray effects can be reduced by increasing the control angle count of the model in the phi direction (N_ϕ), while the errors associated with false scattering can be reduced by increasing the spatial mesh count or using a higher-order DO model. It should be noted that these error reduction strategies should be used in conjunction for the most accurate results. In other words, the accuracy of the CFD solution is determined exclusively by whether the mesh is fine enough, whereas for radiation modelling, both the mesh and DO settings' refinement affect the solution. The model requirements can be determined through the mesh and DO independence studies.

- With the help of the view area approach, which was purely based on geometrical parameters, the thermal objective goal of the collector optimisation was independent from a CFD calculation. This fact led to the suggestion of a series two-phase optimisation approach. In the first phase, the collector domain went through a thermal, optical and economic optimisation study, while the second phase used the results of the first phase to find the thermal and economic optimal insulation around the proposed cavity. This series approach sped up the process of optimisation by reducing the number of independent parameters in each phase, as well as reducing the complexity of the simulation.

- The thermal analysis of the insulation using a CFD approach contained some unique and novel features to improve the accuracy:

- Firstly, for the solution of natural convection, the traditional use of the Boussinesq approximation was replaced with the more accurate incompressible ideal gas assumption to relate the density of the air in the cavity to the temperature.
- Secondly, all of the applicable heat transfer mechanisms were included in a coupled fashion in the CFD model. The insulation material was included in the model because its shape influenced the local conduction, especially in the cavity corner area. The selective absorption of the glass cover was incorporated with a dual-band grey approach into the discrete ordinates method in the CFD simulation. This method allowed for the capture of the greenhouse effect caused by the glass cover. The radiation properties of the cavity and absorber pipe surfaces were treated with a dual grey-band approach based on their surface roughness. This implied that they reflected radiation specularly at high wavelengths but diffusely for the rest of the spectrum. The dual band also enabled the modelling of selective coatings through the band-selective specification of surface absorptance and emissivity.
- Thirdly, the assumption of replacing the effect of solar irradiation with a specified outside temperature (and thereby assuming a uniform flux) was shown to be a good one by validating the approach against a more expensive and elaborate method that incorporated a non-uniform solar heat flux distribution on the pipes.

- A limited investigation of varying the specified tube bundle temperature was conducted for the insulation optimisation to mimic the fact that an LFC cavity receiver would be operating at different temperatures, depending on the location along the length of the plant. Here, the radiation mechanism was again proved to be dominant, while natural convection velocities in the cavity were increased with increasing tube bundle temperatures.

6.2 FUTURE WORK

The following items can receive attention in future work:

- Other objectives can be included in the optimisation formulation. An example is an exergy efficiency goal, which will influence the receiver geometry (particularly the number of tubes and tube diameters) determined in this study. Exergy calculations include the pumping power required to allow the optimal mass flux of HTF given a specific plant layout.

- The calculation of the solar power harvested by the LFC can be extended. For example, the annual optical performance for a specific location can be considered instead of the current daily solar power based on a summer's day. In this calculation, the current constant DNI can also be varied by the specific location's measured DNI profile during the parts of the season selected, thereby accounting for altitude and latitude and local weather patterns.

- Different layouts of the LFC absorber cavity can also be considered. For example, representing a new arrangement for a tube bundle can also lead to a more efficient cavity. Partial submergence of the tubes into the top insulation or using a staggered bundle arrangement is an example. In addition, cavity topology optimisation can give the optimisation process more freedom to come up with an optimum design.

- Finally, the optimisation process can be extended to include more design variables, especially those that are linked to a specific location and plant layout. These can, for example, include the routing of the HTF like using a cross-flow tube arrangement with the HTF flowing in different directions in the absorber. In addition, different HTFs can be considered to maximise the thermal performance of the plant as a whole.

REFERENCES

Abbas, R. (2015). Towards Cost Reduction in Concentrating Solar Power: Innovative Design for an Efficient Fresnel Based Solar Field. *Universidad Politécnica de Madrid*. PhD thesis.

Abbas, R., Munoz, J. & Martinez-Val, J.M. (2012). Steady-State Thermal Analysis of an Innovative Receiver for Linear Fresnel Reflectors. *Applied Energy*, **92**: 503-515.

Abbas, R., Munoz-Anton, J., Valdes, M. & Martinez-Val, J. (2013). High Concentration Linear Fresnel Reflectors. *Energy Conversion Management*, **72**: 60-68.

Alba Nova. (2016a). Available at: http://www.nrel.gov/csp/solarpaces/project_detail.cfm/projectID=221 [Last accessed: 13/04/2016].

Alba Nova. (2016b). Available at: http://www.cspworld.org/cspworldmap/alba-nova-1 [Last accessed: 13/04/2016].

ANSYS. (2006). Fluent UDF Manual, Version 6.3, *ANSYS Incorporated*.

ANSYS. (2013a). Fluent Theory Manual. Version 15, *ANSYS Incorporated*.

ANSYS. (2013b). ANSYS Workbench Manual. Version 15, *ANSYS Incorporated*.

ANSYS. (2013c). Design Exploration User Guide. Version 15. *ANSYS Incorporated*.

AREVA India Projects. (2016). Available at: http://india.areva.com/EN/home-1057/areva-s-solar-projects-in-india-areva-india.html [Last accessed: 13/04/2016].

Areva Solar. (2016). Available at: http://www.areva.com/EN/solar-220/arevasolar.html [Last accessed: 25/04/2016].

Aringhoff, R. & Brakmann, G. (2003). Solar Thermal Power 2020. *GreenPeace*, ISBN: 90-73361-82-6.

Augustin Fresnel 1. (2016a). Available at: http://www.nrel.gov/csp/solarpaces/project_detail.cfm/projectID=222 [Last accessed: 13/04/2016].

Augustin Fresnel 1. (2016b). Available at: http://www.cspworld.org/cspworldmap/augustin-fresnel-1 [Last accessed: 13/04/2016].

Augustin-Jean Fresnel. (2016). Available at: https://en.wikipedia.org/wiki/Augustin-Jean_Fresnel [Last accessed: 12/04/2016].

Bakker, A. (2013). Lecture 7 - Meshing, Applied Computational Fluid Dynamics.

Available at: http://www.bakker.org/dartmouth06/engs150/07-mesh.pdf [Last accessed: 9/10/2013].

Bansal, N.P. & Doremus, R.H. (1986). Handbook of Glass Properties. 1st edition, *Elsevier*.

Bejan, A. (1993). Heat Transfer. 1st edition, *John Wiley & Sons*.

Bennett, H.E. & Porteus, J.O. (1961). Relation Between Surface Roughness and Specular Reflectance at Normal Incidence. *U.S. Naval Ordnance Test Station*.

Bennett, S. (2007). The Encyclopedia of Energy. *Global Media*, Delhi, India.

Bernhard, R., Hein, S., De LaLaing, J., Eck, M., Eickhoff, M., Pfander, M., Morin, G. & Häberle, A. (2008a). Linear Fresnel Collector Demonstration on the PSA, Part I - Design, Construction and Quality Control. In: Presented at the 13th SolarPACES International Symposium, Las Vegas, US.

Bernhard, R., Laabs, H.G., De LaLaing, J., Eck, M., Eickhoff, M., Pottler, K., Morin, G., Heimsath, A., Georg, A. & Häberle, A. (2008b). Linear Fresnel Collector Demonstration on the PSA, Part II - Commissioning and First Performance Tests. In: Presented at the 13th SolarPACES International Symposium, Las Vegas, US.

Bergman, T.L., Lavine, A.S., Incropera, F.P. & Dewitt, D.P. (2011). Fundamentals of Heat and Mass Transfer. 7th edition, *John Wiley & Sons*.

Brunner, T.A. (2002). Forms of Approximate Radiation Transport. *SANDIA Report*, SAND2002-1778.

Bode, S.J. & Gauché, P. (2012). Review of Optical Software for Use in Concentrated Solar Power Systems. In: Presented at the 1st SASEC Conference, Stellenbosch, South Africa.

Canavarro, D., Collares-Pereira, M. & Lopes Guerreiro, L. (2011). Increasing the Efficiency of Conventional LFR Technologies: A New CLFR "Etendue-Matched" CSP Collector. In: Presented at the 17th SolarPACES International Symposium, Granada, Spain.

Cau, G. & Cocco, D. (2014). Comparison of Medium-Size Concentrating Solar Power Plants Based on Parabolic Trough and Linear Fresnel Collectors. *Energy Procedia*, **45**:101-110.

Cengel, Y.A. & Ghajar, A.J. (2010). Heat and Mass Transfer Fundamentals and Applications. 4th edition, *McGraw-Hill*, New York, US.

Centrale Solaire Thermodynamique Llo. (2016). Available at: http://www.cspworld.org/cspworldmap/centrale-solaire-thermoynamique-llo [Last accessed: 13/04/2016].

Chai, J.C., Lee, H.S. & Patankar, S.V. (1993). Ray Effect and False Scattering in the Discrete Ordinates Method. *Numerical Heat Transfer Part B: Fundamental*, **24**: 373-389.

Chai, J.C. & Patankar, S.V. (2006). Discrete-Ordinates and Finite-Volume Methods for Radiative Heat Transfer. Chapter in Handbook of Numerical Heat Transfer. 2nd edition, *John Wiley & Sons*.

Chaves, J. & Collares-Pereira, M. (2009). Primary Concentrator with Adjusted Etendue Combined with Secondaries Associated to Multiple Receivers and with Convection Reduction. *International Patent WO2009142524 A1*.

Chaves, J. & Collares-Pereira, M. (2010). Etendue-Matched Two-Stage Concentrator with Multiple Receivers. *Solar Energy*, **84**:196-207.

Cheng, Z.D., He, Y.L., Cui, F.Q., Xu, R.J. & Tao, Y.B. (2012). Numerical Simulation of a Parabolic Trough Solar Collector with Nonuniform Solar Flux Conditions by Coupling FVM and MCRT Method. *Solar Energy*, **86**: 1770-1784.

Choudhury, C. & Sehgal, H.K. (1986). A Fresnel Strip Reflector-Concentrator for Tubular Solar-Energy Collectors. *Applied Energy*, **23**:143-154.

CNIM eCare Solar Thermal Project. (2016). Available at: http://www.cspworld.org/cspworldmap/cnim-ecare-solar-thermal-project [Last Accessed: 13/04/2016].

Conlon, W.M. (2011). Superheated Steam from CLFR Solar Steam. In: Presented at the 17th SolarPACES International Symposium, Granada, Spain.

Craig, K.J., Harkness, A.W., Kritzinger, H.P. & Hoffmann, J.E. (2010). Analysis of AP1000 Reactor Vessel Cavity and Support Cooling. In: Presented at the European Nuclear Conference (ENC2010), Barcelona, Spain.

Dersch, J., Morin, G., Eck, M. & Häberle, A. (2009). Comparison of Linear Fresnel and Parabolic Trough Collector Systems: System Analysis to Determine Break Even Costs of Linear Fresnel Collectors. In: Presented at the 15th SolarPACES International Symposium, Berlin, Germany.

Dey, C.J. (2004). Heat Transfer Aspects of an Elevated Linear Absorber. *Solar Energy*, **76**: 243-249.

Dhall, A., Datta, A.K., Torrance, K.E. & Almeida, M.F. (2009). Radiative Heat Exchange Modeling Inside an Oven. *AIChE Journal: Bioengineering, Food, and Natural Products*, **55**: 2448-2460.

Dhursar. (2016). Available at: http://www.nrel.gov/csp/solarpaces/project_detail.cfm/projectID=272 [Last accessed: 13/04/2016].

DLR. (2007). WP 1: Review of CSP and Desalination Technology, DLR. Available at: http://www.dlr.de/tt/Portaldata/41/Resources/dokumente/institut/system/projects/aqua-csp/WP01_AQUA-CSP-Technologies-Final.pdf [Last accessed: 08/04/2016].

eCare Solar Thermal Project. (2016). Available at: http://www.nrel.gov/csp/solarpaces/project_detail.cfm/projectID=268 [Last accessed: 13/04/2016].

Effects of Global Warming. (2017). Available at: https://en.wikipedia.org/wiki/Effects_of_global_warming [Last accessed: 15/01/2017].

EIA. (2016). International Energy Outlook 2016. *Energy Information Administration.* Available at: http://www.eia.gov/forecasts/ieo/pdf/0484(2016).pdf [Last accessed: 29/06/2016].

European Commission (EC). (2002). SOLGATE Solar Hybrid Gas Turbine Electric Power System. *European Commission Contract*, ENK5-CT-2000-00333.

Facão, J. & Oliveira, A.C. (2011). Numerical Simulation of a Trapezoidal Cavity Receiver for a Linear Fresnel Solar Collector Concentrator. *Renewable Energy*, **36**: 90-96.

Feuermann, D. & Gordon, J.M. (1991). Analysis of a Two-Stage Linear Fresnel Reflector Solar Concentrator. *Journal of Solar Energy Engineering*, **113**: 272-279.

Flores Larsen, S., Altamirano, M. & Hernández, A. (2012). Heat Loss of a Trapezoidal Cavity Absorber for a Linear Fresnel Reflecting Solar Concentrator. *Renewable Energy*, **39**: 186-206.

Fresnel lens. (2016). Available at: https://en.wikipedia.org/wiki/Fresnel_lens [Last accessed: 04/04/2016].

Garcia, P., Ferriere, A. & Bezian, J.J. (2008). Codes for solar Flux Calculations Dedicated to Central Receiver System Applications: A Comparative Review. *Solar Energy*, **82**: 189-197.

GeoModel Solar. (2016). World Map of Direct Normal Irradiation. Available at: http://geosun.co.za/wp-content/uploads/2014/10/DNI-Solar-map-World.png [Last accesed: 29/06/2016].

Geyer, M., Lüpfert, E., Osuna, R., Esteban, A., Schiel, W., Schweitzer, A., Zarza, E., Nava, P., Langenkamp, J. & Mandelberg, E. (2002). EUROTROUGH: Parabolic Trough Collector Developed for Cost Efficient Solar Power Generation, In: Presented at the 11th SolarPACES International Symposium, Zurich, Switzerland.

Ghadirijafarbeigloo, Sh., Zamzamian, A.H. & Yaghoubi, M., (2014). 3-D Numerical Simulation of Heat Transfer and Turbulent Flow in a Receiver Tube of Solar Parabolic Trough Concentrator with Louvered Twisted-Tape Inserts. *Energy Procedia*, **49**: 373-380.

Göpple, H. (1999). Investitions- und Bilanztheorie. *Institut für Entscheidungstheorie und Unternehmensforschung,TU Karlsruhe*.

Goswami, R.P., Negi, B.S., Sehgal, H.K. & Sootha, G.D. (1990). Optical Designs and Concentration Characteristics of a Linear Fresnel Reflector Solar Concentrator with a Triangular Absorber. *Solar Energy Materials*, **21**: 237-251.

Government of Spain (2012). Royal Decree Law 1/2012, *Boletín Oficial del Estado*. Available at: http://www.boe.es/boe/dias/2012/01/28/pdfs/BOE-A-2012-1310.pdf [Last accessed: 04/04/2016].

Grena, R. & Tarquini, P. (2011). Solar Linear Fresnel Collector Using Molten Nitrates as Heat Transfer Fluid. *Energy*, **36**: 1048-1056.

Günther, M. (2016). Linear Fresnel Technology, *Enermena; Deutsches Zentrum fur Luft- und Raumfahrt.* Available at: http://www.energy-science.org/bibliotheque/cours/1361468614Chapter%2006%20Fresnel.pdf [Last accessed: 28/04/2016].

Guo, P., Li, J. & Wang, Y. (2014). Numerical Simulations of Solar Chimney Power Plant with Radiation Model. *Renewable Energy*, **62**: 24-30.

Häberle, A., Zahler, C., Lerchenmuller, H., Mertins, M., Wittwer, C., Trieb, F. & Dersch, J. (2002). The Solarmundo Line Focussing Fresnel Collector Optical and Thermal Performance and Cost Calculations, In: Presented at the 11th SolarPACES International Symposium, Zurich, Switzerland.

Hachicha, A.A. (2013). Numerical Modelling of a Parabolic Trough Solar Collector. *Polytechnic University of Catalunya*, PhD thesis.

He, Y.L., Xiao, J., Cheng, Z.D. & Tao, Y.B. (2011). A MCRT and FVM Coupled Simulation Method for Energy Conversion Process in Parabolic Trough Solar Collector. *Renewable Energy*, **36**: 976-985.

He, J., Qiu, Z., Li, Q. & Zhang. Y. (2012). Optical Design of Linear Fresnel Reflector Solar Concentrators. *Energy Procedia*, **14**: 1960-1966.

Heimsath, A., Cuevas, F., Hofer, A., Nitz, P. & Platzer, W. (2014). Linear Fresnel Collector Receiver: Heat Loss and Temperatures. *Energy Procedia*, **49**: 386-397.

Hongn, M., Larsen, S.F., Gea, M. & Altamirano, M. (2015). Least Square Based Method for the Estimation of the Optical End Loss of Linear Fresnel Concentrators. *Solar Energy*, **111**: 264-276.

Hoyer, M., Riffelmann, K.J., Benitez, D. & Nava, P. (2009). Performance and Cost Comparison of Linear Fresnel and Parabolic Trough Collectors. In: Presented at the 15th SolarPACES International Symposium, Berlin, Germany.

IEA. (2015a). Key World Energy Statistics 2015. *International Energy Agency.* Available at: https://www.iea.org/publications/freepublications/publication/KeyWorld_Statistics_2015.pdf [Last accessed: 29/06/2016].

IEA. (2015b). Energy and Climate Change: World Energy Outlook Special Report. *International Energy Agency.* Available at: http://www.iea.org/publications/freepublications/publication/WEO2015SpecialReportonEnergyandClimateChangeExecutiveSummaryUKversionWEB.PDF [Last accessed: 29/06/2016].

Incropera, F.P., DeWitt, D.P., Bergman, T.L. & Lavine, A.S. (2006). Fundamentals of Heat and Mass Transfer. 6th Edition, *John Wiley & Sons*.

Industrial Business Link. (2016). Standard Pipe Schedule and Inner Diameter. Available at: http://iblink.com.pk/Links-data/Free-gifts/2_PIPE%20SCHEDULE%20&%20INNER%20DIA%20DIMENSIONS.pdf [Last accessed: 27/06/2016].

Jance, M.J., Morrison, G.L. & Behnia, M. (2000). Natural Convection and Radiation within an Enclosed Inverted Absorber Cavity: Preliminary Experimental Results. In: Presented at the 38th ANZSES conference, Brisbane, Australia.

Jessee J.P. & Fiveland, W.A. (1997). Bounded, High Resolution Differencing Schemes Applied to the Discrete Ordinates Method. *Journal of Thermophysics and Heat Transfer*, **11**: 540-548.

Kennedy, C.E. (2002). Review of Mid- to High-Temperature Solar Selective Absorber Materials. *National Renewable Energy Laboratory*, NREL/TP-520-31267.

Khan, Md.K.A. (1999). Copper Oxide Coating for Use in a Linear Solar Fresnel Reflecting Concentrating Collector. *Renewable Energy*, **7**:603-608.

Kim, T. & Lee, H.S. (1989). Radiative Transfer in Two-Dimensional Anisotropic Scattering Media with Collimated Incidence. *Journal of Quantitative Spectroscopy & Radiative Transfer*, **42**: 225-238.

Kimberlina STTP. (2016). Available at: http://www.cspworld.org/cspworldmap/kimberlina-stpp [Last accessed: 13/04/2016].

Kimberlina Solar Thermal Power Plant. (2016). Available at: http://www.nrel.gov/csp/solarpaces/project_detail.cfm/projectID=37 [Last accessed: 13/04/2016].

Kost, C., Mayer, J.N., Thomsen, J., Hartmann, N., Senkpiel, C., Philipps, S., Nold, S., Lude, S., Saad, N. & Schlegl, T. (2013). Study: Levelized Cost of Electricity- Renewable

Energy Technologies. *Fraunhofer Institut for Solar Energy Systems ISE*. Available at: https://www.ise.fraunhofer.de/en/publications/veroeffentlichungen-pdf-dateien-en/studien-und-konzeptpapiere/study-levelized-cost-of-electricity-renewable-energies.pdf [Last accessed: 29/06/2016].

Lai, Y., Wu, T., Che, Sh., Dong, Z. & Lyu, M. (2013). Thermal Performance Prediction of a Trapezoidal Cavity Absorber for a Linear Fresnel Reflector. *Advances in Mechanical Engineering*. DOI: 10.1155/2013/615742.

LCOE. (2016). Available at: http://en.wikipedia.org/wiki/Cost_of_electricity_by_source [Last accessed: 28/04/2016].

Li, H. (2004). Reduction of False Scattering in Arbitrarily Specified Discrete Directions of the Discrete Ordinates Method. *Journal of Quantitative Spectroscopy & Radiative Transfer*, **86**: 215-222.

Liddell Power Station. (2016). Available at: http://www.nrel.gov/csp/solarpaces/project_detail.cfm/projectID=269 [Last accessed: 13/04/2016].

Liddell Solar Thermal Station. (2016). Available at: http://www.cspworld.org/cspworldmap/liddell-solar-thermal-station [Last accessed: 13/04/2016].

Lienhard IV, J.H. & Lienhard V, J.H. (2003). A Heat Transfer Textbook. 3rd edition, *Phlogiston Press*.

Lin, M., Sumathy, K., Dai, Y.J., Wang, R.Z. & Chen. Y. (2013). Experimental and Theoretical Analysis on a Linear Fresnel Reflector Solar Collector Prototype with V-Shaped Cavity Receiver. *Applied Thermal Engineering*, **51**: 963-972.

Llo Solar Thermal Project. (2016). Available at: http://www.nrel.gov/csp/solarpaces/project_detail.cfm/projectID=266 [Last accessed: 13/04/2016].

Loenen E. & Van der Tempel, L. (1996). Determination of Absorption Coefficients of Glasses at High Temperatures, by Measuring the Thermal Emission. *Philips Electronics N.V.*, Unclassified report, NL-UR 020/96.

Lovegrove, K. & Stein, W.S. (2012). Concentrating Solar Power Technology: Principles, Developments and Applications. *Woodhead Publishing*. ISSN: 2044-9364.

LS-OPT. (2003). User's Manual, s.l.. Version 2. *Livemore Software Technology Corporation*.

Manikumar, R. & Valan Arasu, A. (2014a). Heat Loss Characteristics Study of a Trapezoidal Cavity Absorber with and without Plate for a Linear Fresnel Reflector Solar Concentrator System. *Renewable Energy*, **63**: 98-108.

Manikumar, R. Valan Arasu A. & Jayaraj S. (2014b). Numerical Simulation of a Trapezoidal Cavity Absorber in the Linear Fresnel Reflector Solar Concentrator System. *International Journal of Green Energy*, **11**: 344-363.

Martinek. J. & Weimer, A.W. (2013). Evaluation of Finite Volume Solutions for Radiative Heat Transfer in a Closed Cavity Solar Receiver for High Temperature Solar Thermal Processes. *International Journal of Heat and Mass Transfe*r, **58**: 585-596.

Mathur, S.S., Kandpal, T.C. & Negi, B.S. (1991a). Optical Design and Concentration Characteristics of Linear Fresnel Reflector Solar Concentrators – I. Mirror Elements of Varying Width. *Energy Conversion and Management*, **31**: 205-219.

Mathur, S.S., Kandpal, T.C. & Negi, B.S. (1991b). Optical Design and Concentration Characteristics of Linear Fresnel Reflector Solar Concentrators – II. Mirror Elements of Equal Width. *Energy Conversion and Management*, **31**: 221-232.

Mathur, S.S., Negi, B.S. & Kandpal, T.C. (1990). Geometrical Designs and Performance Analysis of a Linear Fresnel Reflector Solar Concentrator with a Flat Horizontal Absorber. *International Journal of Energy Research*, **14**: 107-124.

Mazumder, R.K., Kandpal, T.C. & Mullick, S.C. (1987). Design and Optical Performance Analysis of Seasonally Adjusted Discrete Mirror Solar Concentrators. *Energy Conversion and Management*, **27**: 237-246.

Mellott, N.P., Brantley, S.L., Hamilton, J.P. & Pantano, C.G. (2001). Evaluation of Surface Preparation Methods for Glass. *Surface and Interface Analysis*, **31**: 362-368.

Mertins, M. (2009). Technische und Wirtschaftliche Analyse von Horizontalen Fresnel-Kollektoren. *University of Karlsruhe*. PhD thesis. In German.

Mills, D. & Morrison, G. (2000). Compact Linear Fresnel Reflector Solar Thermal Power Plants. *Solar Energy*, **68**: 263-283.

Miller, W.F. & Reed, W.H. (1977). Ray-Effect Mitigation Methods for Two-Dimensional Neutron Transport Theory. *Nuclear Science and Engineering*, **62**: 391-411.

Miller, R., Amatya, R., Brushett, F., Campanella, A., Kavlak, G., Macko, J., Maurano, A., Mcnerney, J., Osedach, T., Rodilla, P., Rose, A., Sakti, A., Steinfeld, E., Trancik, J. & Tuller, H. (2015). The Future of Solar Energy. *Massachusetts Institute of Technology*, ISBN: 978-0-928008-9-8.

Modest, M.F. (2013). Radiative Heat Transfer, 3rd edition, *Elsevier*.

Moghimi, M.A., Craig, K.J. & Meyer, J.P. (2014). Optimization of a Trapezoidal Cavity Absorber for the Linear Fresnel Reflector. In: Presented at the 2nd Southern African Solar Energy Conference (SASEC 2014), SASEC, Port Elizabeth, South Africa.

Moghimi, M.A., Rungasamy, A., Craig, K.J. & Meyer, J.P. (2015a). Introducing CFD in the Optical Simulation of Linear Fresnel Collectors. In: Presented at the 21st SolarPACES International Symposium, Cape Town, South Africa.

Moghimi, M.A., Craig, K.J. & Meyer, J.P. (2015b). A Novel Computational Approach to Combine the Optical and Thermal Modelling of a Linear Fresnel Collector Receiver. In: Presented at the 3rd Southern African Solar Energy Conference (SASEC 2015), Kruger National Park, South Africa.

Moghimi, M.A., Craig, K.J. & Meyer, J.P. (2015c). Optimization of a Trapezoidal Cavity Aabsorber for the Linear Fresnel Reflector. *Solar Energy*, **119**: 343-361.

Moghimi, M.A., Craig, K.J. & Meyer, J.P. (2015d). A Novel Computational Approach to Combine the Optical and Thermal Modelling of Linear Fresnel Collectors using the Finite Volume Method. *Solar Energy*, **116**: 407-427.

Moghimi, M.A., Craig, K.J. & Meyer, J.P. (2016a). Combined Thermal, Optical and Economic Optimization of a Linear Fresnel Collector. In: Presented at the 22nd SolarPACES International Symposium, Abu Dhabi, United Arab Emirates.

Moghimi, M.A., Craig, K.J., & Meyer, J.P. (2016b). Optimization of Insulation of a Linear Fresnel Collector In: Presented at the 22nd SolarPACES International Symposium, Abu Dhabi, United Arab Emirates.

Moghimi, M.A., Craig, K.J., & Meyer, J.P. (2016c). Optimization of Fixed Focal Length for Linear Fresnel Collector. In: Presented at 4th Southern African Solar Energy Conference (SASEC 2016), Stellenbosch, South Africa.

Montes, M.J., Abbas, R., Rovira, A., Martinez-Val, J.M. & Muñoz-Antón, J. (2012). Analysis of Linear Fresnel Collectors Designs to Minimize Optical and Geometrical Losses. In: Presented at the 18th SolarPACES International Symposium, Marrakech, Morocco.

Morin, G., Platzer, W., Eck, M., Uhlig, R., Häberle, A., Berger, M. & Zarza, E. (2006). Road Map towards the Demonstration of a Linear Fresnel Collector Using a Single Tube Receiver. In: Presented at the 13th SolarPACES International Symposium, Las Vegas, US.

Morin, G., Dersch, J., Eck, M., Häberle, A. & Platzer, W. (2009). Comparison of Linear Fresnel and Parabolic Trough Collector Systems: Influence of Linear Fresnel Collector Design Variations on Break-Even Cost. In: Presented at the 15th SolarPACES International Symposium, Berlin, Germany.

Morin, G., Dersch, J., Platzer, W. & Häberle. A. (2012). Comparison of Linear Fresnel and Parabolic Trough Collector Power Plants. *Solar Energy*, **86**:1-12.

Mutuberria, A., Monreal, A., Albert, A. & Blanco, M. (2011). Results of the Empirical Validation of Tonatiuh at Mini-Pegase CNRS-PROMES Facility. In: Presented at the 17th SolarPACES International Symposium, Granada, Spain.

NASA. (2016). Available at: http://climatekids.nasa.gov/review/concentrating-solar/ [Last accessed: 08/04/2016].

Natarajan, S.K., Reddy, K.S. & Mallick, T.K. (2012). Heat Loss Characteristics of Trapezoidal Cavity Receiver for Solar Linear Concentrating System. *Applied Energy*, **93**: 523-531.

Negi, B.S., Mathur, S.S. & Kandpal, T.C. (1989). Optical and Thermal Performance Evaluation of a Linear Fresnel Reflector Solar Concentrator. *Solar & Wind Technology*, **6**: 589-593.

Negi, B.S., Kandpal, T.C. & Mathur, S.S. (1990). Designs and Performance Characteristics of a Linear Fresnel Reflector Solar Concentrator with a Flat Vertical Absorber. *Solar & Wind Technology*, **7**: 379-392.

Nixon, J.D. & Davies, P.A. (2012). Cost-Exergy Optimisation of Linear Fresnel Reflectors. *Solar Energy*, **86**: 147-156.

Norton, B. (1992). Solar Energy Thermal Technology. *Springer-Verlag*, 1992.

Novatec-Solar. (2016). Available at: http://www.novatecsolar.com/ [Last accessed: 14/04/2016].

NREL. (2016). Available at: http://www.nrel.gov/csp/solarpaces/linear_fresnel.cfm [Last accessed: 29/04/2016].

PE1. (2016). Available at: http://www.nrel.gov/csp/solarpaces/project_detail.cfm/projectID=46 [Last accessed: 13/04/2016].

PE2. (2016). Available at: http://www.nrel.gov/csp/solarpaces/project_detail.cfm/projectID=159 [Last accessed: 13/04/2016].

Pitz-Paal, R., Dersch, J. & Milow, B. (2005). European Concentrated Solar Thermal Road Mapping (ECOSTAR). *DLR-Project EC contract SES6-CT-2003-50257*.

Pitz-Paal, R. (2011). High Temperature Solar Concentrators. *Encyclopedia of Life Support systems (EOLSS)*. Available at: www.eolss.net/ebooks/Sample%20Chapters/C08/E6-106-06-00.pdf [Last accessed: 08/04/2016].

Puerto Errado 1. (2016). Available at: http://www.cspworld.org/cspworldmap/puerto-errado-1 [Last accessed: 13/04/2016].

Puerto Errado 2. (2016). Available at: http://www.cspworld.org/cspworldmap/puerto-errado-2 [Last accessed: 13/04/2016].

Pye, J.D., Morrison, G.L. & Behnia, M. (2003a). Transient Modelling of Cavity Receiver Heat Transfer for the Compact Linear Fresnel Reflector. In: Presented at the 41st Annual Conference of ANZSES, Melbourne, Australia.

Pye, J.D., Morrison, G.L. & Behnia, M. (2003b). Convection Inside the Cavity Receiver of the CLFR Concentrating Solar Power System. In: Presented at the 7th Natural Convection Workshop, Sydney, Australia.

Pye, J.D., Morrison, G.L., Behnia, M. & Mills, D. (2003c). Modelling of Cavity Receiver Heat Transfer for the Compact Linear Fresnel Reflector. In: Presented at the ISES Solar World Congress, Göteborg, Sweden.

Pye, J.D. (2008). System Modelling of the Compact Linear Fresnel Reflector. *University of New South Wales*. PhD thesis.

Qiu, Y., He, Y.-L., Cheng, Z.-D. & Wang, K. (2015). Study on Optical and Thermal Performance of a Linear Fresnel Solar Reflector Using Molten Salt as HTF with MCRT and FVM Methods. *Applied Energy*, **146**: 162-173.

Rabl, A. (1976). Optical and Thermal Properties of Compound Parabolic Concentrators. *Solar Energy*, **18**: 497-511.

Rabl, A. (1985). Active Solar Collectors and their Applications. *Oxford University Press*, New York.

Ramankutty, M.A. & Crosbie, A.L. (1998). Modified Discrete-Ordinates Solution of Radiative Transfer in Three-Dimensional Rectangular Enclosures. *Journal of Quantitative Spectroscopy & Radiative Transfer*, **60**: 103-134.

Reynolds, D.J., Jance, M.J., Behnia, M. & Morrison, G.L. (2004). An Experimental and Computational Study of the Heat Loss Characteristics of a Trapezoidal Cavity Absorber. *Solar Energy*, **76**: 229-234.

Richter, C., Teske, S. & Nebrera, J. (2009). Concentrating Solar Power Global Outlook 2009, *Greenpeace; SolarPACES; ESTELA*. Available at: http://www.greenpeace.org/international/Global/international/planet-2/report/2009/5/concentrating-solar-power-2009.pdf [Last accessed: 08/04/2016].

Roccia, J.P., Piaud, B., Coustet, C., Caliot, C., Guilliot, E., Flamant, F. & Deltorre, J. (2012). SOLFAST, a Ray-Tracing Monte Carlo Software for Solar Concentrating Facilities. *Journal of Physics conference series*, 369, 012029.

Ross, M.J. (2013). How the 1973 Oil Embargo Saved the Planet. *Foreign Affairs*. Available at: https://www.foreignaffairs.com/articles/north-america/2013-10-15/how-1973-oil-embargo-saved-planet [Last accessed: 04/04/2016].

Rungasamy, A.E., Craig, K.J. & Meyer, J.P. (2015). 3-D CFD Modeling of a Slanted Receiver in a Compact Linear Fresnel Plant with Etendue-Matched Mirror Field. *Energy Procedia*, **69**: 188-197.

Sahoo, S.S., Singh, P.L. & Banerjee, R. (2012). Analysis of Heat Losses from a Trapezoidal Cavity Used for Linear Fresnel Reflector System. *Solar Energy*, **86**: 1313-1322.

Sahoo, S.S., Varghese, S.M., Kumar, C.S., Viswanathan, S.P., Singh, S. & Banerjee, R. (2013a). Experimental Investigation and Computational Validation of Heat Losses from the Cavity Receiver Used in Linear Fresnel Reflector Solar Thermal System. *Renewable Energy*, **55**: 18-23.

Sahoo, S.S., Singh, S. & Banerjee, R. (2013b). Steady State Hydrothermal Analysis of the Absorber Tubes Used in Linear Fresnel Reflector Solar Thermal System. *Solar Energy*, **87**: 84-95.

Schlichting, H. (1979). Boundary-Layer Theory. 7th Edition, *McGraw-Hill Book Company*, New York.

Selig, M. & Mertins, M. (2010). From Saturated to Superheated Direct Solar Steam Generation - Technical Challenges and Economical Benefits. In: Presented at the 16th SolarPACES International Symposium, Perpignan, France.

Sharma, V., Nayak, J.K. & Kedare, S.B. (2015). Effects of Shading and Blocking in Linear Fresnel Reflector Field. *Solar Energy*, **113**: 114-138.

Silvi, C. (2009). The Pioneering Work on Linear Fresnel Reflector Concentrators (LFCs) in Italy. In: Presented at the 15th SolarPACES International Symposium, Berlin, Germany.

Singh, P.L., Ganesan, S. & Yadav, G.C. (1999). Technical Note: Performance Study of a Linear Fresnel Concentrating Solar Device. *Renewable Energy*, **18**: 409-416.

Singh, P.L., Sarviya, R.M. & Bhagoria, J.L. (2010a). Heat Loss Study of Trapezoidal Cavity Absorbers for Linear Solar Concentrating Collector. *Energy Conversion and Management*, **51**: 329-337.

Singh, P.L., Sarviya, R.M. & Bhagoria, J.L. (2010b). Thermal Performance of Linear Fresnel Reflecting Solar Concentrator with Trapezoidal Cavity Absorbers. *Applied Energy*, **87**: 541–550.

Singh, R.N., Mathur, S.S. & Kandpal, T.C. (1980). Some Geometrical Design Aspects of a Linear Fresnel Reflector Concentrator. *International Journal of Energy Research*, **4**:59-67.

Solarflame. (2016). Available at: http://www.solarflame.co.jp/english/ [Last accessed: 08/04/2016].

SolarPACES. (2000). Catalog of Solar Heliostats. *IEA-Solar Power and Chemical Energy Systems*, Technical Report No. III - 1/00 2000.

SolarPACES. (2011a). Technology Characterization Solar Dish Systems. Available at: http://www.solarpaces.org/images/pdfs/solar_dish.pdf. [Last accessed: 08/04/2016].

SolarPACES. (2011b). Technology Characterization Solar Power Tower. Available at: http://www.solarpaces.org/images/pdfs/solar_tower.pdf [Last accessed: 08/04/2016].

SolarPACES. (2011c). Technology Characterization Solar Parabolic Trough. Available at: http://www.solarpaces.org/images/pdfs/solar_trough.pdf [Last accessed: 08/04/2016].

SolTrace. (2016). SolTrace Optical Modeling Software. Available at: http://www.nrel.gov/csp/soltrace [Last accessed: 03/05/2016].

Sootha, G.D. & Negi, B.S. (1994). A Comparative Study of Optical Designs and Solar Flux Concentrating Characteristics of a Linear Fresnel Reflector Solar Concentrator with Tubular Absorber. *Solar Energy Materials and Solar Cells*, **32**: 169-186.

Spiewak, I. (1996). Strategy for Solar Thermal Energy: Research, Development and Industrial Applications. *European Commission Joint Research Center*, EUR 17276 EN.

SUNCNIM. (2017). Available at: http://www.suncnim.com/ [Last accessed: 31/01/2017].

TIASA. (2001). Thermal Insulation Handbook. *Thermal Insulation Association of Southern Africa*.

TieSOL. (2016). TieSOL: Software for Solar Thermal Plants. Available at: http://www.tietronix.com/sites/default/files/Solar_DataSheet.pdf [Last accessed: 03/05/2016].

Tonatiuh. (2016). Tonatiuh. Available at: http://code.google.com/p/tonatiuh/ [Last accessed: 03/05/2016].

TPS. (2016). Tube and pipe sizes. Available at: http://www.tpsd.de/downloads/allgemein/gen_tube_und_pipes_sizes_6th_edition_18.pdf [Last accessed: 27/06/2016].

Trieb, F., Schillings, C., O'Sullivan, M., Pregger, T. & Hoyer-Klick, C. (2009). Global Potential of Concentrating Solar Power. In: Presented at the 15th SolarPACES International Symposium, Berlin, Germany.

UNFCCC. (2009). Copenhagen Accord, The Conference of the Parties to the United Nations Framework Convention on Climate Change (UNFCCC). Available at: http://unfccc.int/resource/docs/2009/cop15/eng/11a01.pdf [Last accessed: 29/06/2016].

United Nations. (2016a). Kyoto Protocol. Available at: https://en.wikipedia.org/wiki/Kyoto_Protocol [Last accessed: 04/07/2016].

United Nations. (2016b). United Nations Climate Change Conference COP 21. Available at: https://en.wikipedia.org/wiki/2015_United_Nations_Climate_Change_Conference [Last accessed: 04/07/2016].

Velázquez, N., García-Valladares, O., Sauceda, D. & Beltrán, R. (2010). Numerical Simulation of a Linear Fresnel Reflector Concentrator Used as Direct Generator in a Solar-Gas Cycle. *Energy Conversion and Management*, **51**: 434-445.

Walker, G.S. (2013). Development of a Low Cost Linear Fresnel Solar Concentrator. *Stellenbosch University*. MEng dissertation.

Wendelin, T., Dobos, A. & Lewandowski, A. (2013). SolTrace: A Ray-Tracing Code for Complex Solar Optical Systems. *NREL – Technical Report*, 303, 275-300.

White, F.M. (2006). Viscous Fluid Flow. 3rd Edition, *McGraw Hill*.

Winston, R. & Hinterberger, H. (1975). Principles of Cylindrical Concentrators for Solar Energy. *Solar Energy*, **17**, 255-258.

Wirz, M., Petit, J., Haselbacher, A. & Steinfeld, A. (2014). Potential Improvements in the Optical and Thermal Efficiencies of Parabolic Trough Concentrators. *Solar Energy*, **107**: 398-414.

Xia Shuai, X.L. & Tan, H.P. (2008). Radiation Performance of Dish Solar Concentrator/Cavity Receiver Systems. *Solar Energy*, **82**: 13–21.

Zahler, C., Schwind, T., Häberle, A. & Berger, M. (2009). Direct Steam Production in a Linear Concentrating Fresnel Collector. In: Presented at the 4th European Solar Thermal Energy Conference (ESTEC), Munich, Germany.

Zhu, G., Wendelin, T., Wagner, M.J. & Kutscher, C. (2014). History, Current State, and Future of Linear Fresnel Concentrating Solar Collectors. *Solar Energy*, **103**: 639-652.

ADDENDUM I SIMULATION IN SOLTRACE

Because of a lack of proper documentation in defining the location and orientation of reflective and absorbing elements in SolTrace, the following description is provided.
Consider the LFC layout in Figure I.1, where each mirror element rotation angle (and hence each mirror normal vector) has to be set, so that reflected rays impinge on a specific point (target point). This target point is different from the aim point in SolTrace. For the definition of the N elements' aiming points, an imaginary plane is defined in Figure I.1 (see "Aiming plane"). This plane is defined for the mirror elements and is normal to the cavity cross-section, which passes through the target point at a distance *H* above the centre of the mirror field. The target vector $\vec{t}$ is defined from the centre of the N_{th} element to the target point in the cavity. The sun vector $\vec{s}$ is defined from the centre of the N_{th} mirror element to the sun position.

So far, one target point, *N* target vectors and *N* sun vectors have been defined for modelling in SolTrace. However, when considered in the global coordinate system, the distance between the sun and the mirror field is many orders (11) of magnitude larger than the distance between adjacent mirrors and the target point, implying that the *N* sun vectors can be reduced to only one vector. This sun vector is defined as the vector between the origin of the global coordinate on the ground and the sun position. By assuming perfect reflection, the impinging ray on a surface has the same angle relative to the face normal as that between the face normal and the reflected ray, therefore the normal unit vector (Figure I.1) is defined as:

$$\hat{n}_{N_{th}\ Element} = \frac{\vec{s} + \vec{t}_{N_{th}\,Element}}{\sqrt{\left|\vec{s}\right|^2 + \left|\vec{t}_{N_{th}\,Element}\right|^2 + 2\left(\vec{s}.\vec{t}_{N_{th}\,Element}\right)}} \qquad \textbf{(I.1)}$$

The SolTrace aim point of an element is the global coordinates of the intersection of its normal vector with the aiming plane, therefore:

$$X_{Aim\ Point\ for\ N_{th}\ Element} = X_{\ Centre\ of\ N_{th}\ Element} + \frac{x_{component\ of\ \hat{n}_{N_{th}\ Element}}}{z_{component\ of\ \hat{n}_{N_{th}\ Element}}} * H \qquad \textbf{(I.2)}$$

$$Y_{Aim\ Point\ for\ N_{th}\ Element} = Y_{\ Centre\ of\ N_{th}\ Element} + \frac{y_{component\ of\ \hat{n}_{N_{th}\ Element}}}{z_{component\ of\ \hat{n}_{N_{th}\ Element}}} * H$$

$$Z_{Aim\ Point\ for\ N_{th}\ Element} = Z_{\ Centre\ of\ N_{th}\ Element} + \frac{z_{component\ of\ \hat{n}_{N_{th}\ Element}}}{z_{component\ of\ \hat{n}_{N_{th}\ Element}}} * H$$

Using Equation (I.2), the aim points are defined in SolTrace. These formulae are only valid for the mirror elements. For the other elements in the cavity enclosure (cavity walls and pipes), the aiming plane, the distance between the aiming plane and the centre of that element are not the same as those defined for the mirror elements.

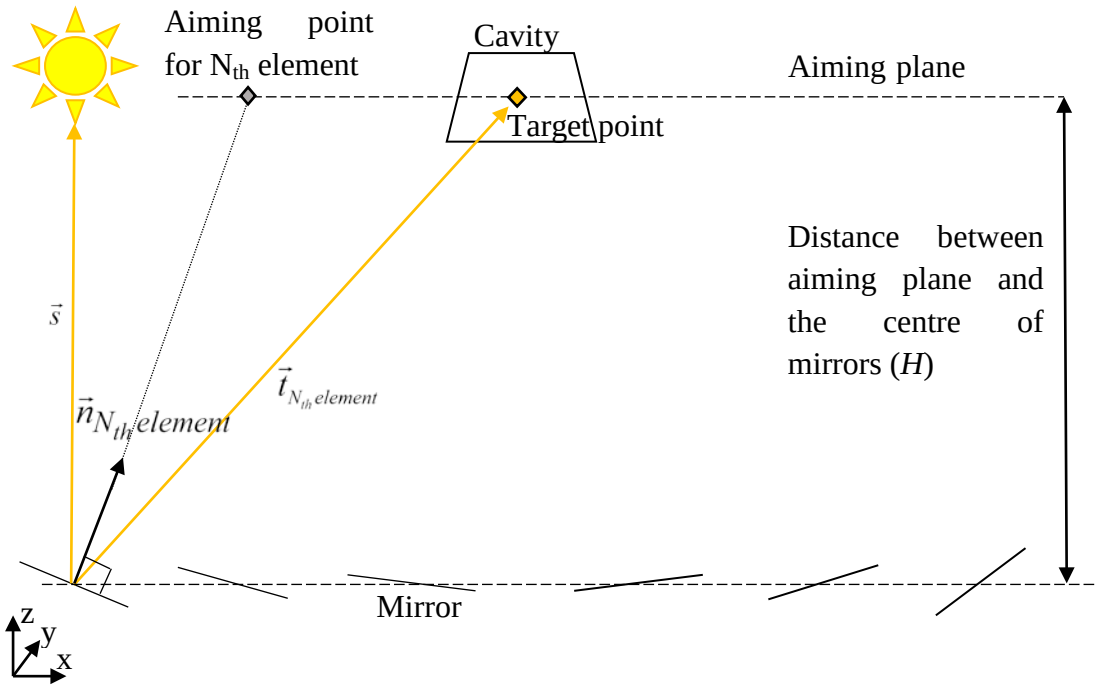

Figure I.1. Effects of schematic of LFC modelling in SolTrace

ADDENDUM II RADIATION GOVERNING EQUATION IN CFD

Writing incorporation of all heat transfer mechanisms in energy conservation equation

$$\rho c_v \frac{DT}{Dt} = \nabla.(k\nabla T) - \nabla.q_R - p\nabla.\nu + \mu\Phi + \dot{Q}''' \quad \textbf{(II.1)}$$

where the summation of the first two terms on the right-hand side is the total heat flux vector, which contains conductive heat flux (k thermal conductivity and T temperature field) and radiative heat flux, the next two terms on the right-hand side describe work due to normal and shear surface stresses (ν is the velocity field, p is the pressure field, μ is the viscosity and Φ is a dissipation function, which is a mathematical definition to present conversion of mechanical energy to heat). The last term on the right-hand side is a heat source or sink of energy in a medium. When considering the modelling of solar radiation using an FV CFD code, the energy equation can be reduced to:

$$\rho c_v \frac{DT}{Dt} = \nabla.(k\nabla T) - \nabla.q_R \quad \textbf{(II.2)}$$

with the last term requiring special attention. As mentioned by Modest (2013), from a physical viewpoint, the net loss of radiative energy from a control volume is equal to emittance of energy from that volume minus the absorbed incident radiation to it. Therefore, the radiative transfer equation (RTE) should be considered in conjunction with the energy conservation equation to determine the last term of Equation (II.2) ($\nabla.q_R$).

The RTE describes the balance of energy through the interaction of emission, absorption and scattering in a participating medium. Imagine a beam with a radiative intensity of $I_\lambda(\vec{r},\vec{s})$, which is a function of the spectral variable (λ), position ($\vec{r}$) and direction ($\vec{s}$), and which travels in an absorbing, scattering and emitting medium in the above-mentioned direction. On the one hand, the beam energy decreases due to absorption and its scattering from its initial trajectory to other directions (out-scattering), while on the other hand, its energy increases due to the medium volume thermal radiation emission and scattering from

other trajectories towards its trajectory (in-scattering). Mathematically, this is expressed as (Modest, 2013):

$$\nabla.\left(I_\lambda\left(\vec{r}.\vec{s}\right)\vec{s}\right)+\beta_\lambda I_\lambda\left(\vec{r}.\vec{s}\right)=a_\lambda n^2 I_{b\lambda}+\frac{\sigma_{s,\lambda}}{4\pi}\int_0^{4\pi} I_\lambda\left(\vec{r}.\vec{s}'\right)\phi\left(\vec{s}.\vec{s}'\right)d\Omega' \qquad \textbf{(II.3)}$$

I_λ is the radiation intensity, a_λ is the absorption coefficient, $\beta_\lambda = a_\lambda + \sigma_{s,\lambda}$ the combination of the absorption and scattering coefficients, and Ω' the solid angle. The scattering coefficient σ_s, the scattering phase function ϕ, and the refractive index *n* are assumed to be independent of wavelength.

In Equation (II.3), $I_{b\lambda}$ is the blackbody emission in the wavelength band per unit solid angle, which is defined as:

$$I_{b\lambda}=\left[F\left(0\to n\lambda_2 T\right)-F\left(0\to n\lambda_1 T\right)\right]n^2\frac{\sigma T^4}{\pi} \qquad \textbf{(II.4)}$$

where T is the local temperature, σ the Stefan-Boltzmann constant, and $F\left(0\to n\lambda_2 T\right)$ is the fraction of radiant energy emitted by the blackbody in the wavelength interval from 0 to λ as defined by the Planck distribution function or blackbody radiation function (Cengel & Ghajar, 2010).

The summation of all terms on the right-hand side of Equation (II.3) is called the source term. Moreover, the difference between incident and outgoing intensity is defined as the radiative flux, defined for a non-grey medium as:

$$q_R\left(r\right)=\int_0^\infty\int_0^{4\pi} I_\lambda\left(\vec{r}.\vec{s}\right)\vec{s}\,d\Omega' d\lambda\,. \qquad \textbf{(II.5)}$$

The mentioned flux is the flux at physical boundaries of the computational domain. However, for a calculating the net radiative energy which is withdrawn from each volume element, a new term (the divergence of heat flux) is defined. This term is calculated by

double integration of the RTE equation over all solid angles over all wavelengths, as follows:

$$\nabla .q_R = \int_0^{\infty} a_\lambda \left(4\pi I_{b\lambda} - \int_0^{4\pi} I_\lambda (\bar{s}') d\Omega' \right) d\lambda . \qquad \textbf{(II.6)}$$

In summary, in the radiative domain, the RTE equation is coupled with the energy equation and for finding a computational solution in such a domain, the radiation intensity in the domain depends on the temperature field and vice versa.

ADDENDUM III RADIATIVE SURFACE PROPERTIES AND THEIR SIMULATION IN CFD

In radiation analysis, four radiative properties (absorptance α, emittance ε, reflectance ρ and transmittance τ) must be specified for each surface. For local thermal equilibrium of a surface and the adjacent fluid layer, Kirchoff's law reduces the properties to three, because in each wavelength band:

$$\alpha_\lambda = \varepsilon_\lambda \qquad \textbf{(III.1)}$$

Based on the definition of the radiative properties of a surface, in each wavelength band, the following relation holds:

$$\alpha_\lambda + \rho_\lambda + \tau_\lambda = 1 \qquad \textbf{(III.2)}$$

The transmission into an opaque surface is zero by definition, implying that for an opaque wall:

$$\rho_\lambda = 1 - \varepsilon_\lambda \qquad \textbf{(III.3)}$$

The reflected energy can be reflected either specularly (in one direction as for a mirror) or diffusely, due to surface roughness. Both types of reflections have the same amount of total energy implying that the diffuse reflection in any direction is less that the total specular amount. In radiation terminology, a rough surface is a surface of which the height of its roughness is much larger than the incident radiation wavelength. Therefore, if the root mean square (RMS) surface roughness is less than incident radiation wavelength, then the surface acts as specular (Bennett & Porteus, 1961), else it acts as diffuse.

Diffuse and specular reflection is defined in ANSYS Fluent using a diffuse fraction parameter f_d for each band. If f_d equals one, it means purely diffuse reflection whereas a zero value implies pure specular reflection for that band.

For, non-grey opaque walls, by combining Kirchoff's law and the radiative surface energy balance, the incident radiative heat flux over a surface would be:

$$q_{in,\lambda} = \Delta\lambda \int_{\vec{s}.\vec{n}>0} I_{in,\lambda}\, \vec{s}.\vec{n}\, d\Omega \qquad \textbf{(III.4)}$$

where $\vec{n}$ is the surface normal unit vector. The net radiative flux leaving the surface in a band is:

$$q_{out,\lambda} = f_d\,(1-\varepsilon_{w\lambda})q_{in,\lambda} + (1-f_d\,)(1-\varepsilon_{w\lambda})q_{in,\lambda} + \varepsilon_{w\lambda}\left[F(0\rightarrow n\lambda_2 T) - F(0\rightarrow n\lambda_1 T)\right]n^2\sigma {T_w}^4 \qquad \textbf{(III.5)}$$

where $\varepsilon_{w\lambda}$ is the wall emissivity in the band. At the wall, the boundary intensity for all outgoing directions in a specific band $\Delta\lambda$ is given by:

$$I_{0\lambda} = \frac{q_{out,\lambda}}{\pi\Delta\lambda} \qquad \textbf{(III.6)}$$

It should be considered that for a non-grey diffuse semi-transparent wall, the heat flux on the two sides of a medium is calculated using Equations (III.5) and (III.6) for each medium, while the incident intensity I_{in} is calculated from a complicated mathematical equation (omitted for brevity), which is related to the refractive indices for that medium.

ADDENDUM IV DO SHORTCOMINGS AND OVERCOMING THEM IN CFD

The numerical procedure which was considered for solving the RTE inside a domain is the discrete ordinate (DO) method or S_N approximation as introduced by Modest (2013) and implemented in ANSYS Fluent (ANSYS, 2013a) as S_2. "Ordinate" refers to a direction in hemispherical space. For each ordinate passing in one direction, there will be another ordinate in the opposite direction. For this reason, there will be an even number of directions in the S_N approximation.

In a 2-D simulation in ANSYS Fluent using the S_2, each quadrant of angular space is discretised into $N_\theta \times N_\phi$ solid angles (control angles) with a fixed vector direction $\vec{s}$ in the global Cartesian system (see Figure IV.1). For 1-D, $2 \times N_\theta \times N_\phi$ directions of the RTE equations are solved, for 2-D, $4 \times N_\theta \times N_\phi$ directions, while for 3-D, $8 \times N_\theta \times N_\phi$ directions are computed, implying that the computational overhead and memory requirements increase linearly with each angular discretisation division and that for each spatial dimension that is added, the overhead doubles. These control angles are then divided into subdivisions (pixellations). The DO method solves the RTE for a finite number of control angles while the incoming or outgoing radiation to each control angle face is computed by the energy contained in each pixel. The RTE is uncoupled from the energy equation, implying that at each cell, the RTE and energy equation are solved sequentially with the RTE implemented through a correction term in the energy equation.

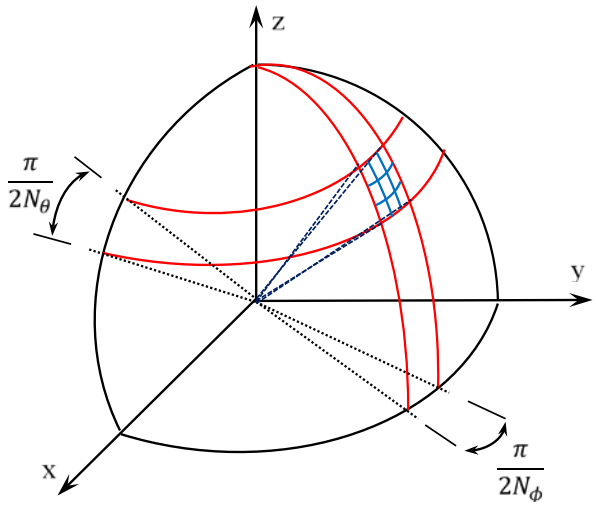

Figure IV.1. Definition of angular discretization and pixellation used in DO method for S_2.

The DO method is easy to implement in FV, and easy to solve especially in serial calculations. In addition, the DO method determines the solution of the RTE on the same mesh as the energy, mass and momentum conservation equations, which leads to a close coupling of surface temperature and radiative energy. This implies that the DO can be applied to complex geometries for different participating media such as non-grey, anisotropically scattering, non-isothermal, absorbing and emitting media. Nevertheless, the DO method has two major shortcomings due to its FV nature, namely the “ray effect” and “false scattering”, which affect result accuracy (Brunner, 2002; Chai & Patankar, 2006). The “ray effect” is also known as “ray concentration” (Martinek & Weimer, 2013), and the “false scattering” as “numerical scattering” (Li, 2004), “numerical smearing” (Jessee & Fiveland, 1997) or “false diffusion” in CFD communities (Hachicha, 2013).

Various methods were suggested by different researchers (Hachicha, 2013; Jessee & Fiveland, 1997; Li, 2004;), but their implementation in ANSYS Fluent due to its closed-source specification is almost impossible. Therefore, in the following paragraphs, the origin of these errors and their alleviation are discussed.

The DO approximation or S_N method, where N is the number of ordinate directions, in FV, assumes that a radiation beam is propagated in a few particular angular directions instead of being propagated in continuum angular directions (as is the case in reality or in the RTE, with its 4π solid angle). The latter is the source of the so-called ray effect or ray concentration errors (Brunner, 2002). This error generates a wavy solution in heat flux and can be alleviated by choosing a higher number of ordinate directions (high-order S_N method) or by increasing the number of subdivisions (control angles), i.e. minimising the solid angle extents, for example, Kim and Lee (1989) used 14 ordinate directions (S_{14}) for presenting benchmark results of collimated incidence in a two-dimensional rectangular, anisotropic scattering medium. Hachicha (2013) illustrated the reduction in the ray effect by increasing the number of control angles in eight separate test cases in his PhD thesis.

False scattering, on the other hand, is a non-physical error that comes from the spatial discretisation. Chai et al. (1993) and Chai and Patankar (2006) reported that if the direction of the radiation beam propagation was aligned with the grid lines, the numerical error which led to a smeared solution would be eliminated. However, this error can be reduced by refining the spatial grid or using more accurate spatial discretisation schemes (Hachicha, 2013).

Therefore, in order to redress these shortcomings, the following practical strategies were suggested by Moghimi et al. (2015a):

1. choosing higher-order S_N method (S_4, S_8, S_{16}, …);
2. increasing the control angle count;
3. increasing the spatial mesh count, and;
4. using a higher-order spatial discretisation scheme for the DO direction equations.

These options are available within open-source CFD or user-defined CFD codes; however, the commercial CFD packages restrict the user's ability to change the order of the S_N method, typically providing S_2 only (ANSYS Fluent).

To illustrate the interaction between the FV mesh density and the angular discretisation of the DO in reducing both the ray effect and false scattering, a test case from literature (Li, 2004) with an available Monte Carlo ray-tracing result is used.

The domain (illustrated in Figure IV.2.) has oblique collimated radiation entering into a black square enclosure filled with a pure isotropical scattering and homogeneous medium $(\sigma_s = 1, a = 0 \, in \, RTE \, Eq.)$ The oblique angle is defined by θ = -90°, ϕ = -60°and enters through a transparent section of the top wall $(0 \le x \le 0.2)$. The other walls of the enclosure are perfectly opaque and cold (0 K Temperature). The reason for choosing this case study is to see how well ANSYS Fluent deals with specular radiation with discontinuities (the expected step change in heat flux on the bottom wall).

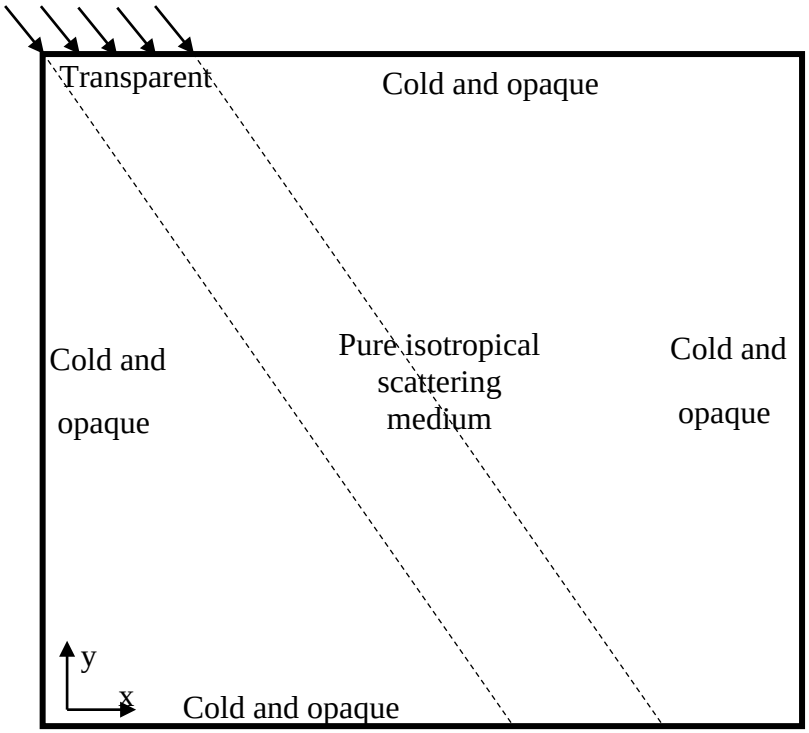

Figure IV.2. Configuration of oblique collimated radiation case study.

A structured Cartesian mesh is used (as in Hachicha, 2013) in order to have an unaligned mesh with the incident radiation direction. This means that false scattering in the computational domain is expected.

The results are reported in Figure IV.3 and Figure IV.4. In Figure IV.3**,** the results are compared with the Monte Carlo solution (Li, 2004) and in Figure IV.4**,** the CFD incident radiation contours are displayed. The following notation is used:

$N_x \times N_y \_ N_\theta \times N_\phi \_ Pixel_\theta \times Pixel_\phi \_ Order\ of\ spatial\ discretisation\ on\ Discrete\ Ordinates$

where the first two terms (N_x, N_y) are the number of cells along *x*- and *y*-directions, respectively, the next four specify the angular discretisation and pixellation in the two angular coordinates and the last term specifies either first- or second-order discretisation as available in ANSYS Fluent.

For this domain, the effect of varying the mesh density, then increasing the angular discretisation divisions, changing the discretisation order, and lastly, combining the optimal combination of these settings is illustrated in Figure IV.3 when using ANSYS Fluent. Note that the value of N_θ needs only to be set to 3 in the second dimension if the assumption of a 2-D planar coordinate system is valid.

In Figure IV.3a, the ray effect due to an insufficient number of angular discretisations is obvious, as the focus of the incoming oblique ray misses the intended target as illustrated by the comparative accurate Monte Carlo ray-tracing solution. The ray effect error decreases with increasing $N_\theta \times N_\phi$ and the peak of each curve shifts towards the expected solution where, due to heat flux step change (between x = 0.577 and x=0.777), a peak in the curve is evident. Settings finer than $N_\phi = 40$ do not result in a change in the peak location, implying that the ray effect error is minimised at this setting. However, it is clear that some false scattering remains.

To reduce the false scattering error, the effects of refining the spatial grid and using a more accurate spatial discretisation scheme for the sufficient ray effect reduction case $(N_\phi = 40)$ are investigated separately in Figure IV.3b and Figure IV.3c respectively. The reduction in the smearing of the wave front is noted as the mesh is refined (Figure IV.3b), but the sharp discontinuity in absorbed radiation is not captured, even for the finest mesh (8-fold

increase). Second-order discretisation improves the smearing in a marked fashion. Figure IV.3c shows that switching to second-order spatial discretisation sharpens the peak even for the coarsest mesh (50*50) for the case that reduced the ray effect error (3*40_3*3 for angular discretisation), but it does not perfectly predict Monte Carlo solution, which exhibits a flat peak. Finally, by combining all the above methods, the false scattering and ray effect can be significantly reduced, with the discontinuity greatly captured (Figure IV.3d). Finally, the effects of the discussed strategies on CFD incident radiation contours are displayed in Figure IV.4.

In summary, ANSYS Fluent has the ability to lead to a reasonably accurate solution of a specular radiation case with available CFD algorithms without any extra UDF coding. To reduce the effects of these errors for the converged solution in an optical modelling simulation, in addition to a mesh study, a control angle study with higher-order spatial discretisation has to be done, before relying on the converged solution.

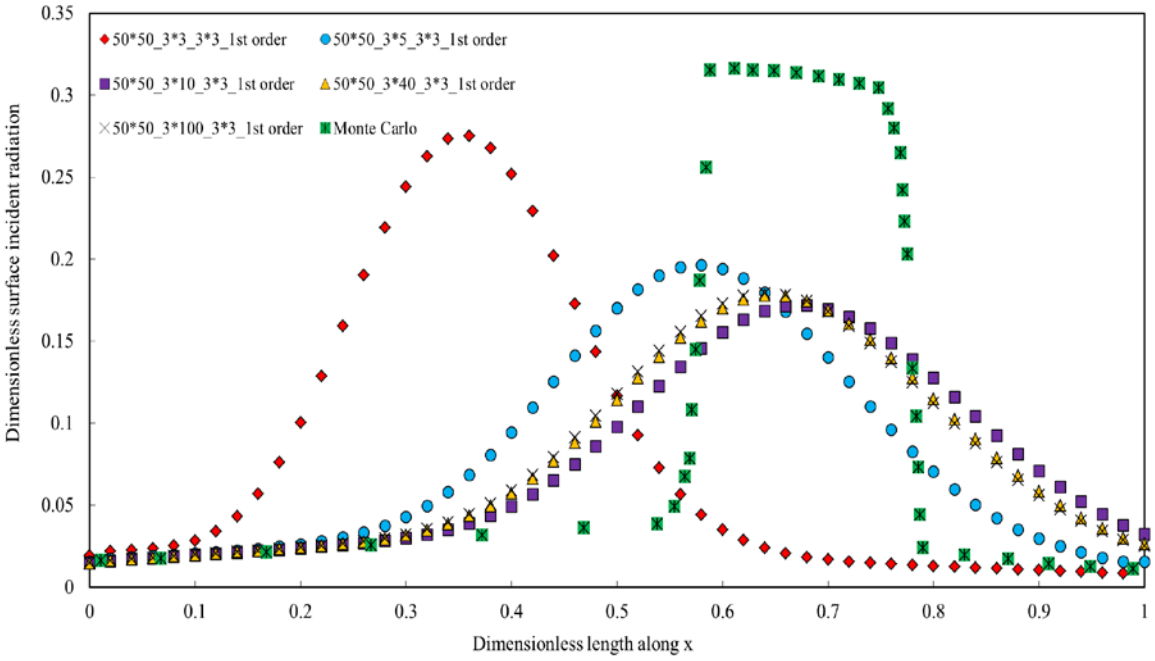

(a)

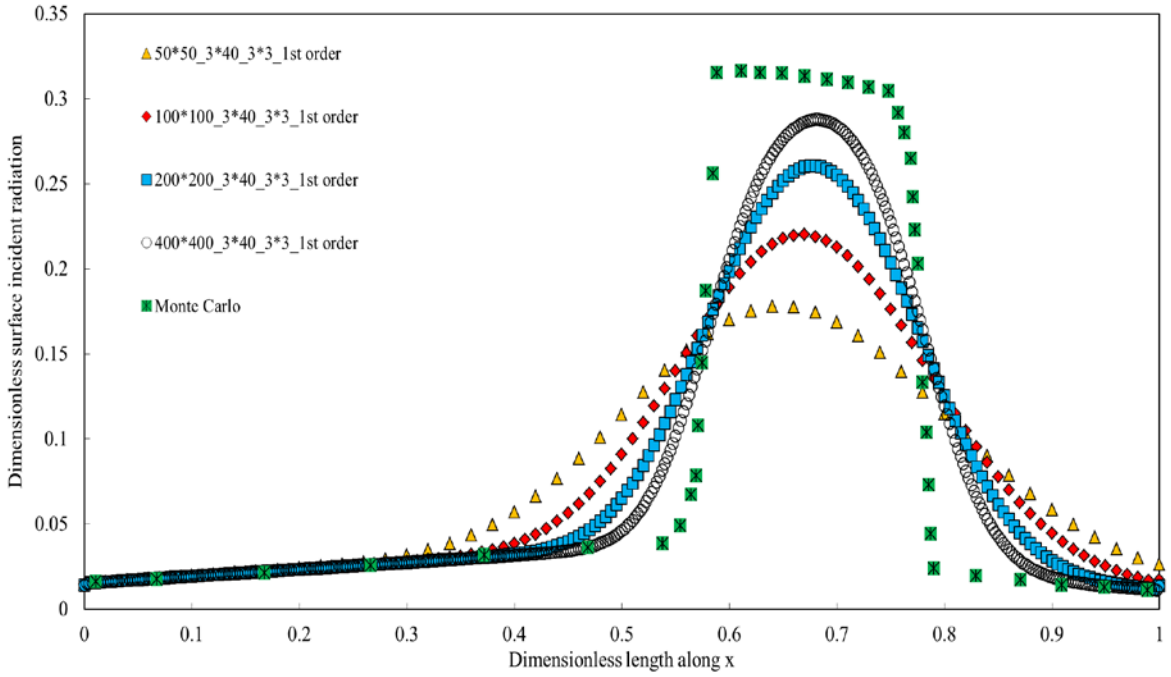

(b)

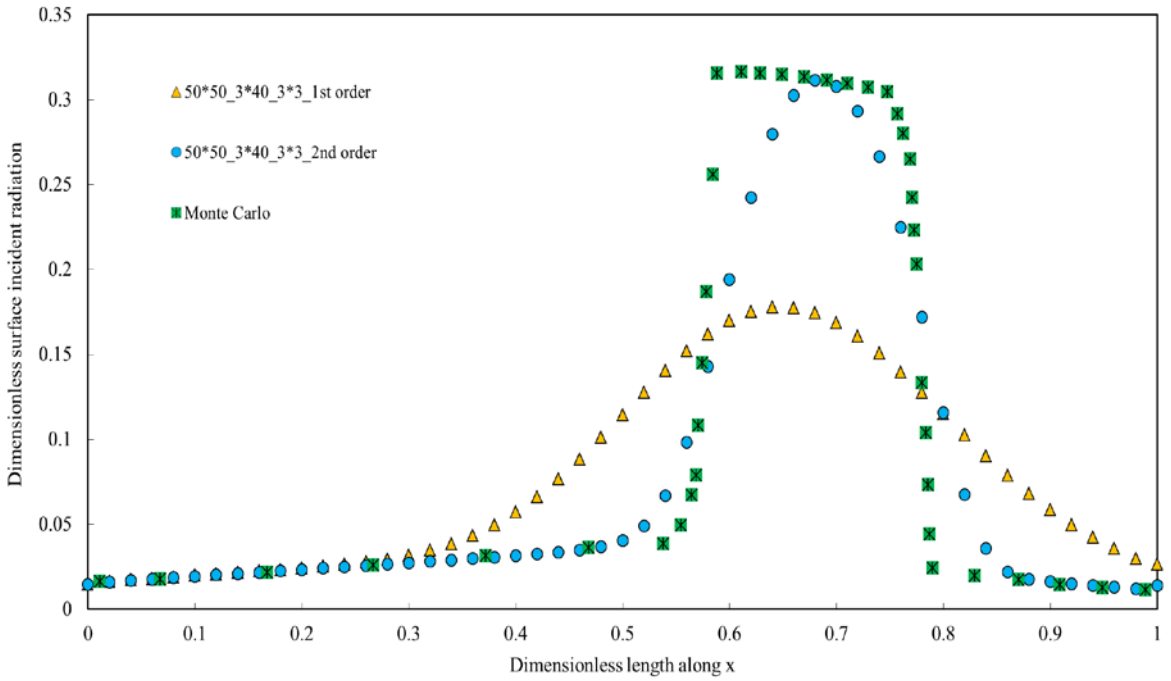

(c)

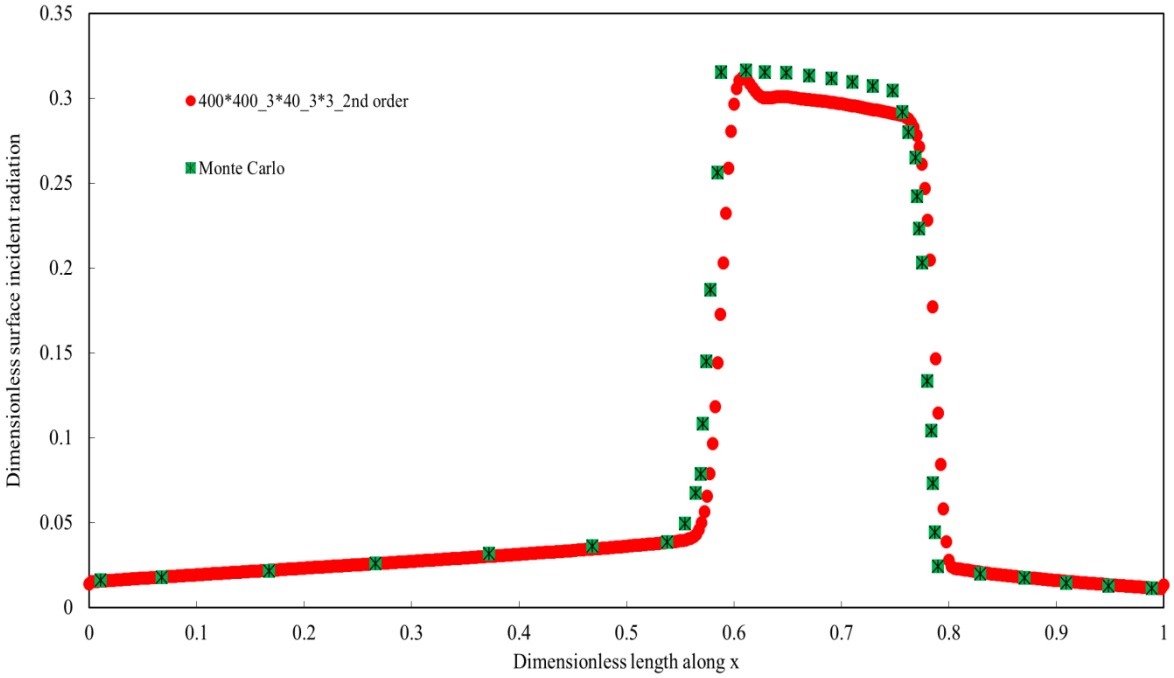

(d)

Figure IV.3. Variation of (a) angular discretisation, (b) mesh density, (c) discretisation order, (d) optimal combination of settings; for oblique collimated radiation test case, as compared with Monte Carlo solution (Li, 2004).

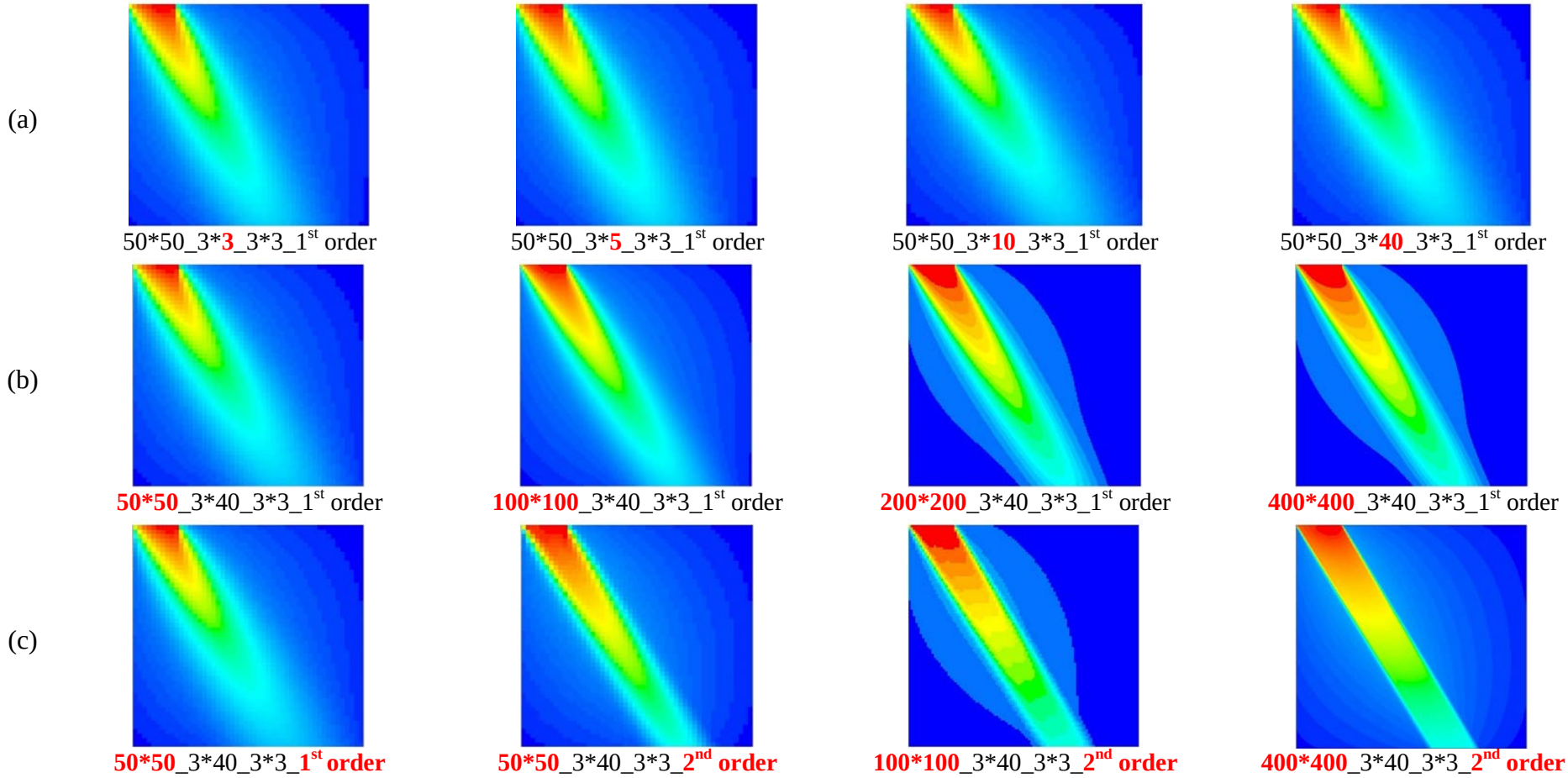

Figure IV.4. Incident radiation contour plots.

(a) Effects of refining angular discretisation. (b) Effects of mesh refinement. (c) Effects of increasing order of solution and refining the mesh.

ADDENDUM V PATCHING SOLAR LOAD FROM OPTICAL TO THERMAL DOMAIN IN CFD

The ability of ANSYS Fluent to model the thermal characteristics of a cavity receiver is well known (e.g. Cheng et al., 2012; He et al., 2011; Lin et al., 2013; Martinek & Weimer, 2013). In most cases, a separate code is used for the optical modelling of the solar field, resulting in interface definitions and linking issues. In this section, the author introduces an approach that uses ANSYS Fluent features for integration of the optical and thermal modelling in a single software domain, that of ANSYS Workbench. Because of this integration and the availability of parameters and design optimisation tools within this environment, the extension to conducting optimisation studies or further investigations based on the optical and thermal modelling described in this section is straightforward.
In this regard, this addendum shows how the suggested mapping approach can be implemented in practice. Hence this section describes the 3-D thermal model of the LFC cavity discussed in Section 3.2 by using ANSYS Fluent. With the help of the suggested mapping approach, this thermal model incorporates the non-uniform heat flux distribution taken from the optical simulation (described in Section 3.3).

In the following, the thermal modelling geometry and meshing of the mentioned problem are discussed. The non-uniform heat flux determined by either a ray-tracing code or an FV implementation of the RTE needs to be included in the conjugate heat transfer model of the cavity receiver for the thermal efficiency of the cavity to be calculated. Since the external surfaces of the pipes are internal surfaces in a CFD model of the cavity, it is not possible to apply the heat source as a standard boundary condition profile. This means that the heat flux must be converted to an internal volumetric heat source. Cheng at al. (2012) and He et al. (2011) treat the volumetric heat source as a surface phenomenon because of the fact that the absorption occurs very close to the surface (within 1μm, according to Bergman et al. (2011)). To mimic this surface/volumetric interaction, the current study applies a

volumetric heat source to a very thin shell region of each pipe ($1/10^{th}$ of the pipe thickness).

For the thermal modelling of an LFC, a 3-D model of the trapezoidal cavity was created in ANSYS Workbench (ANSYS, 2013b) and meshed in ANSYS Meshing tool based on the parameters defined in Table 3.6. The symmetrical 3-D CFD model and meshes are displayed in Figure **V**.1. The thin shell for the application of the volumetric heat source is indicated in Figure **V**.1b.

Figure **V**.1a shows that a symmetrical half of the cavity is considered with insulation on top and on the sides. The aperture is covered by a glass cover. The external faces of these solids are now boundary conditions in this model. It can be seen that the cavity is extruded in the heat transfer fluid (HTF) flow direction by only a small distance (1cm) (Figure **V**.1c). This is justified by using fully developed flow profiles for the HTF and is based on a sensitivity study that indicated that five computational cells in the flow direction were sufficient to capture the effects of the third dimension. The HTF considered is single-phase liquid water. The HTF domain is subdivided to allow for mapped (quadrilateral) meshing (Figure **V**.1b) for increased accuracy and faster convergence of the turbulent flow. The rest of the cavity fluid is paved with quad/tri elements whereas the insulation, glass and pipes have mapped meshes. After generating the mesh of the cavity cross-section, a swept mesh (or Cooper mesh) is considered along the *z*-direction (left part of Figure **V**.1c). The volumetric heat source in the outer shell of each pipe conducts through the inner section of each pipe towards the HTF and also interact with the air in the cavity, and other cavity surfaces through convection and radiation.

Boundary conditions and material properties of the described thermal modelling are discussed in the following. As mentioned above, fully developed profiles are used for the HTF inlet. These include the three velocity components and the turbulent kinetic energy and turbulence dissipation rate. A User-Defined Function (UDF) is used to define these boundary conditions, based on the following:

The velocity profile is based on the 1/7th power law (Schlichting, 1979):

$$\frac{v_z}{V_{centerline}} = \left(1 - \frac{r}{R}\right)^{\frac{1}{7}} \quad \textbf{(V.1)}$$

where $V_{centerline}$ is the free-stream velocity, which is calculated by the average velocity across the pipe, R is the inner radius of the pipe and v_z is the z-velocity at a distance r from the pipe centre.

For defining the turbulent kinetic energy and the turbulence dissipation rate, the wall shear stress must be determined. Using the power law above will result in a very high velocity gradient at the wall and will, therefore, lead to an unrealistic wall shear stress and friction velocity. Hence Blasius' law of friction is used for the wall shear stress (Schlichting, 1979), valid for a range of Reynolds numbers based on diameter of 4 000 to 1e5 (White, 2006):

$$\frac{\tau_w}{\rho} = 0.03955 \times V_{average}^2 \times \left(\frac{\rho V_{average} R}{\mu}\right)^{\frac{-1}{4}} \quad \textbf{(V.2)}$$

A Reynolds number of about 5 000 is used in the current study. For an average or mean velocity that is 80% of the centre line velocity (Schlichting, 1979), Equation (V.2) becomes:

$$\frac{\tau_w}{\rho} = 0.0225 \times V_{centerline}^2 \times \left(\frac{\rho V_{centerline} R}{\mu}\right)^{\frac{-1}{4}} = \nu_\tau^2 \quad \textbf{(V.3)}$$

where v_τ is the friction velocity.

The turbulent kinetic energy at the wall (obeying the log law) follows from the friction velocity (White, 2006):

$$k_{near-wall} = \frac{{v_\tau}^2}{\sqrt{C_\mu}} \quad \textbf{(V.4)}$$

and is assumed to vary linearly from this value to its free-stream value (ANSYS, 2006):

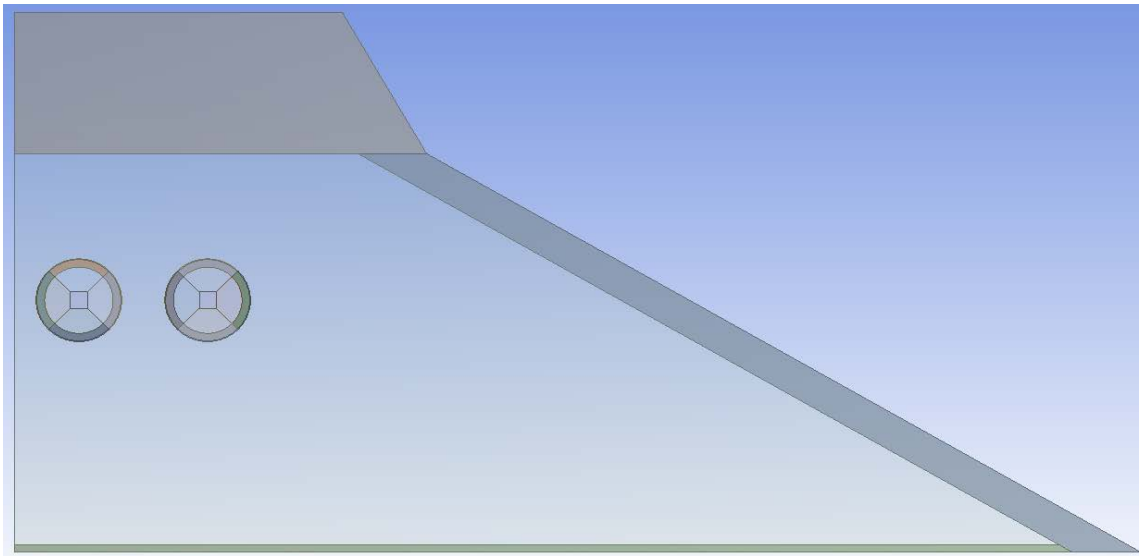

(a)

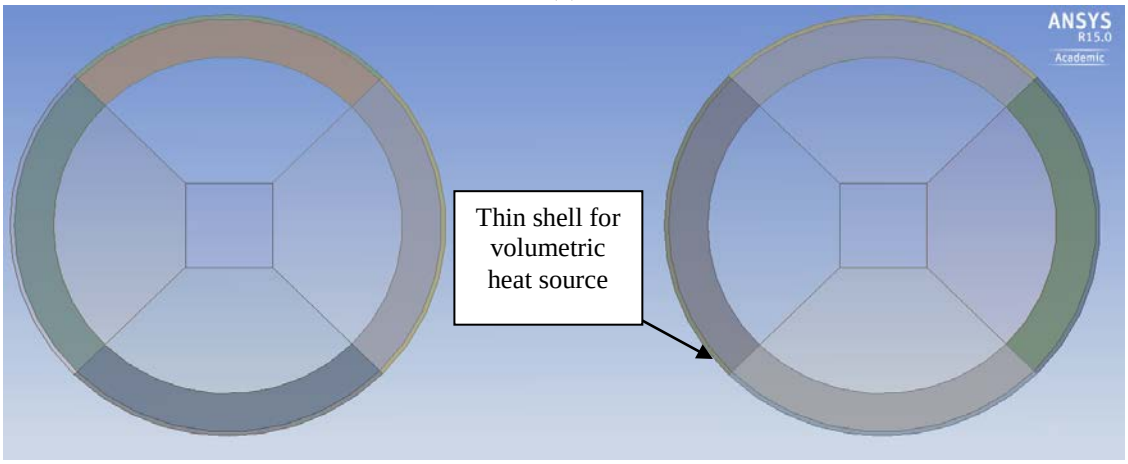

(b)

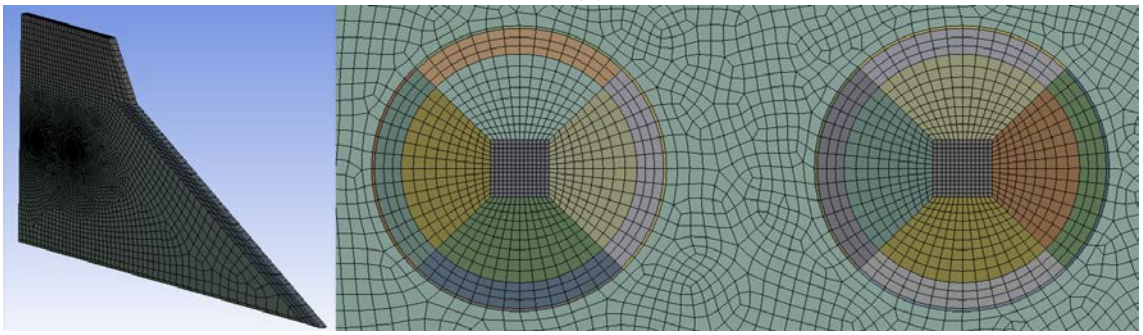

(c)

Figure V.1. The symmetrical 3-D CFD domain and mesh.

(a) Entire thermal domain. (b) Zoom of pipes. (c) Mesh on entire thermal domain and zoom area.

$$k_{free\_stream} = 0.002V^2_{centerline} \quad \textbf{(V.5)}$$

The turbulence dissipation rate is related to the friction velocity (White, 2006):

$$\varepsilon = \frac{\nu_\tau^3}{l} \quad \textbf{(V.6)}$$

where l is a mixing length. Hence

$$\varepsilon = \frac{C_\mu^{3/4}\left(k^{3/2}\right)}{l} \quad \textbf{(V.7)}$$

where the mixing length l is the minimum $0.041(R-r)$ and $0.085R$ (ANSYS, 2006).

For referral purposes, the plane at z = 0 is called the In-plane, z = 1 the Out-plane (except for the pipe outlets) and x = 0 (centre line) is called the Mid-plane.

In this study, both convective and radiative thermal boundary conditions are applied to external boundaries of the cavity domain.

The 3-D thermal model uses a dual-band approach (Moghimi et al., 2014; 2015c). A dual-band absorption coefficient is defined in ANSYS Fluent to capture glass physical property below and above 4.25μm. The result is that the re-radiated energy from the cavity surfaces will be absorbed by the glass because of the spectral shift in emissive power of lower temperature surfaces due to Planck's law.

Last but not least, the reflected energy from a surface depends on the surface roughness, and can be reflected either specularly (in one direction as for a mirror) or diffusely (in all directions) or a combination of these ways. The first one occurs on smooth surfaces while the second one occurs on rough surfaces. In radiation terminology, a rough surface is a surface that has a roughness height that is much larger than the incident radiation wavelength. In other words, if the root mean square (RMS) of the surface roughness is much higher than the incident radiation wavelength, the surface acts as diffuse, and if it is much lower, it acts as specular. It is noteworthy that both types of reflections have the

same amount of total energy implying that the diffuse reflection in any direction is less than the total specular amount. The diffuse versus specular property of a surface is defined in ANSYS Fluent using the diffuse fraction option.

Based on the above discussion, the boundary conditions are tabulated in Table V.1. In addition, material properties of this study are mentioned in Table 4.1.

Patching the non-uniform solar heat flux in the optical domain on the absorber tubes of thermal domain as volumetric heat source is conducted via the following procedure (Craig et al., 2010):

1) Convert the absorbed radiation (solar load) on the pipes from the 2-D optical simulation into an interpolation file with the required 3-D Fluent format (*.ip). This process involves scaling the heat flux [W/m^2] q'' to a volumetric heat source [W/m^3] Q by satisfying the formula:

$$q''2\pi RL = Q\pi\left(R^2 - r^2\right)L$$

$$\therefore Q = q''\frac{2\pi RL}{\pi\left(R^2 - r^2\right)L} = q''\frac{2R}{(R+r)(R-r)} \approx \frac{q''}{(R-r)} \; for \; 2R \approx R + r \qquad \textbf{(V.8)}$$

with L the tube length, R the outer and r the inner radius of the shell. For a very thin shell, this reduces to division by the shell thickness as indicated.

2) Under Define/User-Defined, activate one scalar UDS-0 for all cell zones (fluid and solid) and one User-Defined Memory location (UDM-0).

3) Initialise case and data, or if the data exist, patch zero values to UDS-0 and UDM-0 for all cell zones.

4) In the File/Interpolate, interpolate each individual source file (*.ip file) to the UDS in each corresponding cell zone.

5) Define and interpret a UDF: DEFINE_ON_DEMAND (copy_UDS_to_UDM) to copy the interpolated scalar data from UDS-0 to UDM-0 (see Addendum VI for the UDF code).

6) Define and interpret a UDF: DEFINE_SOURCE that links a source name to the UDM (see Addendum VI for the UDF code).

7) Assign the source term of the appropriate name-selected solid cell zone to the UDF name in 6).

8) For saving memory during the ensuing simulation, the scalar “UDS-0” can now be deactivated.

After executing the procedure, the UDM data (containing the heat source) can be plotted as in Figure V.2 to check the success of the patching operation.

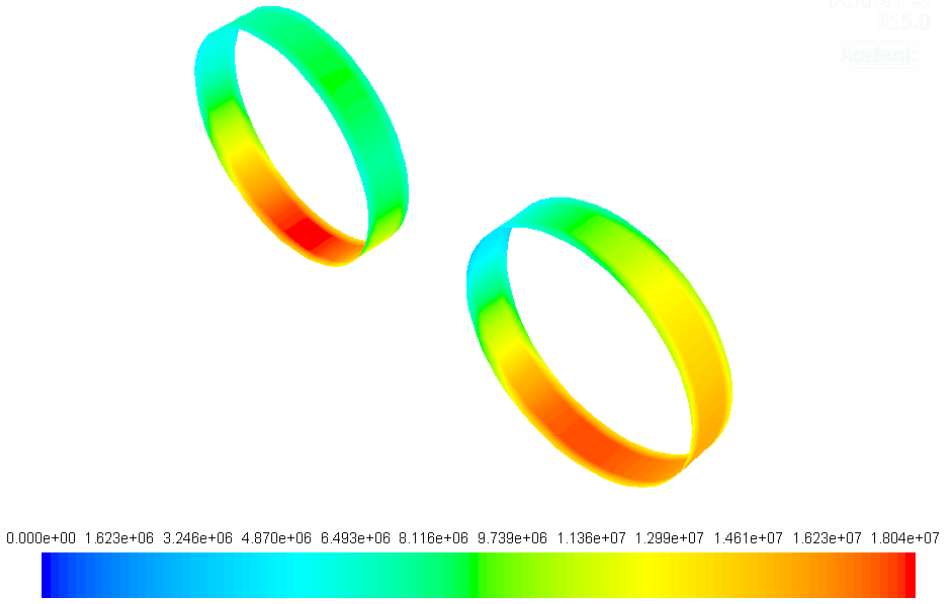

Figure V.2. Contours of patching data (non-uniform solar heat flux for 346 900 mesh and 3x200 angular discretisations) as volumetric heat source [W/m^3] in UDM

Table V.1 Boundary conditions of thermal domain in 3-D model

Surface	**BC type**	**Velocity components [m/s]**	**Temperature [K]**	**Heat transfer coefficient [W/m^2-K]**	**Emissivity**	**Other**
Pipe inner side	Stationary wall and coupled thermal condition	0,0	-	-	-	-
Pipe outer side	Stationary wall and opaque with selective absorber coating and coupled thermal condition	0, 0	-	-	Band0= 0.95, Band1= 0.1 (Kennedy, 2002)	Diffuse Fraction: Band0= 1, Band1= 0
Top and side wall	Stationary wall and opaque with reflective coating and coupled thermal condition	0, 0	-	-	Band0= 0.05, Band1= 0.05	Diffuse Fraction: Band0= 1, Band1= 0
Glass inner side	Stationary wall, semi-transparent and coupled thermal condition	0, 0	-	-	-	Diffuse Fraction: Band0= 0,Band1= 0
Glass outer side	Mixed thermal condition	-	300 (conv), 305 (rad)	5	0.9	-
Insulation outer side	Mixed thermal condition	-	300 (conv), $T_{sky}=0.0522*300^{1.5}$ (rad)	5	0.75	-
Pipe inlet	Fully developed turbulent velocity inlet	UDF (See Addendum VI)	500	-	-	Equations (V.4), (V.5) and (V.6)
Pipe outlet	Outflow	-	-	-	-	-
In-plane, Out-plane, Mid-plane	Symmetry	-	-	-	-	-

To validate the accuracy of the suggested patching approach, the discussed 2-D optical:3-D thermal simulation (simulated optical domain in 2-D (discussed in Section 3.3) and exporting non-uniform solar heat flux load to be patched on the absorber tubes of the 3-D thermal model by the suggested patching approach) is compared with a full 3-D simulation of the optical and thermal performance combined. A full 3-D (the depth of full 3-D case is 1 cm) simulation is run, which incorporates both the 3-D mirror field and 3-D cavity thermal model with pipes and HTF. This model is more expensive to run because of the increased domain and solution of the RTE, energy and Navier-Stokes equations. However, it will not have any interpolation inaccuracies that may arise from the patching procedure.

The geometry of the full 3-D domain and its mesh are displayed in Figure V.3. For comparison, the boundary conditions, material properties and CFD settings of the full 3-D domain and 3-D patching thermal domain are the same as previously discussed except for the air in the cavity being considered a solid and the glass having no absorption in Band 0. In addition, since the full 3-D model cannot be run with the same mesh density and angular discretisation settings as the 2-D optical model (discussed in Section 3.4) because of computer memory limitations, a lower resolution 2-D optical result is used in the comparison. In order to do this, the absorbed flux distribution obtained with the 2-D optical model is scaled to be the same as that obtained with the full 3-D model (see Figure V.4 for the respective heat sources).

The integrated results of the two methods are compared in Table **V**.2. The results show a good agreement with the total amount of energy transferred to the HTF indicating a 0.4% difference. This fact proves the reliability of the mapping approach and the much less expensive phased 2-D:3-D simulation.

Table V.2 Comparison of 2-D optical:3-D thermal and full 3-D results.

Idea	**Pipe**	**T_{in} [K]**	**T_{out} [K]**	**Mass flow rate [kg/s]**	**c_p [J/kgK]**	**Total energy transferred to HTF [W]**
2-D optical: 3-D thermal	3rd tube	500	500.0191	0.158273	4182	12.662
	4th tube	500	500.0208	0.158273	4182	13.774
	total (divergence percentage)					26.436 (-0.42%)
Full 3-D	3rd tube	500	500.0192	0.158027	4182	12.689
	4th tube	500	500.021	0.157795	4182	13.858
	total (divergence percentage)					26.547 (0%)

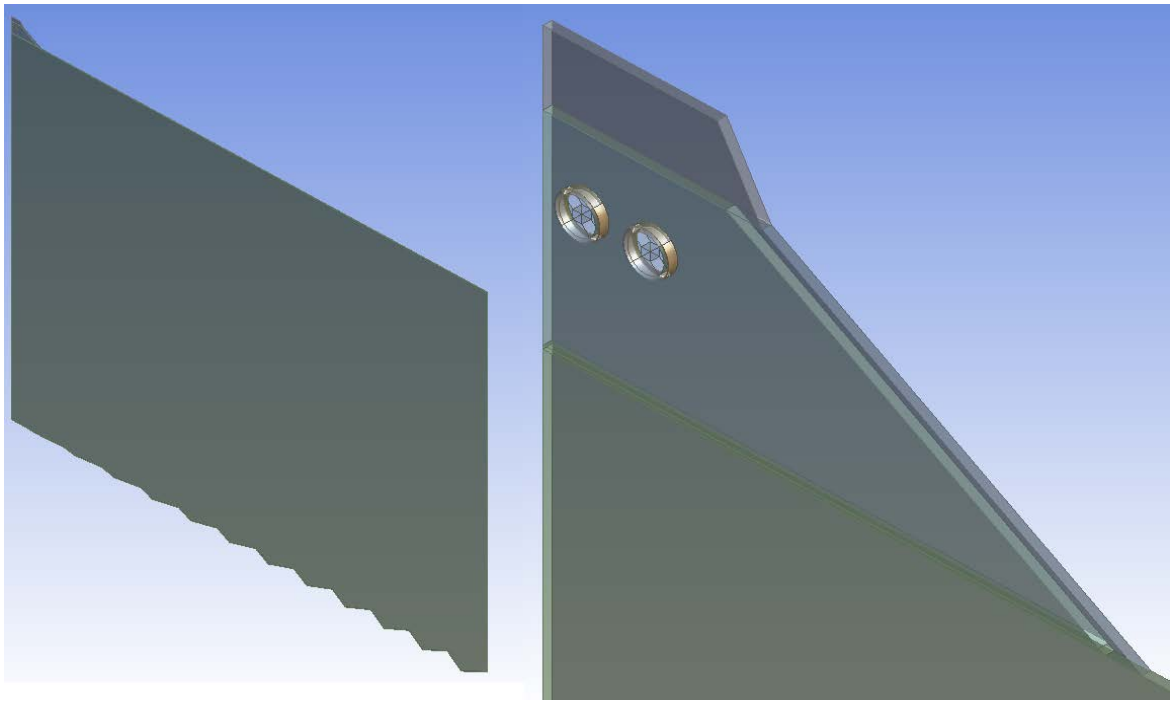

(a)

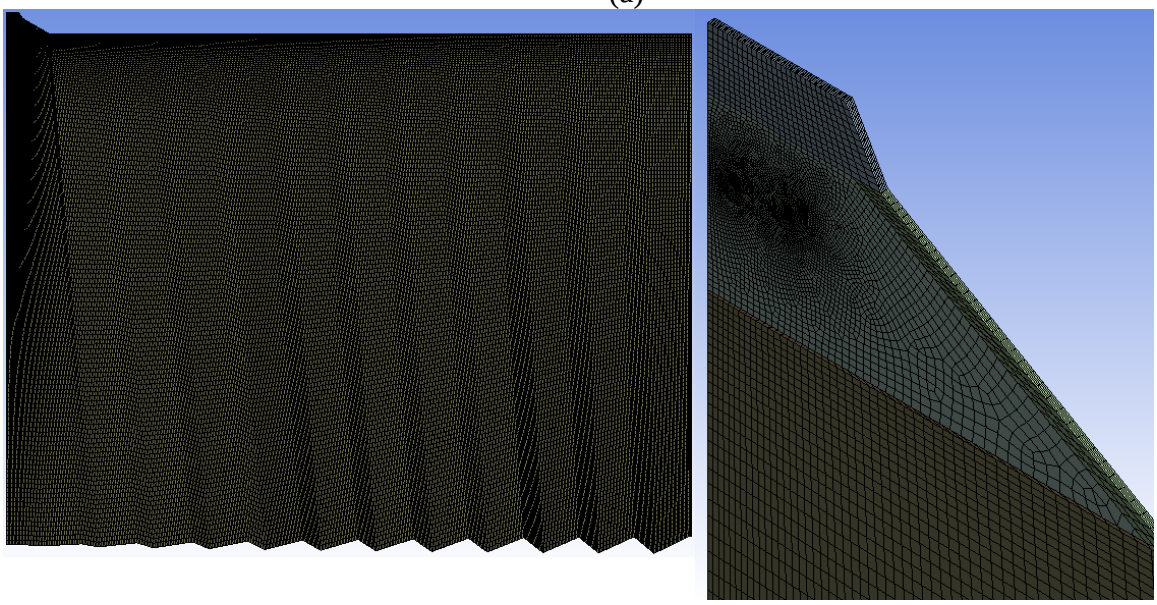

(b)

Figure V.3. Geometry and mesh for full 3-D model.

(a) Geometry of full 3-D domain with mirror field and a close-up of the 3-D cavity. (b) Meshing of full 3-D domain and close-up of the cavity.

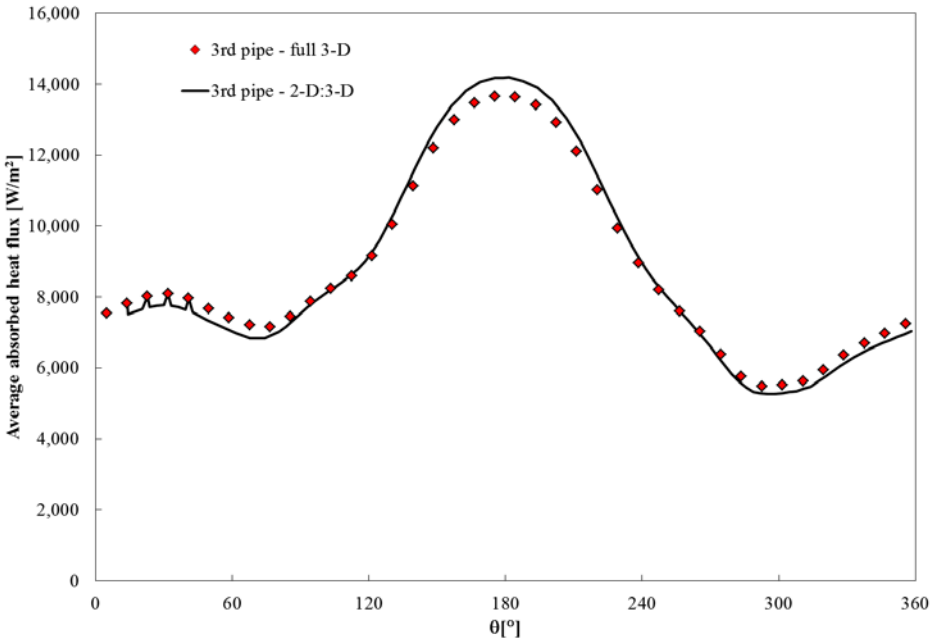

(a)

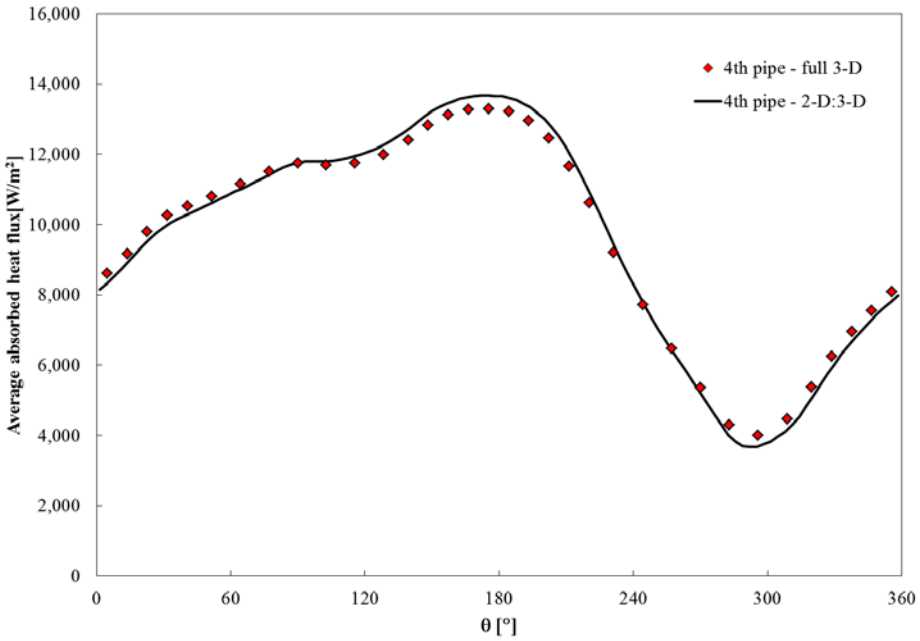

(b)

Figure V.4. Comparison of heat flux distribution [W/m^2] around absorber tubes for 2-D:3-D and full 3-D models.

(a) Around the 3rd tube (b) Around the 4th tube.

ADDENDUM VI UDF IN ANSYS FLUENT

UDF WRITTEN FOR CALCULATING FULLY DEVELOPED PROFILES IN INLET OF TUBES OF THE MULTI-TUBE CAVITY CASE

```
#include "udf.h"
#define ReynoldsNumber 5033.477392
#define PipeDiameter 0.04
#define FluidDensity 998.2
#define FluidViscosity 1.003e-03
#define pi 3.1415927
#define CMU 0.09
#define VonKarman 0.041
#define yyy 7.977903

DEFINE_PROFILE(velProf, thread, position)
{
real x[ND_ND];
real xx, yy, BulkVelocity, MaximumVelocity, r,MaximumR, NormalY, MassFraction;
face_t f;
BulkVelocity = (ReynoldsNumber * FluidViscosity) / (PipeDiameter * FluidDensity);
MaximumVelocity = 1.22449 * BulkVelocity;
MassFraction = FluidDensity * BulkVelocity * PiNumber * (PipeDiameter/2)*
(PipeDiameter/2);
 begin_f_loop(f,thread)
 {
 F_CENTROID(x, f, thread);
   yy=x[1]-yyy;
   if ((x[0]>0) && (x[0]<0.075))
          {
            xx=x[0]-0.0375;
          }
   else
          {
            xx=x[0]-0.1125;
          }
 r = pow(xx*xx + yy*yy, 0.5);
 MaximumR = PipeDiameter / 2;
 NormalY = (MaximumR-r)/MaximumR;
 F_PROFILE(f, thread, position) = MaximumVelocity * pow(NormalY, 1./7.);
}
 end_f_loop(f, thread)
}
DEFINE_PROFILE(k_profile,t,i)
 {
```

```
 real KinematicViscosity, ff, utau, kNearWall, kFreeStream, xx, yy, r, x[ND_ND];
 real MaximumR, NormalY, BulkVelocity, MaximumVelocity;
 face_t f;
KinematicViscosity = FluidViscosity / FluidDensity;
MaximumR = PipeDiameter / 2;
BulkVelocity = (ReynoldsNumber * FluidViscosity) / (PipeDiameter * FluidDensity);
MaximumVelocity = 1.22449 * BulkVelocity;
ff = 0.045/pow(MaximumVelocity*MaximumR/KinematicViscosity,0.25);
utau=sqrt(ff*pow(MaximumVelocity,2.)/2.0);
kNearWall=pow(utau,2.)/sqrt(CMU);
kFreeStream=0.002*pow(MaximumVelocity,2.);
begin_f_loop(f,t)
 {
 F_CENTROID(x,f,t);
yy=x[1]-yyy;
   if ((x[0]>0) && (x[0]<0.075))
          {
           xx=x[0]-0.0375;
          }
   else
          {
           xx=x[0]-0.1125;
          }
 r = pow(xx*xx + yy*yy, 0.5);
 MaximumR = PipeDiameter / 2;
 NormalY = (MaximumR-r)/MaximumR;
F_PROFILE(f,t,i)=kNearWall + NormalY*(kFreeStream-kNearWall);
}
 end_f_loop(f,t)
}
DEFINE_PROFILE(e_profile,t,i)
 {
 real KinematicViscosity, ff, utau, kNearWall, kFreeStream, xx, yy, r, x[ND_ND];
 real MaximumR, NormalY, BulkVelocity, MaximumVelocity, tke, l;
 face_t f;
 KinematicViscosity = FluidViscosity / FluidDensity;
 MaximumR = PipeDiameter / 2;
 BulkVelocity = (ReynoldsNumber * FluidViscosity) / (PipeDiameter * FluidDensity);
 MaximumVelocity = 1.22449 * BulkVelocity;
 ff = 0.045/pow(MaximumVelocity*MaximumR/KinematicViscosity,0.25);
 utau=sqrt(ff*pow(MaximumVelocity,2.)/2.0);
 kNearWall=pow(utau,2.)/sqrt(CMU);
 kFreeStream=0.002*pow(MaximumVelocity,2.);
 begin_f_loop(f,t)
 {
 F_CENTROID(x,f,t);
```

```
 yy=x[1]-yyy;
   if ((x[0]>0) && (x[0]<0.075))
          {
           xx=x[0]-0.0375;
          }
  else
          {
           xx=x[0]-0.1125;
          }
 r = pow(xx*xx + yy*yy, 0.5);
 MaximumR = PipeDiameter / 2;
 NormalY = (MaximumR-r)/MaximumR;
 tke = kNearWall + NormalY*(kFreeStream-kNearWall);
if (VonKarman*(MaximumR-r) < 0.085*MaximumR)
 l = VonKarman*(MaximumR-r);
 else
 l = 0.085*MaximumR/2;
F_PROFILE(f,t,i)=pow(CMU,0.75)*pow(tke,1.5)/l;
}
 end_f_loop(f,t)
}
```

UDF FOR COPYING UDS-0 TO UDM-0

```
#include "udf.h"
#include "sg.h"
DEFINE_ON_DEMAND(copy_uds_to_udm)
{
Domain* d=Get_Domain(1);
Thread *t;
cell_t c;
thread_loop_c(t,d)
  {
   begin_c_loop(c,t)
    {
     C_UDMI(c,t,0)=C_UDSI(c,t,0);
    }
   end_c_loop (c,t)
  }
 return;
}
```

UDF FOR DEFINING SOURCES

```
DEFINE_SOURCE(solar_heat,c,t,dS,eqn)
{
real source;
dS[eqn]=0.0;
source=C_UDMI(c,t,0);
return source;
}
```

ADDENDUM VII HEAT TRANSFER MECHANISMS IN A MULTI-TUBE CAVITY RECEIVER

To formulate the thermal optimisation problem, a thorough understanding of the heat transfer mechanisms present is required. The heat transfer mechanisms in and around the proposed cavity of Figure 3.1 are illustrated in Figure VII.1. The four absorber tubes are enclosed with a trapezoidal geometry. Typically, high-pressure water, which flows inside the tubes, will absorb the incident solar energy that is irradiated to the cavity by mirrors and passes through the glass cover, which covers the bottom side of the cavity. This energy, therefore, increases the HTF temperature until it reaches the liquid saturation temperature at the relevant pressure. Beyond this point, the HTF quality increases and a boiling process will occur. In other words, the HTF will change from a single-phase flow to a two-phase flow. The HTF could then return to a single phase depending on the conditions, but the only parameter of concern in the current implementation is the average temperature of the tubes' exterior surface. A constant tube outer-surface temperature replaces the effect of the solar irradiation absorbed by all the cavity surfaces. This assumption has been used widely by previous researchers, as discussed in Section 4.2.1.

Inside the cavity domain, all three heat transfer mechanisms exist. Natural convection is driven by temperature differences that cause density differences in the fluid. Because of the gaps between the tubes and the space above and on either side of the tubes, low resistance paths exist for this convection flow to occur. Due to the location of the tubes inside the cavity, one could expect to see such phenomena in the upper part of the cavity domain with conductive heat transfer dominating in the lower half of the cavity, leading to stratification of the temperature in that region. However, radiation remains the dominant heat transfer mechanism in the entire cavity and therefore also the main heat loss contributor. The cavity components (tubes and side and top walls) are considered to be opaque to radiation, i.e. they absorb radiation and reflect it in a way that depends on the incident radiation wavelength (which interacts with the surface roughness height such that reflection is either

specular or diffuse). The absorbed energy increases the temperature of each surface, leading to thermal re-radiation that is proportional to the emissivity of the surface. It is important to note that the radiative energy leaves a surface (radiosity) and is combined with the emissive radiation and reflected radiation in a specific direction, then reaches other surfaces where it is defined as the incident radiation. On the other hand, the energy which reaches the cavity bottom surface (covered with glass) is transmitted by conduction and radiation.

The glass window has interesting properties. Glass is opaque to high wavelength (infrared) radiation and semi-transparent for the rest of the spectrum (see, for example, glass properties as tested by Loenen & Van der Tempel, 1996). This is explained in detail in Section 4.2.1.

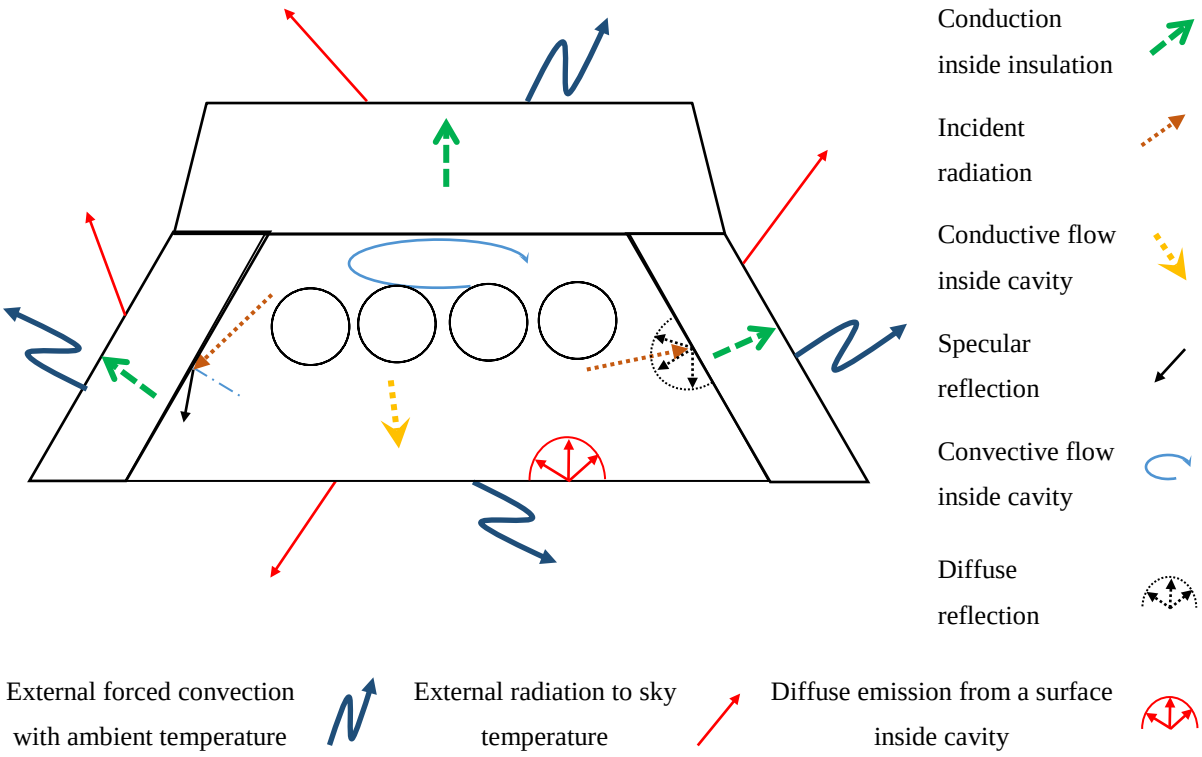

Figure VII.1. Heat transfer mechanisms for cavity receiver.

The rest of the domain includes conduction through the insulation, and along its outer edge, an external boundary condition of radiation and convection (due to an external wind) is considered. The insulation, apart from limiting heat transfer across it, is required beacuse its absence would lead to high temperatures on the upper and side walls of the cavity, which would emit radiation to the sky temperature, with significant radiation losses. For simplicity, the heat transfer mechanisms inside the glass, tubes and those over some surfaces inside and outside the cavity have not been shown in Figure VII.1.

ADDENDUM VIII DAILY SOLAR POWER CODES

VBA CODES FOR MUTLI-TUBE TRAPEZOIDAL CAVITY RECEIVER OF AN LFC WITH INDIVIDUAL MIRROR FOCAL LENGTH ACROSS MIRROR FIELD

```
Sub moghimi()
Dim myFile As String, text As String, textline As String, Flux As Integer
Multiplication_per_degree = 15
FileCounter = (180 - Multiplication_per_degree) / Multiplication_per_degree
For j = 1 To FileCounter
   Sun_angle = Multiplication_per_degree * j
   ThisWorkbook.Sheets(2).Cells(11, 2) = Sun_angle
   Data = ""
   Data = ThisWorkbook.Sheets(1).Cells(13, 2) ' adding number of mirrors
   Data = Data & vbNewLine & ThisWorkbook.Sheets(1).Cells(21, 2) ' adding Number of Tubes
   """"""""""""""""""""""""""""""""""""""""""""""""""""""
   """"adding Mirror coordinates
   """"""""""""""""""""""""""""""""""""""""""""""""""""""
   Mirror_Numbers = ThisWorkbook.Sheets(1).Cells(13, 2)
   For k = 1 To 6
      For i = 1 To Mirror_Numbers
         If k <= 3 Then
            Data = Data & vbNewLine & ThisWorkbook.Sheets(3).Cells(4 + k, 1 + i)
         Else
            Data = Data & vbNewLine & ThisWorkbook.Sheets(3).Cells(18 + k, 1 + i)
         End If
      Next i
   Next k  'adding X,Y,Z,Xaim,Yaim and Zaim for each indiviual mirror
   For i = 1 To Mirror_Numbers
     Data = Data & vbNewLine & ThisWorkbook.Sheets(3).Cells(4, 1 + i) 'adding Mirror width
   Next i
   """"""""""""""""""""""""""""""""""""""""""""""""""""""
   """"adding Tube coordinates
   """"""""""""""""""""""""""""""""""""""""""""""""""""""
   Tube_Numbers = ThisWorkbook.Sheets(1).Cells(21, 2)
   For k = 1 To 6
      For i = 1 To Tube_Numbers
         Data = Data & vbNewLine & ThisWorkbook.Sheets(5).Cells(1 + k, 1 + i)
      Next i
   Next k 'adding X,Y,Z,Xaim,Yaim and Zaim for Tubes
   """"""""""""""""""""""""""""""""""""""""""""""""""""""
   """"adding Cavity walls
   """"""""""""""""""""""""""""""""""""""""""""""""""""""
   For k = 1 To 7
      For i = 1 To 3
         If k <= 3 Then
```

```
            Data = Data & vbNewLine & ThisWorkbook.Sheets(4).Cells(3 + k, 1 + i)
         Else
            Data = Data & vbNewLine & ThisWorkbook.Sheets(4).Cells(16 + k, 1 + i)
         End If
      Next i
   Next k 'adding X,Y,Z,Xaim,Yaim and Zaim, wall width for cavity walls
   Data = Data & vbNewLine & ThisWorkbook.Sheets(1).Cells(16, 2) -
ThisWorkbook.Sheets(1).Cells(18, 2) + 0.004 'adding z location of Top Glass wall (m)
   Data = Data & vbNewLine & ThisWorkbook.Sheets(1).Cells(23, 4)  'adding width of Top Glass
wall (m)
   Data = Data & vbNewLine & ThisWorkbook.Sheets(1).Cells(16, 2) -
ThisWorkbook.Sheets(1).Cells(18, 2) 'adding z location of Bottom Glass wall (m)
   Data = Data & vbNewLine & ThisWorkbook.Sheets(1).Cells(23, 2)  'adding width of Bottom
Glass wall (m)
   Data = Data & vbNewLine & ThisWorkbook.Sheets(1).Cells(17, 2) 'adding tube radius (m)
   Data = Data & vbNewLine & ThisWorkbook.Sheets(1).Cells(15, 2) 'adding pipe center location
(m)
   pth = "C:\Users\User\Desktop\New folder\Soltrace Data"
   Set fs = CreateObject("Scripting.FileSystemObject")
   Set textfilecreation = fs.CreateTextFile(pth & "\" & Sun_angle & "degree.txt", True)
   textfilecreation.writeline (Data)
   textfilecreation.Close
Next j
Dim wsh As Object
Set wsh = VBA.CreateObject("WScript.Shell")
Dim waitOnReturn As Boolean: waitOnReturn = True
Dim wndowsStyle As Integer: windowsStyle = 1
wsh.Run ("C:\SolTrace\2012.7.9\SolTrace.exe -s
C:\SolTrace\2012.7.9\scripts\mohammad_auto.lk"), windowStyle, waitOnReturn
'Shell ("C:\SolTrace\2012.7.9\SolTrace.exe -s C:\SolTrace\2012.7.9\scripts\mohammad_auto.lk")
'ThisWorkbook.Sheets(1).Cells(27, 2).Value = 0
''''''''''''''''''''''''''''''''''''''''''''''''''''''''''''''''
''''''''''''''''Setting Format
''''''''''''''''''''''''''''''''''''''''''''''''''''''''''''''''
ThisWorkbook.Worksheets(1).Activate
Range("A37:D200").Select
Selection.ClearContents
Selection.Borders(xlDiagonalDown).LineStyle = xlNone
Selection.Borders(xlDiagonalUp).LineStyle = xlNone
Selection.Borders(xlEdgeLeft).LineStyle = xlNone
Selection.Borders(xlEdgeTop).LineStyle = xlNone
Selection.Borders(xlEdgeBottom).LineStyle = xlNone
Selection.Borders(xlEdgeRight).LineStyle = xlNone
Selection.Borders(xlInsideVertical).LineStyle = xlNone
Selection.Borders(xlInsideHorizontal).LineStyle = xlNone
Range("A37:C" & 36 + FileCounter).Select
Selection.Borders(xlDiagonalDown).LineStyle = xlNone
Selection.Borders(xlDiagonalUp).LineStyle = xlNone
```

```
With Selection.Borders(xlEdgeLeft)
    .LineStyle = xlContinuous
    .ColorIndex = 0
    .TintAndShade = 0
    .Weight = xlThin
End With
With Selection.Borders(xlEdgeTop)
    .LineStyle = xlContinuous
    .ColorIndex = 0
    .TintAndShade = 0
    .Weight = xlThin
End With
With Selection.Borders(xlEdgeBottom)
    .LineStyle = xlContinuous
    .ColorIndex = 0
    .TintAndShade = 0
    .Weight = xlThin
End With
With Selection.Borders(xlEdgeRight)
    .LineStyle = xlContinuous
    .ColorIndex = 0
    .TintAndShade = 0
    .Weight = xlThin
End With
With Selection.Borders(xlInsideVertical)
    .LineStyle = xlContinuous
    .ColorIndex = 0
    .TintAndShade = 0
    .Weight = xlThin
End With
With Selection.Borders(xlInsideHorizontal)
    .LineStyle = xlContinuous
    .ColorIndex = 0
    .TintAndShade = 0
    .Weight = xlThin
End With
With Selection
    .HorizontalAlignment = xlLeft
    .Orientation = 0
    .AddIndent = False
    .IndentLevel = 0
    .ShrinkToFit = False
    .ReadingOrder = xlContext
    .MergeCells = False
End With
With Selection.Interior
    .Pattern = xlNone
    .TintAndShade = 0
```

```
   .PatternTintAndShade = 0
End With
"""""""""""""""""""""""""""""""""""""""""""""""""""
""""""""Reading Data from Soltrace results
"""""""""""""""""""""""""""""""""""""""""""""""""""
For j = 1 To FileCounter
   Sun_angle = Multiplication_per_degree * j
   myFile = pth & "\" & Dir(pth & "\" & Sun_angle & "degreeResults.txt")
   'NumFile = Dir(pth & "\" & Sun_angle & "degreeResults.txt")
   text = ""
   Open myFile For Input As #j
   Do While Not EOF(j)
      Line Input #j, textline
      text = text & textline
   Loop
   Close #j
   'StartingArea = InStr(text, "Area")
   'EndingArea = InStr(text, "Element_Hits")
   StartingFlux = InStr(text, "Element_Watts")
   EndingFlux = InStr(text, "Element_Power")
   EndingFlux2 = Len(text)
   ThisWorkbook.Sheets(1).Cells(36 + j, 1).Value = Mid(text, 7, 8)
   ThisWorkbook.Sheets(1).Cells(36 + j, 2).Value = Mid(text, StartingFlux + 15, EndingFlux -
StartingFlux - 15)
   ThisWorkbook.Sheets(1).Cells(36 + j, 3).Value = Mid(text, EndingFlux + 15, EndingFlux2 -
EndingFlux - 15)
   'ThisWorkbook.Sheets(1).Cells(36 + j, 4).Value = Mid(text, StartingArea + 6, EndingArea -
StartingArea - 6)
Next j
ActiveSheet.ChartObjects("Chart 4").Activate
ActiveChart.SeriesCollection(1).Select
Selection.Formula = "=SERIES(,,Sheet1!R37C2:R" & 36 + FileCounter & "C2,1)"
Range("B" & 36 + FileCounter + 1).Select
ActiveCell.FormulaR1C1 = "=AVERAGE(R[" & -1 * FileCounter & "]C:R[-1]C)"
ThisWorkbook.Sheets(1).Cells(34, 2).Select
ActiveCell.FormulaR1C1 = "=AVERAGE(R[3]C[1]:R[" & FileCounter + 2 & "]C[1])"
'ThisWorkbook.Sheets(1).Cells(35, 2) = ThisWorkbook.Sheets(1).Cells(37, 4) / 2 *
ThisWorkbook.Sheets(1).Cells(21, 2)
tube_pitch = ThisWorkbook.Sheets(1).Cells(20, 2)
pipes_view_factor = 0
For i = 1 To Tube_Numbers
ThisWorkbook.Sheets(1).Cells(37, 6) = i
ThisWorkbook.Sheets(1).Cells(40, 6) = ThisWorkbook.Sheets(1).Cells(38, 6) + (i - 1) * tube_pitch
'qleft=p+(i-1)*m
ThisWorkbook.Sheets(1).Cells(36 + i, 4) = ThisWorkbook.Sheets(1).Cells(44, 6)
pipes_view_factor = pipes_view_factor + ThisWorkbook.Sheets(1).Cells(44, 6)
Next i
ThisWorkbook.Sheets(1).Cells(35, 2) = pipes_view_factor
```

End Sub

LK SCRIPT FOR SOLTRACE SIMULATION

```
Multiplication_per_degree = 15;
FileCounter = (180 - Multiplication_per_degree) / Multiplication_per_degree;
for (j=1;j<=FileCounter;j++)
{
	/* ****************************************
		Allocating Data to Array
	   **************************************** */
	cwd("C:\\Users\\User\\Desktop\\New folder");
	ProjectName=j*Multiplication_per_degree+"degree";
	RawData=split(read_text_file(cwd()+ '\\Soltrace Data\\'+ ProjectName+ ".txt"),"\n");
	//Number_Rows=  #RawData;
	Mirror_Number=to_real(RawData[0]);
	Tube_Number=to_real(RawData[1]);
	Line_Number=0;
	while(Line_Number<Mirror_Number)
	{
		Array[Line_Number][0]=to_real(RawData[Mirror_Number*0+Line_Number+2]);
// X of mirror
		Array[Line_Number][1]=to_real(RawData[Mirror_Number*1+Line_Number+2]);
//Y of mirror
		Array[Line_Number][2]=to_real(RawData[Mirror_Number*2+Line_Number+2]);
//Z of mirror
		Array[Line_Number][3]=to_real(RawData[Mirror_Number*3+Line_Number+2]);
//XAim of mirror
		Array[Line_Number][4]=to_real(RawData[Mirror_Number*4+Line_Number+2]);
//YAim of mirror
		Array[Line_Number][5]=to_real(RawData[Mirror_Number*5+Line_Number+2]);
//ZAim of mirror

	Array[Line_Number][6]=to_real(RawData[Mirror_Number*6+Line_Number+2]);//Project
ion of Mirror Width
		Line_Number=Line_Number+1;
	}
	Line_Number=0;
	while(Line_Number<Tube_Number)
	{

	Array2[Line_Number][0]=to_real(RawData[Mirror_Number*7+2+Tube_Number*0+Line
_Number]); // X of tube

	Array2[Line_Number][1]=to_real(RawData[Mirror_Number*7+2+Tube_Number*1+Line
_Number]); //Y of tube
```

```
        Array2[Line_Number][2]=to_real(RawData[Mirror_Number*7+2+Tube_Number*2+Line
_Number]); //Z of tubes

        Array2[Line_Number][3]=to_real(RawData[Mirror_Number*7+2+Tube_Number*3+Line
_Number]); //XAim of tube

        Array2[Line_Number][4]=to_real(RawData[Mirror_Number*7+2+Tube_Number*4+Line
_Number]); //YAim of tube

        Array2[Line_Number][5]=to_real(RawData[Mirror_Number*7+2+Tube_Number*5+Line
_Number]); //ZAim of tube
                Line_Number=Line_Number+1;
        }
        Line_Number=0;
        while(Line_Number<3)
        {

        Array3[Line_Number][0]=to_real(RawData[Mirror_Number*7+2+Tube_Number*6+3*0+
Line_Number]); // X of cavity wall

        Array3[Line_Number][1]=to_real(RawData[Mirror_Number*7+2+Tube_Number*6+3*1+
Line_Number]); //Y of cavity wall

        Array3[Line_Number][2]=to_real(RawData[Mirror_Number*7+2+Tube_Number*6+3*2+
Line_Number]); //Z of cavity wall

        Array3[Line_Number][3]=to_real(RawData[Mirror_Number*7+2+Tube_Number*6+3*3+
Line_Number]); //XAim of cavity wall

        Array3[Line_Number][4]=to_real(RawData[Mirror_Number*7+2+Tube_Number*6+3*4+
Line_Number]); //YAim of cavity wall

        Array3[Line_Number][5]=to_real(RawData[Mirror_Number*7+2+Tube_Number*6+3*5+
Line_Number]); //ZAim of cavity wall

        Array3[Line_Number][6]=to_real(RawData[Mirror_Number*7+2+Tube_Number*6+3*6+
Line_Number]); //cavity wall width
                Line_Number=Line_Number+1;
        }
        counter=0;
        while (counter<6)
        {

        Nodes[counter]=to_real(RawData[Mirror_Number*7+2+Tube_Number*6+3*7+counter]);
                counter=counter+1;
        }
        /* ****************************************
```

```
                Defining Sun Shape
            ****************************************** */
        sunopt({'shape'= 'Gaussian', 'sigma'=2.73,'x'=cos(j*Multiplication_per_degree/180*pi()),
'y'=0, 'z'=sin(j*Multiplication_per_degree/180*pi())});

        /* ******************************************
                Defining Optical Properties
            ****************************************** */
        clearoptics();
        addoptic('Mirror');
        opticopt('Mirror', 1, {'refl'=1, 'trans'=0, 'errslope'=0.0001, 'errspec'=0.0001, 'refractr'=1.5});
        opticopt('Mirror', 2, {'refl'=0, 'trans'=0, 'errslope'=0.0001, 'errspec'=0.0001, 'refractr'=1});
        addoptic('Glass Properties Outer');
        opticopt('Glass Properties Outer', 1, {'refl'=0.02, 'trans'=0.98, 'errslope'=0.0001,
'errspec'=0.0001, 'refractr'=1.5});
        opticopt('Glass Properties Outer', 2, {'refl'=0.02, 'trans'=0.98, 'errslope'=0.0001,
'errspec'=0.0001, 'refractr'=1});
        addoptic('Glass Properties Inner');
        opticopt('Glass Properties Inner', 1, {'refl'=0.02, 'trans'=0.98, 'errslope'=0.0001,
'errspec'=0.0001, 'refractr'=1});
        opticopt('Glass Properties Inner', 2, {'refl'=0.02, 'trans'=0.98, 'errslope'=0.0001,
'errspec'=0.0001, 'refractr'=1.5});
        addoptic('Tube Wall');
        opticopt('Tube Wall', 1, {'refl'=0.05, 'trans'=0, 'errslope'=0.0001, 'errspec'=0.0001,
'refractr'=1});
        opticopt('Tube Wall', 2, {'refl'=0.05, 'trans'=0, 'errslope'=0.0001, 'errspec'=0.0001,
'refractr'=1});
        addoptic('Cavity Back Side');
        opticopt('Cavity Back Side', 1, {'refl'=0, 'trans'=0, 'errslope'=0.0001, 'errspec'=0.0001,
'refractr'=1});
        opticopt('Cavity Back Side', 2, {'refl'=0.95, 'trans'=0, 'errslope'=0.0001, 'errspec'=0.0001,
'refractr'=1});
        addoptic('Cavity Front Side');
        opticopt('Cavity Front Side', 1, {'refl'=0.95, 'trans'=0, 'errslope'=0.0001, 'errspec'=0.0001,
'refractr'=1});
        opticopt('Cavity Front Side', 2, {'refl'=0, 'trans'=0, 'errslope'=0.0001, 'errspec'=0.0001,
'refractr'=1});
        /* ******************************************
                Defining System Stages
            ****************************************** */
        clearstages();
        addstage('Fresnel');
        activestage('Fresnel');
        stageopt('Fresnel',{'virtual'=false,'multihit'=true,'tracethrough'=false});
        clearelements();
        /*      ***********************************
                        Definition of Mirror Field
                        *********************************** */
```

```
	addelement(Mirror_Number);
	i=0;
	while (i<Mirror_Number)
	{
		elementopt(i,{'en'=true, 'x'=Array[i][0],'y'=Array[i][1], 'z'=Array[i][2],
'ax'=Array[i][3], 'ay'=Array[i][4], 'az'=Array[i][5],
			'zrot'=0, 'aper'=['r',Array[i][6],1,0,0,0,0,0,0],
'surf'=['p',1/(2*sqrt(pow(Nodes[2],2)+pow(Array[i][0],2))),0,0,0,0,0,0,0],'interact'= 'reflection',
	'optic' = 'Mirror' , 'comment' = 'Mirror Field'} );
		i=i+1;
	}

	/*	**********************************
			Definition of tube bundle
			********************************** */
	addelement(Tube_Number);
	Tube_Radiuse=Nodes[4];
	i=0;
	while (i<Tube_Number)
	{
		elementopt(Mirror_Number+i,{'en'=true, 'x'=Array2[i][0],'y'=Array2[i][1],
'z'=Array2[i][2], 'ax'=Array2[i][3], 'ay'=Array2[i][4], 'az'=Array2[i][5],
			'zrot'=0, 'aper'=['l',0,0,1,0,0,0,0,0],
'surf'=['t',1/Tube_Radiuse,0,0,0,0,0,0,0],'interact'= 'reflection',	'optic' = 'Tube Wall' , 'comment' =
'Tubes'} );
		i=i+1;
	}
	/*	**********************************
			Definition of cavity walls
			********************************** */
	addelement(3);
	i=0;
	while (i<3)
	{
		elementopt(Mirror_Number+Tube_Number+i,{'en'=true,
'x'=Array3[i][0],'y'=Array3[i][1], 'z'=Array3[i][2], 'ax'=Array3[i][3], 'ay'=Array3[i][4],
'az'=Array3[i][5],
			'zrot'=0, 'aper'=['r',Array3[i][6],1,0,0,0,0,0,0],
'surf'=['f',0,0,0,0,0,0,0,0,0],'interact'= 'reflection',	'optic' = 'Cavity Front Side' , 'comment' = 'Cavity
walls'} );
		i=i+1;
	}
	addelement(2);
	elementopt(Mirror_Number+Tube_Number+3+0,{'en'=true, 'x'=0,'y'=0, 'z'=Nodes[0],
'ax'=0, 'ay'=0, 'az'=0.151656,
			'zrot'=0, 'aper'=['r',Nodes[1],1,0,0,0,0,0,0],
'surf'=['f',0,0,0,0,0,0,0,0,0],'interact'= 'refraction',	'optic' = 'Glass Properties Inner' , 'comment' =
'Glass Surface'} );
```

```
	elementopt(Mirror_Number+Tube_Number+3+1,{'en'=true, 'x'=0,'y'=0, 'z'=Nodes[2],
'ax'=0, 'ay'=0, 'az'=0.147656,
				'zrot'=0, 'aper'=['r',Nodes[3],1,0,0,0,0,0,0],
'surf'=['f',0,0,0,0,0,0,0,0,0],'interact'= 'refraction',    'optic' = 'Glass Properties Outer' , 'comment' =
'Glass Surface'} );
	/* ******************************************
		Run Simulation
	  ****************************************** */
	Ray_Count = 1000000;
	traceopt({'rays'= Ray_Count, 'maxrays' = 10*(Ray_Count), 'include_sunshape'=true,
'optical_errors'=true});
	trace();
	/* ******************************************
		Calculation Heat flux and writing it to a file according to simulation
	  ****************************************** */
	FileName=cwd() + '\\Soltrace Data\\'+ProjectName+"Results.txt";
	if (file_exists(FileName))
		{remove_file(FileName);}
	mkdir(cwd() + '\\Soltrace Data',true);
	T_area = ((sundata(){"xmax"})-(sundata(){"xmin"}))*((sundata(){"ymax"})-
(sundata(){"ymin"}));
	DNI = to_real(1000);
	Power_Per_Ray = DNI*T_area/sundata(){"nrays"};
	//Power_Per_Ray=1;
	Element_Power=0;
	Element_Watts=0;
	for (i=0;i<Tube_Number;i++)
	{
		Rinverse =to_real(elementopt(Mirror_Number+i){"surf"}[1]);//Tube Element
Number for elementopt
		Area=3.14*2/Rinverse;//Pi()*D*length
		Element_Hits = rayhits(0,Mirror_Number+i,1); //final intersections only (last
digit=1)
		Element_Power= Element_Power+(Power_Per_Ray*Element_Hits); //[W]
		Element_Watts = Element_Watts+(Power_Per_Ray*Element_Hits)/(Area);
//[W/m^2]
	}
	write_text_file(FileName,("file: "+j*Multiplication_per_degree+"degree"+"\n"+"T_area:
"+ T_area+ "\n"+"DNI: "+ DNI+ "\n"+"Power_Per_Ray: "+ Power_Per_Ray+ "\n"+"Area: "+
Area+ "\n"+"Element_Hits: "+ Element_Hits+ "\n"+"Element_Watts: "+ Element_Watts+
"\n"+"Element_Power: "+ Element_Power+ "\n"));
	cwd(cwd()+ '\\Soltrace Data\\');
	save_project(ProjectName + ".stinput");
}
```

ADDENDUM IX KRIGING

Kriging is named after D.G. Krige, who utilised empirical methods for the determination of a true ore grade distribution from a sample ore grade distribution (LS-OPT, 2003). The basic postulate of its formulation is a combination of a polynomial model plus departures:

$$y(x) = f(x) + Z(x) \quad \textbf{(IX.1)}$$

where $y(x)$ is the unknown function of interest, $f(x)$ is a known polynomial function, and $Z(x)$ is the stochastic component with mean zero, variance σ^2, and non-zero covariance as listed in Equation (IX.2). $f(x)$ approximates the global design space while localised deviations are generated by $Z(x)$.

$$Cov\left[Z(x^i), Z(x^j)\right] = \sigma^2 R\left(\left[r(x^i, x^j)\right]\right) \quad \textbf{(IX.2)}$$

with an M number of sampling points, R is the correlation matrix ($M*M$ symmetric positive definite with unit diagonal matrix) and $r(x^i, x^j)$ is the spatial correlation of the function between any two arbitrary sample points (x^i, x^j).

The commonly used correlation functions are Exponential (Equation (IX.3a)) and Gaussian (Equation (IX.3b)) forms:

$$r = \prod_{k=1}^{N} e^{-\vartheta_k \left| x_k^i - x_k^j \right|} \quad \textbf{(IX.3a)}$$

$$r = \prod_{k=1}^{N} e^{-\vartheta_k \left(x_k^i - x_k^j \right)^2} \quad \textbf{(IX.3b)}$$

where N is the number of design variables, and x_k^i, x_k^j are the k^{th} components of two arbitrary sample points. There are thus M number of unknown ϑ parameters which must be set to fit the model. The correlation which ANSYS DX uses is the Gaussian function (Equation (IX.3b)). Using a single correlation parameter does not always provide good results, therefore, ANSYS DX provides an option which lets users choose between a single correlation parameter (one correlation parameter for all design variables), or multiple

correlation variables (one correlation parameter for each design variable), which means that only one unknown ϑ parameter exists. The choice is made by selecting the Variable or Constant option for the Kernel Variation Type in DX.

$Z(x)$ can be written as follows (ANSYS, 2013c).

$$Z(x) = \sum_{i=1}^{N} \lambda_i r(x^i, x) \qquad \textbf{(IX.4)}$$

ADDENDUM X MULTI-OBJECTIVE GENETIC ALGORITHM (MOGA)

Consider $\min_{x \in X} \vec{f}(x)$, where $\vec{f}$ is a multi-objective function. All feasible solutions are defined by (ANSYS, 2013c):

$$X := \{x \in \Re'' : g(x) \geq 0, h(x) = 0, x_i \leq x \leq x_u\} \quad \textbf{(X.1)}$$

where x is the vector of design parameters (or variables) and $x' \in X$ such that for all m objective functions, x^* is optimal, then

$$f_i(x^*) \leq f_i(x) \ \forall x \in X \quad for\ i = 1, 2, ..., m \quad \textbf{(X.2)}$$

This indicates that x^* is the utopian solution. Unfortunately, such a solution rarely exists, because the probability of the event that all $f_i(x)$ reach their minimum values at a common point (x^*) in X would be rare. The concept of a Pareto optimum was defined by V. Pareto in 1986. The concept of Pareto dominance is a highly important part of multi-objective optimisation, particularly when some or all of the objectives and constraints are mutually conflicting. In such a case, there is no utopian point which leads to a best answer for all objectives and constraints. The aim of multi-objective optimisation in such a case is to find the best solutions (a Pareto or non-dominated set) that are a group of solutions, when selecting any one of these solutions; on the one hand, the quality of one objective or constraint will be sacrificed, while on the other hand, the quality of at least one other objective or constraint will be boosted.

In general, for the generic optimisation of any problem, the optimal Pareto could be defined as an ideal vector of which the components are separately attainable minima for all objective functions. Therefore, the vector $f^* = (f_1^*, f_2^*, ..., f_m^*)$ where f_i^* represents the scalar optimisation solution of the i^{th} objective function as $\min_{x \in X} f_i(x) \leq f_i^*$ $for\ i = 1, 2, ..., m$ at its relevant x'.

Therefore, the ideal solution of a multi-objective optimisation problem is the point (Pareto Optimal) in X which determines x^*. Unfortunately, the Pareto optimisation almost always gives a set of solutions, rather than a single solution.

The MOGA optimiser in ANSYS DX incorporates global Pareto filters and leads to a global Pareto front. To achieve this, a hybrid variant of controlled elitism concepts, NSGA-II, is used. The Pareto ranking scheme and objective and constraint handling are executed by a fast, non-dominated sorting method that is an order of magnitude faster than traditional Pareto ranking methods. To avoid premature convergence, ANSYS DX uses a "Percent Pareto" parameter, which lets users control the selection pressure (and consequently, the elitism of the process).

ADDENDUM XI INSULATION AREA FORMULA FOR INSULATION OPTIMISATION STUDY

According to Figure 5.3, the mathematical formulations for calculating the surrounding insulation area are as follows:

The summation of the side insulation area is:

$$Side\,areas = 2 \times b \times h\left[mm^2\right] \quad \textbf{(XI.1)}$$

The top insulation area is:

$$Top\ area = 0.5 \times t \times \left[2 \times \left(332 + 2 * b - \frac{2 \times h}{\tan\theta} \right) - \frac{2 \times t}{\tan\delta} \right] \left[mm^2\right] \quad \textbf{(XI.2)}$$

Therefore, the total insulation area is:

$$Total\ area = 2 \times h \times b + 2 \times b \times t - \frac{t^2}{\tan\delta} + \left(332 - \frac{2 \times h}{\tan\theta} \right) \times t \ \left[mm^2\right] \quad \textbf{(XI.3)}$$

By substituting 144 and 51 for h and θ respectively (the results of the optimum cavity in Section 5.5.1) in Equation (XI.4), the total insulation area is:

$$Total\ area = 288 \times b + 2 \times b \times t - \frac{t^2}{\tan\delta} + \left(332 - \frac{288}{\tan 51} \right) \times t \ \left[mm^2\right] \quad \textbf{(XI.4)}$$